

# Novel Semiconductor Block Copolymers for Organic Electronic Devices: Synthesis, Properties and Applications

DISSERTATION

zur Erlangung des akademischen Grades  
eines Doktors der Naturwissenschaften (Dr. rer. nat.)  
im Fach Chemie der Fakultät für  
Biologie, Chemie und Geowissenschaften der Universität Bayreuth

vorgelegt von

**Michael Sommer**

Geboren in Stuttgart / Deutschland

Bayreuth, 2009



Die vorliegende Arbeit wurde in der Zeit von Februar 2006 bis April 2009 am Lehrstuhl Angewandte Funktionspolymere/ Makromolekulare Chemie I unter der Betreuung von Prof. Dr. Mukundan Thelakkat angefertigt.

Vollständiger Abdruck der von der Fakultät für Biologie, Chemie und Geowissenschaften der Universität Bayreuth genehmigten Dissertation zur Erlangung des akademischen Grades eines Doktors der Naturwissenschaften (Dr. rer. Nat.)

Dissertation eingereicht am: 17.04.2009

Wissenschaftliches Kolloquium: 28.07.2009

Prüfungsausschuss:

Erstgutachter: Prof. Dr. Mukundan Thelakkat

Zweitgutachter: Prof. Dr. Peter Strohriegel

Vorsitzender: Prof. Dr. Helmut Alt

Prof. Dr. Andreas Fery



*Meiner Familie*



---

## TABLE OF CONTENTS

	Summary/ Zusammenfassung	
1.	Introduction	I-1
2.	Overview of Thesis	II-1
3.	Semiconductor Block Copolymer Nanocomposites with Lamellar Morphology via Self-Organization	III-1
4.	Crystalline-Crystalline Donor Acceptor Block Copolymers	IV-1
5.	Semiconductor Block Copolymers for Photovoltaic Applications	V-1
6.	Influence of the Molecular Weight of Double-Crystalline Donor-Acceptor Block Copolymers on the Performance of Polymer Solar Cells	VI-1
7.	Novel Electron Conducting Block Copolymers: Morphological, Optical and Electronic Properties	VII-1
8.	<i>n</i> -Type Organic Field Effect Transistors from Perylene Bisimide Block Copolymers and Homopolymers	VIII-1
9.	In Situ Imaging of Evolution of Morphology of Semiconductor Polymer Blends and Block Copolymers Using Focused Ion Beam and Scanning Electron Microscopy: Scope and Limitations	IX-1
10.	Appendix: Synthesis, Characterization and Application of Donor Acceptor Block Copolymers in Nanostructured Bulk Heterojunction Solar Cells	X-1
11.	Appendix: Microphase-Separated Donor Acceptor Diblock Copolymers: Influence of HOMO Energy Levels and Morphology on Polymer Solar Cells	XI-1
12.	List of Publications	XII-1



## Summary

This thesis is concerned with original work on the tailor-made synthesis, characterization and application of well-defined semiconductor donor-acceptor (D-A) block copolymers for high-performance organic field effect transistors and organic photovoltaics. Two types of D-A block copolymer architectures are presented: Amorphous-crystalline block copolymers and crystalline-crystalline block copolymers. The materials developed are complex in terms of their synthesis, since organic methods have to be combined with one or more polymerization methods. The importance of D-A block copolymers is illustrated by their capability to microphase separate into domain sizes commensurate to the exciton diffusion length, which makes such materials highly suitable for efficient charge separation and charge transport. The self-assembling behaviour is governed by the interplay of different forces: Crystallization of one or more blocks and microphase separation. Currently such materials enjoy wide interest in academics, as they enable precise interface tuning of electro-optically active chromophores.

Two controlled polymerization methods were employed, combined and adapted in order to create well-defined, multi-functional, and innovative block copolymer structures: Nitroxide Mediated Controlled Radical Polymerization (NMRP) and Grignard Metathesis Polymerization (GRIM). NMRP was used to polymerize *N,N'*-bis(4-methoxyphenyl)-*N*-phenyl-*N'*-4-vinylphenyl-(1,1'-biphenyl)-4,4'-diamine (vDMTPD), and well-defined PvDMTPD polymers with low polydispersity were obtained. These amorphous building blocks were subsequently used as macroinitiators to polymerize the acceptor monomer perylene bisimide acrylate (PerAcr), yielding the desired D-A PvDMTPD-*b*-PPerAcr block copolymer architecture. Furthermore, the PvDMTPD homopolymers and PvDMTPD-*b*-PPerAcr block copolymers were compared to simpler, triphenylamine-based homopolymers and block copolymers (PvTPA-*b*-PPerAcr) in terms of morphology, energy levels, absorption, hole carrier mobility, and photocurrent generation.

Furthermore, NMRP is used to synthesize several block copolymers PvDMTPD-*b*-P4vP and PS-*b*-PPerAcr with different compositions. Here, one electronically active segment is combined with commercially available monomers such as styrene (S) and 4-vinylpyridine (4vP). The morphology is investigated as a function of composition and molecular weight. Such materials enable to confine the active chromophore geometrically in nanosized block copolymer domains.

Solar cells were constructed from the fully functionalized block copolymers and the performance of single layer devices was compared and correlated to the changes in morphology, energy levels, and charge carrier mobility. The exploitation of the synergetic interplay of these parameters increased the power conversion efficiencies five-fold compared to block copolymers with unsubstituted triphenylamine blocks that were investigated earlier in our group.

In the third part of this thesis, the library of amorphous donor segments is broadened by the incorporation of main chain conjugated poly(3-hexylthiophene)s (P3HT) to further enhance the hole carrier mobility and extend the absorption to longer wavelengths. P3HT was synthesized via GRIM. This method was successfully optimized in order to gain excellent control over molecular weight and polydispersity. For the purpose of preparing P3HT

macroinitiators for NMRP in a straightforward fashion, a simple one-pot procedure was developed. The resulting narrow-distributed, main-chain conjugated P3HT macroinitiators were successfully employed for the NMRP of the acceptor monomer PPerAcr. Special attention was paid to the preparation of well-defined, double-crystalline P3HT-*b*-PPerAcr block copolymers containing P3HT segments with different molecular weights and compositions.

All novel materials P3HT-*b*-PPerAcr were extensively characterized by standard, optical, electrical and microscopic methods. The double-crystalline nature of P3HT-*b*-PPerAcr is verified by differential scanning calorimetry and X-ray diffraction, revealing lamellar P3HT regions among stacks of PPerAcr. The coexistence of these two different types of crystalline domains is strikingly influenced by the relative segment lengths, the overall molecular weights, and the annealing conditions. While thermal annealing promotes the crystallinity of PPerAcr, chloroform vapor annealing gives rise to rearrangement of P3HT. These effects are observed consistently in the optical, thermal, morphological, and electrical properties of P3HT-*b*-PPerAcr. The construction of organic photovoltaic devices revealed outstanding external quantum efficiencies (EQE) of 31 % for a device made of a high molecular weight P3HT-*b*-PPerAcr with balanced composition. This is a real breakthrough in the field of solar cells with perylene bisimide as the acceptor material. The highest EQE values ever reported for blends of P3HT and low molecular weight perylene bisimide lie only around 20 % after extensive optimization. We ascribe the excellent device performance to microdomain confinement of PPerAcr crystallization, while maintaining a high hole carrier mobility. The high hole mobility is due to a high degree of P3HT crystallinity, which again is achieved by the considerably high segment length of P3HT. In the block copolymers with the smaller molecular weights of P3HT, hole transport is about two orders of magnitude lower, not only due to the smaller molecular weight itself, but also due to partial suppression of P3HT aggregation by the crystallization of PPerAcr.

Furthermore, excellent electron mobilities of  $1.2 \cdot 10^{-3} \text{ cm}^2/\text{Vs}$  of the PPerAcr homopolymer were measured in organic field effect transistors. Surprisingly, a block copolymer PS-*b*-PPerAcr with 30 wt.-% polystyrene exhibits the same electron mobility. These results are promising not only because polymeric n-type materials with high electron mobilities are rare, but also because the charge carrier mobility of block copolymers has been reported to decrease with the attachment of the electronically non-active amorphous blocks.

In the last part of this thesis, the scope and limitation of the combination of focused ion beam (FIB) and scanning electron microscopy (SEM) is investigated to image buried structures of vertically phase separated, semiconducting thin films. Two model systems are used: Several semiconducting D-A block copolymers and polymer blends. Thereby, major artefacts are produced under certain circumstances. Several experimental parameters are elucidated under which these artefacts appear or are absent.

## Zusammenfassung

Diese Arbeit beschreibt die Synthese und Charakterisierung von neuartigen, maßgeschneiderten Donor-Akzeptor (D-A) Blockcopolymeren mit elektronisch funktionellen Blöcken, sowie deren Anwendung in organischen Feldeffekttransistoren und organischen Solarzellen. Die hergestellten D-A Blockcopolymere können in zwei Klassen unterteilt werden: Blockcopolymere mit einem amorphen und einem kristallinen Block und Blockcopolymere mit zwei kristallinen Blöcken. Die Synthese dieser neuen Materialien verlangt die geschickte Kombination von klassischer organischer Chemie mit einer oder zwei Polymerisationsmethoden. Die Besonderheit solcher aufwendigen Blockcopolymere liegt in ihrer Fähigkeit zur Mikrophasenseparation. Die dadurch entstehenden Domänengrößen liegen im Bereich der Exzitonendiffusionslänge, wodurch D-A Blockcopolymere als äußerst vielversprechend für Ladungstrennung und Ladungstransport gelten. Die Selbstaggregation der D-A Blockcopolymere wird vom Zusammenspiel verschiedener Kräfte geleitet: Kristallisation eines oder zweier Blöcke und Mikrophasenseparation. Solche Materialien mit definierten Moleküleigenschaften sind bisher sehr wenig erforscht und ermöglichen es, die D-A Grenzfläche in dünnen Filmen präzise einzustellen. Daher besteht großes wissenschaftliches Interesse an solchen Polymeren, das sich bald auch auf industrielle Anwendungen ausweiten könnte.

Um komplexe, innovative, aber auch definierte Blockcopolymerarchitekturen herzustellen, wurden zwei verschiedene Polymerisationsmethoden mit lebendem Charakter verwendet, kombiniert und angepasst: Nitroxid-vermittelte radikalische Polymerisation (NMRP) und Grignard Metathese Polymerisation (GRIM). Mithilfe der NMRP wurde N,N'-bis(4-methoxyphenyl)-N-phenyl-N'-4-vinylphenyl-(1,1'-biphenyl)-4,4'-diamin (vDMTPD) polymerisiert, und es wurden definierte Polymere PvDMTPD mit kontrolliertem Molekulargewicht und niedriger Polydispersität hergestellt. PvDMTPD wurde dann als Makroinitiator verwendet um Perylenbisimidacrylat (PerAcr) zu polymerisieren, was die gewünschte D-A PvDMTPD-*b*-PPerAcr Blockcopolymerarchitektur ergab. Weiterhin wurden diese Polymere bezüglich ihrer morphologischen, optischen und elektronischen Eigenschaften untersucht, und mit D-A Blockcopolymeren, die einfachere Triphenylaminblöcke als Donor besitzen, verglichen. Als gemeinsames Merkmal weisen solche Blockcopolymere ein amorphes Donorsegment und ein kristallines Akzeptorsegment auf. Die Besonderheit des zweiten Blocks PPerAcr liegt in der Seitenkettenkristallisation der Perylenbisimide, die in durch  $\pi$ - $\pi$ -Wechselwirkungen verursacht wird. Alle amorph-kristallinen Blockcopolymere wurden in organischen Solarzellen getestet, und die Leistung der Bauteile wurde mit den elektronischen und morphologischen Eigenschaften der Blockcopolymere korreliert. Dabei konnten synergetische Effekte ausgenutzt werden, welche die Solarzelleneffizienz der Blockcopolymere im Vergleich zu früheren Arbeiten verfünffacht haben.

Darüber hinaus wurden Blockcopolymere mit nur einem elektronisch aktiven Block und Polystyrol oder Poly(4-vinylpyridin) hergestellt. Mithilfe solcher Materialien kann ein elektronisch aktives Segment (Donor oder Akzeptor) geometrisch eingeschränkt werden, wodurch fundamentale Eigenschaften als Funktion der Morphologie untersucht werden können.

Im Hauptteil dieser Arbeit wurde die Reihe der amorph-kristallinen D-A Blockcopolymere auf hauptkettenkonjugierte D-A Blockcopolymere ausgeweitet. Dabei wurde Poly(3-hexylthiophen), P3HT, als Lochleiter verwendet, der im Vergleich zu den amorphen

Polytriphenylaminen weiter im sichtbaren Spektrum absorbiert und gleichzeitig die Ladungsträgermobilität abermals erhöht. Die Grignard Metathese Polymerisation wurde erfolgreich optimiert und verwendet, um mehrere P3HT-Blöcke mit kontrolliertem Molekulargewicht und niedriger Polydispersität herzustellen. Weiterhin wurde eine einfache und zielgerichtete Eintopfreaktion entwickelt, um P3HT-Makroinitiatoren für die NMRP herzustellen. Ausgehend von diesen Makroinitiatoren wurden mehrere definierte Blockcopolymerere P3HT-*b*-PPerAcr mit unterschiedlicher Komposition und unterschiedlichem Molekulargewicht synthetisiert. Die Besonderheit von P3HT-*b*-PPerAcr liegt in der kristallin-kristallinen Blockcopolymerarchitektur, wobei das erste Segment hauptkettenkristallin und das zweite Segment seitenkettenkristallin ist.

Alle Blockcopolymerere P3HT-*b*-PPerAcr wurden mit Standardmethoden, mit optischen, elektronischen, und mit mikroskopischen Methoden charakterisiert. Der kristallin-kristalline Charakter wurde mittels differentieller Wärmeflußkalorimetrie und Röntgenstreuung bestätigt, wobei eine Koexistenz von lamellaren P3HT- und eindimensionalen PPerAcr Stapeln festgestellt wurde. Die Koexistenz dieser Aggregate ist maßgeblich von der Komposition, dem Molekulargewicht, und der Vorbehandlung von P3HT-*b*-PPerAcr abhängig. Während thermisch vorbehandelte Proben eine verstärkte Ausbildung von kristallinen PPerAcr Domänen zeigen, fördert die Lösungsmitteldampfbehandlung die Aggregation von P3HT. Dieser Effekt wird übereinstimmend bei der Untersuchung der optischen, thermischen, morphologischen und elektrischen Eigenschaften gefunden. Die Herstellung von organischen Solarzellen mit P3HT-*b*-PPerAcr als aktiver Schicht ergab einen Rekordwert der externen Quantenausbeute von 31 %, was für die beiden Komponenten P3HT und Perylenbisimid den jemals höchsten gemessenen Wert darstellt. Einfache Mischungen haben bisher nur Werte von ca. 20 % gezeigt. Diese Ergebnis liegt in der ausgeglichenen Komposition von Donor und Akzeptor begründet: Die Kristallisation von PerAcr ist geometrisch eingeschränkt, und lässt gleichzeitig eine Kristallisation von P3HT zu, was zu relativ hohen Lochmobilitäten führt. Die hohe Lochmobilität ist eine Folge des hohen Kristallinitätsgrades von P3HT, der mit relativ hohen P3HT Molekulargewichten erreicht werden kann. In P3HT-*b*-PPerAcr mit gleicher Komposition aber kleinerem P3HT-Molekulargewicht ist die Lochmobilität um zwei Größenordnungen niedriger, was einerseits durch das niedrigere Molekulargewicht an sich verursacht wird, andererseits aber auch eine Folge der unterdrückten P3HT-Kristallisation ist.

Darüber hinaus konnten exzellente Elektronenmobilitäten im Bereich von  $1.2 \cdot 10^{-3} \text{ cm}^2/\text{Vs}$  in organischen Feld-Effekttransistoren mit PPerAcr gemessen werden. Blockcopolymerere mit Polystrol und PPerAcr zeigen einen gleich hohen Wert, obwohl der Anteil von PPerAcr 70 % beträgt. Diese Ergebnisse sind sehr vielversprechend, da elektronenleitende Polymere mit hohen Mobilitäten gefragt, jedoch selten sind.

Im letzten Teil dieser Arbeit wurden die Anwendbarkeit und die Grenzen der Kombination von Focused Ion Beam (FIB) und Rasterelektronenmikroskopie (REM) benutzt, um verborgene Strukturen in dünnen binären Polymerfilmen abzubilden. Als Modellsysteme wurden dazu wird ein Polymerblend aus einem amorphem Donorpolymer und PPerAcr und verschiedene Blockcopolymerere benutzt. Unter gewissen Umständen wurden dabei Artefakte erzeugt, die sich der Blend- und Blockcopolymerstruktur überlagern und die beobachtete Morphologie verfälschen können. Es wurden verschiedene Parameter identifiziert, die zur Artefaktbildung führen können.

## 1. Introduction

### Semiconducting Polymers for Organic Electronic Devices

With the discovery of conducting polymers in 1977, the door towards plastic electronics was opened.<sup>[1]</sup> Since then, extensive research has been devoted to the synthesis and application of electronically active polymers for the application in organic thin film transistors (OFETs)<sup>[2]</sup> and organic photovoltaics (OPVs)<sup>[3]</sup>, driven by the inherent advantages of low cost manufacturing, light-weight and the use of flexible substrates. Such materials, also referred to as semiconducting polymers in their non-oxidized form, exhibit excellent film-forming properties when processed from organic solvents, and therefore enjoy wide interest in academics and industry.<sup>[4-6]</sup> Figure 1a shows the schematic architecture and the working principle of an OFET device with bottom-contact bottom-gate configuration. Here, charge transport occurs laterally in a very thin channel between the source and the drain, typically  $\sim 1$  nm above the dielectric layer.<sup>[4]</sup> Therefore, the morphology and the packing of the electroactive moieties in this thin layer determines the transport characteristics, and conversely the OFET performance can give information of the morphology of the active layer. OFETs are commonly characterized by their output characteristics (source drain current vs drain voltage), and by their transfer characteristics (source drain current vs gate voltage), as shown in figure 1b and 1c. Polymeric materials with electronic functionalities have been classified in two main categories: p-type materials and n-type materials. These terms refer to the observation of p-channel (accumulation of holes) or n-channel (accumulation of electrons) behaviour of the respective material in organic thin film transistors.<sup>[7]</sup> p-channel materials are built up on the basis of electron-rich aromatic systems, whereas n-channel materials require electron-deficient aromatic units. In terms of polymer architecture, such planar  $\pi$ -systems can be incorporated into side-chain or main chain polymer architectures. In main chain polymers, conjugation along the backbone is required for an extended overlap of  $\pi$ -orbitals, and such architectures are therefore referred to as conjugated polymers. Here, special attention has to be paid to appropriate solubilizing groups responsible for sufficient solubility in common organic solvents and ordered solid-state packing. Semiconductor polymers exhibiting p-channel behaviour are widely available and good operation in ambient conditions has been demonstrated.

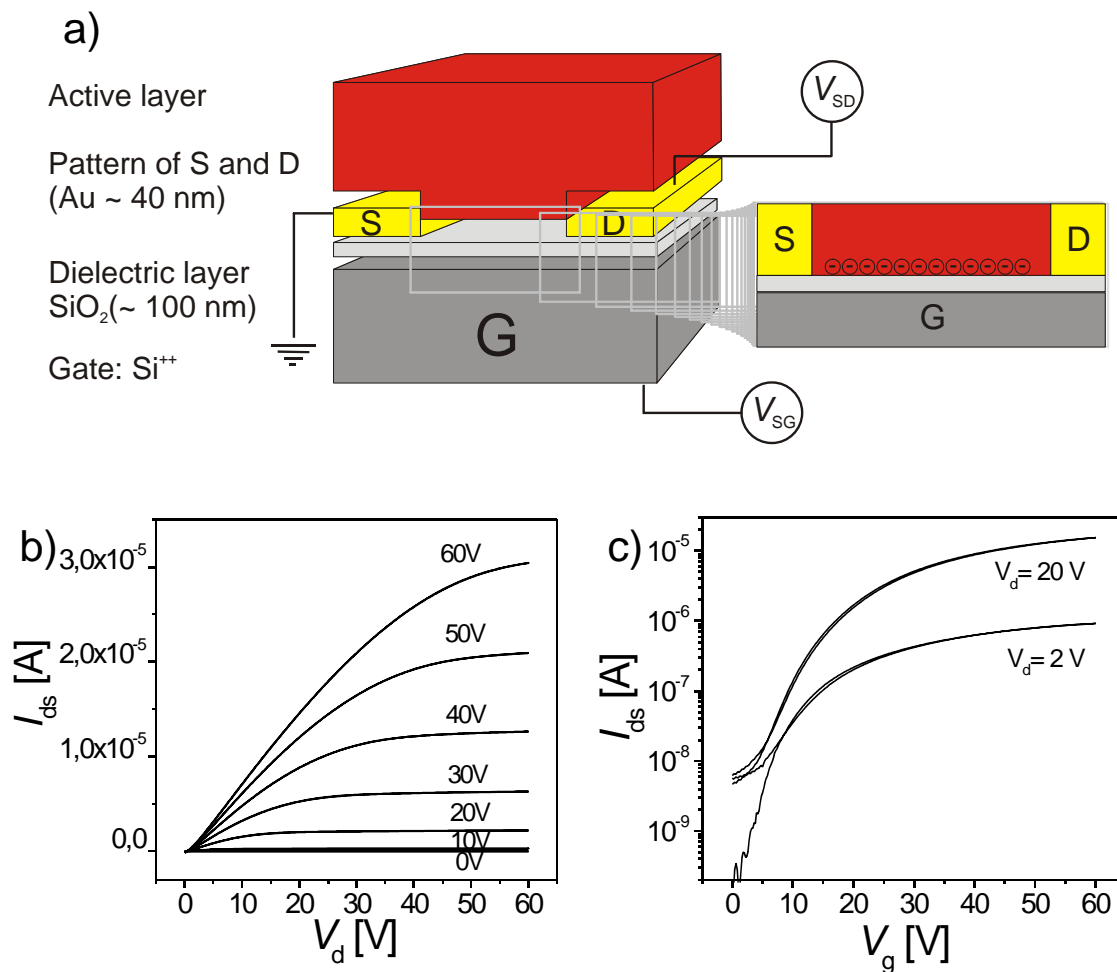
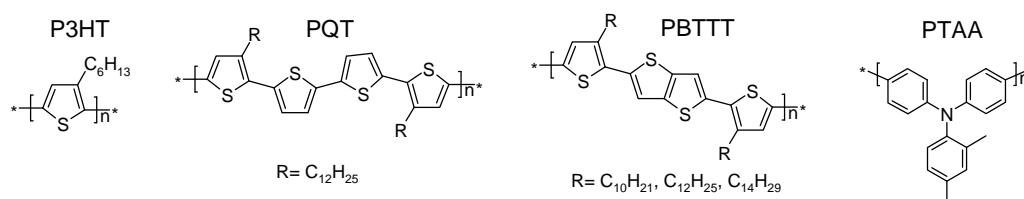


**Figure 1.** a) Schematic device architecture of an organic field effect transistor (OFET) in bottom contact bottom gate configuration. b) Output characteristics for different gate voltages and c) transfer characteristics for different drain voltages of an n-channel material.

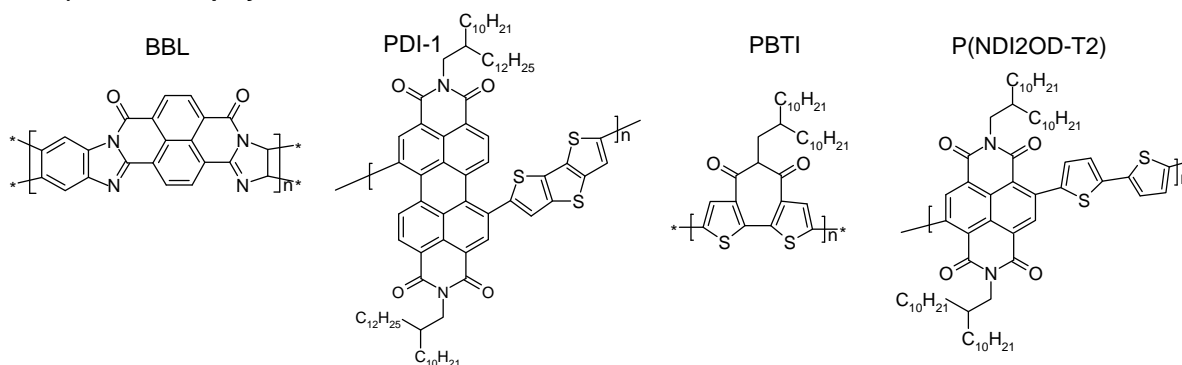
Among the several conjugated polymers known, polythiophenes have been studied extensively.<sup>[8]</sup> In particular, regioregular poly(3-hexylthiophene), P3HT, has shown some of the best OFET performances up to now.<sup>[9,10]</sup> Several other conjugated polymers bearing thiophenes in the backbone and showing promising OFET performance have been reported, to name a few.<sup>[11-13]</sup> However, for low power consuming organic complementary metal-oxide semiconductor (CMOS) circuits to be realized, p-channel as well n-channel materials are much needed.<sup>[14]</sup> Until recently, few examples of n-channel polymers were known. On the one hand, this was ascribed to the fact that electrons are more likely to be trapped by impurities or polar groups in the device than holes.<sup>[15]</sup> On the other hand, extensive synthetic efforts have been made in developing polymeric n-channel materials in the last two years. Several promising architectures with bithiophene-dicarboximide, naphthalene bisimide, or perylene bisimide moieties in the main chain emerged.<sup>[16-20]</sup> A major

breakthrough has been achieved by Facchetti *et al.*, demonstrating that alternating main chain-conjugated copolymers comprised of naphthalene bisimide and bithiophene can be designed in such a way that the issues of solubility, high mobility and stable device operation under ambient conditions are possible at the same time.<sup>[19]</sup> In scheme 1, the most important p- and n- channel polymers known to date are summarized.

#### a) p-channel polymers



#### b) n-channel polymers



**Scheme 1.** a) p-channel polymers poly(3-hexylthiophene) (P3HT), poly(3,3'-didodecylquaterthiophene) (PQT), poly(2,5-bis(3-alkylthiophen-2-yl)thieno[3,2-b]thiophene) (PBTTT), and poly(triarylamine) (PTAA). b) n-channel polymers poly(benzobisimidazobenzophenanthroline) (BBL), poly{[N,N'-bis(2-decyl-tetradecyl)-3,4,9,10-perylene diimide-1,7-diy]-alt-(dithieno[3,2-b:2',3'-d]thiophene-2,6-diy)} (PDI-1), poly(N-(2-octyldodecyl)-2,22-bithiophene-3,3,2-dicarboximide) (PBTI), and poly{[N,N9-bis(2-octyldodecyl)-naphthalene-1,4,5,8-bis(dicarboximide)-2,6-diy]-alt-5,59-(2,29-bithiophene)}, P(NDI2OD-T2).

Ambipolar transport is the ability of a thin film transistor to accumulate holes as well as electrons depending on the applied voltage.<sup>[7]</sup> There are several ways to realize such device performance. Bilayer devices of vapor-deposited small molecules were first reported.<sup>[21]</sup> Solution-processable blends of two different materials exhibiting p-channel and n-channel behaviour are interesting systems owing to their advantages of low-cost device fabrication. However, the ambipolar transport behaviour will be largely affected by the phase separation and wetting effects of the polymer blend above the dielectric layer.<sup>[22]</sup> Single materials can

also show ambipolar charge transport behaviour, dependent on the gate dielectric, electrode material, processing conditions, and the measurement atmosphere applied. Here, either small molecules<sup>[23]</sup> or a conjugated polymer<sup>[24]</sup> were reported to conduct both holes and electrons.

The process of phase separation in semiconducting binary polymer thin films is even more crucial for the operation of organic photovoltaics (OPVs). These devices rely on a bulk heterojunction of a hole conducting donor (D) and an electron conducting acceptor (A) material.<sup>[25,26]</sup> Here, not only the interface between the active layer and the device is important, but also the internal bulk morphology. Excitons that are created upon irradiation with visible light must subsequently diffuse to the D-A interface, where they may be separated into holes and electrons, if sufficient energy level offset of the two materials is provided to overcome the exciton binding energy (coulombic interaction of hole and electron).<sup>[27]</sup> The donor, also referred to as hole transporting material, is built up of electron-rich aromatic building blocks and therefore characterized by a low ionization potential between 4-5 eV (highest occupied molecular orbital, HOMO), and serves as the hole transport site from the interface to the anode. The acceptor material is electron-deficient, with an electron affinity in the range between 3-4 eV, and is needed for electron transport from the D-A interface to the cathode. Only those holes and electrons that travel to their respective electrode will be collected and can contribute to the photocurrent. OPV devices are commonly characterized by their current density-voltage characteristics (*J-V*-curves) and by the external quantum efficiency (EQE). The latter is a measure for the percentage of electrons collected per incident photon at a distinct wavelength. Figure 2 illustrates the schematic device architecture, a *J-V*-curve, and an EQE curve of an organic solar cell. The various processes of exciton diffusion, charge separation, charge transport and charge collection require precise arrangement of the D and A material. The role of the active layer morphology is therefore explained in the next section.

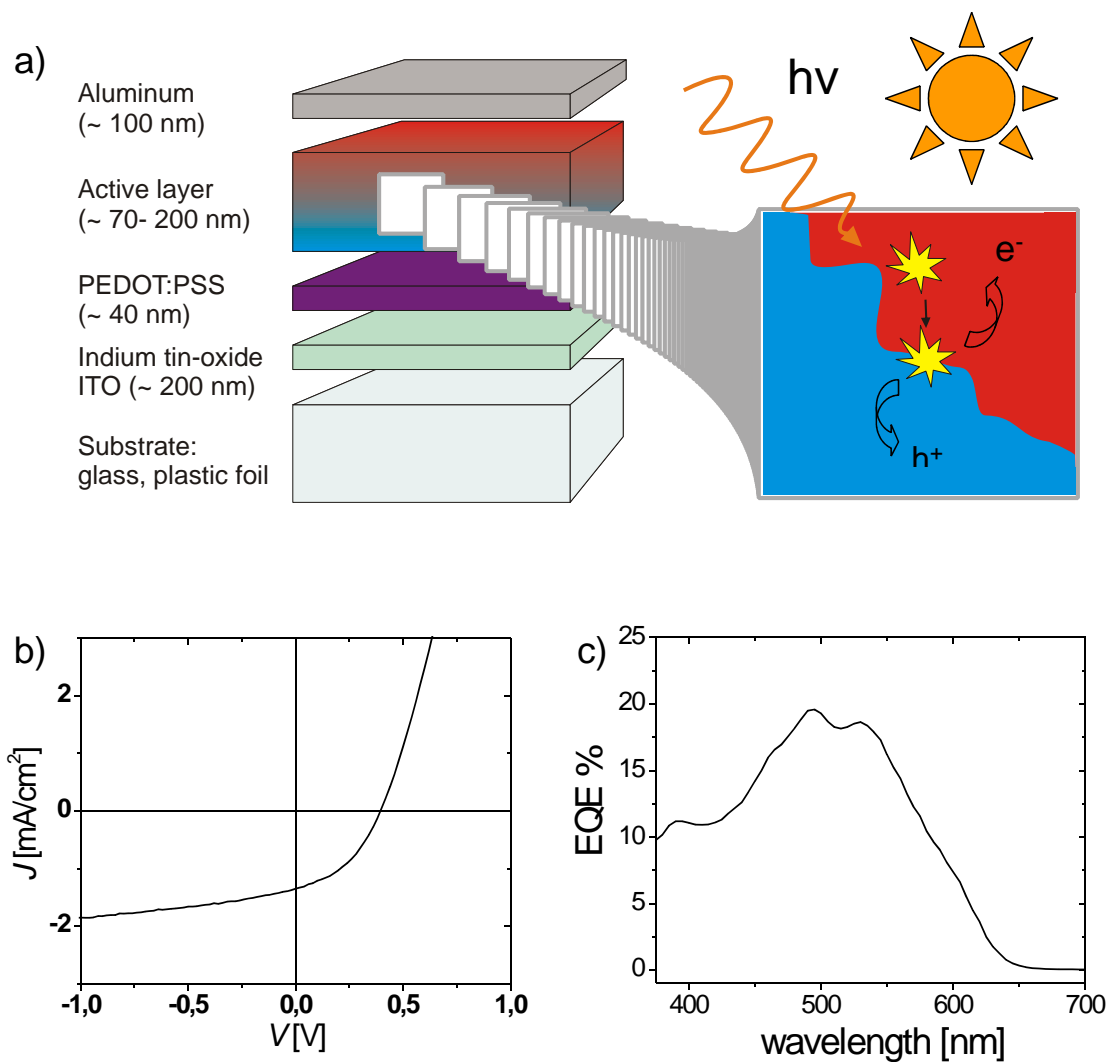


**Figure 2.** a) Device architecture of an organic solar cell. An indium tin-oxide (ITO) substrate covered with poly(3,4-ethylenedioxythiophene):poly(4-styrene sulphonate) (PEDOT:PSS) is used as the anode. The active layer is processed from solution, either by spin coating or doctor blading. The device is completed by evaporating the cathode, which commonly is aluminum. b) and c) show a J-V curve and an EQE plot of such a device, respectively.

## Morphology of active layers in organic solar cells

Active layers suitable for organic photovoltaics are comprised of a donor and an acceptor material. Straightforward and efficient device fabrication involves depositing a blend of the two components from solution. Subsequently, a phase separation occurs since each component seeks to minimize its interfacial area during the drying process of the film. This process of demixing is critical in bulk heterojunction solar cells. Excitons that are created upon light absorption need to reach the D-A interface within their diffusion length (10- 20

nm) in order to be separated into holes and electrons. Therefore, the generation of free charges will be extremely dependent on the degree of intermixing, and accordingly, the lack of sufficient interfacial area in strongly phase separated blends will cause significant recombination prior to charge separation.<sup>[28]</sup> Subsequently, charge transport and finally charge collection at the electrodes may occur, given that co-continuous pathways of donor and acceptor domains are provided.<sup>[29-32]</sup> Since an active layer thickness of 100- 200 nm is required for the complete absorption of visible light, pathways with a high aspect ratio of either phase have to percolate vertically through the film. Numerous studies have dealt with the dilemma of accelerating and subsequently freezing in the phase separation of polymer/small molecule bulk heterojunction solar cells<sup>[33-37]</sup>, the power conversion efficiencies of which have reached 4- 6 %.<sup>[38-42]</sup> However, the resulting morphologies are metastable and the domains are ill-defined. More desirable would be the accomplishment of accurate control over the active layer morphology on a nanometer scale, with tunable donor and acceptor domains in terms of size and shape.

In block copolymers, two or more polymers are covalently linked. Here, thermodynamic equilibrium can be achieved as a result from the interplay of demixing and molecular connectivity of the blocks.<sup>[43,44]</sup> A so-called microphase separation results in the formation of various morphologies of well-defined size and shape, as a function of the volume fraction, the degree of polymerization, and the Flory-Huggins interaction parameter. Furthermore, the domain sizes of such block copolymer microdomains typically range within ~ 10-30 nm, and are therefore commensurate with the exciton diffusion length.<sup>[45]</sup> Therefore, block copolymers that carry electronic functions, also referred to as semiconductor block copolymers, hold great promise for the application in OPV's.<sup>[46,47]</sup> Among the common microstructures known from conventional coil-coil block copolymers, a cylindrical, lamellar, or gyroidal phase would meet with the morphological requirements of photovoltaic applications. Furthermore, techniques for preparing ordered microstructures - meaning macroscopically aligned block copolymer domains oriented perpendicular to the electrodes - are developed well and have been successfully demonstrated using conventional block copolymers without electronic functions.<sup>[48-50]</sup> A graphical illustration of the ideal morphological picture of a block copolymer photovoltaic cell, together with an unfavorable morphology of a D-A blend is depicted in figure 3.

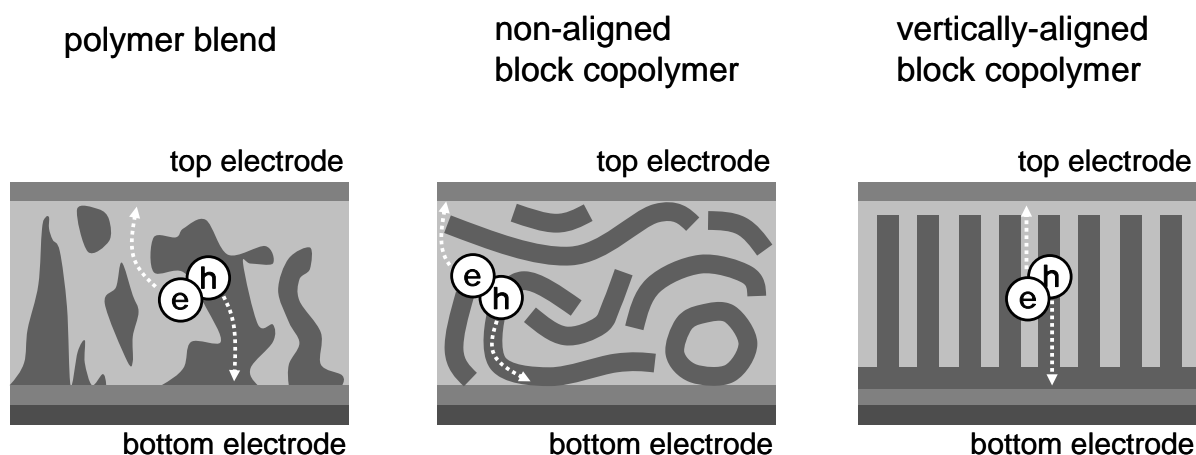


**Figure 3.** Different donor-acceptor active layer morphologies between the devices' electrodes. The left drawing depicts a polymer blend morphology with large, undefined and inhomogeneous domains. In the middle and at the right, schematic active layer morphologies of disordered and vertically aligned microphase separated donor-acceptor block copolymer thin films are shown. Light gray: acceptor phase, dark gray: donor phase.

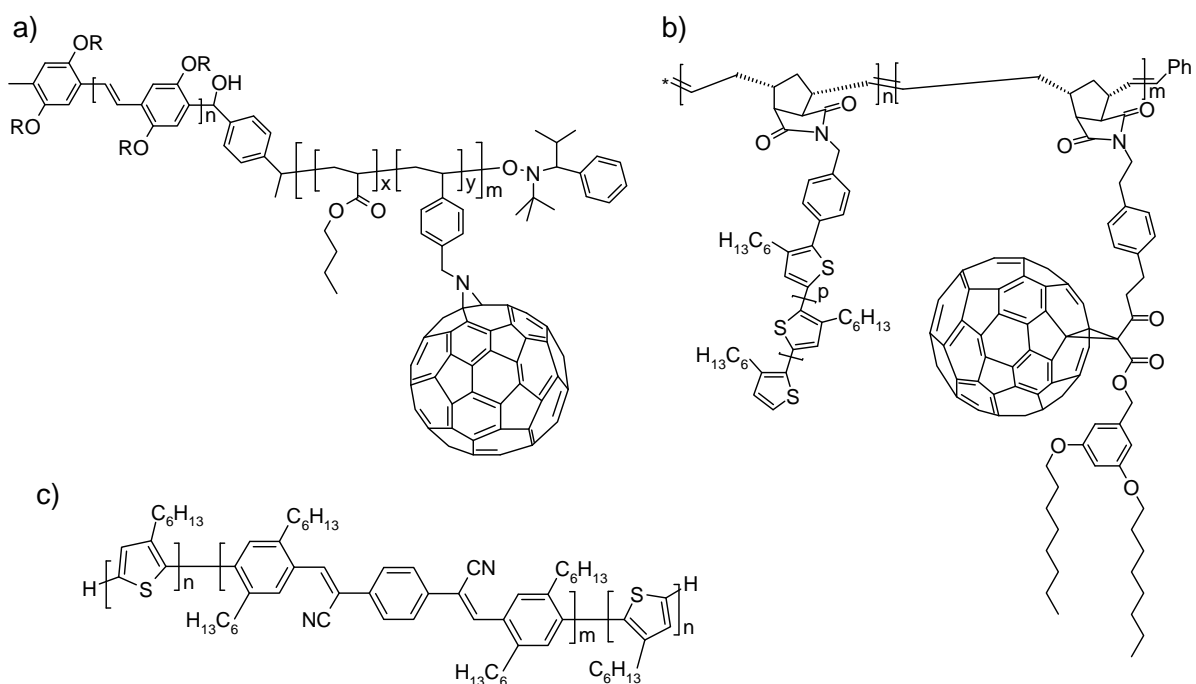
Whereas the vertical alignment of block copolymers with a cylindrical or a lamellar morphology might be advantageous for improving the device performance, gyroidal films do not require alignment. Recently, an elegant example has been given by Snaith et al., who used a double sacrificial block copolymer to incorporate a gyroidal  $\text{TiO}_2$  replicate into liquid electrolyte dye-sensitized solar cells.<sup>[51]</sup> McGehee *et al.* pursued a similar approach by the infiltration of poly(3-hexylthiophene) into block copolymer-templated, nanoporous  $\text{TiO}_2$  films.<sup>[52]</sup>

Note that the aromaticity, concomitant with some stiffness of the electronically active block or moiety, alters the phase behaviour of donor acceptor block copolymers considerably. The phase diagrams of rod-coil block copolymers<sup>[53]</sup> or block copolymers with one or more crystallizable blocks<sup>[54,55]</sup> therefore seem to have more relevance for those highly complex donor acceptor block copolymers. Here, enthalpic contributions from the crystallization of the blocks compete with microphase separation. This fact on the one hand, together with large polydispersities<sup>[56]</sup>, homopolymer impurities<sup>[57]</sup> or even cross linking<sup>[58]</sup>, might have not permitted the direct formation of highly ordered microstructures in donor acceptor block copolymers up to now. On the other hand, the crystallization of one block can also give rise to extremely well-defined morphologies if the other block is amorphous, as shown by pioneering work of Thelakkat et al.<sup>[59]</sup> The following section summarizes the synthesis and

resulting architectures of donor acceptor block copolymers with functionalities suitable for organic photovoltaics.

## Donor-Acceptor Block Copolymers

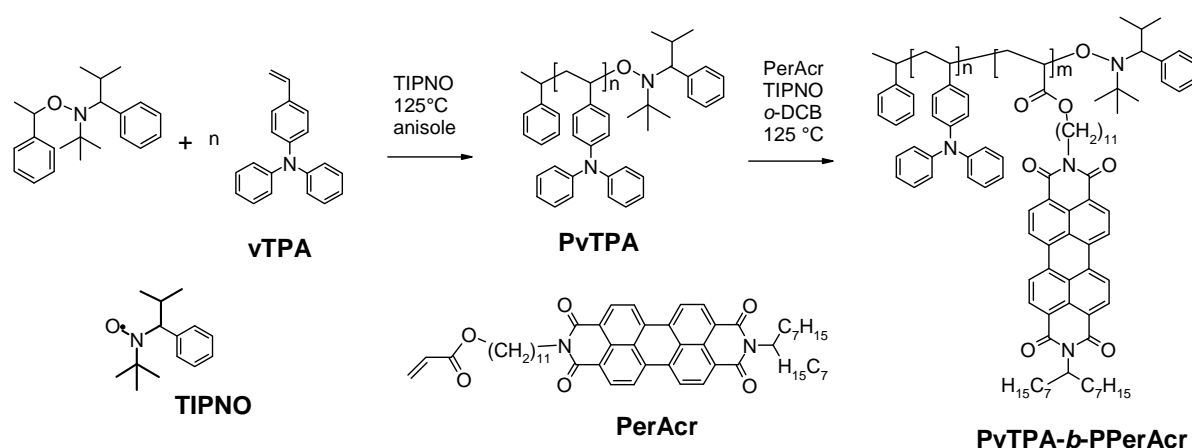
The first D-A block copolymers with suitable electronic properties were synthesized in the group of Hadziioannou *et al.*, using a conjugated poly(phenylene vinylene) (PPV) block as macroinitiator for the nitroxide mediated radical polymerization (NMRP) of a second styrenic coil block. This second block was rendered n-type using a polymer analogous reaction by attaching C<sub>60</sub> molecules.<sup>[60]</sup> As pointed out by the authors, crosslinking<sup>[58]</sup> and crystallization of the side-chain fullerenes possibly accounted for the lack of microdomains after functionalization with C<sub>60</sub>.<sup>[61]</sup> In another study, Scherf *et al.* prepared D-A triblock copolymers from monobromo-terminated poly(3-hexylthiophene) (P3HT) and dibromo-terminated cyano-substituted poly(phenylene vinylene) (CN-PPV) via Yamamoto coupling. Even though the energy levels of these building blocks did not suit the requirements for electron transfer nor the products showed a microphase separation either, all-conjugated triblock copolymers with donor as well as acceptor blocks were prepared and a point was made on the importance of solubilizing groups.<sup>[62]</sup> Fréché *et al.* made use of ring opening metathesis polymerization (ROMP) to subsequently polymerize two macromonomers containing P3HT and fullerene units. This approach is interesting since the most efficient OPV devices are produced from blends of P3HT and fullerene derivatives. While a photovoltaic effect was not reported for the single block copolymer material, applications as compatibilizers in ternary blend devices with increased thermal stability were demonstrated.<sup>[57]</sup> Despite all these efforts, only in two cases a weak photovoltaic effect was observed using solely the block copolymer as the active layer.<sup>[61,63]</sup> Scheme 2 summarizes the chemical structures of the donor-acceptor block copolymers by Hadziioannou *et al.*, Fréché *et al.*, and Scherf *et al.*



**Scheme 2.** Donor acceptor block copolymer architectures. a) Rod-coil block copolymer by Hadziioannou et al. b) Side-chain block copolymer by Frechet et al. c) All-conjugated triblock copolymer by Scherf et al..

The D and A moieties used in the majority of the synthetic approaches towards donor-acceptor block copolymers are conjugated polymers and/or fullerene derivatives. This makes the preparation very challenging and special attention has to be given to appropriate solubilizing groups. A low weight fraction of e.g. alkyl chains renders the polymer insoluble whereas a solubilizing group fraction that is too high will result in poor performance of the device since the amount of active material decreases. This problem becomes visible in the case of polymers containing fullerene.<sup>[64]</sup> Perylene bisimide (PBI) as an alternative electron acceptor has been investigated to a lesser degree since the power conversion efficiencies did not reach those of comparable P3HT:PCBM blend cells. The main reason was seen in the uncontrolled crystallization of PBI, resulting in large crystals concomitant with poor morphological control.<sup>[65]</sup> Yet, suitable electronic properties and absorption in the visible range make this acceptor compound interesting for light harvesting applications and apparently, PBI is regaining interest for photovoltaic applications.<sup>[66-69]</sup> Also, the chemical derivatization of the PBI core is feasible since the two distinct imide positions can be substituted independently without altering the electronic properties. Making use of these facts, Thelakkat et al. designed a highly soluble and polymerizable perylene bisimide

derivative, referred to as perylene bisimide acrylate (PerAc). This monomer bears a branched alkyl substituent at one imide position and a linear, acrylate-functionalized alkyl spacer at the other imide position. The incorporation of PerAc into block copolymers with poly(triphenylamine) as the donor via NMRP yielded D-A block copolymers exhibiting *all* important requirements for photovoltaic applications, such as high solubility, suitable energy levels, absorption in the visible range, *and* microphase separation for the first time (scheme 3).<sup>[59]</sup> Finally, the valuable design and synthesis of PerAc opened the door to D-A block copolymers with side-chain crystalline perylene bisimide blocks and various donor blocks, which is the central topic of this thesis.



**Scheme 3.** Synthesis of donor-acceptor block copolymers poly(vinyltri(phenyl)amine)-b-poly(perylene bisimide acrylate) (PvTTPA-b-PPerAc) by Thelakkat et al. and chemical structures of the monomer perylene bisimide acrylate PerAc and the mediating free nitroxide 2,2,5-Trimethyl-4-phenyl-3-azahexane-3-nitroxide (TIPNO).

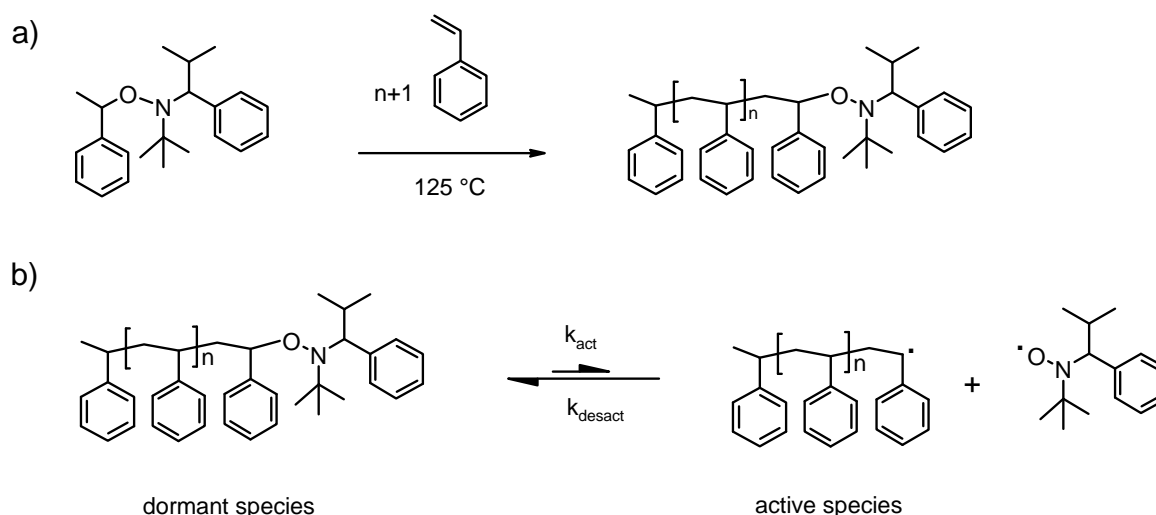
## Controlled Polymerization Methods

For a well-defined block copolymer to be synthesized, controlled polymerization methods have to be employed. This is important in terms of low polydispersity, a controlled molecular weight, and tuning of endgroup functionalization. Among various methods available, reversible addition-fragmentation chain transfer polymerization (RAFT)<sup>[70]</sup> and nitroxide mediated radical polymerization (NMRP) seem to be most appropriate for the preparation of electronically active block copolymers, owing to their metal-free nature and the high tolerance towards functional groups. In order to synthesize conjugated, semiconducting poly(3-alkylthiophene)s, the Grignard Metathesis Polymerization (GRIM) proved successful.

The latter two methods are subject of this thesis and the principles are therefore presented in the next two sections.

## Nitroxide Mediated Radical Polymerization (NMRP)

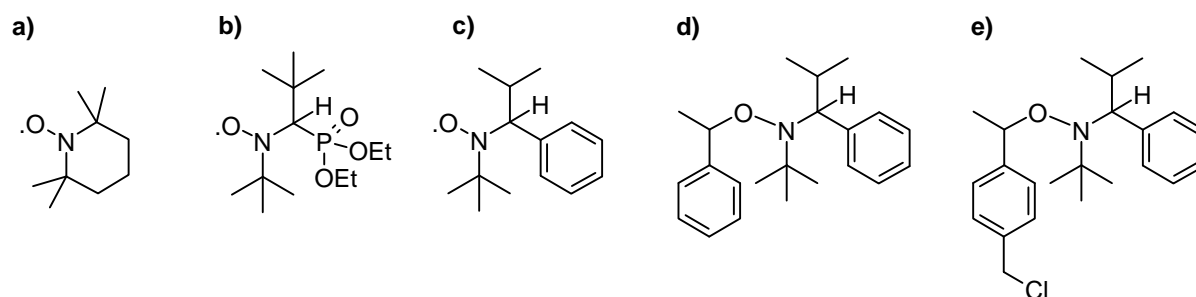
Nitroxide mediated radical polymerization is based on the reversible termination of a growing polymer chain and the resulting thermal equilibrium between a dormant species and an active species. Since the probability for the recombination or disproportionation of two radical chains is very low, a living character evolves. Initiator systems can basically be classified in bimolecular and unimolecular systems. In a bimolecular system, the polymerization is started using conventional free radical polymerization initiators, and the resulting polymer radicals are reversibly terminated with an additional mediating radical. Monomolecular initiators are based on alkoxyamines. Here, a carbon-oxygen bond is cleaved upon thermal heating. While one fragment can start the polymerization, the other one will act as the mediating radical. This is shown in scheme 4 for the case of an unimolecular alkoxyamine initiator and styrene as monomer.



**Scheme 4.** a) Polymerization of styrene using an unimolecular alkoxyamine initiator. b) Thermally activated equilibrium between dormant and active species.

The so-called persistent radical effect is crucial for the control of the polymerization.<sup>[71]</sup> Upon starting the polymerization, the concentration of free radicals is high and the equilibrium is

shifted to the right side. Free polymeric radicals are then terminated by the mediating radical and the concentration of active polymer chains decreases. The equilibrium is reached faster when an excess amount of the mediating radical is used. A key requirement is the stability of the mediating radical (nitroxide): It must be stable enough not to add monomers thus initiating additional polymer chains, but should be unstable enough to reversibly terminate the growing polymer chain. In the first stage of development, common radical initiators for free radical polymerizations were used together with the mediating radical 2,2,6,6-tetramethylpiperidinoxy (TEMPO).<sup>[72]</sup> However, the control of polymerization using this “bimolecular initiating system” was poor, due to the high stability of TEMPO. A major improvement was then achieved with N-tert-butyl-N-[1-diethylphosphono-(2,2-dimethylpropyl)] nitroxide (SG1), which bears a  $\alpha$ -hydrogen.<sup>[73]</sup> Finally, 2,2,5-Trimethyl-4-phenyl-3-azahexane-3-nitroxide (TIPNO) and the use of unimolecular alkoxyamines based thereon broadened the applicability of NMRP towards acrylates, acrylamides and acrylonitriles.<sup>[74]</sup> Scheme 5 shows the chemical structures of TEMPO, the phosphonate-based nitroxide, TIPNO, and two TIPNO-based alkoxyamines.



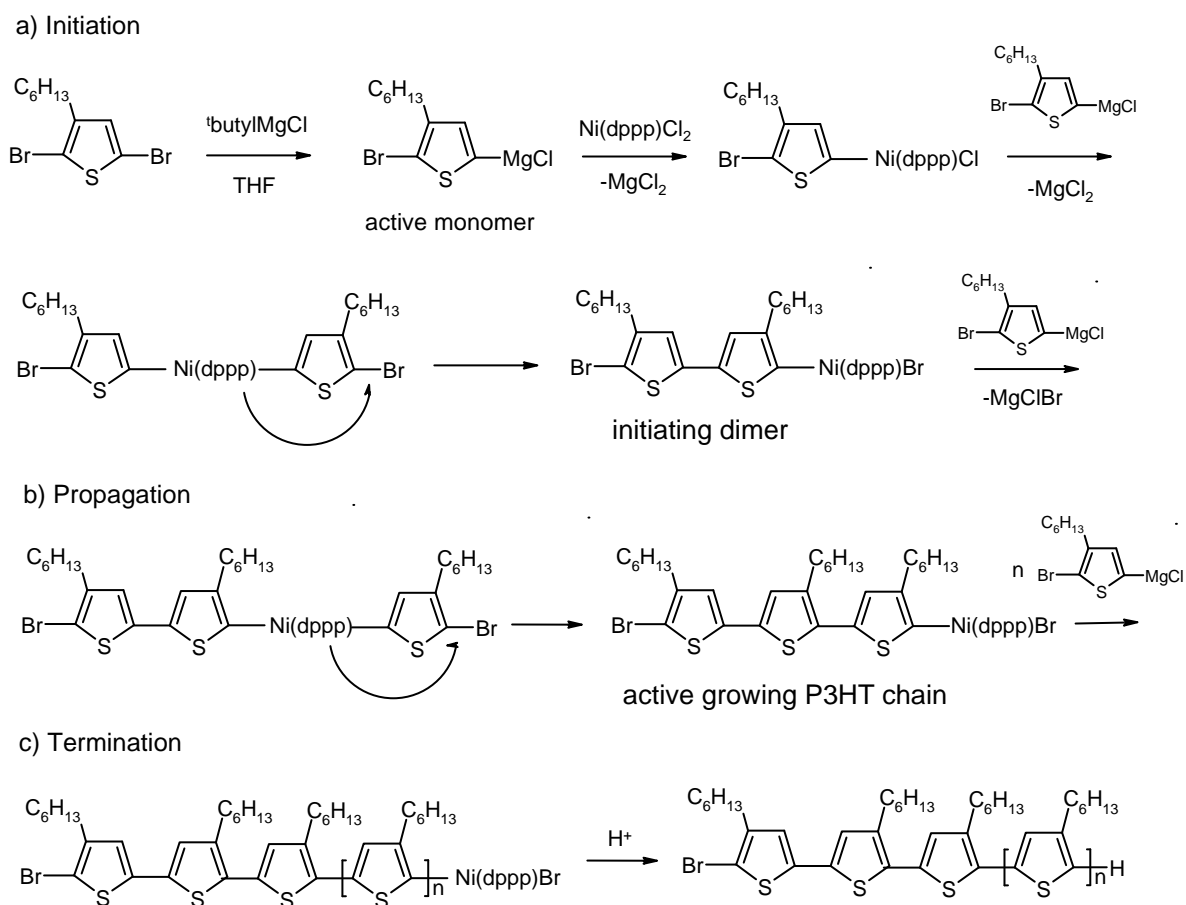
**Scheme 5.** Chemical structures of a) 2,2,6,6-tetramethylpiperidinoxy (TEMPO), b) N-tert-butyl-N-[1-diethylphosphono-(2,2-dimethylpropyl)] (SG1), c) 2,2,5-Trimethyl-4-phenyl-3-azahexane-3-nitroxide (TIPNO), and d, e) TIPNO-based unimolecular alkoxyamines developed by Hawker et al..

Unimolecular alkoxyamines as shown in figure 5d can also be synthesized with a chloromethyl-group in 4-position of the benzylic group (5e).<sup>[74,75]</sup> This allows for further derivatization, e.g. for labelling of the alkoxyamine<sup>[76]</sup>, or for the generation of a Grignard function<sup>[77]</sup>, both of which have expanded the range of polymer architectures with novel properties. Further details on controlled polymer architectures via NMRP can be found in the literature.<sup>[78,79]</sup> Nowadays, almost every monomer can be polymerized via NMRP if side

reactions of polymer radicals are widely absent at elevated temperatures. Note that these high temperatures can also be an advantage when large monomers with  $\pi$ -systems and intrinsically diluted double bonds have to be polymerized in highly viscous reaction mixtures.<sup>[59]</sup>

## Grignard Metathese Polymerization

Several methods towards the preparation of poly(3-alkylthiophenes) are known.<sup>[80]</sup> Most notably, the McCullough method<sup>[81]</sup> and the Rieke method<sup>[82]</sup> have been used in the past. These two methods require cryogenic temperatures and the use of highly reactive lithiation reagents. A major improvement was the development of the Grignard Metathese Polymerization (GRIM) of poly(3-alkylthiophene)s (P3AT), sometimes referred to as *catalyst transfer condensation polymerization*. Here, pioneering work has been carried out by the group of McCullough and Yokozawa.<sup>[83,84]</sup> The GRIM has become extremely popular during the last years, owing to the high regioregularity which can be achieved, the convenient reaction conditions (room temperature and commercially available Grignard reagents can be used) and the promising applications of poly(3-hexylthiophene)s in OFETs<sup>[9,10]</sup> and OPVs.<sup>[38,40]</sup> The mechanism of the GRIM is based on the nickel(II)-catalyzed Kumada cross-coupling reaction of 2-bromo-3-alkyl-5-chloromagnesiumthiophene. Compared to classical Kumada cross-coupling reactions, the speciality of the GRIM method is based on the structure of the thiophene-based monomer: The both functions required for cross coupling, a bromine atom in 2-position and a Grignard function in 5-position, are provided. When the catalyst 1,3-bis(diphenylphosphino)propanenickel(II) chloride ( $\text{Ni}(\text{dppp})\text{Cl}_2$ ) is added, the formation of a dimeric initiating species occurs, followed by the further addition of 2-bromo-3-alkyl-5-chloromagnesiumthiophene. Scheme 6 shows the mechanism of initiation, propagation, and termination. Chain termination is done by the addition of protons, whereby quenching the reaction with hydrochloric acid is more favorable than quenching with methanol.<sup>[85]</sup>



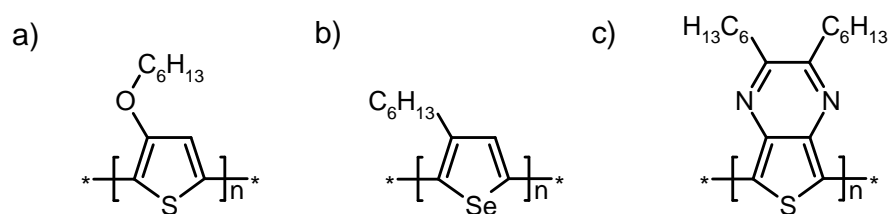
**Scheme 6.** Mechanism of the Grignard Metathesis Polymerization of (GRIM) 2-bromo-3-hexyl-5-chloromagnesiumthiophene: a) process of initiation, b) propagation, and c) termination.

Interestingly, the nickel complex is shifted *intramolecularly* to the end of the polymer chain and therefore one polymer chain is started by one catalyst molecule. The exact origin of the exclusively intramolecular transfer of the nickel complex remains unclear. Basically, two reasons are discussed: firstly, the bromine-carbon bond at the active site of the polymer chain where the insertion takes place is more reactive than the bromine-carbon bond of the remaining monomers. Secondly, the nickel complex is considered to interact with the  $\pi$ -orbitals of the conjugated main chain.<sup>[86]</sup> Due to the “quasi-living” mechanism of the GRIM<sup>[87]</sup>, the molecular weight can be controlled by the monomer to catalyst ratio and the resulting polymers can exhibit polydispersities below 1.1.<sup>[85]</sup> Also, P3HT obtained via this method is highly regioregular, only the two first units exhibit a tail-to-tail coupling due to dimer formation in the beginning of the polymerization.

The possibility of making defined and narrow distributed P3AT blocks on the one hand, and the ease of the polymerization method on the other hand have rendered the GRIM method

fairly popular among material scientists and polymer chemists. Thus, fundamental investigations concerning the morphology and the electronic properties can be carried out on poly(3-hexylthiophene) as a function of the molecular weight.<sup>[88-91]</sup>

It is also noteworthy that the scope of the GRIM method has been expanded to several other monomers and polymers. For example, low-band gap conjugated polymers have been synthesized (scheme 7).<sup>[92-94]</sup> Although less control is observed here and the polydispersities are accordingly lower, the extended light absorption up to at least 750 nm makes these materials particularly interesting for organic photovoltaics.



**Scheme 7.** Chemical structures of low band-gap conjugated polymers synthesized via the GRIM method. a) Poly(3-hexyloxythiophene), b) poly(3-hexylselenophene), and c) poly(2,3-dihexylthieno[3,4-b]pyrazine).

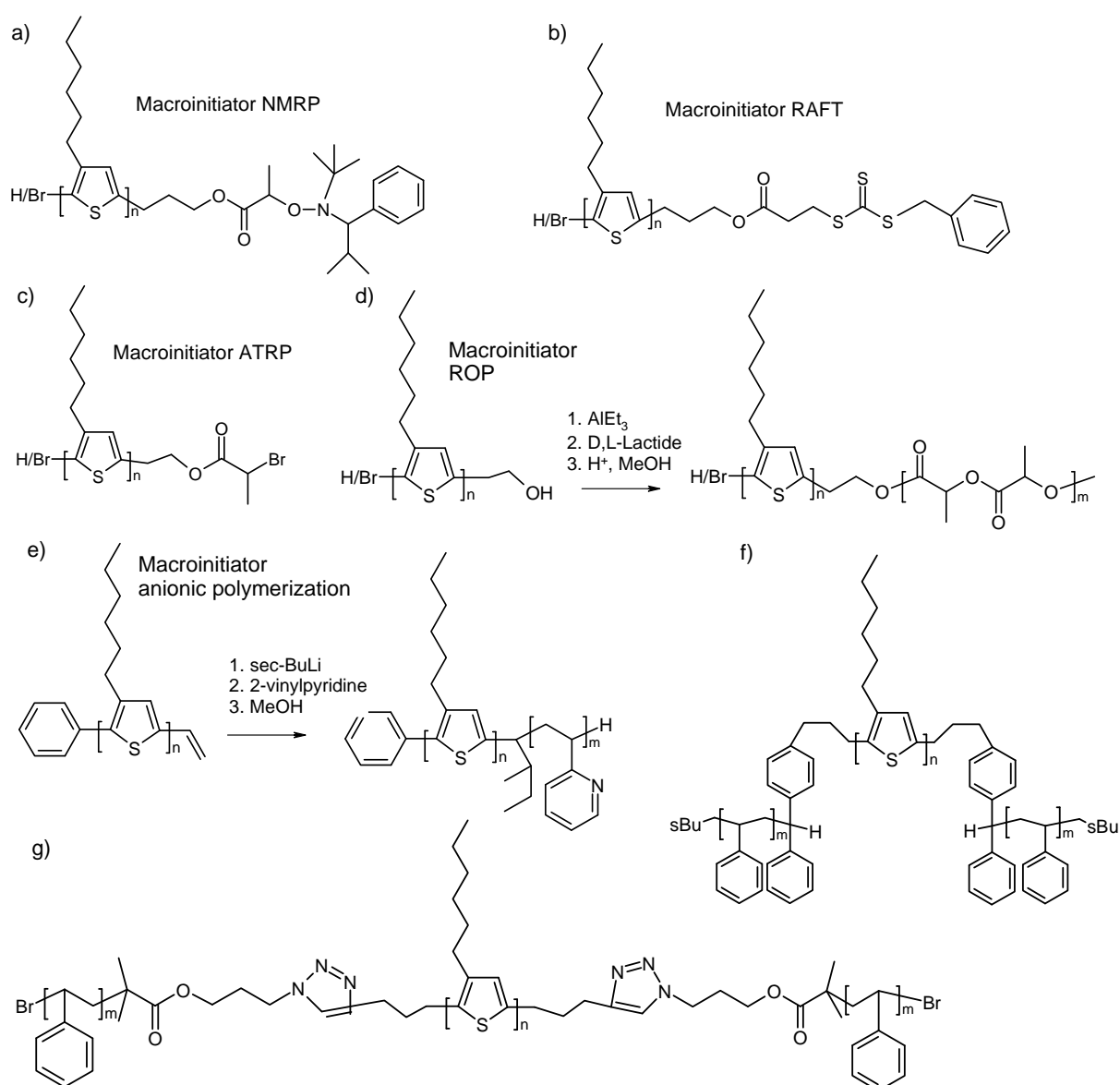
Furthermore, the GRIM has been used for the polymerization of aromatic monomers without heteroatoms<sup>[95,96]</sup>, and for “grafting-from” polymerizations.<sup>[97]</sup> The GRIM method thus seems to be of general applicability to a wide range of monomeric substrates, and the rigorous exploitation of this method has not only led to a plethora of novel conjugated polymers for the use in organic electronic devices, but also has enriched existing macromolecular architectures with well-defined, semiconducting donor blocks.

### Poly(3-hexylthiophene)-Based Block Copolymers

The GRIM method has also stimulated the synthesis of P3AT block copolymers with a huge variety of methods used. Since every polymer chain forms a complex with the nickel catalyst, the chains can be extended to conjugated-conjugated block copolymers when a second thiophene monomer with a different side chain is added to the reaction mixture.<sup>[87,98-101]</sup>

Quenching of the polymerization with an excess of Grignard reagents allows to react the active polymer chain with a variety of endgroups.<sup>[102]</sup> The procedure of this facile in-situ

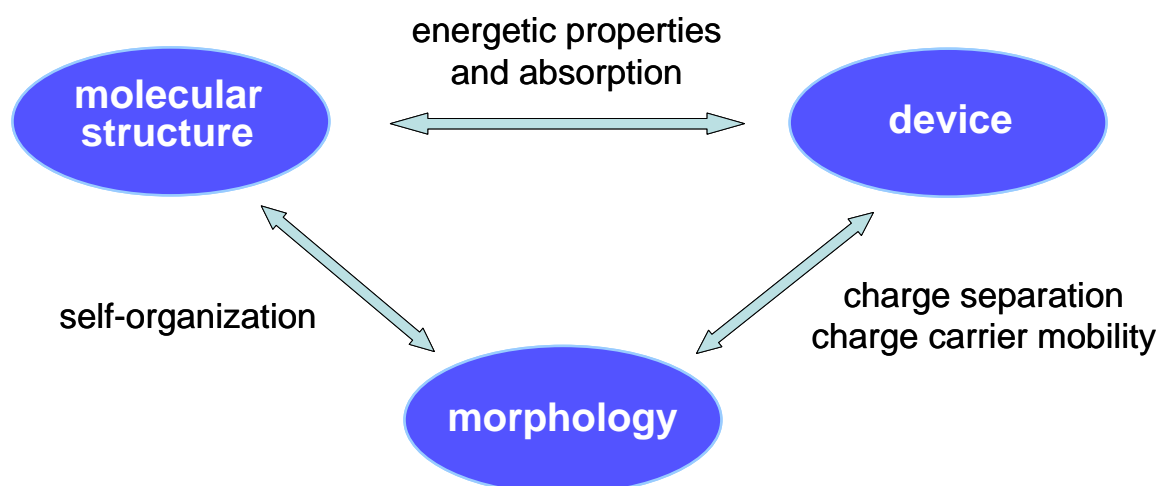
introduction of endgroups has been the platform for the preparation of P3AT block copolymers containing a second coil block. Up to now, P3AT macroinitiators for the atom transfer radical polymerization (ATRP)<sup>[103,104]</sup>, ring opening metathese polymerization (ROMP)<sup>[105]</sup>, ring opening polymerization (ROP)<sup>[106]</sup>, NMRP and RAFT<sup>[107]</sup>, and anionic polymerization<sup>[108]</sup> have been presented. In addition, polymer analogous reactions of P3ATs made by the GRIM with preformed polymers or dendrons have been carried out using anionic polymerization<sup>[109,110]</sup>, click chemistry<sup>[111]</sup> and esterification reactions<sup>[112]</sup>. Some of these preparation pathways towards P3HT-coil block copolymer architectures are summarized in scheme 8.



**Scheme 8.** Different approaches towards P3HT-based block copolymers. The coil blocks can be synthesized via ATRP, NMRP, RAFT, ROP, or anionic polymerization. In f) and g) P3HT triblock copolymers with polystyrene segments are prepared via endcapping of polystyryllithium and via a “click reaction”, respectively.

## Objective of this thesis

The aim of this thesis was the synthesis and characterization of novel semiconductor block copolymers containing both, donor as well as acceptor blocks, with well-defined architectures, by using one or more controlled polymerization methods. A particular focus was laid on the synthesis of donor blocks with high hole carrier mobilities, their incorporation into block copolymers with acceptor blocks, and their characterization by standard, microscopic, optical, and electrical methods. Furthermore, the fabrication of prototype organic electronic devices with the novel materials was an important aspect. Hereby, not only these individual points were to be addressed. Special attention was drawn to the relationship between molecular structure, morphology, and device performance in such a way that the direct outcome of the latter could be used for further improvement of the molecular structure. Most of the donor acceptor block copolymers synthesized up to now contain donor blocks with low or moderate hole carrier mobilities, which is due to the nature of material.<sup>[59,61]</sup> The hole mobility of semicrystalline homopolymers depends on the molecular weight<sup>[88]</sup>, and this is also expected when these building blocks are incorporated into block copolymers. Here, the molecular weight decides on the domain size, and thus will affect the device performance. Beside this molecular weight dependence, the polydispersity plays a role as well. Therefore, controlled polymerization methods with high tolerance towards functional groups were to be employed, combined and adapted in this thesis.



**Scheme 9.** Dependence of molecular structure, morphology, and device performance. These three main aspects are addressed in the thesis by synthesizing novel, fully functionalized donor-acceptor block copolymers via controlled polymerization methods.

## References

1. H. Shirakawa, E. J. Louis, A. G. MacDiarmid, C. K. Chiang, A. J. Heeger *J. Chem. Soc. Chem. Commun.* **1977**, 578.
2. C. D. Dimitrakopoulos, P. R. L. Malenfant, *Adv. Mater.* **2002**, *14*, 99.
3. S. S. Sun, N. S. Sariciftci, *Organic Photovoltaics: Mechanisms, Materials, and Devices* (Marcel Dekker, 2005).
4. H. Klauk, *Organic Electronics: Materials, Manufacturing and Applications* (Wiley-VCH, 2006).
5. G. Malliaras, R. Friend, *Phys. Today* **2005**, *58*, 53.
6. J. E. Anthony, M. Heeney, B. S. Ong, *MRS Bulletin*, **2008**, *33*, 698.
7. J. Zaumseil, H. Sirringhaus, *Chem. Rev.*, **2007**, *107*, 1296.
8. *Handbook of oligo and polythiophenes*, edited by D. Fichou, (Wiley-VCH, 1999).
9. H. Sirringhaus, P. J. Brown, R. H. Friend, M. M. Nielsen, K. Bechgaard, B. M. W. Langeveld-Voss, A. J. H. Spiering, R. A. J. Janssen, E. W. Meijer, P. T. Herwig, D. M. de Leeuw, *Nature* **1999**, *401*, 685.
10. S. Goffri, C. Müller, N. Stingelin-Stutzmann, D. W. Breiby, C. P. Radano, J. W. Andreasen, R. Thompson, R. A. J. Janssen, M. M. Nielsen, P. Smith, H. Sirringhaus, *Nature Mat.*, **2005**, *5*, 950.
11. M. Heeney, C. Bailey, K. Genevicius, M. Shkunov, D. Sparrowe, S. Tierney, I. McCulloch, *J. Am. Chem. Soc.* **2005**, *127*, 1078.
12. B. S. Ong, Y. Wu, P. Liu, S. Gardner, *J. Am. Chem. Soc.* **2004**, *126*, 3378.
13. I. McCulloch, M. Heeney, C. Bailey, K. Genevicius, I. MacDonald, M. Shkunov, D. Sparrowe, S. Tierney, R. Wagner, W. Zhang, M. L. Chabiny, R. J. Kline, M. D. McGehee, M. F. Toney, *Nat. Mater.* **2006**, *5*, 328.
14. A. Facchetti, *Mater. Today* **2007**, *10*, 28.
15. L.-L. Chua, J. Zaumseil, J.-F. Chang, E. C.-W. Ou, P. K.-H. Ho, H. Sirringhaus, R. H. Friend, *Nature* **2005**, *434*, 194.
16. A. L. Briseno, S. C. B. Mannsfeld, P. J. Shamberger, F. S. Ohuchi, Z. Bao, S. A. Jenekhe, Y. Xia, *Chem. Mater.* **2008**, *20*, 4712.
17. X. Zhan, Z. Tan, B. Domercq, Z. An, X. Zhang, S. Barlow, Y. Li, D. Zhu, B. Kippelen, S. R. Marder, *J. Am. Chem. Soc.* **2007**, *129*, 7246.

18. Z. Chen, Y. Zheng, H. Yan, A. Facchetti, *J. Am. Chem. Soc.* **2009**, *131*, 8.
19. H. Yan, Z. Chen, Y. Zheng, C. Newman, J. R. Quinn, F. Dötz, M. Kastler, A. Facchetti, *Nature* **2009**, *457*, 679.
20. J. A. Letizia, M. R. Salata, C. M. Tribout, A. Facchetti, M. A. Ratner, T. J. Marks, *J. Am. Chem. Soc.* **2008**, *130*, 9679.
21. A. Dodabalapur, H. E. Katz, L. Torsi, R. C. Haddon, *Science* **1995**, *269*, 1560.
22. M. Shkunov, R. Simms, M. Heeney, S. Tierney, I. McCulloch, *Adv. Mater.* **2005**, *17*, 2608.
23. T. B. Singh, F. Meghdadi, S. Günes, N. Marjanovic, G. Horowitz, P. Lang, S. Bauer, N. S. Sariciftci, *Adv. Mater.* **2005**, *17*, 2315.
24. J. Zaumseil, C. L. Donley, J. S. Kim, R. H. Friend, H. Sirringhaus, *Adv. Mater.* **2006**, *18*, 2708.
25. J. J. M. Halls, C. A. Walsh, N. C. Greenham, E. A. Marseglia, R. H. Friend, S. C. Moratti, A. B. Holmes, *Nature* **1995**, *376*, 495.
26. G. Yu, J. Gao, J. Hummelen, F. Wudl, A. Heeger, *Science* **1995**, *270*, 1789.
27. B. A. Gregg, *J. Phys. Chem. B* **2003**, *107*, 4688.
28. S. King, M. Sommer, S. Hüttner, M. Thelakkat, S. A. Haque, *J. Mater. Chem.*, **2009**, *19*, 5436.
29. H. Hoppe, N. S. Sariciftci, *J. Mater. Chem.* **2006**, *16*, 45.
30. A. R. Campbell, J. M. Hodgkiss, S. Westenhoff, I. A. Howard, R. A. Marsh, C. R. McNeill, R. H. Friend, N. C. Greenham, *Nano Lett.* **2008**, *8*, 3942.
31. P. Peumans, S. Uchida, S. R. Forrest, *Nature* **2003**, *425*, 158.
32. K. M. Coakley, M. D. McGehee, *Chem. Mater.* **2004**, *16*, 4533.
33. F. Padinger, R. S. Rittberger, N. S. Sariciftci, *Adv. Funct. Mater.* **2003**, *13*, 85.
34. J. K. Lee, W. L. Ma, C. J. Brabec, J. Yuen, J. S. Moon, J. Y. Kim, K. Lee, G. C. Bazan, A. J. Heeger, *J. Am. Chem. Soc.* **2008**, *130*, 3619.
35. S. Miller, G. Fanchini, Y. Lin, C. Li, C. Chen, W. Su, M. Chhowalla, *J. Mater. Chem.* **2008**, *18*, 306.
36. F. Zhang, K. G. Jespersen, C. Björström, M. Svensson, M. R. Andersson, V. Sundström, K. Magnusson, E. Moons, A. Yartsev, O. Inganäs, *Adv. Funct. Mater.* **2006**, *16*, 667.

37. M. C. Quiles, T. Ferenczi, T. Agostinelli, P. G. Etchegoin, Y. Kim, T. D. Anthopoulos, P. N. Stavrinou, D. D. C. Bradley, J. Nelson, *Nat. Mater.* **2008**, *7*, 158.
38. W. Ma, C. Yang, X. Gong, K. Lee, A. J. Heeger, *Adv. Funct. Mater.* **2005**, *15*, 1617.
39. J. Peet, J. Y. Kim, N. E. Coates, W. L. Ma, D. Moses, A. J. Heeger, G. C. Bazan, *Nat. Mater.* **2007**, *6*, 497.
40. G. Li, V. Shrotriya, J. Huang, Y. Yao, T. Moriarty, K. Emery, Y. Yang, *Nat. Mater.* **2005**, *4*, 864.
41. Y. Kim, S. Cook, S. M. Tuladhar, S. A. Choulis, J. Nelson, J. R. Durrant, D. D. C. Bradley, M. Giles, I. McCulloch, C.-S. Ha, M. Ree, *Nature Mater.* **2006**, *5*, 197.
42. J.-Y. Kim, K. Lee, N. E. Coates, D. Moses, T.-Q. Nguyen, M. Dante, A. J. Heeger, *Science* **2007**, *317*, 222.
43. F. S. Bates, G. H. Fredrickson, *Ann. Rev. Phys. Chem.* **1990**, *41*, 525.
44. C. Park, J. Yoon, E. Thomas, *Polymer* **2003**, *44*, 6725.
45. L. A. A. Pettersson, L. S. Roman, O. Inganäs, *J. Appl. Phys.* **1999**, *86*, 487.
46. M. Sommer, S. Hüttner, M. Thelakkat, *J. Mater. Chem.*, submitted.
47. G. Buxton, N. Clarke, *Phys. Rev. B* **2006**, *74*, 085207.
48. S. H. Kim, M. J. Misner, T. P. Russell, *Adv. Mater.* **2004**, *16*, 2119.
49. T. Thurn-Albrecht, J. DeRouchey, T. P. Russell, H. M. Jaeger, *Macromolecules* **2000**, *33*, 3250.
50. D. E. Angelescu, J. H. Waller, R. A. Register, P. M. Chaikin, *Adv. Mater.* **2005**, *17*, 1878.
51. E. J. W. Crossland, M. Nedelcu, C. Ducati, S. Ludwigs, M. A. Hillmyer, U. Steiner, H. J. Snaith, *Nano Lett.*, **2009**, *9*, 2813.
52. K. M. Coakley, M. D. McGehee, *Appl. Phys. Lett.* **2003**, *83*, 3380.
53. M. Lee, B.-K. Cho, W.-C. Zin, *Chem. Rev.* **2001**, *101*, 3869.
54. Y.-L. Loo, R. A. Register, in: *Developments in Block Copolymer Science and Technology*, p. 213-243 (Wiley- VCH, 2004).
55. I. W. Hamley, in: *Advances in Polymer Science*, *148*, p. 113-137 (Springer, 1999).
56. C. Zhang, S. Choi, J. Haliburton, T. Cleveland, R. Li, S.-S. Sun, A. Ledbetter, C. E. Bonner *Macromolecules* **2006**, *39*, 4317.
57. K. Sivula, Z. Ball, N. Watanabe, J. Freché, *Adv. Mater.* **2006**, *18*, 206.

58. M. H. van der Veen, B. de Boer, U. Stalmach, K. I. van de Wetering, G. Hadziioannou, *Macromolecules* **2004**, *37*, 3673.
59. S. M. Lindner, M. Thelakkat, *Macromolecules* **2004**, *37*, 8832.
60. U. Stalmach, B. de Boer, C. Videlot, P. F. van Hutten, G. Hadziioannou, *J. Am. Chem. Soc.*, **2000**, *122*, 5464.
61. S. Barrau, T. Heiser, F. Richard, C. Brochon, C. Ngov, K. van de Wetering, G. Hadziioannou, D. V. Anokhin, D. A. Ivanov, *Macromolecules* **2008**, *41*, 2701.
62. G. Tu, H. Li, M. Forster, R. Heiderhoff, L. J. Balk, U. Scherf, *Macromolecules* **2006**, *39*, 4327.
63. S.-S. Sun, C. Zhang, A. Ledbetter, S. Choi, K. Seo, C. E. Bonner, M. Drees, N. S. Sariciftci, *Appl. Phys. Lett.* **2007**, *90*, 043117.
64. M. Prato, *J. Mater. Chem.* **1997**, *7*, 1097.
65. J. J. Dittmer, E. A. Marseglia, R. H. Friend, *Adv. Mater.* **2002**, *12*, 1270.
66. P. E. Keivanidis, I. A. Howard, R. H. Friend, *Adv. Funct. Mater.* **2008**, *18*, 3189.
67. W. S. Shin, H.-H. Jeong, M.-K. Kim, S.-H. Jin, M.-R. Kim, J.-K. Lee, J. W. Lee, Y.-S. Gal, *J. Mater. Chem.* **2006**, *16*, 384.
68. J. J. Dittmer, R. Lazzaroni, P. Leclere, P. Moretti, M. Granstrom, K. Petritsch, E. A. Marseglia, R. H. Friend, J. L. Bredas, H. Rost, A. B. Holmes, *Sol. En. Mater. Sol. Cells* **2000**, *61*, 53.
69. S. Foster, C. E. Finlayson, P. E. Keivanidis, Y.-S. Huang, I. Hwang, R. H. Friend, M. B. J. Otten, L.-P. Lu, E. Schwartz, R. J. M. Nolte, A. E. Rowan, *Macromolecules* **2009**, *42*, 2023.
70. J. Chiefari, Y. K. Chong, F. Ercole, J. Krstina, J. Jeffery, T. P. T. Le, R. T. A. Mayadunne, G. F. Meijs, C. L. Moad, G. Moad, E. Rizzardo, S. H. Thang, *Macromolecules* **1998**, *31*, 5559.
71. H. Fischer, *Chem. Rev.* **2001**, *101*, 3581.
72. B. Keoshkerian, M. K. Georges, R. Quinlan, R. Veregin, R. Goodbrand, *Macromolecules* **1998**, *31*, 7559.
73. D. Benoit, S. Grimaldi, J. P. Finet, P. Tordo, M. Fontanille, Y. Gnanou, *Polym. Prepr.* **1997**, *38*, 729.
74. D. Benoit, V. Chaplinski, R. Braslau, C. J. Hawker, *J. Am. Chem. Soc.*, **1999**, *121*, 3904.

75. J. Dao, D. Benoit, C. J. Hawker, *J. Polym. Sci., Part A: Polym. Chem.* **1998**, *36*, 2161.
76. S. M. Lindner, M. Thelakkat, *Macromol. Chem. Phys.*, 2006, **207**, 2084.
77. M. Sommer, A. Lang, M. Thelakkat, *Angew. Chem. Int. Ed.* **2008**, *47*, 7901.
78. C. Hawker, A. W. Bosman, E. Harth, *Chem. Rev.* **2001**, *101*, 3661
79. J. Pyun, X. Z. Zhou, E. Drockenmuller, C. J. Hawker, *J. Mater. Chem.* **2003**, *13*, 2653.
80. R. D. McCullough, *Adv. Mater.* **1998**, *10*, 93.
81. R. D. McCullough, R. D. Lowe, *J. Chem. Soc., Chem. Commun.* **1992**, 70.
82. T.-A. Chen, X. Wu, R. D. Rieke, *J. Am. Chem. Soc.* **1995**, *117*, 233.
83. R. S. Loewe, S. M. Khersonsky, R. D. McCullough, *Adv. Mater.* **1999**, *11*, 250.
84. R. Miyakoshi, A. Yokoyama, T. Yokozawa, *J. Am. Chem. Soc.* **2005**, *127*, 17542.
85. R. Miyakoshi, A. Yokoyama, T. Yokozawa, *Macromol. Rapid Commun.* **2004**, *25*, 1663
86. T. Beryozkina, V. Senkovskyy, E. Kaul, A. Kiriya, *Macromolecules* **2008**, *41*, 7817.
87. M. C. Iovu, E. E. Sheina, R. R. Gil, R. D. McCullough, *Macromolecules* **2005**, *38*, 8649.
88. R. J. Kline, M. D. McGehee, E. N. Kadnikova, J. Liu, J. M. J. Fréchet, *Adv. Mater.* **2003**, *15*, 1519.
89. A. Zen, M. Saphiannikova, D. Neher, J. Grenzer, S. Grigorian, U. Pietsch, U. Asawapirom, S. Janietz, U. Scherf, I. Lieberwirth, G. Wegner, *Macromolecules* **2006**, *39*, 2162.
90. J.-F. Chang, J. Clark, N. Zhao, H. Sirringhaus, D. W. Breiby, J. W. Andreasen, M. M. Nielsen, M. Giles, M. Heeney, I. McCulloch, *Phys. Rev. B* **2006**, *74*, 115318.
91. Z. Wu, A. Petzold, T. Henze, T. Thurn-Albrecht, R. Lohwasser, M. Sommer, M. Thelakkat, *Macromolecules*, submitted.
92. E. E. Sheina, S. M. Khersonsky, E. G. Jones, R. D. McCullough, *Chem. Mater.* **2005**, *17*, 3317.
93. M. Heeney, W. Zhang, J. D. Crouch, M. L. Chabinyc, S. Gordeyev, R. Hamilton, S. J. Higgins, I. McCulloch, P. J. Skabara, D. Sparrowea, S. Tierney, *ChemComm* **2007**, 5061.
94. L. Wen, B. C. Duck, P. C. Dastoor, S. C. Rasmussen, *Macromolecules* **2008**, *41*, 4576.
95. R. Miyakoshi, K. Shimono, A. Yokoyama, T. Yokozawa, *J. Am. Chem. Soc.* **2006**, *128*, 16012.
96. M. C. Stefan, A. E. Javier, I. Osaka, R. D. McCullough, *Macromolecules* **2009**, *42*, 30.

97. V. Senkovskyy, N. Khanduyeva, H. Komber, U. Oertel, M. Stamm, D. Kuckling, A. Kiriya, *J. Am. Chem. Soc.* **2007**, *129*, 6626.
98. Y. Zhang, K. Tajima, K. Hirota, K. Hashimoto, *J. Am. Chem. Soc.* **2008**, *130*, 7812.
99. K. Ohshimizu, M. Ueda, *Macromolecules* **2008**, *41*, 5289.
100. T. Yokozawa, I. Adachi, R. Miyakoshi, A. Yokoyama, *High Performance Polymers* **2007**, *19*, 684.
101. P.-T. Wu, G. Ren, C. Li, R. Mezzenga, S. A. Jenekhe, *Macromolecules* **2009**, *42*, 2317.
102. M. Jeffries-El, G. Sauve, R. D. McCullough, *Adv. Mater.* **2004**, *16*, 1017.
103. J. Liu, E. Sheina, T. Kowalewski, R. D. McCullough, *Angew. Chem. Int. Ed.* **2002**, *41*, 329.
104. M. C. Iovu, M. Jeffries-El, E. Sheina, J. R. Cooper, R. D. McCullough, *Polymer* **2005**, *46*, 8582.
105. C. P. Radano, O. A. Scherman, N. Stingelin-Stutzmann, C. Müller, D. W. Breiby, P. Smith, R. A. J. Janssen, E. W. Meijer, *J. Am. Chem. Soc.* **2005**, *127*, 12502.
106. B. W. Boudouris, C. D. Frisbie, M. A. Hillmyer, *Macromolecules* **2008**, *41*, 67.
107. M. C. Iovu, C. R. Craley, M. Jeffries-El, A. B. Krankowski, R. Zhang, T. Kowalewski, R. D. McCullough, *Macromolecules* **2007**, *40*, 4733.
108. C.-A. Dai, W.-C. Yen, Y.-H. Lee, C.-C. Ho, W.-F. Su, *J. Am. Chem. Soc.* **2007**, *129*, 11036.
109. M. C. Iovu, M. Jeffries-El, R. Zhang, T. Kowalewski, R. D. McCullough, *J. Macromol. Sci. Part A: Pure and Applied Chemistry* **2006**, *43*, 1991.
110. T. Higashihara, K. Ohshimizu, A. Hirao, M. Ueda, *Macromolecules* **2008**, *41*, 9505.
111. M. Urien, H. Erothu, E. Cloutet, R. C. Hiorns, L. Vignau, H. Cramail, *Macromolecules* **2008**, *41*, 7033.
112. N. Watanabe, C. Mauldin, J. M. J. Freché, *Macromolecules* **2007**, *40*, 6793.



## Overview of Thesis

The thesis contains nine publications. Seven are presented in chapters 3-9 and two more appear in the appendix (chapter 10 and 11). I was mainly interested in creating and investigating innovative block copolymer architectures with one or more electronic functions for the use in organic field effect transistors (OFETs) or organic photovoltaics (OPVs). The central point leading through my thesis is the extension of absorption in the visible region and the improvement of the hole carrier mobility of donor (D) blocks synthesized by controlled polymerization methods, as well as their incorporation into donor acceptor block copolymers with the acceptor (A) monomer perylene bisimide acrylate. Figure 1 illustrates the chemical structures and properties of the different donors employed.

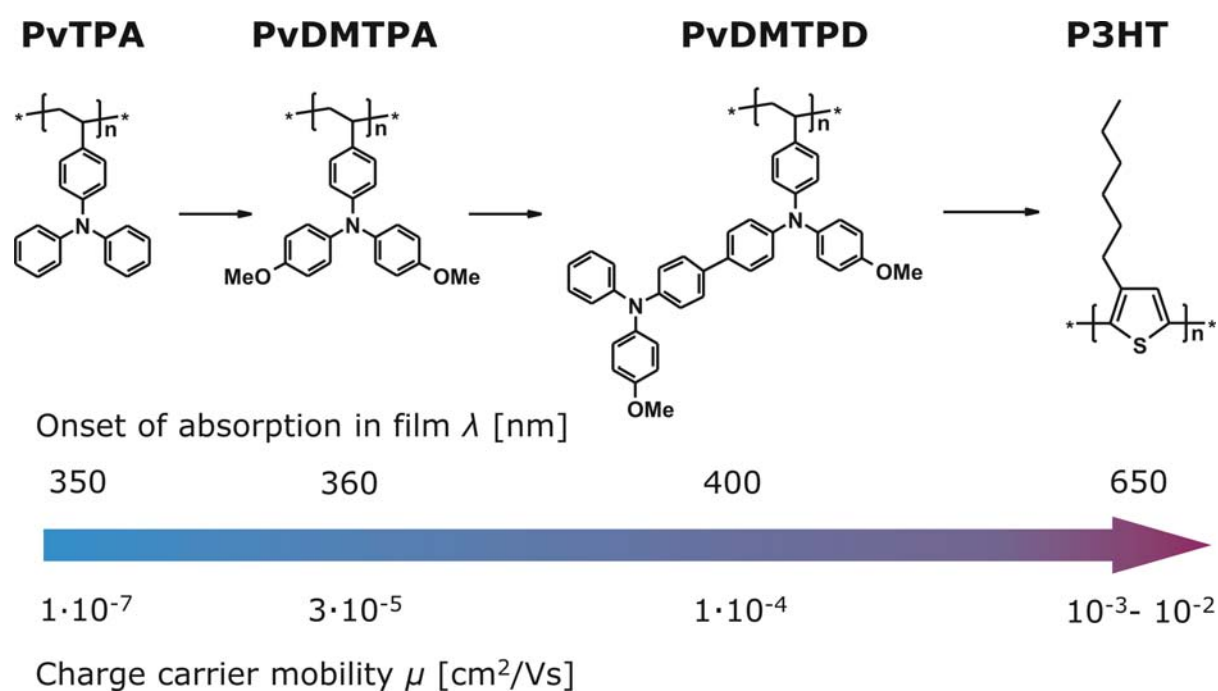


**Figure 1.** Chemical structures, onsets of absorption and charge carrier mobilities of the donor blocks. The first three polymers are amorphous poly(triarylamines) (for the exact names see section on amorphous-crystalline donor acceptor block copolymers) and the last one is a main-chain conjugated poly(3-hexylthiophene) P3HT. The absorption and the charge carrier mobilities increase from left to right, both of which is of utmost importance for the application of these building blocks in OPVs. The hole carrier mobility of P3HT is strongly dependent on its molecular weight and the mobility range given here corresponds to the values of the different segment lengths used in this thesis.

However, many other fruitful findings were found on the way, and some of them are included here. There are several ways to classify and connect the individual topics and chapters, e.g. by the polymer architecture, the polymerization method used or by the final application. All of them are used for a comprehensive structuring of this thesis, which is explained in the following:

The first part is concerned with amorphous-crystalline D-A block copolymers synthesized by one polymerization method, Nitroxide Mediated Controlled Radical Polymerization (NMRP). Thereby, an amorphous poly[N,N'-bis(4-methoxyphenyl)-N-phenyl-N'-4-vinylphenyl-(1,1'-biphenyl)-4,4'-diamine] carrying tetraphenylbenzidine units (referred to as PvDMTPD, see figure 1 and 2) is synthesized and used as macroinitiator for the NMRP of perylene bisimide acrylate (PerAcr). The resulting second block of PvDMTPD-*b*-PPerAcr is side-chain crystalline, owing to the strong  $\pi$ - $\pi$  interactions of neighbored perylene bisimide moieties. The novel materials are characterized thoroughly using standard, optical, electrical and microscopic methods, and are subsequently tested in single layer organic solar cells. These results are included in a comparative study with two other types of block copolymers, PvDMTPA-*b*-PPerAcr and PvTPA-*b*-PPerAcr (figure 1), some of which were synthesized during my preceeding diploma thesis. Therefore, the two publications dealing with these amorphous-crystalline D-A block copolymers appear as appendices at the end of the thesis (chapters 10 and 11).

The second part takes advantage of the first part in that the amorphous donor with the highest hole carrier mobility, PvDMTPD, is selected and used to generate block copolymer nanoparticle hybrids. PvDMTPD macroinitiators with relatively high molecular weights of  $\sim 20$  kg/mol are employed to polymerize 4-vinylpyridine, 4vP. The resulting amphiphilic block copolymers PvDMTPD-*b*-P4vP contain hole transport units and a highly polar segment capable of efficient coordination to inorganic n-type nanoparticles. Various block copolymers are successfully synthesized via NMRP. The preferential incorporation of CdSe:Te nanoparticles into P4vP domains of microphase separated bulk samples is furthermore demonstrated, yielding innovative self-assembling hybrid materials (chapter 3).

In the third part of the thesis the hole carrier mobility is further enhanced by using main chain conjugated poly(3-hexylthiophene) (P3HT) blocks. Double-crystalline D-A block copolymers P3HT-*b*-PPerAcr are synthesized by the straightforward combination of two polymerization methods: Grignard Metathese Polymerization (GRIM) and NMRP. The GRIM is modified and used in order to synthesize well-defined P3HT macroinitiators for NMRP via a novel one-pot procedure. Then, PerAcr is polymerized in a second step. Thus, a series of main-chain crystalline- side-chain crystalline D-A block copolymers P3HT-*b*-PPerAcr with varying composition is successfully synthesized for the first time (chapter 4). Next, a comprehensive analysis of competing crystallization of P3HT-*b*-PPerAcr as a function of molecular weight, composition, and preparation conditions is carried out using calorimetry and X-ray diffraction (chapter 5). Furthermore, the photovoltaic performance of P3HT-*b*-PPerAcr is elucidated as a function of composition and molecular weight of P3HT, and record external quantum efficiencies exceeding 30 % are measured (chapter 6).

The fourth part covers further amorphous-crystalline block copolymers with one electronically inactive polystyrene segment and one PPerAcr acceptor block. A series of polystyrene-*b*-poly(perylene bisimide acrylate), PS-*b*-PPerAcr, with varying PS block length is synthesized via NMRP. We study the self-assembling behaviour of PS-*b*-PPerAcr by microscopic, scattering, and optical methods (chapter 7). Furthermore, organic field-effect transistors (OFETs) are constructed from these materials, and the OFET performance of the block copolymer is compared to those of the analogous homopolymer and blend systems (chapter 8).

In the last part of the thesis the feasibility of combining focused ion beam (FIB) with scanning electron microscopy (SEM) in terms of detecting buried structures in semiconductor blend and block copolymer thin films exhibiting a vertical phase separation is investigated. The FIB allows for a precise and stepwise etching of the film, while in between the etching steps SEM pictures of the treated area are taken. This approach demonstrates how structural evolution can proceed from the surface through the bulk of the film, and is applicable to any other vertically phase separated system in which sufficient contrast between the components is provided (chapter 9).

Figure 2 illustrates all the various D-A block copolymer architectures synthesized by NMRP and GRIM in this thesis.

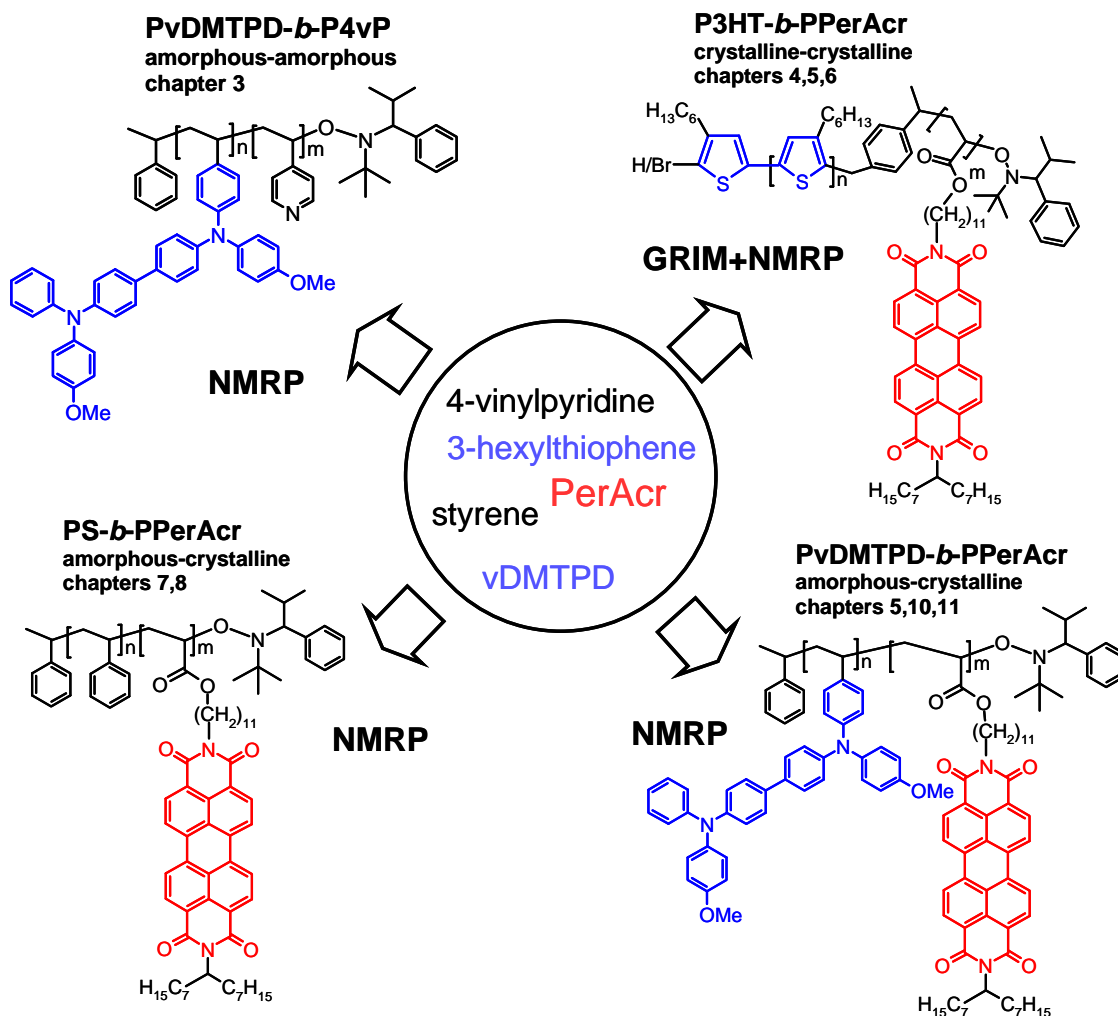


**Figure 2.** Monomers, polymerization methods used, and block copolymer architectures synthesized in this thesis. PvDMTPD-*b*-P4vP exhibits two amorphous segments, PvDMTPD-*b*-PPerAc and PS-*b*-PPerAc are amorphous-crystalline, and P3HT-*b*-PPerAc is double-crystalline. NMRP is employed to prepare block copolymers PvDMTPD-*b*-P4vP, PvDMTPD-*b*-PPerAc, and PS-*b*-PPerAc, whereas GRIM is combined with NMRP for the preparation of P3HT-*b*-PPerAc.

The key results of the individual publications are summarized in the following, with a particular focus on how one theme interacts with the next, thus bridging the gaps between the chapters. More details concerning the synthesis, characterization and device preparation are found in the respective chapters and in the supporting informations.

## Amorphous-Crystalline Donor Acceptor Block Copolymers

Amorphous crystalline D-A block copolymers comprised of poly[N,N'-bis(4-methoxyphenyl)-N-phenyl-N'-4-vinylphenyl-(1,1'-biphenyl)-4,4'-diamine], PvDMTPD, and poly(perylene bisimide acrylate), PPerAc, are synthesized by NMRP. Extensive characterization is carried out, and a comparison with two simpler, poly(triphenylamine)-based block copolymers poly[bis(4-methoxyphenyl)-4'-vinylphenylamine]-*b*-poly(perylene bisimide acrylate), PvDMTPA-*b*-PPerAc, and poly(vinyltriphenylamine)-*b*-poly(perylene bisimide acrylate), PvTPA-*b*-PPerAc is made. The polymers PvTPA-*b*-PPerAc and PvDMTPA-*b*-PPerAc available from earlier work and my preceding diploma thesis were fully characterized here in order to elucidate the influence of different substituents on the properties of the amorphous donor blocks. The schematic D-A block copolymer architecture, the chemical structures and the resulting thermal properties are shown in figure 3 (chapters 5, 10, and 11).

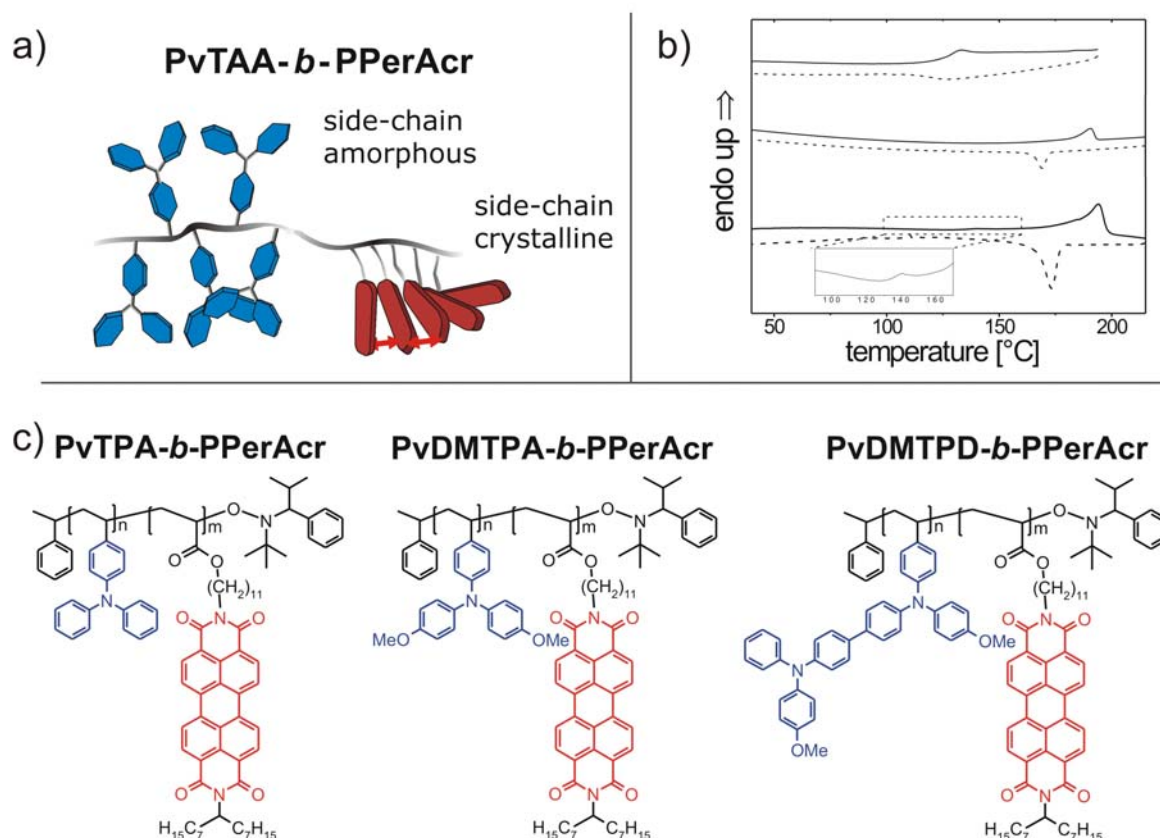


**Figure 3.** a) Schematic architecture of amorphous-crystalline PvDMTPA-*b*-PPerAc. b) Differential scanning calorimetry (DSC) of PvDMTPA-*b*-PPerAc, showing the amorphous and crystalline nature of the two blocks. This behaviour is observed for all three types of block copolymers. Top: PvDMTPA, middle: PPerAc, bottom: PvDMTPA-*b*-PPerAc. The block copolymer exhibits both transitions of the respective homopolymers, curves are offset in y-direction for clarity. c) Chemical structures of the three block copolymers with varying donor block.

Besides standard polymer characterization, the novel materials were investigated extensively in terms of their optical, electrochemical and electronic properties. The substitution of the triphenylamine core at 4-position allows to tune the highest occupied molecular orbital (HOMO) and lowest unoccupied molecular orbital (LUMO) energy levels as well as the charge carrier mobility. Figure 4 shows the optical densities in film, the cyclic voltammograms (CV) in solution, the resulting estimated HOMO/ LUMO energy levels, and the charge carrier mobilities of all homopolymers (chapters 5 and 11).

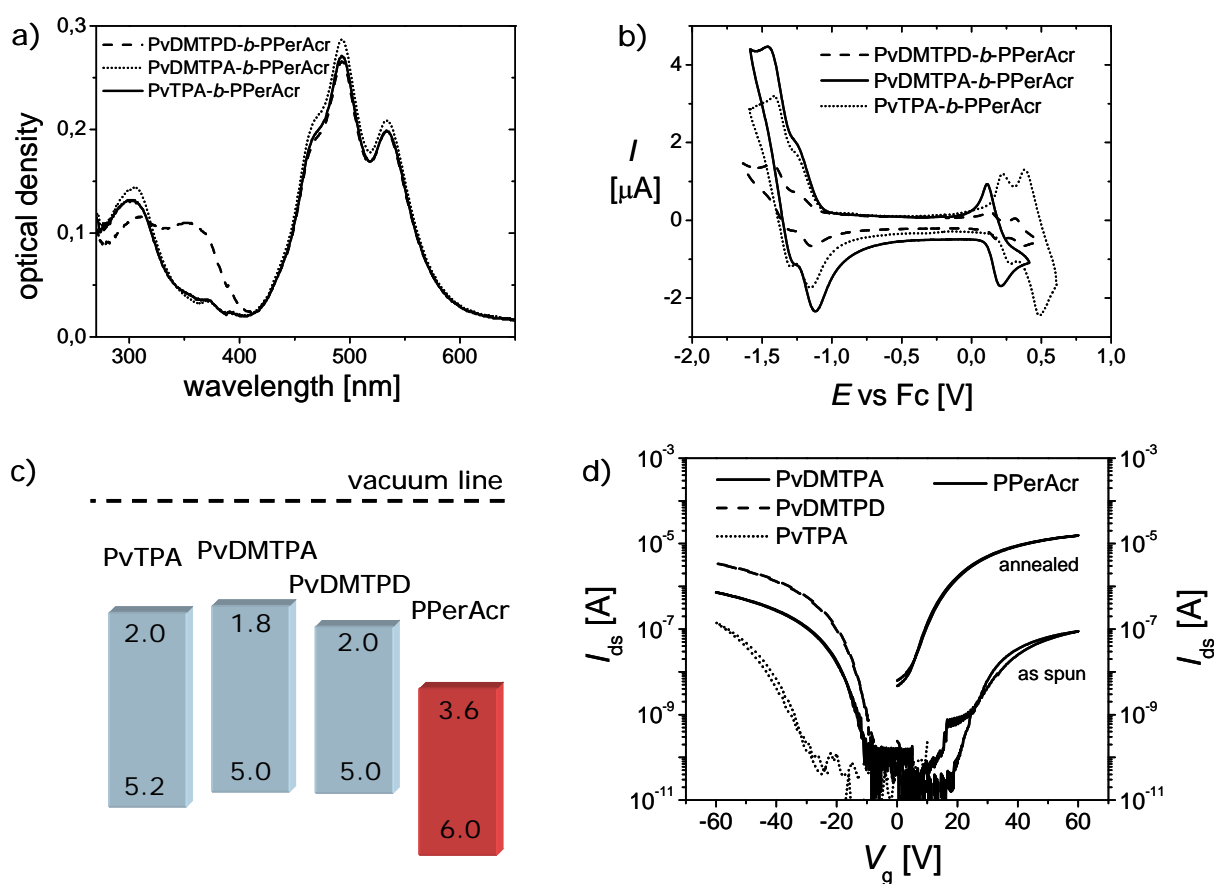


**Figure 4.** Optical, electrochemical and electrical characterization of the homo- and block copolymers. a) Optical density in film. b) Cyclic voltammograms in solution plotted vs ferrocene (Fc). Curves were measured at 50 mV/s and tetrabutylammonium hexafluorophosphate was used as conducting electrolyte. c) Schematic representation of the resulting HOMO/LUMO energy levels. d) Transfer plots of homopolymer OFET devices (bottom gate bottom contact architecture). The left part of the plot (negative gate voltages) shows the performance of the amorphous donor polymers, and the right part (positive gate voltages) the acceptor polymer PPerAcr. Thermal annealing of the PPerAcr device increases the electron mobility by more than two orders of magnitude.

The optical densities between 250 and 400 nm vary according to the different donor segments, whereas the finger-print absorption of PPerAcr between 400 and 600 nm is almost unchanged (figure 4a). The impact of substituting the triphenylamine (TPA) core is clearly visible from figure 4b. Upon attaching two methoxygroups, the oxidation potential of PvTPA is shifted from 0.4 V to 0.2 V in PvDMTPA, resulting in a HOMO level of PvDMTPA of 5.0 eV compared to 5.2 eV of PvTPA (figure 4c). Additionally, the electrochemical stability of PvDMTPA is greatly enhanced. PvTPA is unstable upon oxidation due to dimerization at 4-position, whereas PvDMTPA can be reversibly oxidized. PvDMTPD also exhibits a high electrochemical stability and its HOMO energy level is 5.0 eV as well. The charge carrier mobilities  $\mu$  of PvTPA, PvDMTPA, and PvDMTPD, obtained from OFET devices, are  $1 \cdot 10^{-7}$  cm<sup>2</sup>/Vs,  $3 \cdot 10^{-5}$  cm<sup>2</sup>/Vs and  $1 \cdot 10^{-4}$  cm<sup>2</sup>/Vs, respectively (figure 4d). This means a continuous increase in the hole carrier mobility of these three building blocks. Therefore, PvDMTPD is an especially promising candidate for the application in OPV devices. The combination with PPerAcr, showing an electron mobility of  $1 \cdot 10^{-3}$  cm<sup>2</sup>/Vs, guarantees balanced charge transport. Furthermore, the series of PvTPA-*b*-PPerAcr, PvDMTPA-*b*-PPerAcr and PvDMTPD-*b*-PPerAcr is ideal for a comparative study in which the device performance is correlated with the donor HOMO energy level and the charge carrier mobility. Whereas substitution of the TPA core alters the electronic properties, changing the molecular weight of the donor blocks in the block copolymers allows to tune the nanomorphology. Figure 5a-d shows transmission electron microscopy (TEM) images of thermally annealed bulk samples. For block copolymers with a  $M_{n,donor}$  higher than 12 kg/mol and PPerAcr weight fractions between 65-85 %, PPerAcr lamellae are observed in the amorphous donor matrix after thermal annealing (figure 5b,c). Block copolymers with donor blocks of lower molecular weights exhibit shorter structures of PPerAcr (figure 5a,d).

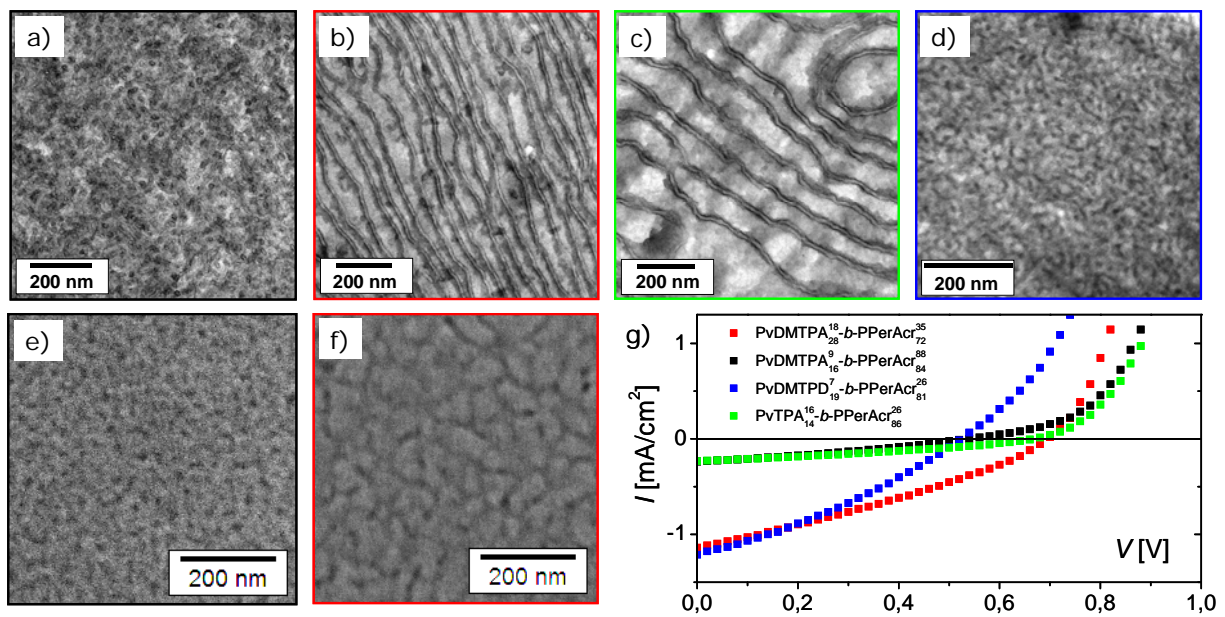


**Figure 5.** Morphology and photovoltaic performance of PvDMTPA<sub>16</sub><sup>18</sup>-b-PPerAc<sub>84</sub><sup>88</sup> (a and e, black), PvDMTPA<sub>28</sub><sup>18</sup>-b-PPerAc<sub>72</sub><sup>35</sup> (b and f, red), PvTPA<sub>14</sub><sup>16</sup>-b-PPerAc<sub>86</sub><sup>26</sup> (c, green), and PvDMTPD<sub>19</sub><sup>7</sup>-b-PPerAc<sub>81</sub><sup>26</sup> (d, blue). The first superscript denotes the  $M_n$  of the donor and the second one the overall  $M_n$  of the block copolymer. The subscripts denote the respective weight fractions. a)-d) TEM cross sections of thermally annealed bulk samples after staining with RuO<sub>4</sub>. e) and f) Top-view SEM images of the devices itself prepared by spin coating from chloroform. Domains of PPerAc are dark in TEM and bright in SEM. g) J-V-characteristics of all block copolymers. The color corresponds the colored border of the micrographs of a)-f).

For the purpose of a comparative study, these four block copolymers with lamellar and shorter PPerAc morphologies are tested in OPV devices. Thereby, the HOMO levels, the charge carrier mobilities, and the nanomorphologies are correlated with their photovoltaic performance. We find a five-fold improvement of the short circuit current ( $J_{sc}$ ) (Fig. 5g) between PvTPA-*b*-PPerAc and PvDMTPA-*b*-PPerAc. This is caused by the higher charge carrier mobility and the larger HOMO level offset of PvDMTPA (see Fig. 4c,d). The  $J_{sc}$  of the two devices with PvDMTPA-*b*-PPerAc exhibiting different nanostructures (Fig. 5a,b) is increased by a factor of five. Additionally, the open circuit voltage  $V_{oc}$  is increased. These improvements are due to a more favorable charge percolation in the lamellar PvDMTPA<sub>28</sub><sup>18</sup>-*b*-PPerAc<sub>72</sub><sup>35</sup> compared to PvDMTPA<sub>16</sub><sup>9</sup>-*b*-PPerAc<sub>84</sub><sup>88</sup> exhibiting shorter PPerAc structures. However, thermally annealed volume samples are used for TEM cross sectioning, whereas the J-V-characteristics are obtained from thin films spun from chloroform. Yet, the SEM pictures of the active layers themselves (Fig. 5e,f) can reproduce the morphological trend of the two corresponding TEM pictures (Fig. 5a,b) and therefore confirm our argumentation:

The domains are larger in figure 5f than in 5e. These facts inevitably picture the much enhanced charge percolation in  $\text{PvDMTPA}_{28}^{18}\text{-}b\text{-PPerAcr}_{72}^{35}$ . With these results in mind, the OPV performance of  $\text{PvDMTPD}_{19}^7\text{-}b\text{-PPerAcr}_{81}^{26}$  can be explained as follows: Arising from the low  $M_n$  of PvDMTPD of 7 kg/mol, an unfavorable morphology with short PPerAcr structures forms (Fig. 5d). Nevertheless, the highest  $J_{sc}$  among the four block copolymers is obtained. This leads us to the following essential conclusions: Very efficient OPV device performance can be obtained by using a block copolymer with a donor HOMO of 5.0 eV, a hole carrier mobility of around  $10^{-4} \text{ cm}^2/\text{Vs}$ , and a favorable charge percolation. Donor-acceptor block copolymers such as  $\text{PvDMTPD-}b\text{-PPerAcr}$  with  $M_{n,\text{donor}}$  higher than 15 kg/mol and PPerAcr weight fractions ranging between 65-85 % are therefore expected to fulfill these predictions (chapter 11).

## Block Copolymer Nanoparticle Hybrid Materials

A novel approach towards self-assembling D-A block copolymer nanoparticle hybrid materials with outstanding morphology control is presented. Taking into consideration the results on the charge carrier mobilities from the previous part, a series of block copolymers with a high molecular weight PvDMTPD segment and a polar poly(4-vinylpyridine) block, P4vP, is successfully prepared by NMRP. While the first block provides the electronic function of transporting holes efficiently, the highly polar P4vP block can coordinate to light-harvesting n-type nanoparticles such as CdSe. We elucidate the order of polymerization of the two monomers: Polymerizing vDMTPD from P4vP macroinitiators yields ill-defined block copolymers owing to homopolymerization of vDMTPD, whereas better-defined block copolymers are obtained when PvDMTPD is used as a macroinitiator for the NMRP of 4vP. Using the latter, various  $\text{PvDMTPD-}b\text{-P4vP}$  block copolymers are synthesized via the withdrawal of aliquots. For P4vP weight fractions between 55-75 % we find highly ordered lamellae, the asymmetry of which increases with increasing P4vP content. As an example, the asymmetric lamellae of  $\text{PvDMTPD}_{26}^{21}\text{-}b\text{-P4vP}_{74}^{82}$  is shown in figure 6a.

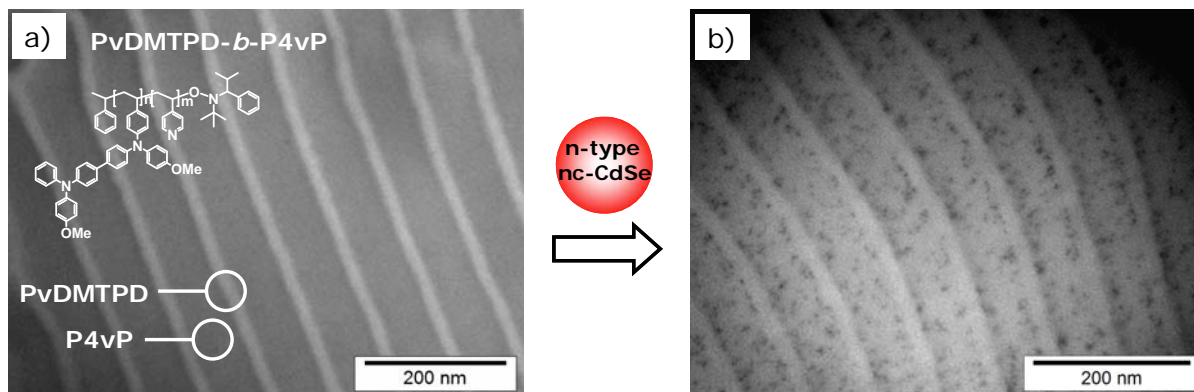


**Figure 6.** TEM of  $\text{PvDMTPD}_{26}^{21}\text{-}b\text{-P4vP}_{74}^{82}$ . Volume morphologies after slow evaporation from pyridine without (a) and with CdSe nanoparticles (b). P4vP is stained with iodine and appears gray, PvDMTPD appears brighter. The light-harvesting CdSe nanoparticles are exclusively sequestered in the polar P4vP domains (dark spots in b)) and gather predominantly at the interface of the two phases. Thicknesses of domain sizes are  $\sim 20$  and  $\sim 60$  nm for PvDMTPD and P4vP, respectively.

The formation of asymmetric lamellae in a broad range of varying P4vP content is ascribed to the relatively high polydispersity of the second block. The PDI of the first PvDMTPD block is 1.15, whereas the resulting PDI of the block copolymer is 1.78. Note that the moderate polydispersity of the block copolymer is not at all a disadvantage in terms of long-range order, but even helps us to maintain a lamellar morphology while widening up the P4vP phase at the same time. Additionally, by using  $\text{PvDMTPD}_{26}^{21}\text{-}b\text{-P4vP}_{74}^{82}$  as an example, we demonstrate preferential sequestering of n-type CdSe nanoparticles in the polar P4vP domains without altering the morphology (figure 6b). Thus, the self-assembly of this highly ordered block copolymer hybrid material leads to spatial separation of hopping sites for both, holes and electrons. The tunability of the P4vP lamellar thickness upon increasing the P4vP block length enables to establish structure-property relationships while only one parameter is varied. These findings open up novel opportunities for the fabrication of innovative next-generation block copolymer hybrid photovoltaic devices (chapter 3).

### Crystalline-Crystalline Donor Acceptor Block Copolymers

This part covers the synthesis, characterization and the application of crystalline-crystalline D-A block copolymers comprised of poly(3-hexylthiophene) P3HT and PPerAcr. A variation of the acceptor content is important to investigate its impact on competing aggregation of the

two blocks, as well as the changes in the photovoltaic performance. Since the morphological, optical, and electrical properties of P3HT strongly depend on its molecular weight, it is also necessary to synthesize various macroinitiators with different block lengths and incorporate them into block copolymers with PPerAc. In order to realize this, two controlled polymerization methods are combined efficiently: The Grignard metathese polymerization (GRIM) and NMRP. First, well-defined and narrow-distributed P3HT macroinitiators (PDI $\sim$  1.1) with two different molecular weights of 9 and 17 kg/mol, referred to as P3HT-9 and P3HT-17, respectively, are synthesized by adjusting the monomer to catalyst ratio. A novel one-pot procedure is developed, allowing the active P3HT chain to be endcapped in-situ with the Grignard derivative of a unimolecular alkoxyamine initiator. Starting from these macroinitiators, block copolymers P3HT-*b*-PPerAc with low PDIs (1.2- 1.5) and PPerAc contents between 55- 80 wt.-% are prepared. Figure 7 depicts the schematic block copolymer architecture, the size exclusion chromatography curves, and the synthesis of the block copolymers (Chapter 4).

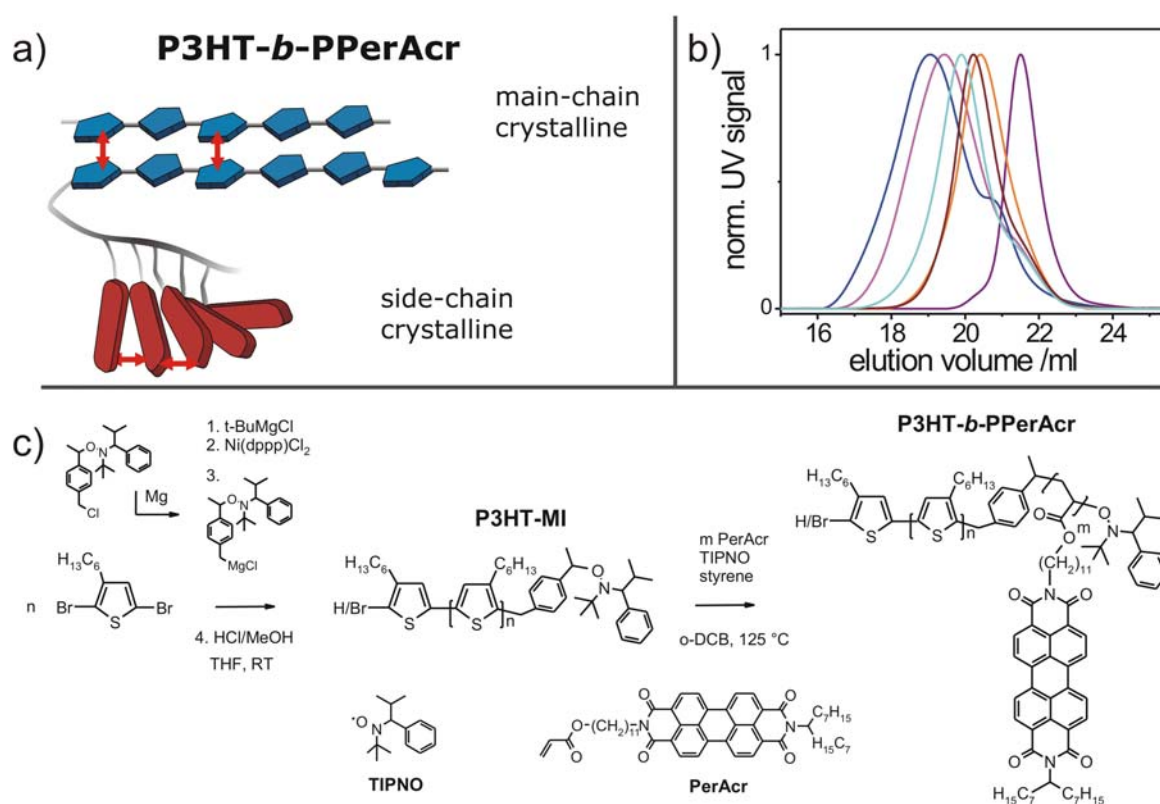


**Figure 7.** a) Schematic architecture of double-crystalline P3HT-*b*-PPerAc block copolymers. b) Size exclusion chromatography (SEC) of macroinitiator P3HT-9 (solid), P3HT<sub>45</sub><sup>9</sup>-*b*-PPerAc<sub>55</sub><sup>16</sup> (dashes), P3HT<sub>41</sub><sup>9</sup>-*b*-PPerAc<sub>59</sub><sup>17</sup> (dashes-dots), P3HT<sub>27</sub><sup>9</sup>-*b*-PPerAc<sub>73</sub><sup>21</sup> (dashes-dots-dots), P3HT<sub>19</sub><sup>9</sup>-*b*-PPerAc<sub>81</sub><sup>25</sup> (short dashes). c) One-pot synthesis of P3HT macroinitiators and P3HT-*b*-PPerAc block copolymers.

In a series containing P3HT-9, the block length of PPerAcr is controlled by varying the monomer to macroinitiator ratio. The SEC curves show a clear shift towards smaller elution volumes (Fig. 7b). Increasing the PPerAcr content in P3HT<sub>x</sub><sup>9</sup>-*b*-PPerAcr<sub>100-x</sub> affects the crystallization behaviour to a large extent. Competing crystallization of PPerAcr and P3HT is investigated using differential scanning calorimetry (DSC), X-ray diffraction (XRD), and UV-vis. The results from DSC show that PPerAcr crystallizes first upon cooling, since the first melting peak and the first recrystallization peak becomes more intense with increasing PPerAcr fraction. Thus, P3HT has to solidify subsequently within the confinement of the already crystallized PPerAcr domains (Fig. 8a). As a result, P3HT crystallinity is reduced with increasing block length of PPerAcr after thermal annealing. Comparing two block copolymers P3HT<sub>45</sub><sup>9</sup>-*b*-PPerAcr<sub>55</sub><sup>16</sup> and P3HT<sub>46</sub><sup>17</sup>-*b*-PPerAcr<sub>54</sub><sup>30</sup> with different block lengths of P3HT but same composition reveals a higher degree of P3HT crystallinity of the latter (Fig. 8b). XRD data of thermally annealed powders are in accordance with this interpretation (Fig. 8c,d). The prominent reflections in the XRD pattern of PPerAcr homopolymer (red) at 2θ= 2.97°, 4.7°, and 25.6° can be assigned to one-dimensional stacks of PPerAcr that are separated by the alkyl chains. The latter reflection at 25.6° depicts the “π-π stacking” of perylene bisimide moieties inside one stack. P3HT-9 (black) shows reflections at 2θ= 5.34° and 23.17°, arising from the well-known P3HT lamellar morphology, and these peaks correspond to the parameters a= 16.54 Å and c= 7.67 Å of an orthorombic lattice. The (020) reflection of P3HT is expected to appear at 2θ= 24.0° but is hardly visible in the thermally annealed sample. The XRD patterns of the block copolymers with the highest P3HT content P3HT<sub>45</sub><sup>9</sup>-*b*-PPerAcr<sub>55</sub><sup>16</sup> (orange) and P3HT<sub>41</sub><sup>9</sup>-*b*-PPerAcr<sub>59</sub><sup>17</sup> (brown) exhibit all homopolymer reflections, whereas in P3HT-*b*-PPerAcr with the lower P3HT weight contents P3HT<sub>27</sub><sup>9</sup>-*b*-PPerAcr<sub>73</sub><sup>21</sup> (cyan) and P3HT<sub>19</sub><sup>9</sup>-*b*-PPerAcr<sub>81</sub><sup>25</sup> (magenta) crystallization of PPerAcr dominates and the P3HT features are almost not visible anymore. The diffraction pattern of P3HT-17 is not shown here since it is similar to P3HT-9. The block copolymer P3HT<sub>46</sub><sup>17</sup>-*b*-PPerAcr<sub>54</sub><sup>30</sup> (blue) containing this higher molecular weight P3HT macroinitiator exhibits a higher P3HT crystallinity compared to P3HT<sub>45</sub><sup>9</sup>-*b*-PPerAcr<sub>55</sub><sup>16</sup> (orange), as deduced from the peak ratios P3HT<sub>100</sub>/PPerAcr<sub>2.97°</sub> and P3HT<sub>002</sub>/PPerAcr<sub>25.6°</sub>, both of which are higher for P3HT<sub>46</sub><sup>17</sup>-*b*-PPerAcr<sub>54</sub><sup>30</sup>. Major changes are observed when treating the powder samples with chloroform vapor (Fig. 8e,f): The π-π stacking of the PPerAcr homopolymer remains at 2θ= 25.6°, but is less

distinctive after chloroform annealing, and instead of the two sharp reflections observed after thermal annealing, a single and broad peak appears at  $2\theta = 3.87^\circ$ . We ascribe this peak to disordered PPerAc stacks with a mean distance of 2.3 nm. The (002) reflection of P3HT-9 is resolved better, and the (020) reflection additionally appears at  $24.0^\circ$ . We therefore conclude that chloroform vapor annealing induces chain mobility in both homopolymers, but only in P3HT-MI 9, a more defined diffraction pattern evolves, whereas less distinctive reflections are observed in PPerAc. The different degrees of order in the two homopolymers PPerAc and P3HT-9 after chloroform vapor annealing have consequences for the morphologies of the block copolymers. In all block copolymers P3HT-*b*-PPerAc, the P3HT (100) and (002) peaks are visible better compared to the thermally annealed samples. In the block copolymers with the higher P3HT contents (orange, brown), the P3HT (100) and (002) peaks are the most intensive ones after solvent annealing, whereas in the block copolymers with the lower P3HT contents (cyan, magenta), these same reflections only then become visible at all. The reflection at  $2\theta = 25.6^\circ$  of PPerAc (red) is broad in the block copolymers with the higher PPerAc contents and hardly visible in the ones with the lower PPerAc contents. Thus, in the block copolymer samples, chloroform vapor annealing induces a rearrangement of P3HT chains, while reducing the order in the PPerAc domains. In the block copolymer with the higher molecular weight of P3HT, P3HT<sub>46</sub><sup>17</sup>-*b*-PPerAc<sub>54</sub><sup>30</sup> (blue), the (100) P3HT-peak is broader and slightly shifted to larger d-spacings. While (100) is at  $2\theta = 5.74^\circ$  in P3HT<sub>45</sub><sup>9</sup>-*b*-PPerAc<sub>55</sub><sup>16</sup> (orange), this peak is seen at  $2\theta = 5.08^\circ$  in P3HT<sub>46</sub><sup>17</sup>-*b*-PPerAc<sub>54</sub><sup>30</sup> (blue). The higher crystallinity of P3HT<sub>46</sub><sup>17</sup>-*b*-PPerAc<sub>54</sub><sup>30</sup> compared to P3HT<sub>45</sub><sup>9</sup>-*b*-PPerAc<sub>55</sub><sup>16</sup> observed in the thermally annealed powders is not observed in the solvent vapor annealed samples.

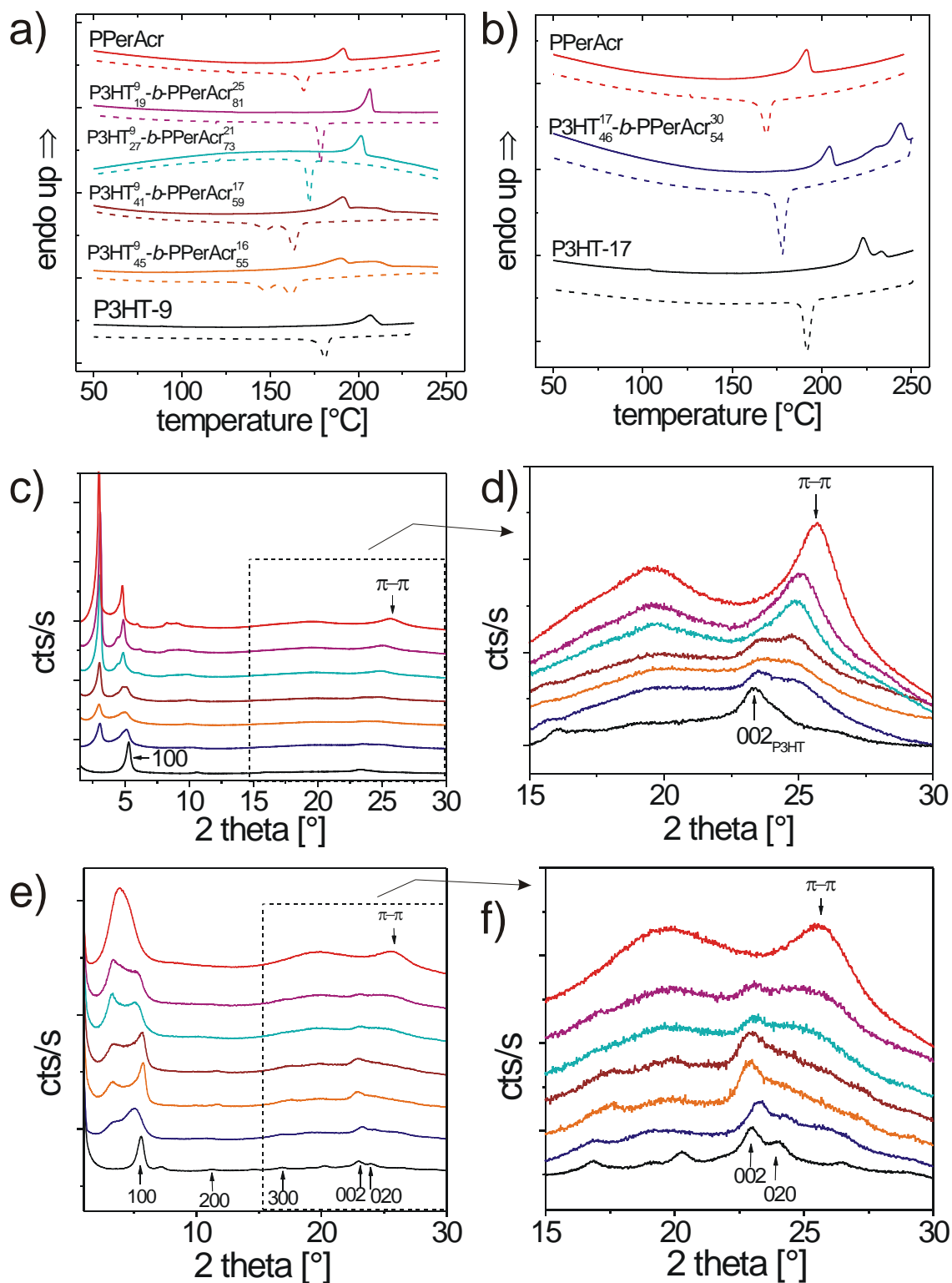


**Figure 8.** Crystallinity of double-crystalline D-A block copolymers P3HT-*b*-PPerAcr. Color code is same in all graphs: P3HT-9 (black), P3HT<sub>45</sub><sup>9</sup>-*b*-PPerAcr<sub>55</sub><sup>16</sup> (orange), P3HT<sub>41</sub><sup>9</sup>-*b*-PPerAcr<sub>59</sub><sup>17</sup> (brown), P3HT<sub>27</sub><sup>9</sup>-*b*-PPerAcr<sub>73</sub><sup>21</sup> (cyan), P3HT<sub>19</sub><sup>9</sup>-*b*-PPerAcr<sub>81</sub><sup>25</sup> (magenta), P3HT<sub>46</sub><sup>17</sup>-*b*-PPerAcr<sub>54</sub><sup>30</sup> (blue), and PPerAcr (red). a) DSC of P3HT<sub>*x*</sub><sup>9</sup>-*b*-PPerAcr<sub>100-*x*</sub>. b) DSC of P3HT<sub>46</sub><sup>17</sup>-*b*-PPerAcr<sub>54</sub><sup>30</sup> (blue), P3HT-17 (black), and PPerAcr (red). c,d,e,f) XRD patterns of powder samples (Guinier) after thermal annealing (c,d), and after chloroform vapor annealing (e,f). Curves are offset in y-direction.

The improved aggregation of P3HT after chloroform vapor annealing is therefore complementary to thermal annealing: Preferential aggregation of PPerAcr is observed after thermal annealing, whereas chloroform vapor annealing gives rise to the rearrangement of P3HT chains (chapter 5).

The application of these unique materials in photovoltaic devices is demonstrated next. In the series of  $\text{P3HT}_x^9\text{-}b\text{-PPerAcr}_{100-x}$ , the device performance decreases with increasing PPerAcr, since the hole carrier mobilities decrease. The best performing block copolymer  $\text{P3HT}_{45}^9\text{-}b\text{-PPerAcr}_{55}^{16}$  (orange) is then selected and compared to  $\text{P3HT}_{46}^{17}\text{-}b\text{-PPerAcr}_{54}^{30}$  (blue) with a similar composition but a different molecular weight. These two block copolymers are additionally characterized by OFET measurements, and the results are compared with the photovoltaic performance (EQE and  $J$ - $V$ -characteristics). Block copolymer  $\text{P3HT}_{46}^{17}\text{-}b\text{-PPerAcr}_{54}^{30}$  (blue) shows enormous improvements in the external quantum efficiency (EQE) and the power conversion efficiency *by factors of 10 and 30*, respectively, compared to the devices made of  $\text{P3HT}_{45}^9\text{-}b\text{-PPerAcr}_{55}^{16}$  (orange). This impressive result is explained by the following: The higher  $M_n$  of P3HT in  $\text{P3HT}_{46}^{17}\text{-}b\text{-PPerAcr}_{54}^{30}$  leads to a higher degree of crystallinity and to larger crystals, as revealed by the higher melting enthalpy and the higher melting point, respectively (Fig. 9a). As a result, the hole carrier transport is improved by more than *two orders of magnitude*, and hole mobilities of  $3 \cdot 10^{-5}$  and  $5 \cdot 10^{-3}$   $\text{cm}^2/\text{Vs}$  are obtained for  $\text{P3HT}_{45}^9\text{-}b\text{-PPerAcr}_{55}^{16}$  (orange) and  $\text{P3HT}_{46}^{17}\text{-}b\text{-PPerAcr}_{54}^{30}$  (blue), respectively (Fig. 9b). This again influences the photovoltaic performance to a large extent: The external quantum efficiency increases from 3 to 31 % (Fig. 9c), and the power conversion efficiency from 0.007 to 0.2 % (Fig. 9d). This is a real breakthrough in this field, since the highest EQE values of devices with active layers of P3HT and low molecular weight perylene bisimides were only around  $\sim 20$  % after extensive optimization. Thus, we show for the first time that donor acceptor morphologies with conjugated blocks can have advantages over their simple blend systems in terms of morphology control and device performance (chapter 6).

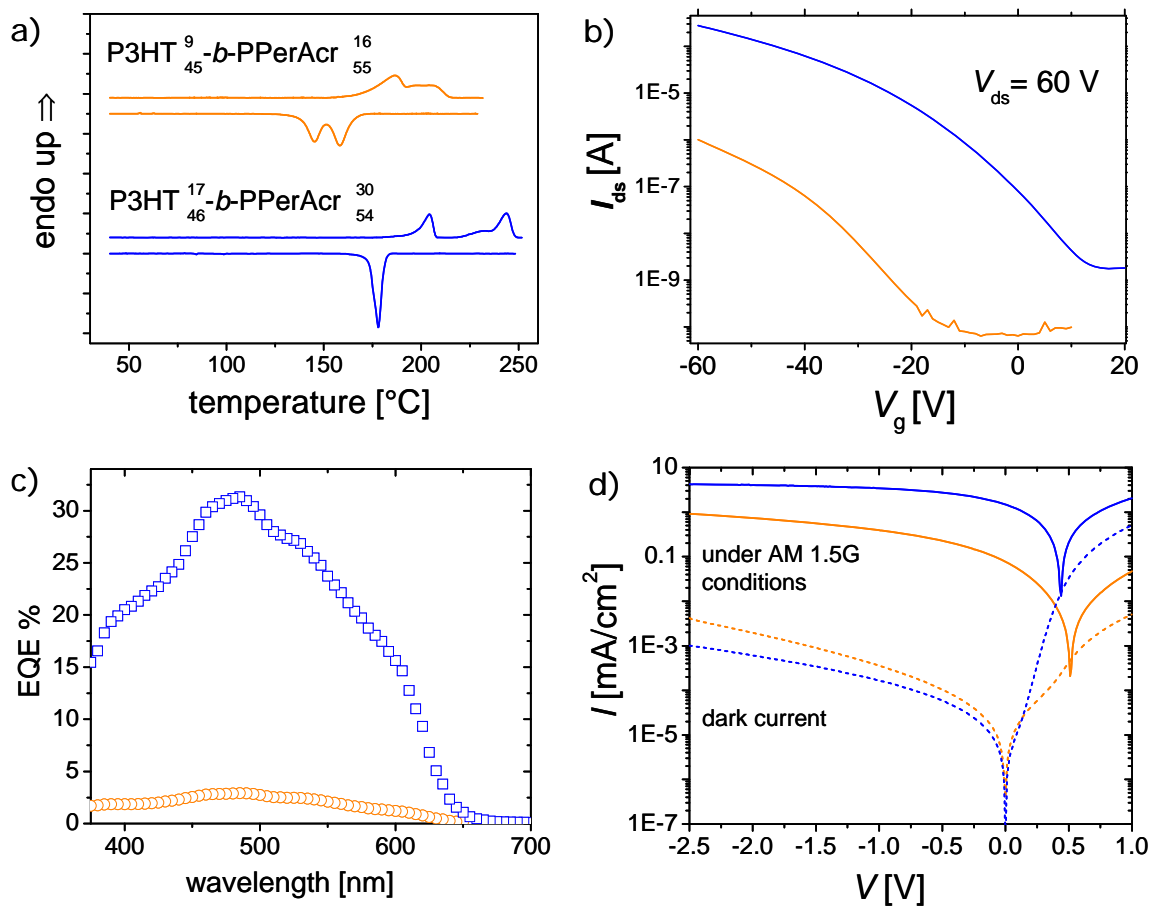


**Figure 9.** Crystallinity, charge carrier mobilities (OFET), and photovoltaic performance of double-crystalline D-A block copolymers P3HT-b-PPerAc. Color code is same in all graphs: P3HT<sub>45</sub><sup>9</sup>-b-PPerAc<sub>55</sub><sup>16</sup> is orange and P3HT<sub>46</sub><sup>17</sup>-b-PPerAc<sub>54</sub><sup>30</sup> is blue. a) Differential scanning calorimetry. The first  $T_m$ s is due to PPerAc melting in both curves. PPerAc recrystallizes first in P3HT<sub>45</sub><sup>9</sup>-b-PPerAc<sub>55</sub><sup>16</sup>. b) Transfer plots of OFET devices, showing p-type behaviour. The hole carrier mobility in P3HT<sub>46</sub><sup>17</sup>-b-PPerAc<sub>54</sub><sup>30</sup> is two orders of magnitude higher than in P3HT<sub>45</sub><sup>9</sup>-b-PPerAc<sub>55</sub><sup>16</sup>. c) External quantum efficiency (EQE). An improvement of one order of magnitude is achieved by employing the block copolymer with the higher P3HT molecular weight. d) J-V-characteristics in the dark (dotted lines) and under one sun illumination.

## Electron Conducting Block Copolymers

Here, the complexity of the donor acceptor architecture is reduced to one electronic function by replacing the donor block with an insulating polystyrene. These materials are useful for fundamental studies such as investigation of electron transport in confined geometries, or for elucidating the interplay of  $\pi$ - $\pi$  stacking and microphase separation. Tailor-made electron conducting block copolymers PS-*b*-PPerAcr are synthesized by NMRP, starting from three polystyrene macroinitiators with molecular weights of 10, 20 and 30 kg/mol and low PDIs of 1.1. The weight fraction of PPerAcr is roughly kept constant between 65- 70 wt.-%. The morphology of thermally annealed bulk samples is characterized by TEM and small angle X-ray scattering (SAXS), revealing cylindrical and lamellar morphologies with domain sizes of 8 to 15 nm. SEM of thermally annealed thin films suggests parallel alignment of the domains to the substrate, since lamellar and cylindrical bulk morphologies yield unstructured and striped pattern in thin films (figure 10). The block copolymer with the highest  $M_n$  (PS) of 30 kg/mol shows coexisting lamellae together with a fiber-like morphology in TEM (Fig. 10h), and the shoulder of the first peak of the SAXS pattern (Fig. 10i) most probably is due to the larger distance between these individual fibers. Accordingly, the SEM pattern of this block copolymer exhibits flat and structured regions, due to flat-lying lamellae and fibers (Fig. 10g). The non-uniform morphology of PS<sub>35</sub><sup>31</sup>-*b*-PPerAcr<sub>65</sub><sup>24</sup> can be due to the bimodal nature of the SEC curve, indicating a non-negligible amount of PPerAcr homopolymer. Nevertheless, all three methods are perfectly consistent (Chapter 7).

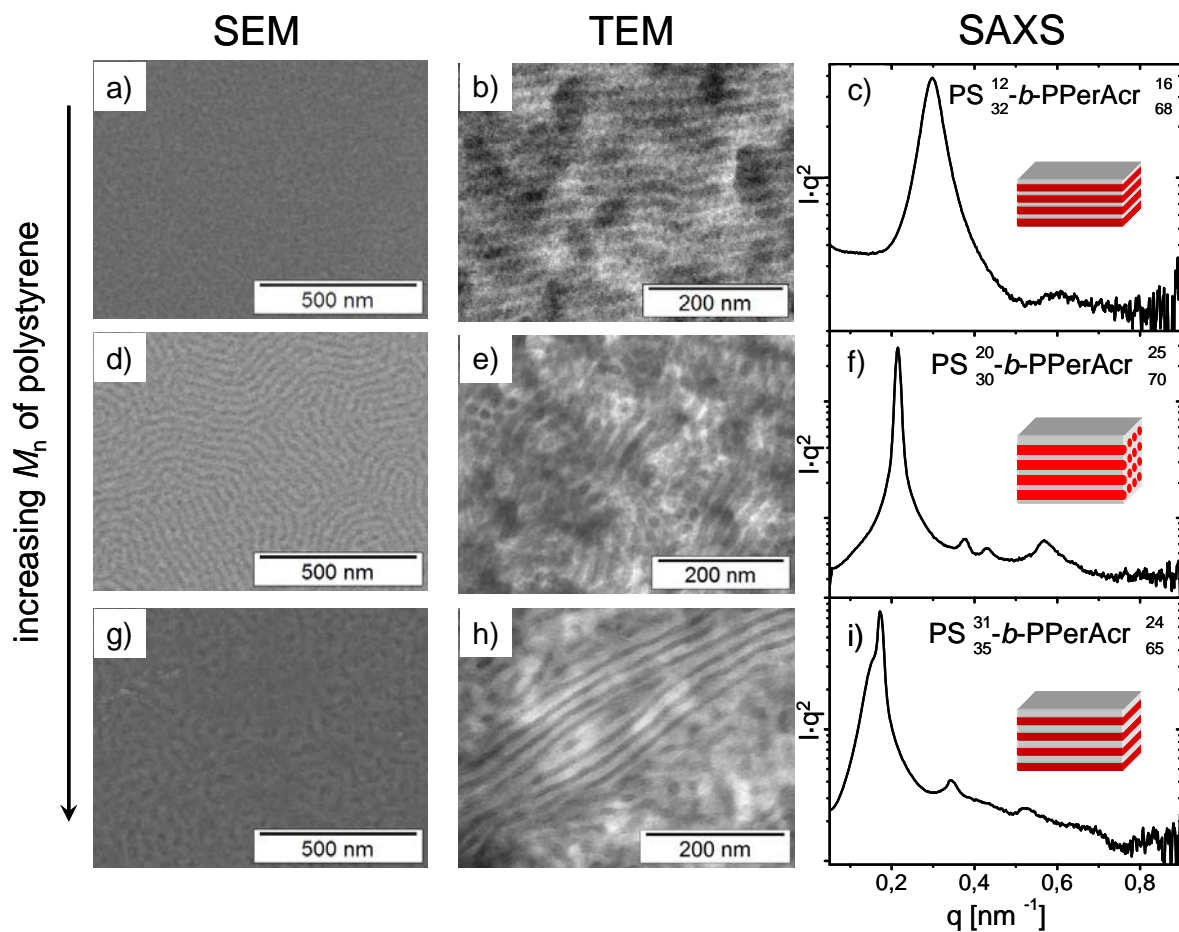


**Figure 10.** Morphology of PS-*b*-PPerAc after thermal annealing above the melting temperature of PPerAc. a)-c) PS<sub>32</sub><sup>12</sup>-*b*-PPerAc<sub>68</sub><sup>16</sup>, d)-f) PS<sub>30</sub><sup>20</sup>-*b*-PPerAc<sub>70</sub><sup>25</sup> and g)-i) PS<sub>35</sub><sup>31</sup>-*b*-PPerAc<sub>65</sub><sup>24</sup>. Pictures a), d) and g) are top-view SEM images of thin films (100 nm) and b), e) and h) are TEM images of volume samples after staining with RuO<sub>4</sub>. The SAXS patterns c), f) and i) confirm these morphologies.

In order to elucidate the geometric confinement on the charge transport properties of perylene bisimide, all block copolymers are additionally characterized in OFET devices. As a reference, the PPerAc homopolymer is measured as well. PPerAc exhibits an outstanding performance, with a very high electron mobility of  $1 \cdot 10^{-3} \text{ cm}^2/\text{Vs}$ , a low threshold voltage of 6.8 V and an on/off ratio of  $10^4$ . Strikingly, the cylindrical block copolymer exhibits the same electron carrier mobility after the thermal annealing step and even outperforms the homopolymer in terms of the threshold voltage. A fast onset of the linear regime indicates low contact resistance to the gold electrodes. The almost similar performance of PS<sub>30</sub><sup>20</sup>-*b*-PPerAc<sub>70</sub><sup>25</sup> indicates the formation of a monolayer at the device-polymer interface. Thus, we demonstrate for the first time that dilution with amorphous segments does not lead to a

decrease of the electron mobility and the high performance of the PPerAcr in an OFET device is therefore maintained (Chapters 7 and 8). These outstanding results, together with the unique possibility to confine the perylene bisimide moieties in cylindrical or lamellar domains renders PS-*b*-PPerAcr highly interesting for further investigations on their photophysical and electrical properties.

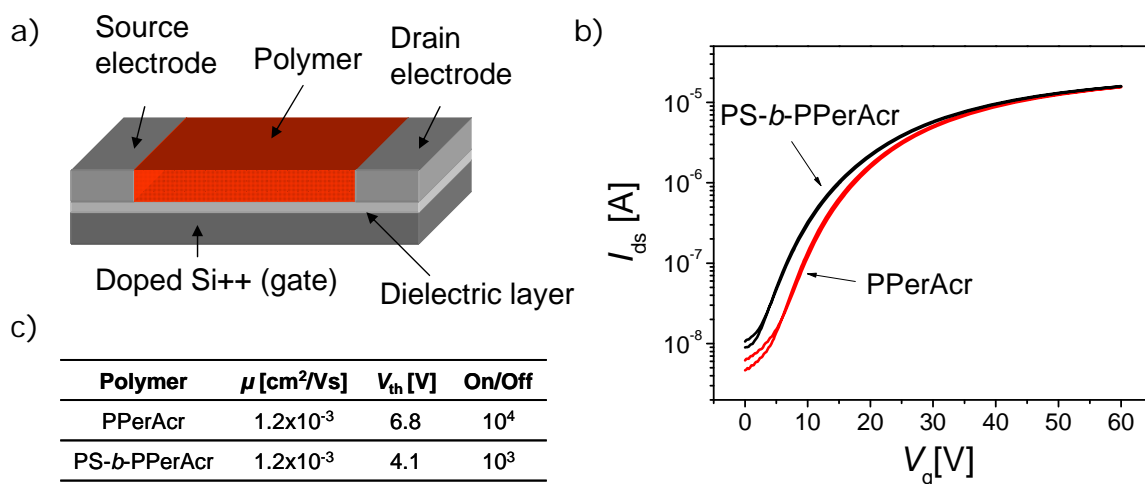


**Figure 11.** a) Schematic bottom gate bottom contact OFET device architecture, using b) Transfer plots of the homopolymer PPerAcr and PS<sub>30</sub><sup>20</sup>-*b*-PPerAcr<sub>70</sub><sup>25</sup> after thermal annealing for a drain voltage of 20 V, a channel length of 10  $\mu$ m, and a channel width of 10 mm. Au was used as bottom contact and hexamethyldisilazane (HMDS) for hydrophobization of the substrate. c) Standard OFET parameters of PPerAcr and PS<sub>30</sub><sup>20</sup>-*b*-PPerAcr<sub>70</sub><sup>25</sup>.

## Structural Evolution of Vertically Segregated Films with Progressive Etching Depth by Combining Focused Ion Beam with Scanning Electron Microscopy

We present a general method for monitoring the morphology of vertically and laterally phase separated polymer blends with increasing depth of the film. The in-situ combination of focused ion beam (FIB) and scanning electron microscopy (SEM) enables to image the morphological changes of films of a donor acceptor polymer blend and a block copolymer with progressive etching depth. The polymer blend consists of PvDMTPA and PPerAcr and undergoes a vertical and lateral phase separation due to the differences in solubility and preferential substrate interaction: In chloroform, from which the films are produced, the solubility of the amorphous PvDMTPA is higher and it also exhibits a preferential interaction

with the substrate (ITO). This leads to an enrichment and to large and rounded domains of PPerAcr at the polymer-air interface. With increasing depth, these domains become smaller (figure 12). However, we also elucidate the extent of artefact formation when the area imaged is perpendicular to the incident FIB beam. A block copolymer film of PvTTPA-*b*-PPerAcr is employed, exhibiting a wetting layer of PPerAcr at the polymer-air interface after drop casting. Removal of this monolayer via FIB reveals a morphology that is accompanied by artefacts due to local heating and melting of the film (chapter 9).

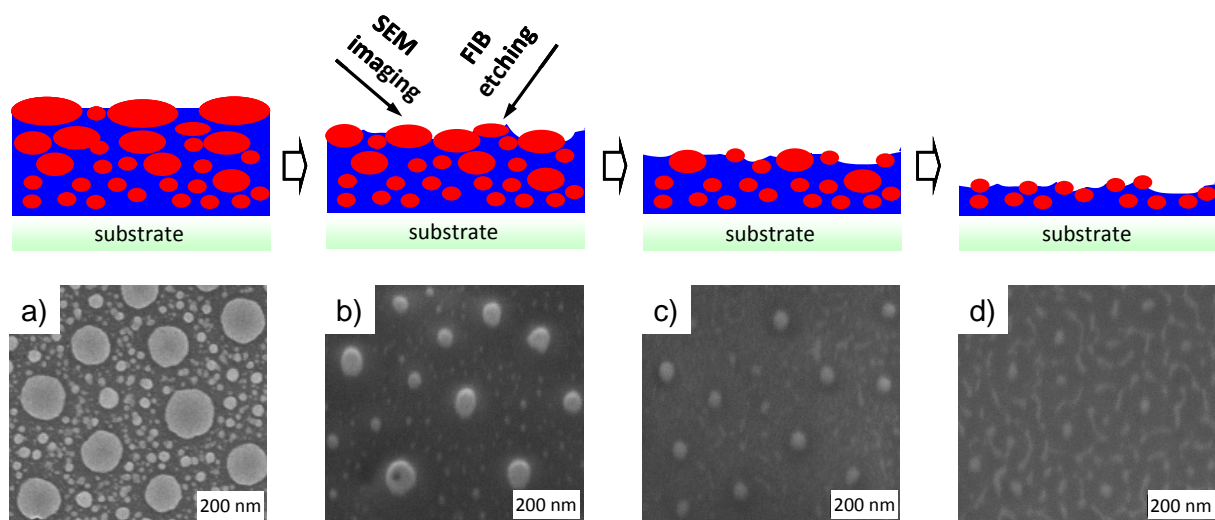


**Figure 12.** Schematic cross sections (upper row) and scanning electron micrographs (lower row) of a polymer blend PvDMTPA:PPerAcr after spin casting from chloroform and focus ion beam (FIB) etching for different times. The films were stained with  $\text{RuO}_4$  for 10 min, bright depicts PPerAcr, and dark PvDMTPA. The domain sizes of the PPerAcr droplets change with progressive etching depth. Etching times are a) 0 s, b) 30 s, c) 60 s, and d) 90 s (milling current is 100 pA). Scale bar is 200 nm in all pictures.

## Individual contributions to joint publications

In the following, the contributions of the individual authors to the papers are specified.

### Chapter 3

This work is published in *Macromolecules* (2008, 41, 6081) under the title:

“Semiconductor Block Copolymer Nanocomposites with Lamellar Morphology via Self-Organization”

by Sebastien Maria, Andrei S. Susha, **Michael Sommer**, Dimitry. V. Talapin, Andrey L. Rogach, and Mukundan Thelakkat.

I synthesized the macroinitiators PvDMTPD, was involved in the scientific discussion of the project and corrected the manuscript.

Sebastien Maria synthesized the block copolymers, fabricated the composites and TEM cross sections and wrote a first draft of the manuscript.

Andrei S. Susha synthesized the nanoparticles.

Dimitry V. Talapin and Andrey L. Rogach were involved in the scientific discussion of the project.

Mukundan Thelakkat supervised the project and corrected the manuscript.

### Chapter 4

This work is published in *Angewandte Chemie International Edition* (2008, 47, 7901) under the title:

“Crystalline-Crystalline Donor Acceptor Block Copolymers”

by **Michael Sommer**, Andreas Lang, and Mukundan Thelakkat.

I synthesized and characterized all block copolymers, performed scanning electron microscopy and wrote the manuscript.

Andreas Lang synthesized the monomer PerAcr.

Mukundan Thelakkat supervised the project and corrected the manuscript.

## Chapter 5

This work is submitted as a *Feature Article* to the *Journal of Materials Chemistry* with the title:

“Semiconductor Block Copolymers for Photovoltaic Applications”

by **Michael Sommer**, Sven Hüttner, and Mukundan Thelakkat.

Some results from chapters 4, 6, 10 and 11 also appear here for a comprehensive outline of the topic. However, this *Feature Article* additionally contains key results of utmost importance that do not appear in any other publication. Furthermore, individual aspects are connected here and presented in a clear and comprehensive fashion. Therefore, this piece of work is presented as a full chapter.

I synthesized and characterized all block copolymers, fabricated solar cells and wrote the publication.

Sven Hüttner fabricated organic field effect transistors and solar cells, was involved in the scientific discussion and corrected the manuscript.

Mukundan Thelakkat supervised the project and corrected the manuscript.

## Chapter 6

This work is published in *Applied Physics Letters* (in print) under the title:

“Influence of the molecular weight of double-crystalline block copolymers on the performance of polymer solar cells”

by **Michael Sommer**, Sven Hüttner, Ullrich Steiner, and Mukundan Thelakkat.

I synthesized and characterized all block copolymers, fabricated solar cell devices and wrote the publication.

Sven Hüttner characterized the materials in organic field effect transistors and additional solar cells, was involved in the scientific discussion and corrected the manuscript.

Ullrich Steiner was involved in the scientific discussion and corrected the manuscript.

Mukundan Thelakkat supervised the project and corrected the manuscript.

## Chapter 7

This work is published in *Advanced Materials* (2008, 20, 2523) under the title:

“Novel Electron Conducting Block Copolymers: Morphological, Optical and Electronic Properties”

by **Michael Sommer**, Sven Hüttner, Stefanie Wunder, and Mukundan Thelakkat.

I synthesized and characterized all block copolymers with the help of Stefanie Wunder who did her advanced lab course on the topic. The publication was written by me.

Sven Hüttner characterized the materials in organic field effect transistors, was involved in the scientific discussion and corrected the manuscript.

Mukundan Thelakkat supervised the project and corrected the manuscript.

## Chapter 8

This work is published in *Applied Physics Letters* (2008, 92, 093302) under the title:

“n-Type Organic Field Effect Transistors from Perylene Bisimide Block Copolymers and Homopolymers”

by Sven Hüttner, **Michael Sommer**, and Mukundan Thelakkat.

I synthesized and characterized all homopolymers and block copolymers, performed scanning electron microscopy and was involved in the scientific discussion and correction of the manuscript.

Sven Hüttner fabricated the organic field effect transistors and wrote the publication.

Mukundan Thelakkat supervised the project and corrected the manuscript.

## Chapter 9

This work is provisionally accepted in *Applied Materials and Interfaces* under the title:

“In Situ Imaging of Evolution of Morphology of Semiconductor Polymer Blends and Block Copolymers Using Focused Ion Beam and Scanning Electron Microscopy”

by **Michael Sommer** and Mukundan Thelakkat.

I synthesized and characterized all homopolymers and block copolymers, performed scanning electron microscopy/focused ion beam with the help of Werner Reichstein and wrote the publication.

Mukundan Thelakkat supervised the project and corrected the manuscript.

## Chapter 10: Appendix

This work appears as appendix since the two block copolymers PvDMTPA-*b*-PPerAcr were synthesized and characterized during my diploma thesis. The synthesis of all other block copolymers and the preparation of the manuscript was done afterwards during the PhD thesis. This work is published in *The European Physical Journal: Applied Physics* (2006, 36, 245) under the title:

“Synthesis, Characterization and Application of Donor Acceptor Block Copolymers in Nanostructured Bulk Heterojunction Solar Cells”

by **Michael Sommer** and Mukundan Thelakkat.

I synthesized and characterized all block copolymers, fabricated the devices and wrote the manuscript.

Mukundan Thelakkat supervised the project and corrected the manuscript.

## Chapter 11: Appendix

This work appears as appendix since two block copolymers PvDMTPA-*b*-PPerAcr were synthesized and characterized during my diploma thesis. All other experiments and the preparation of the manuscript was done afterwards during my PhD thesis. This work is published in *Advanced Functional Materials* (2007, 17, 1493) under the title:

“Microphase-Separated Donor Acceptor Diblock Copolymers: Influence of HOMO Energy Levels and Morphology on Polymer Solar Cells”

by **Michael Sommer**, Stefan M. Lindner, and Mukundan Thelakkat.

I synthesized and characterized all block copolymers, fabricated the devices and wrote the manuscript except:

Stefan M. Lindner synthesized one block copolymer PvTPA-*b*-PPerAcr.

Mukundan Thelakkat supervised the project and corrected the manuscript.

### 3. Morphology Control in Polymer Nanocomposites using Self-Organizing Semiconductor Block Copolymers

Sébastien Maria,<sup>a</sup> Andrei S. Susha,<sup>b</sup> Michael Sommer,<sup>a</sup> Dmitri V. Talapin,<sup>c</sup> Andrey L. Rogach,<sup>b</sup> and Mukundan Thelakkat<sup>a</sup>

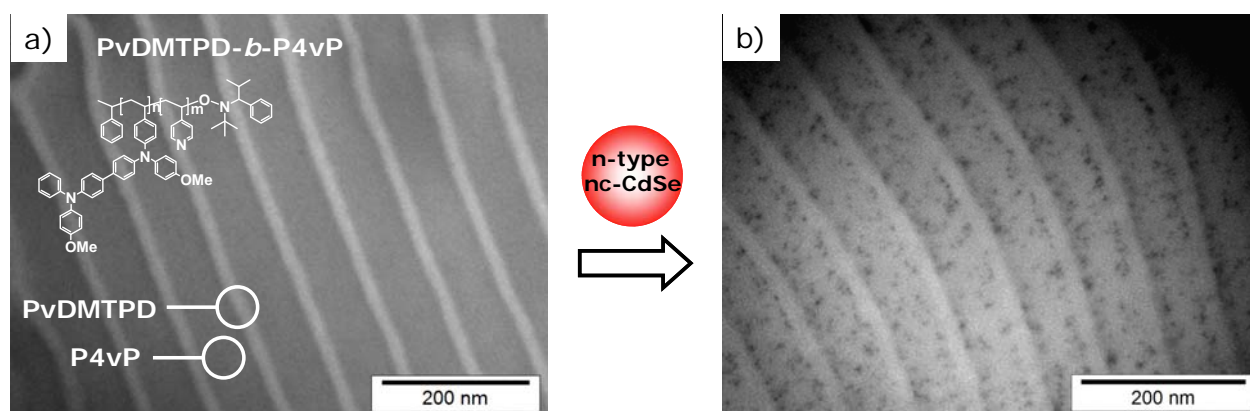
<sup>a</sup> Applied Functional Polymers and Macromolecular Chemistry I

Universität Bayreuth, Universitätsstr. 30, University of Bayreuth, 95444 Bayreuth, Germany

<sup>b</sup> Photonics and Optoelectronics Group, Physics Department and Center for Nanoscience  
Ludwig-Maximilians Universität München, Amalienstr. 54, 80799 München, Germany

<sup>c</sup> Department of Chemistry, The University of Chicago, Chicago, Illinois 60637

[Michael.Sommer@uni-bayreuth.de](mailto:Michael.Sommer@uni-bayreuth.de), [Mukundan.Thelakkat@uni-bayreuth.de](mailto:Mukundan.Thelakkat@uni-bayreuth.de)



Published in *Macromolecules* **2008**, *41*, 6081.

**Abstract**

Novel semiconductor block copolymers were synthesized using nitroxide-mediated radical polymerization (NMRP). They are comprised of a hole conductor block carrying tetraphenylbenzidine pendant units (PvDMTPD) and a second poly(4-vinylpyridine) (P4vP) block suitable for the preferential incorporation of n-type semiconductor nanocrystals. The conditions of NMRP for both monomers were optimized in order to get macroinitiators with well-defined molecular weights and very low polydispersities (<1.2). The resulting block polymers exhibit a lamellar morphology due to microphase separation. Furthermore, semiconductor nanocomposites were prepared by using these diblock copolymers and light harvesting CdSe:Te nanocrystals, and their bulk morphologies were characterized by TEM. This new hybrid nanocomposite material maintains the original lamellar structure in which the hole conductor domains are separated from electron conducting/light harvesting nanocrystals that are confined in the P4vP domains. Thus, the challenging task of applying the block copolymer strategy to obtain fully functionalized semiconductor hybrid nanocomposites with morphological control and stability has been realized.

## Introduction

Polymer nanocomposites are one of the innovative approaches in material science to tune material properties suitable for novel applications.<sup>[1,2]</sup> A common strategy is to blend nanoobjects such as nanodots, nanorods etc. in a polymer matrix to obtain the required mechanical, optical, electrical or magnetic properties in thin films.<sup>[3,4]</sup> For example, solar cells with good efficiency were obtained by spin-casting a hybrid blend of light-harvesting nanocrystals (CdSe) with poly(3-hexylthiophene).<sup>[5]</sup>

The use of block copolymers instead of homopolymers as the matrix has been reported recently, allowing a better control of the spatial distribution of the nanoparticles. This is achieved by exploiting the order-disorder phase transition of block copolymers, which leads to well-defined morphologies at the nanometer scale.<sup>[6-11]</sup> One of the major issues in developing nanoparticles/polymer composites is to stabilize the hybrid blend against macrophase separation or agglomeration of the nanoparticles which negates any benefits associated with the nanoscopic dimension. Usually the nanoparticles agglomerate over long term and therefore, they have to be surface-modified with electronically inactive (isolating) tensides. It would be elegant if the nanocrystals could be directly incorporated into a stabilizing block copolymer segment and thus preferentially be confined in that domain. This would result in self-organizing nanocomposites with well-defined morphologies at the nanoscopic scale.<sup>[12-14]</sup> This material could lead to novel concepts in the fields of spintronics<sup>[15]</sup> or photovoltaics. However, the concept is challenging and requires tailor-made functional block copolymers with different relevant functionalities for charge transport and charge separation, and additional segments which stabilize the nanoparticles. Previously, we reported microphase-separated donor-acceptor block copolymers with poly(perylene bisimide acrylate) (PPerAcr) as electron conducting block and several poly(vinyltriarylamine) derivatives as hole conducting segment. The morphologies of these block copolymers play a crucial role in improving the performance of solar cells compared to a blend of the respective homopolymers.<sup>[16-18]</sup>

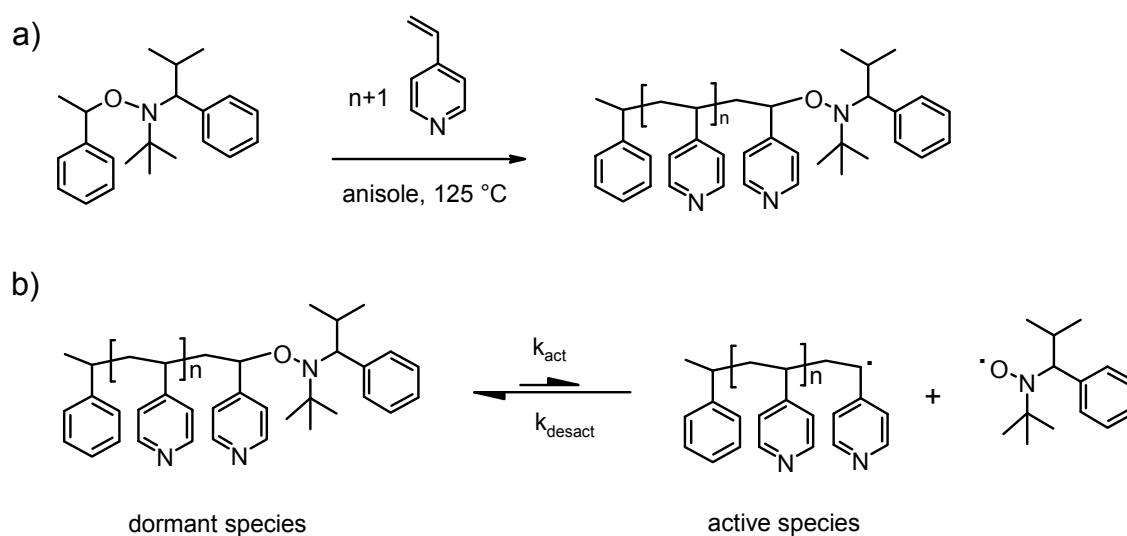
In this paper, we report the synthesis and characterization of functional diblock copolymers, PvdMTPD-*b*-P4vP with poly(N,N'-bis(4-methoxyphenyl)-N,N'-diphenyl-(1,1'-biphenyl)-4,4'-diamine) (PvdMTPD) as the first block and poly(4-vinylpyridine) (P4vP) as the second block. In such a system, the P4vP can stabilize electron conducting/light-harvesting nanoparticles

whereas the PvDMTPD acts as a hole transporting block. After incorporating inorganic semiconductor quantum dots, this hybrid system can lead to nanostructured bulk heterojunctions suitable for solar cell applications. To accomplish this task, we prepared a series of PvDMTPD-*b*-P4vP, by Nitroxide-Mediated Radical Polymerization (NMRP). First, the conditions of the polymerization of 4-vinylpyridine were optimized to get P4vP macroinitiators with well-defined molecular weights and very low polydispersity (< 1.2). The order of polymerization of 4vP and vDMTPD is elucidated and then different block copolymers are prepared. The morphology of these novel materials was studied in the bulk using transmission electron microscopy (TEM). Polymer nanocomposites with these block copolymers and light-harvesting CdSe:Te nanocrystals were prepared and the first results of self-organizing hybrid nanostructures are presented.

## Results and Discussion

**NMRP of 4-vinyl pyridine (1).** Up to now, the controlled/living polymerization of 4vP has been carried out successfully by anionic polymerization.<sup>[19]</sup> In case of Atom Transfer Radical Polymerization (ATRP), the polymerization of 4vP is quite tedious due to the possible coordination of the monomer to the catalyst.<sup>[20]</sup> In contrast, Reversible Addition-Fragmentation Chain Transfer (RAFT)<sup>[21]</sup> and NMRP do not require transition metal complexes and therefore are suitable for the polymerization of 4vP. Relatively few reports deal with the NMRP of 4vP, using 2,2,6,6-tetramethyl-1-piperidine-*N*-oxyl (TEMPO).<sup>[22-24]</sup> To the best of our knowledge, only one report used an alkoxyamine generating the nitroxide (2,2,5-trimethyl-4-phenyl-3-azahexane-3-oxyl) TIPNO.<sup>[25]</sup>

First, we studied the polymerization of 4VP by NMRP in bulk and in solution. This is required to obtain macroinitiators with defined length and narrow polydispersity that are suitable for the synthesis of defined block copolymers using functional monomers such as vinyl-*N,N'*-bis(4-methoxyphenyl)-*N,N'*-diphenyl-(1,1'-biphenyl)-4,4'-diamine (VDMTPD). The scheme of synthesis of P4VP and the mechanism of NMRP are shown in Scheme 1.



**Scheme 1.** a) Scheme of synthesis of P4VP using NMRP. b) Mechanism showing the NMRP equilibrium of poly(4-vinylpyridine) chain growth.

The bulk polymerization of 4VP was carried out at 125 °C with a  $[\text{monomer}]_0:[\text{initiator}]_0:[\text{TIPNO}]_0$  molar ratio of 318:1:0.07. The initial addition of TIPNO allows shifting the equilibrium, as shown in Scheme 1b, to the side of the dormant species and reduces the instantaneous concentration of growing radicals due to the persistent radical effect. The polymerization proceeded relatively fast (42% conversion after 1 h), and the first-order monomer consumption rate was investigated by plotting  $\ln([M]_0/[M])$  vs time (Figure 1a). The plot does not reveal a straight line, but is slightly curved, indicating that the concentration of active radicals is not constant throughout the polymerization as expected for a controlled process. Hence, the polymerization does not take place under steady-state conditions; e.g. termination occurs continuously, resulting in a decrease of the transient radical concentration and an increase of the free nitroxide concentration. Nevertheless, this does not significantly affect the control of the polymerization. The molecular weights were measured by size exclusion chromatography (SEC) and are in good agreement with the theoretical values calculated on the basis of the monomer-to-initiator ratio (see Figure 1b). Moreover, the polydispersity indices (PDI) are quite small ( $\sim 1.2$ ). This might be a consequence of the fast rate of polymerization compared to the rate of bimolecular termination. Table 1 summarizes the data of samples under different conditions of polymerization; in each case two samples at two different conversions are given for each batch of polymerization. The data of the two samples that were drawn during bulk polymerization at two different conversions, **1a** and **1b**, are given in Table 1.

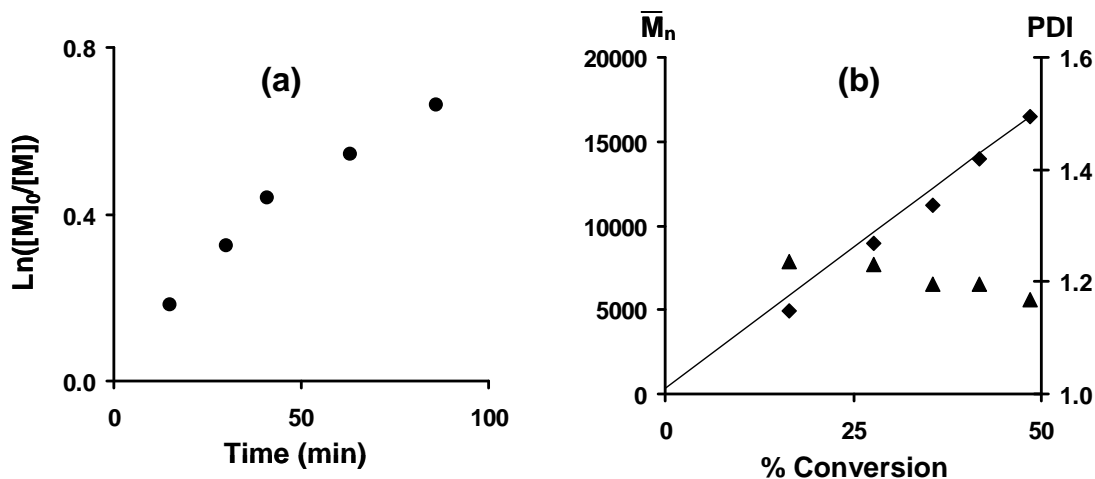


**Figure 1.** Kinetics and control of 4vP polymerization in bulk at 125 °C. a) pseudo-first order kinetics b)  $M_n$  (diamonds) and PDI (triangles) as a function of conversion. The straight line corresponds to the theoretical  $M_n$  values.  $[4vP]:[Initiator]:[TIPNO]$  is equal to = 318:1:0.07.

One way to limit the bimolecular termination and to improve the control of the polymerization is to increase the initial ratio of  $[TIPNO]_0:[Initiator]_0$ . Therefore two additional polymerizations were conducted with  $[Monomer]_0:[Initiator]_0:[TIPNO]_0$  ratios equal to 321:1:0.12 and 294:1:0.19. Thus, compared to the above bulk polymerization with  $[Initiator]_0:[TIPNO]_0 = 1:0.07$ , the relative amount of initial free nitroxide was augmented to 1:0.12 and 1:0.19. Additionally the polymerization media were slightly diluted with anisole at a monomer:anisole volume ratio of 5:1. The first pronounced effect to be observed is related to the kinetics. Now, the plots of  $\ln([M]_0/[M])$  versus time show a perfect linear behaviour in both cases (see Figure 2). Consequently, the rate of the monomer consumption is first-order and the concentration of the active radical can be considered constant throughout the polymerization.

Another interesting point is to check the equation of the linear regression of the plots. The difference between the values of the slope is quite small. For the different polymerizations with  $[Initiator]_0:[TIPNO]_0 = 1:0.12$  and  $1:0.19$ , the apparent rate constant of polymerization  $k_{app}$  is equal to  $10.4 \times 10^{-3}$  and  $9.47 \times 10^{-3} \text{ min}^{-1}$  respectively. Thus, for the polymerization with the highest concentration of free TIPNO,  $k_{app}$  is slightly smaller, as expected. The small difference can be attributed to growing radicals that are provided by autoinitiation, maintaining a reasonable rate of polymerization and counterbalancing irreversible termination. Also, the regression lines should theoretically intersect the origin, which is the

case for  $[\text{Initiator}]_0:[\text{TIPNO}]_0 = 1:0.19$ . This indicates the positive effect of the initial addition of TIPNO. Indeed with increasing amount of TIPNO, the control equilibrium is shifted towards the dormant species (see Scheme 1), avoiding an accumulation of the radicals. Therefore, the bimolecular termination reactions are limited in the first stage of the polymerization. This analysis is confirmed by the comparison of PDIs. For both experiments, low PDIs were obtained (Figure 3) and the initial PDI values for low conversion depends on the amount of free nitroxide. For the lower amount of TIPNO, the broadening of the molecular weights is higher, with a PDI of 1.28 at 13.7% conversion (Figure 3a). On comparison, for the polymerization with  $[\text{Initiator}]_0:[\text{TIPNO}]_0$  ratio of 1:0.19, the PDI is 1.16 at 8.6% conversion (Figure 3b). This comparison supports the beneficial effect of the higher concentration of nitroxide on the initial stage of the process. For both experiments, the molecular weights grow linearly with the conversion and fit with the prediction. It should be noted that the molecular weights were measured by SEC calibrated with polystyrene standards, so they probably deviate from the real values. For comparison, data concerning the samples **1c** and **1d** obtained at different conversions with  $[\text{Initiator}]_0:[\text{TIPNO}]_0$  ratio of 1:0.12 as well as **1e** and **1f** obtained for  $[\text{Initiator}]_0:[\text{TIPNO}]_0$  ratio of 1:0.19 are shown in Table 1.

**Table 1.** Experimental conditions, molecular weights, polydispersity indices and thermal properties of macroinitiators **1a-g**, **2a-d**. MI: macroinitiator, M: monomer, I: initiator, and N: nitroxide. Solvent: anisole.

MI	entry	$[\text{M}]_0$ wt%	conversion (%)	$[\text{M}]_0:[\text{I}]_0:[\text{N}]_0$ ratio	$M_n$ [kg/mol]	$M_w$ [kg/mol]	PDI
P4vP	<b>1a</b>	bulk	16.6	318:1:0.07	4.9	6.1	1.24
	<b>1b</b>	bulk	41.9	318:1:0.07	14.0	16.7	1.20
	<b>1c</b>	82.4	13.7	320:1:0.12	4.7	6.1	1.28
	<b>1d</b>	82.4	38.7	320:1:0.12	13.6	15.6	1.15
	<b>1e</b>	82.4	8.6	294:1:0.19	3.4	3.9	1.16
	<b>1f</b>	82.4	44.4	294:1:0.19	14.0	16.0	1.14
	<b>1g</b>	82.4	-	295:1:0.2	14.9	16.8	1.13
PvDMTPD	<b>2a</b>	43.7	47.5	74:1:0.9	10.6	12.1	1.14
	<b>2b</b>	43.7	77.3	74:1:0.9	12.5	15.5	1.24
	<b>2c</b>	78.1	-	200:1:0.2	13.3	23.1	1.23
	<b>2d</b>	24.9	-	120:1:0.1	20.8	23.9	1.15

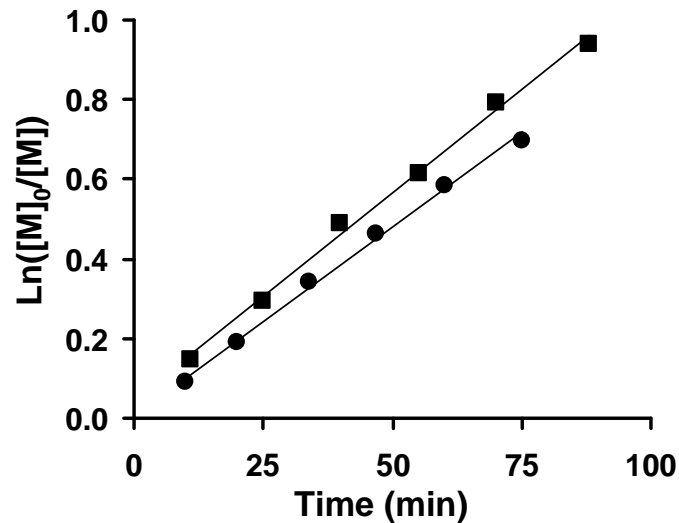


**Figure 2.** Influence of the concentration of free nitroxide on the first-order kinetics of the polymerization of P4VP in anisole (5:1, v:v) at 125 °C: [4VP]:[initiator]:[TIPNO] is equal to 321:1:0.12 (diamonds) and 294:1:0.19 (circles).

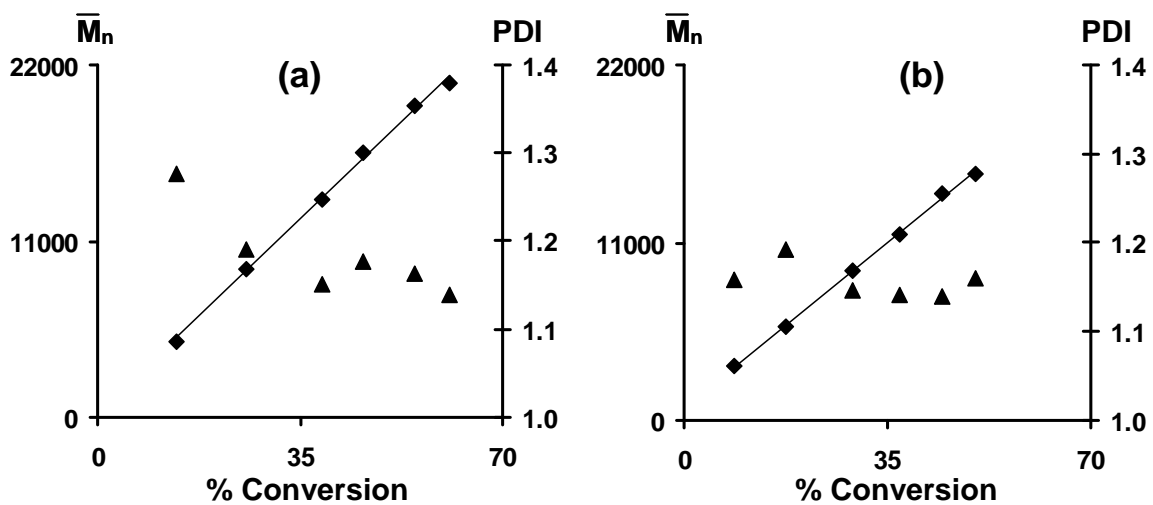


**Figure 3.** Influence of free nitroxide concentration on control of 4vP polymerization in anisole (16.7% v/v) at 125°C:  $M_n$  (diamonds) and PDI (triangles) as a function of conversion. 4vP:Initiator:TIPNO = 321:1:0.12 (a) and 294:1:0.19 (b). The straight line corresponds to the theoretical  $M_n$  values.

**NMRP of vDMTPD (2).** The nitroxide-mediated radical polymerization of vDMTPD with low polydispersity (PDI  $\sim$  1.15) has already been reported.<sup>[18]</sup> However the kinetics of the polymerization of vDMTPD had not been studied in detail and therefore, it was investigated here. For this purpose, a [vDMTPD]<sub>0</sub>:[Initiator]<sub>0</sub>:[TIPNO]<sub>0</sub> molar ratio of 74:1:0.49 was used. In order to withdraw the periodic aliquots properly, the viscosity had to be lowered.

Therefore, the reaction mixture was diluted with anisole four times more than the optimal conditions of polymerization reported earlier. Figure 4a shows the plot of  $\ln([M]_0/[M])$  versus time. The curved shape of the plot indicates that the concentration of radicals is not constant over the course of the polymerization. Concerning the control of the polymerization (Figure 4b), the polydispersity is quite narrow ( $PDI < 1.3$ ) but the experimental molecular weights  $M_n$  are much lower than expected and reach a plateau at high conversions. Apparently, side reactions affect the kinetics of the polymerization. Since the conversion increased and the value of  $M_n$  remained nearly unchanged, permanent termination of the chains and creation of new growing radicals should have taken place. This can be rationalized when considering H-transfer from a growing radical chain-end to the mediating nitroxide radical, leading to the corresponding hydroxylamine and a dead unsaturated polymer chain-end.<sup>[26]</sup> Hydroxylamine could then be involved in H-transfer back to an active radical to regenerate the nitroxide and a second dead chain (H-terminated). At the same time new radicals could be created by autoinitiation of the monomer. These side reactions competed with the mechanism of NMRP and became preponderant probably because of the high dilution with anisole.

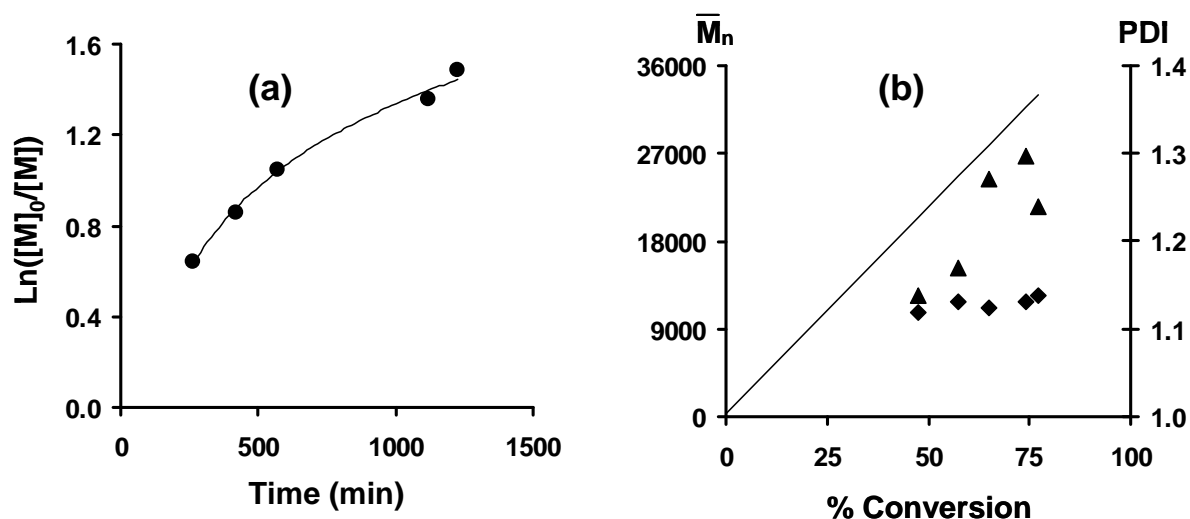
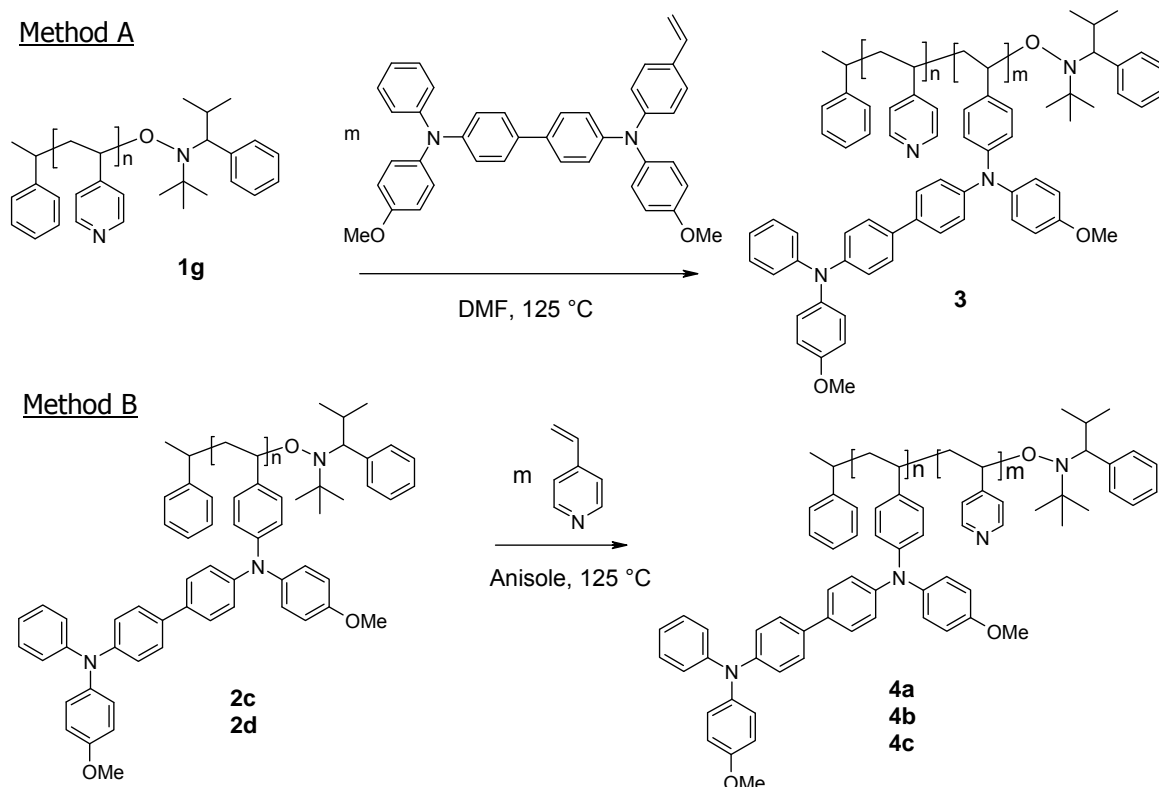


**Figure 4.** Polymerization of vDMTPD in anisole at 125°C. a) first-order kinetics. b)  $M_n$  (diamonds) and PDI (triangles) as a function of conversion. The straight line corresponds to the theoretical  $M_n$  values.  $[Anisole]:[4vP]:[Initiator]:[TIPNO]$  is equal to 499:74:1:0.49.

**Synthesis of P4vP-*b*-PvDMTPD (3).** Two strategies towards the targeted block copolymer can now be envisaged. The polymerization can be started either by using a P4vP (method A) or by using a PvDMTPD macroinitiator (method B), which is shown in Scheme 2.



**Scheme 2.** Possible pathways towards diblock copolymers starting from P4vP Method A) or PvDMTPD macroinitiator (Method B).

**Table 2.** Experimental conditions, molecular weights, and polydispersity indices of block copolymers **3**, **4a**, **4b** and **4c**. BC: block copolymer, MI: macroinitiator, M: monomer, I: initiator, N: nitroxide.

BC	entry	MI	[M] <sub>0</sub> wt% (solvent)	[M] <sub>0</sub> :[I] <sub>0</sub> : [N] <sub>0</sub>	M <sub>n</sub> [kg/mol]	PDI	wt% 4vP
P4vP - <i>b</i> -PvDMTPD	<b>3</b>	1g	10.5 (DMF)	195:1:0.2	15.9	1.60	-
PvDMTPD - <i>b</i> -P4vP	<b>4a</b>	2a	67.5 (anisole)	1612:1:0.62	28.9	2.82	bim.
	<b>4b</b>	2b	63.4 (anisole)	2269:1:2.19	52.4	1.65	65.3
	<b>4c</b>	2b	63.4 (anisole)	2269:1:2.19	82.4	1.78	74.2

The approach with P4vP as macroinitiator was carried out first (method A in Scheme 2). A crucial problem to solve is the selection of the correct amount of a suitable solvent. Indeed the solvent needs to dissolve both the polar P4vP macroinitiator and the monomer vDMTPD, both of which are solids. Dimethylformamide (DMF) was chosen as solvent for the block copolymerization. The P4vP macroinitiator **1g** ( $M_n = 14.8 \text{ kg}\cdot\text{mol}^{-1}$ ; PDI = 1.15) was used (see Table 1) and the block copolymer synthesis was carried out at  $[\text{vDMTPD}]_0:[\text{P4vP}]_0:[\text{TIPNO}]_0$  molar ratio of 195:1:0.2. It is important to note that vDMTPD and P4vP were drastically diluted, with  $[\text{vDMTPD}]_0$  and  $[\text{P4vP}]_0$  equal to  $0.196 \text{ mol}\cdot\text{L}^{-1}$  and  $0.001 \text{ mol}\cdot\text{L}^{-1}$ , respectively. This dilution was necessary due to the limited solubility of the two components. In comparison, homopolymerization of the vDMTPD was done at a concentration of  $[\text{vDMTPD}]_0$  equal to  $3.25 \text{ mol}\cdot\text{L}^{-1}$  and  $[\text{Initiator}]_0$  equal to  $0.0434 \text{ mol}\cdot\text{L}^{-1}$ . The reaction was quenched after 220 minutes, and the block copolymer **3** was analyzed by SEC (see Figure 5). As can be seen in the chromatogram, the peak only slightly shifted towards higher molecular weights. Furthermore, broadening of the SEC curve towards smaller molecular weights was observed, indicating that another polymerization process has occurred. Most probably, autoinitiation of vDMTPD took place.

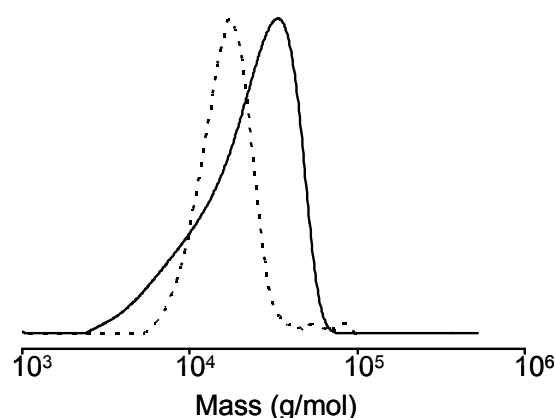


**Figure 5.** SEC chromatograms. a) of the Pv4P macroinitiator **1g** (dots) and the corresponding Pv4P-*b*-PvDMTPD block copolymer **3** (solid line). 2-N-methylpyrrolidone containing 0.05 M LiBr was used as eluent.

**Synthesis of PvDMTPD-*b*-P4vP (4).** Method B starting from PvDMTPD macroinitiators was tested with the goal of avoiding homopolymerization of vDMTPD and obtaining well-defined and pure block copolymer (Scheme 2).

A first attempt was carried out starting from PvDMTPD macroinitiator **2c** ( $M_n = 13.3 \text{ kg}\cdot\text{mol}^{-1}$ ; PDI = 1.23). The  $[\text{4vP}]_0:[\text{PvDMTPD}]_0:[\text{TIPNO}]_0$  molar ratio was 1612:1:0.62 and anisole was

also added to facilitate the dissolution of the macroinitiator. The results are shown in Figure 6a. The SEC curve of block copolymer **4a** is bimodal and the superposition with the chromatogram of the macroinitiator clearly shows that initiation was incomplete, leading to a mixture of PvDMTPD and PvDMTPD-*b*-P4vP. Nevertheless, the majority peak is shifted to higher molecular weights relative to the macroinitiator, which demonstrates that a block copolymer with appreciably high molecular weight was generated. The presence of a significant amount of PvDMTPD could be attributed to the low solubility of this polymer in the reaction mixture as well as a significant percentage of dead chains of PvDMTPD.

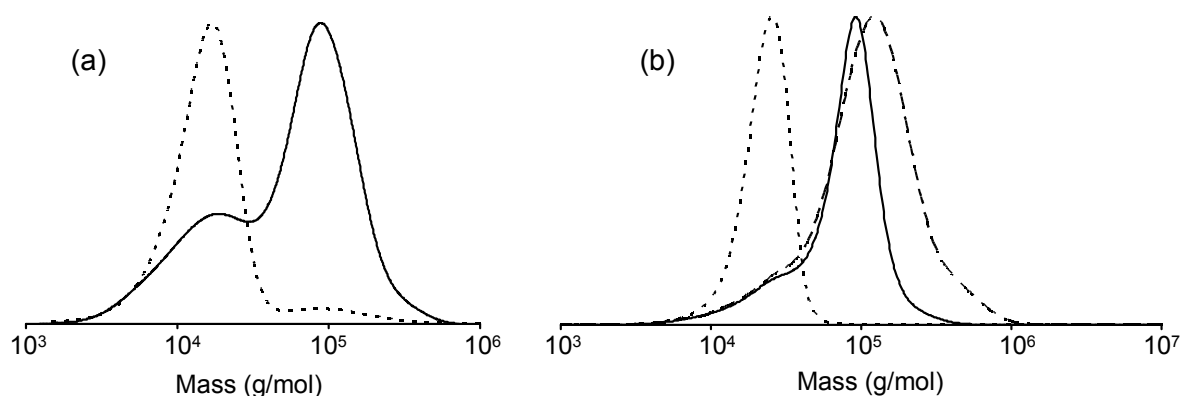


**Figure 6.** SEC chromatograms. a) macroinitiator PvDMTPD **2c** (dots) and the corresponding block copolymer P4VP-*b*-PvDMTPD **4a** (lines). b) Macroinitiator PvDMTPD **2d** (dots) and the corresponding block copolymers P4VP-*b*-PvDMTPD **4b** (lines) and **4c** (dashes) obtained at different conversions. 2-N-Methylpyrrolidone containing 0.05 M LiBr was used as eluent.

In order to avoid this problem, a PvDMTPD macroinitiator **2d** ( $M_n = 20.8 \text{ kg}\cdot\text{mol}^{-1}$ ; PDI = 1.15) was synthesized using styrene as comonomer. This should enhance the solubility of the macroinitiator and also might decrease the amount dead chain ends formed during macroinitiator synthesis. Moreover, the use of styrene as comonomer was reported to result in a higher degree of control for the NMRP of acrylates<sup>[27]</sup> and methacrylates<sup>[28]</sup>. Therefore we assumed that termination reactions in the polymerization of vDMTPD, as discussed before, might be reduced which finally should lead to a higher initiation efficiency of the block copolymerization. copolymerization. The slight dilution of the DMTPD moieties with an electronically inactive monomer is not expected to lead to a decrease in the charge carrier mobility. This is supported by reports from Borsenberger et al., who found that the charge carrier mobility of hole transport molecules blended in polystyrene was almost maintained

for polystyrene weight fractions of up to 60 %.<sup>[29]</sup> A detailed study of the dilution effect of styrene as comonomer on the charge carrier mobility in PVDMTPD is currently underway. This new macroinitiator **2d**, containing a weight fraction of styrene units of 19.3 %, was subsequently used for the synthesis of the second block together with a larger amount of anisole ([4VP]:[anisole] equal to 2:1 v/v) and a [4VP]<sub>0</sub>: [PvDMTPD]<sub>0</sub>: [TIPNO]<sub>0</sub> molar ratio of 2675:1:2.13. Two aliquots were isolated after 1h (16.5% conversion) and 2h of reaction time (25.5% conversion), to get the block copolymers **4b** and **4c** containing 65 and 74 wt% of P4vP respectively. The SEC chromatograms of **2b**, **4b** and **4c** are presented in Figure 6b. Clearly, the initiation was more efficient as indicated by the low amount of residual macroinitiator in the block copolymers. Consequently, block copolymers **4b** and **4c** exhibit lower polydispersities than **4a**. The block copolymers **4b** and **4c** are amorphous in nature as determined from differential scanning calorimetry (DSC) measurements and exhibit glass transition temperatures  $T_g$  of 155 and 156 °C, respectively. This is in close agreement with the values of the macroinitiators P4vP and PvDMTPD, which show  $T_g$  values of 154 and 157 °C, respectively. All data regarding the block copolymers are given in Table 2.

**Self-assembly of PvDMTPD-*b*-P4vP.** Block copolymers **4b** and **4c** containing a hole conducting block and a P4vP block were then investigated using transmission electron microscopy (TEM). Cross-sections of bulk samples can be seen in Figure 7. After staining with iodine, P4vP appears dark. The block copolymer **4b** was annealed at 180°C. The morphology of this diblock copolymer shows disordered short cylinders or worm-like structures of PvDMTPD in a matrix of P4VP (Fig. 7a). A bulk sample of **4c** was also prepared, but with a different method. Here, a pyridine solution was slowly evaporated at 65 °C and then annealed at 170°C for 2 days. TEM images are shown in Figure 7b-d and display a lamellar morphology. The observed lamellae are disordered on the large scale (Figure 7b) but can be small-scale alignments of the structure can be observed (Figure 7c,d), which probably is due to slow evaporation of pyridine. Note that we observed a lamellar structure in our block copolymer (with 74wt.-% P4VP), which should rather result in a cylindrical microstructure. Moreover, the lamellae are asymmetric with domain sizes of 20 and 60 nm for PvDMTPD and P4vP, respectively. These two phenomena can be reasonably explained by the moderate

polydispersity of the P4VP block compared to the PvDMTPD block. This is in accordance with reports in the literature.<sup>[30-32]</sup>

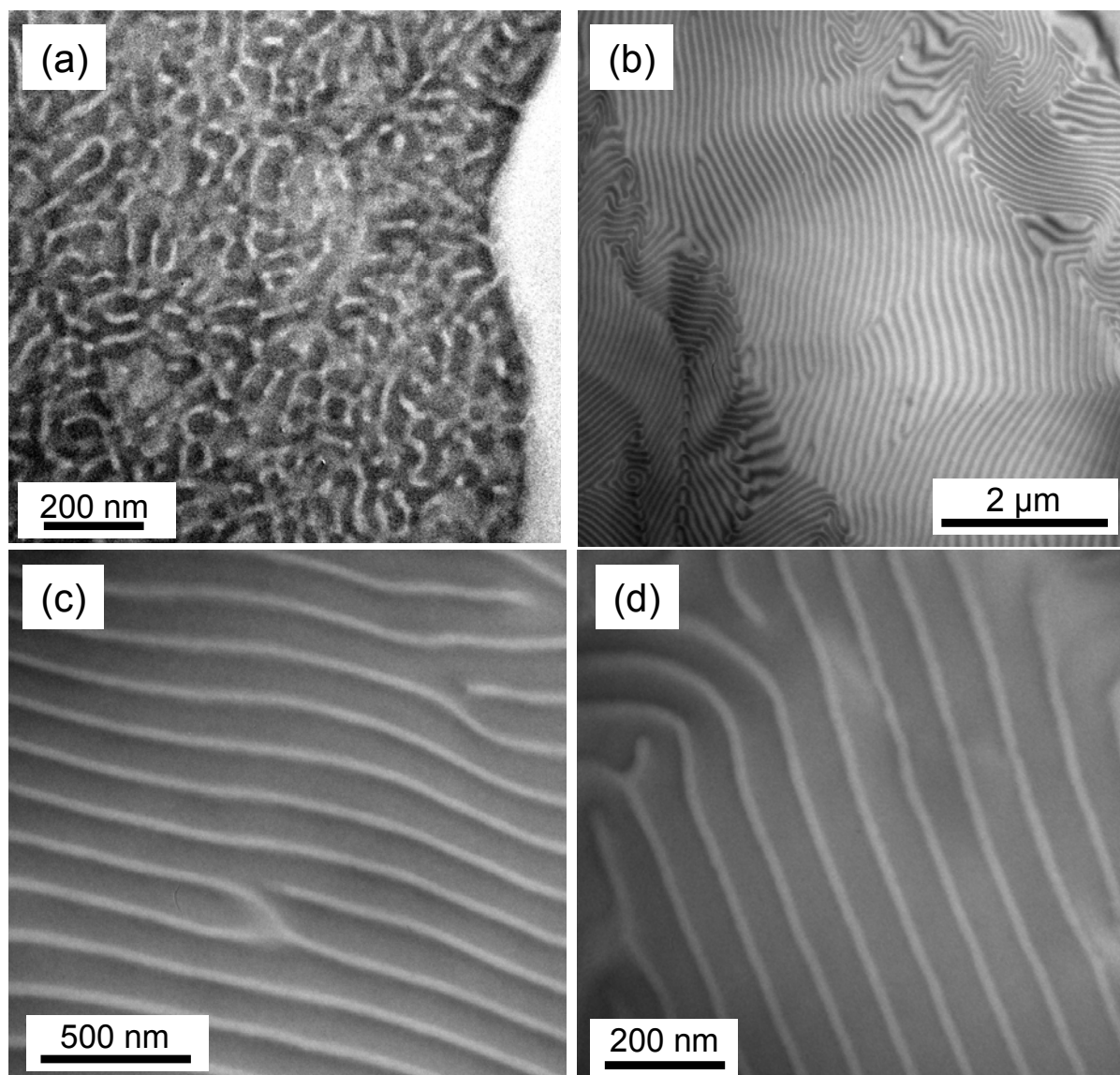


**Figure 7.** TEM cross-sections of block copolymers. a) Bulk sample of 4b obtained after thermal annealing at 180°C. b, c, d) Bulk samples obtained after slow evaporation of a pyridine solution of 4c and annealing for 2 days at 170 °C. All samples were embedded in epoxy resin, cut, and stained with  $I_2$ . P4vP and PvDMTPD domains are gray and light, respectively.

**Self-assembly of hybrid bulk samples containing CdSe:Te nanocrystals.** The synthesized block copolymer **4c** containing a hole conducting block and a 4vP block was then mixed with CdSe:Te nanocrystals<sup>[33]</sup> and the self-assembly behaviour was investigated using TEM. CdSe nanoparticles were previously reported to selectively distribute in the P4vP block of PS-*b*-

P4vP. The above-mentioned procedure for TEM imaging was applied to a solution of **4c** and CdSe:Te nanocrystals in pyridine (containing 2 wt% of Te and with an average diameter of 3.4 nm). The CdSe:Te nanoparticles were initially stabilized with a three component mixture of trioctylphosphine, hexadecylamine and trioctylphosphine oxide, which was partially exchanged with pyridine, in order to provide better affinity for the P4vP domains. TEM images of the bulk nanocomposites samples are presented in Figure 8. No difference in morphology can be observed between the sample simply obtained by slow evaporation of pyridine (Figure 8a,b) and the sample with additional thermal annealing (Figure 8c,d). Interestingly, the morphology did not change after incorporation of nanocrystals, and the domain sizes for PVDMTPD and P4VP are still around 20 and 60 nm, respectively. The most interesting result concerns the CdSe:Te nanoparticles which are exclusively sequestered in the P4VP domains and preferentially located close to the interface of the two domains. Thus, a fully functionalized nanostructured hybrid nanocomposite material comprised of hole transporting PVDMTPD domains and P4VP domains with sequestered light harvesting/electron conducting CdSe:Te nanocrystals was prepared. These results offer many opportunities to utilize these materials in thin films for future applications in novel device concepts.<sup>[34]</sup> Since the bulk is completely microphase separated, thicker films of this material for photovoltaic devices can be used, which is of essential advantage in harvesting all the incident light. Still, for this purpose, the concentration of the nanocrystals in P4VP domains has to be increased in order to get efficient light harvesting and charge percolation via nanocrystals, which is the subject matter of our current research.

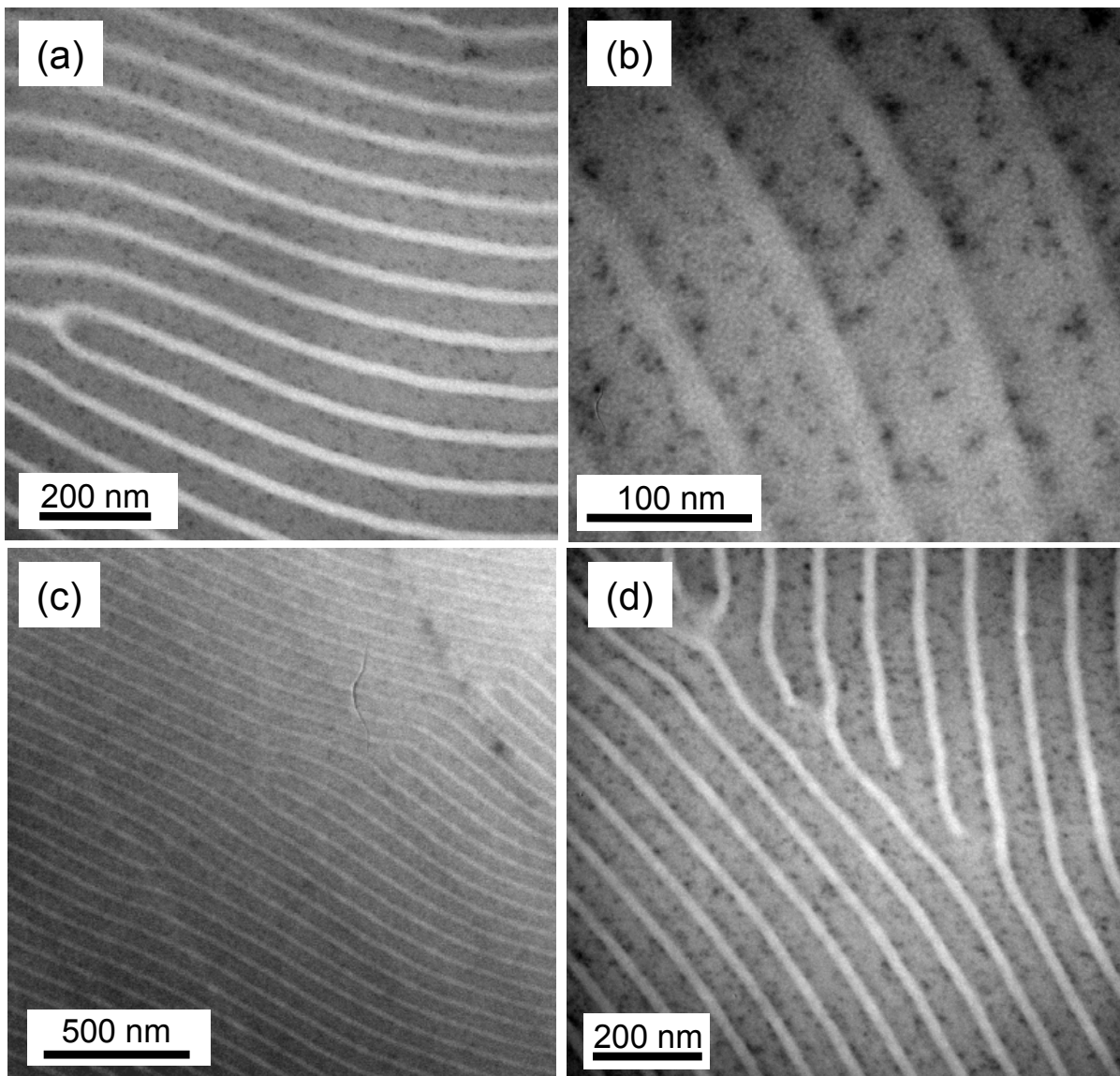


**Figure 8.** TEM cross-sections of composites of block copolymers 4c and CdSe:Te nanocrystals. All volume samples were obtained after slow evaporation of a solution of CdSe:Te nanoparticles (volume fraction 0.5% to the P4vP block) and 4c in pyridine. (a) and (b) were not annealed. (c) and (d) were annealed 2 days at 170 °C. The samples were embedded in epoxy resin, cut, and stained with I<sub>2</sub>. PvDMTPD domains are light. P4vP and PvDMTPD domains are gray and light, respectively. Nanocrystals are darker.

## Conclusions

The polymerizations of 4-vinylpyridine (4vP) and vinyl-N,N'-bis(4-methoxyphenyl)-N,N'-diphenyl-(1,1'-biphenyl)-4,4'-diamine (vDMTPD) by Nitroxide-Mediated Radical Polymerization was studied and optimized. Moreover, a strategy of block copolymer synthesis of PVDMTPD-*block*-P4VP was developed, and the resulting microphase-separated bulk morphologies were investigated using transmission electron microscopy (TEM). Furthermore, nanocomposites from these functional diblock copolymers and CdSe:Te nanoparticles were successfully prepared and characterized by TEM. This new hybrid semiconductor material exhibits lamellar nanostructures in which the hole conductor domains of PVDMTPD are separated from light harvesting nanocrystals, which are exclusively confined in the P4VP domains. We also find the nanoparticles preferentially located at the domain interface of the lamellar structure. These results show that the challenging task of applying the block copolymer strategy to semiconductor nanocomposites with morphological stability can be realized, making innovative hybrid devices feasible. Potentially, these nanostructures can be varied by changing the length of both blocks or by using different nanoparticles. Thus, future applications such as new photovoltaic or spintronic devices can be envisioned using this exciting material.

## Experimental

**General information.** All glass apparatus were dried at 115 °C and cooled down under nitrogen. Solvents used for column chromatography and precipitation were distilled before use. TIPNO<sup>[35]</sup>, alkoxyamine initiator<sup>[31]</sup>, vDMTPD<sup>[36]</sup> were synthesized according to the literature. The synthesis of CdSe:Te nanocrystals was published elsewhere.<sup>[33]</sup> These nanocrystals was prepared via high-temperature pyrolysis of Cd, Se, and Te precursors (dimethylcadmium, trioctylphosphine selenide, and trioctylphosphine telluride), in a three-component mixture of highly boiling coordinating solvents trioctylphosphine, hexadecylamine, and tri-*n*-octylphosphine oxide. 4-vinylpyridine (Aldrich, 95%) was dried over calcium hydride, distilled under reduced pressure, and degassed with nitrogen. Anisole was dried over sodium and distilled at 170°C under nitrogen. Toluene (Acros Organics, >99.99%) was distilled over sodium and degassed with nitrogen. Acetone (VWR, >99.8%) was

distilled over anhydrous calcium sulfate and degassed with nitrogen. Dry THF was distilled over Na/benzophenone. DMF was obtained from Fluka and distilled over CaH<sub>2</sub>.

**Instrumentation.** <sup>1</sup>H NMR spectra were recorded on a Bruker AC 250 spectrometer (250 MHz) and calibrated to the signal of the respective solvent. SEC measurements of vDMTPD polymerization were carried out in THF containing 0.25 wt% tetrabutylammonium bromide using UV and RI detectors (Waters). For calibration, polystyrene standards and 1,2-dichlorobenzene as an internal standard were used. All the other samples were analyzed in two PSS GRAM 7μm, 1000 and 100 Å columns at 70°C; Waters 486 UV detector and Bischoff RI-detector 8110. 50 μL of the sample diluted in 2-N-methylpyrrolidone containing 0.05 M LiBr were injected. Linear PS standards were used for calibration and methyl benzoate was used as an internal standard.

Differential scanning calorimetry was carried out at heating rates of 10 K/min between 30 °C and 200 °C under N<sub>2</sub> with a Perkin Elmer Diamond DSC.

For TEM sample preparation, molten samples were embedded in epoxy resin, cut, and stained with iodine. Measurements were performed on a Zeiss 902 instrument at 80 kV.

**Polymerization procedures.** *Synthesis of P4vP.* A typical procedure is described as a representative example. A solution of 52 mg (0.159 mmol) alkoxyamine and 7.1 mg (0.032 mmol) nitroxide were added to a 10 mL Schlenk tube equipped with a stir bar in a small amounts of chloroform. The chloroform was evaporated under vacuum. Anisole (1 mL, 9.201 mmol) and 4-vinylpyridine (5 mL, 46.985 mmol) were added to the reaction flask under nitrogen. This flask was degassed by three freeze thaw cycles and then immersed in an oil bath kept at 125°C for 76 min. Dilution with chloroform and precipitation (2x) into diethyl ether yielded **1g** as a white powder.

For monitoring kinetics, aliquots were withdrawn periodically from the polymerization mixture. <sup>1</sup>H-NMR was used to determine the conversion (GC and <sup>1</sup>H-NMR data for monomer consumption were identical).

*Synthesis of PvDMTPD.*<sup>[17]</sup> 0.745 g (1.3 mmol) vDMTPD was filled into a 10 ml flask under nitrogen. A solution of initiator (5.65 mg, 0.0174 mmol) and TIPNO (1.90 mg, 0.0086 mmol) in 400 μL anisole was added. After degassing, the mixture was stirred at 125 °C for 300 min

and the polymerization was quenched by rapid cooling. Dilution in toluene and precipitation (2x) in acetone yielded PvDMTPD as white powder.  $^1\text{H-NMR}$  (250 MHz,  $\text{CD}_2\text{Cl}_2$ );  $\delta$  (ppm)= 7.10 (br, CHar), 6.88 (br, CHar), 6.80 (br, CHar), 6.53 (br, CHar), 3.76 (br,  $\text{OCH}_3$ ), 3.64 (br,  $\text{OCH}_3$ ), 1.97 (br, CH), 1.57 (br,  $\text{CH}_2$ ).

*Synthesis of P4vP-b-PvDMTPD.* 0.04 mg ( $0.181 \times 10^{-3}$  mmol) of nitroxide a in a small amount chloroform was added to a 10 mL Schlenk tube equipped with a stirring bar. Chloroform was evaporated under vacuum. 13.4 mg ( $0.905 \times 10^{-3}$  mmol) of macroinitiator **1g** and vDMTPD (101.3 mg, 0.177 mmol) were added to the Schlenk flask. DMF (0.9 mL, 11.624 mmol) was added to the reaction flask under nitrogen. This flask was evacuated under vacuum in a liquid nitrogen bath and backfilled with nitrogen gas. The Schlenk tube was immersed in an oil bath heated to 125°C. The polymerization was stopped by rapid cooling. Dilution in chloroform and precipitation in diethyl ether yielded P4vP-*b*-PvDMTPD as a white solid.

*Synthesis of PvDMTPD-b-P4vP.* 3.3 mg (0.015 mmol) nitroxide in a small amount chloroform was added to a 10 mL Schlenk tube equipped with a stir bar. The chloroform was evaporated under vacuum. 144 mg ( $7.03 \times 10^{-3}$  mmol) PvDMTPD was placed in the Schlenk flask. Anisole (1 mL, 9.201 mmol) and 4-vinylpyridine (2 mL, 18.794 mmol) were added to the reaction flask under nitrogen. After three freeze thaw cycles, the flask immersed in an oil bath heated to 125 °C. The polymerization was stopped by rapid cooling after 120 min. Dilution in chloroform and precipitation in diethyl ether (3x) yielded PvDMTPD-*b*-P4vP **4d** as white solid.

$^1\text{H-NMR}$  (250 MHz,  $\text{CD}_2\text{Cl}_2$ );  $\delta$  (ppm)= 8.30 (br, CHar 4vP), 7.15 (br, CHar TPD), 6.98 (br, CHar vDMTPD), 6.78 (br, CHar vDMTPD), 6.43 (br, CHar 4vP), 3.66 (br,  $\text{OCH}_3$ ), 3.44 (br,  $\text{OCH}_3$ ), 1.81 (br, CH, 4vP), 1.51 (br,  $\text{CH}_2$ , 4vP).

## Acknowledgements

The Bayreuth group acknowledges the financial support from DFG and the European Science Foundation (EUROCORES SONS II, SOHYDs, and SFB 481). A.L.R. and D.V.T. are grateful to the German Excellence Initiative for funding via the “Nanosystems Initiative Munich (NIM)” and the LMUexcellent program. We also thank Carmen Kunert and Sabine Wunder for the TEM and the SEC measurements, respectively.

## References

1. L. L. Beecroft, C. Ober, *Chem. Mater.* **1997**, *9*, 1302.
2. A. Haryono, W. H. Binder, *Small* **2006**, *5*, 600.
3. W. J. E. Beek, M. M. Wienk, R. A. J. Janssen, *Adv. Mater.* **2004**, *16*, 1009.
4. L. Liang, K. L. Dzienis, Q. Wang, *Adv. Funct. Mater.* **2006**, *16*, 542.
5. . Gur, N. A. Fromer, C. P. Chen, A. G. Kanaras, A. P. Alivisatos, *Nano Lett.* **2007**, *7*, 409.
6. S.-W. Yeh, H.-H. Wei, Y.-S. Sun, U.-S. Jeng, K. S. Liang, *Macromolecules* **2005**, *38*, 6559.
7. Y. Lin, A. Böker, J. He, K. Sill, H. Xiang, C. Abetz, X. Li, J. Wang, A. Balazs, T. P. Russel, *Nature* **2005**, *434*, 55.
8. C.-T. Lo, B. Lee, R. E. Winans, P. Thiyagarajan, *Macromolecules* **2006**, *39*, 6318.
9. J. J. Chiu, B. J. Kim, G.-R. Yi, J. Bang, E. J. Kramer, D. J. Pine, *Macromolecules* **2007**, *40*, 3361.
10. M. R. Bockstaller, R. A. Mickiewicz, E. L. Thomas, *Adv. Mater.* **2005**, *17*, 1331.
11. S. Förster, M. Antonietti, *Adv. Mater.* **1998**, *10*, 195.
12. A. C. Balazs, T. Emrick, T. P. Russel, *Science* **2006**, *314*, 1107.
13. M. E. Mackay, A. Tuteja, P. M. Duxbury, C. J. Hawker, B. Van Horn, Z. Guan, G. Chen, R. S. Krishnan, *Science* **2006**, *311*, 1740.
14. C.-P. Li, K.-H. Wei, J. Y. Huang, *Angew. Chem. Int. Ed.* **2006**, *45*, 1449.
15. K. M. Krishnan, A. B. Pakhomov, Y. Bao, P. Blomqvist, Y. Chun, M. Gonzales, X. Griffin, X. Ji, B. K. Roberts, *J. Mater. Sci.* **2006**, *41*, 793.
16. S. M. Lindner, S. Hüttner, A. Chiche, M. Thelakkat, G. Krausch, *Angew. Chemie Int. Ed.* **2006**, *45*, 3364.
17. S. M. Lindner, M. Thelakkat, *Macromolecules* **2004**, *37*, 8832.
18. M. Sommer, S. M. Lindner, M. Thelakkat, *Adv. Funct. Mater.* **2007**, *17*, 1493.
19. S. Creutz, P. Teyssier, R. Jérôme, *Macromolecules* **1997**, *30*, 1.
20. J. Xia, X. Zhang, K. Matyjaszewski, *Macromolecules* **1999**, *32*, 3531.
21. A. J. Convertine, B. S. Sumerlin, D. B. Thomas, A. B. Lowe, C. L. McCormick, *Macromolecules* **2003**, *36*, 4679.
22. A. Fischer, A. Brembilla, P. Lochon, *Macromolecules* **1999**, *32*, 6069.
23. T. Diaz, A. Fischer, A. Jonquière, A. Brembilla, P. Lochon, *Macromolecules* **2003**, *36*, 2235.

24. J. Bohrisch, U. Wendler, W. Jaeger, *Macromol. Rapid. Commun.* **1997**, *18*, 975.
25. B. G. G. Lohmeijer, U. S. Schubert, *J. Polym. Sci., Part A* **2005**, *43*, 6331.
26. C. J. Hawker, A. W. Bosman, E. Harth, *Chem. Rev.* **2001**, *101*, 3661.
27. T. Fukuda, T. Terauchi, A. Goto, Y. Tsujii, T. Miyamoto, *Macromolecules* **1996**, *29*, 3050.
28. B. Charleux, J. Nicolas, O. Guerret, *Macromolecules* **2005**, *38*, 5485.
29. P. M. Borsenberger, W. T. Gruenbaum, U. Wolf, H. Bässler, *Chem. Phys.* **1998**, *234*, 277.
30. N. T. Lynd, B. D. Hamilton, M. A. Hillmyer, *J. Polym. Sci. Part B* **2007**, *45*, 3386.
31. N. T. Lynd, M. A. Hillmyer, *Macromolecules* **2005**, *38*, 8803.
32. A.-V. Ruzette, S. Tence-Girault, L. Leibler, F. Chauvin, D. Bertin, O. Guerret, P. Gerard, *Macromolecules* **2006**, *39*, 5804.
33. T. Franzl, J. Müller, T. A. Klar, A. L. Rogach, J. Feldmann, D. V. Talapin, H. Weller, *J. Phys. Chem. C* **2007**, *111*, 2974.
34. E. Holder, N. Tessler, A. L. Rogach, *J. Mater. Chem.* **2008**, *18*, 1064.
35. D. Benoit, V. Chaplinski, R. Braslau, C. J. Hawker, *J. Am. Chem. Soc.* **1999**, *121*, 3904.
36. C. Schmitz, M. Thelakkat, H. W. Schmidt, *Adv. Mater.* **1999**, *11*, 821.



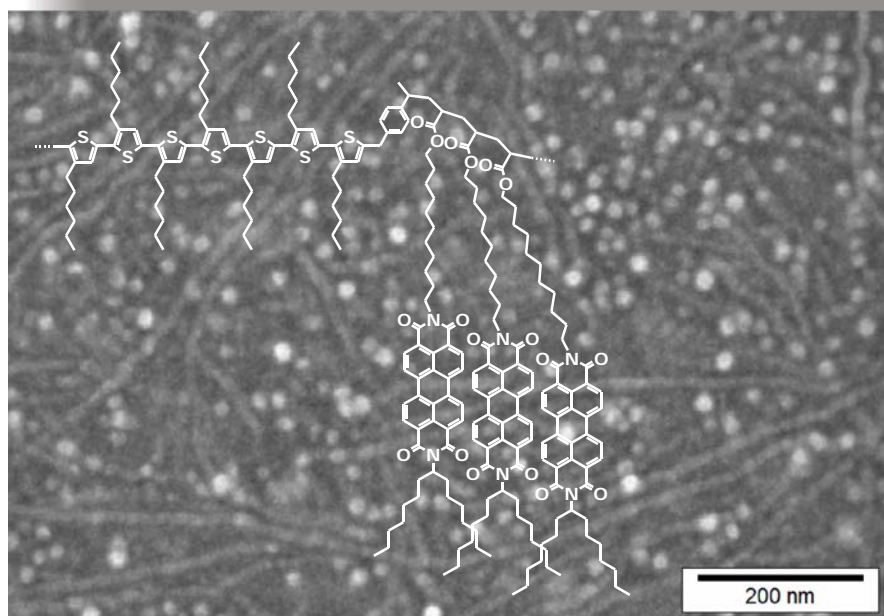
## 4. Crystalline-Crystalline Donor Acceptor Block Copolymers

Michael Sommer, Andreas Lang, and Mukundan Thelakkat

Applied Functional Polymers and Macromolecular Chemistry I

Universität Bayreuth, Universitätsstr. 30, University of Bayreuth, 95444 Bayreuth, Germany

[Michael.Sommer@uni-bayreuth.de](mailto:Michael.Sommer@uni-bayreuth.de), [Mukundan.Thelakkat@uni-bayreuth.de](mailto:Mukundan.Thelakkat@uni-bayreuth.de)



One of the challenging issues in designing new materials for organic electronics, such as photovoltaics or field effect transistors, is that film forming properties have to be combined with functional and well-defined nanostructured morphologies in order to fulfill the complex requirements of light absorption, charge separation and charge transport in confined geometries.<sup>[1,2]</sup> Morphological control on a nanoscopic level is also required to tune the interface between the functional domains and to satisfy the long term stability of such devices. Block copolymers can meet these requirements as they phase segregate into versatile equilibrium microdomains such as cylinders, gyroids or lamellae<sup>[3]</sup>, thus offering the possibility to control the type, size and orientation of microstructure in the device. We have demonstrated the chain of control on all length scales - from molecular over mesoscopic to macroscopic - using the principle of self-assembly of donor-acceptor block copolymers for photovoltaic (PV) applications.<sup>[4,5,6]</sup> A polymerizable perylene bisimide derivative was used as electron acceptor and crystalline microdomains in an amorphous poly(triarylamine) matrix (donor) were observed as a result of the strong  $\pi$ - $\pi$  interactions between adjacent perylene bisimide moieties.<sup>[7]</sup> Block copolymers that contain conjugated donor segments and electron acceptor segments have also been presented<sup>[8-11]</sup>, but microphase separation was not reported.

The design of the grignard metathese polymerization (GRIM) of poly(3-hexylthiophene) (P3HT)<sup>[12,13]</sup> and the in situ introduction of defined endgroups<sup>[14]</sup> has stimulated the synthesis of P3HT block copolymers.<sup>[15-18]</sup> Recently, nitroxide mediated radical polymerization (NMRP)<sup>[20]</sup> starting from P3HT macroinitiators was demonstrated.<sup>[11,19]</sup>

Herein, we report on the first synthesis of crystalline-crystalline donor-acceptor block copolymers with P3HT as donor block and poly(peryene bisimide acrylate) (PPerAcr) as acceptor block (figure 1). The crystallinity of both blocks not only can give rise to a rich phase behaviour in the bulk of these materials, but is also advantageous for the charge carrier mobilities in the domains. We show that all important prerequisites for PV applications such as a high optical density, photoluminescence quenching in film and microphase separation can be achieved in one molecule at the same time.

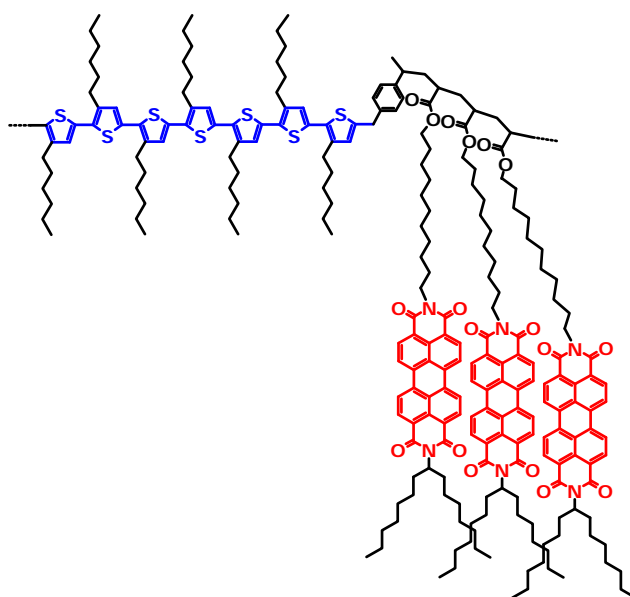
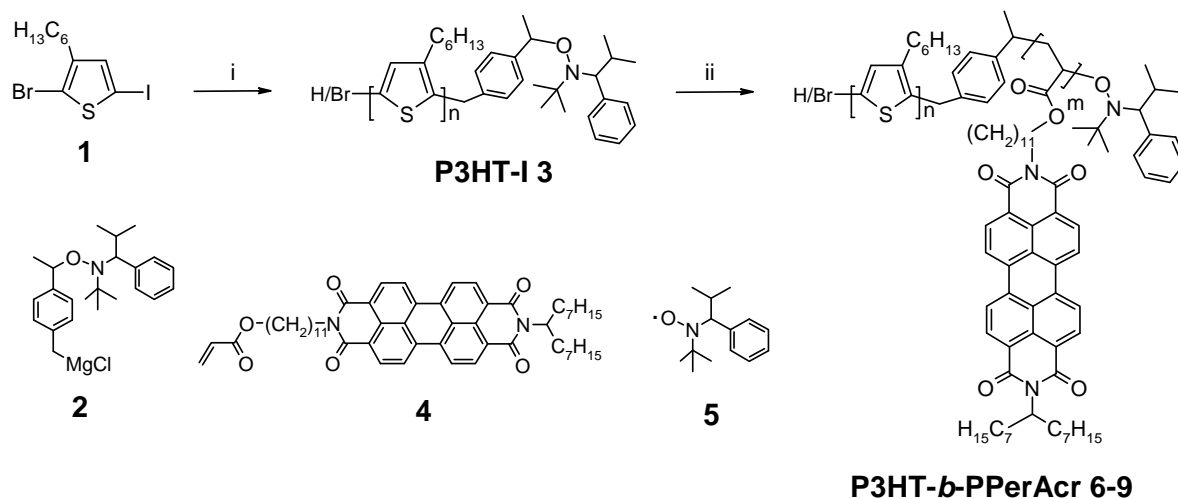


**Figure 1:** Schematic representation of poly(3-hexylthiophene)-*b*-poly(peryene bisimide acrylate) P3HT-*b*-PPerAc. The first block consists of a rigid-rod poly(3-hexylthiophene) (blue), the second segment is built up of a flexible polyacrylate backbone with pendant side chain crystalline perylene bisimides (red).

A set of donor-acceptor block copolymers poly(3-hexylthiophene)-*b*-poly(peryene bisimide acrylate) (P3HT-*b*-PPerAc) is prepared in only two steps (scheme 1). In the first step, we use a modified procedure of Yokozawa et al. starting from 2-bromo-3-hexyl-5-iodothiophene **1**.<sup>[21]</sup> In the last stage of the polymerization the active P3HT chain end is quenched in situ with 2,2,5-trimethyl-3-(1-(4'-magnesiumchloromethyl)phenylethoxy)-4-phenyl-3-azahexane **2**, which yields a well-defined and narrow-distributed macroinitiator P3HT **3** (PDI  $\sim$ 1.1,  $M_{n,SEC}$  = 8900 g/mol). The introduction of **2** at the end of the P3HT block is verified by <sup>1</sup>H-NMR. 84 % of the chains are found to be functionalized, which is outweighed by the simple and straightforward one-pot procedure of **3**. Non-functionalized P3HT and the resulting block copolymers with perylene bisimide acrylate can be separated in a later purification process which is necessary anyway. In the second step, P3HT **3** is used to polymerize perylene bisimide acrylate PerAc **4**. In order to obtain a series of block copolymers with different segment lengths of **4**, the reaction time as well as the ratio [**3**]:[**4**] is varied. All other reaction parameters, including the solvent 1,2-dichlorobenzene, 0.2 equivalents of 2,2,5-trimethyl-4-phenyl-3-azahexane-3-oxyl **5** (TIPNO) and 5 mol.-% of styrene (relative to **4**), are kept constant. Similar reaction conditions were already applied in earlier polymerizations of PerAc.<sup>[22]</sup> The addition of a small amount of styrene as comonomer<sup>[23]</sup>

results in an improved control of the polymerization of PerAcr, whereby self-initiation of styrene leading to a possible homopolymerization of PerAcr **4** is not observed. Also, the incorporation of few styrene units into the chain does not affect the charge transport properties of PPerAcr negatively.<sup>[24]</sup> In this manner, four block copolymers P3HT-*b*-PPerAcr **6**, **7**, **8** and **9** with different block lengths of PPerAcr were successfully synthesized.



**Scheme 1:** Synthesis of poly(3-hexylthiophene) macroinitiator P3HT-I 3 and block copolymers poly(3-hexylthiophene)-*b*-poly(perylene bisimide acrylate) 6-9. i) 1. THF, 0 °C, *i*-prMgCl, 90 min; 2. Ni(dppp)Cl<sub>2</sub>, 60 min; 3. 2, 30 min; 4. HCl, MeOH. ii) 4, styrene, 2,2,5-trimethyl-4-phenyl-3-azahexane-3-oxyl (TIPNO), 1,2-dichlorobenzene, 125 °C, 10-24 h. Since the styrene comonomer fraction is too small for determination via <sup>1</sup>H-NMR, it is not depicted in the chemical structure of the second block PPerAcr.

PerAcr monomer and unreacted P3HT were removed by soxhlet extraction of the block copolymers. The size exclusion chromatography (SEC) curves of the macroinitiator and the purified block copolymers are shown in figure 2a. Obviously, the peaks of the block copolymers shift towards smaller elution volumes. The number average molecular weights ( $M_n$ ) of **6**, **7**, **8** and **9** increase to 16.1, 16.9, 20.6 and 24.8 kg/mol, respectively (table 1), while the polydispersity indices (PDI) are exceptionally low for fully functionalized block copolymers<sup>[4,6]</sup>, ranging between 1.24 and 1.53. The PPerAcr weight fractions (determined by <sup>1</sup>H-NMR) for **6**, **7**, **8** and **9** are 53.2, 59.7, 73.7 and 81.4 %, respectively, thus providing a set of polymers in which the acceptor content is systematically varied.

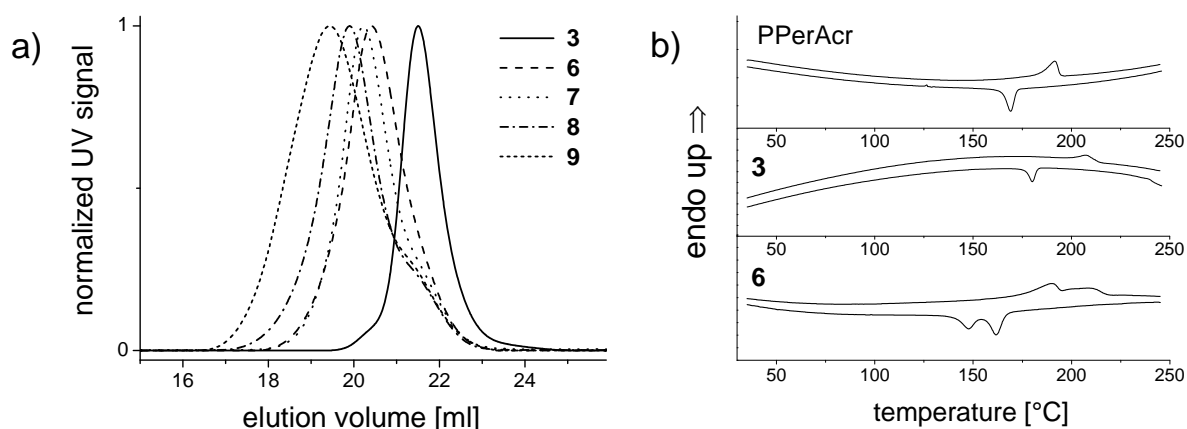


**Figure 2:** a) SEC traces of macroinitiator P3HT-I **3** and block copolymers P3HT-b-PPerAc **6-9** measured in THF containing 0.25 wt.-% tetrabutylammonium bromide at a flow rate of 0.5 ml/min. b) Differential scanning calorimetry (DSC) traces of P3HT macroinitiator **3**, PPerAc homopolymer and P3HT-block-PPerAc **6**. The second heating and cooling traces are presented, curves were measured under nitrogen at 10 K/min.

**Table 1.** Molecular weights  $M_n$ , polydispersities PDI, composition and thermal properties of macroinitiator P3HT-I **3** and block copolymers P3HT-b-PPerAc **6-9**. <sup>a</sup>: from size exclusion chromatography (SEC) <sup>b</sup>: from <sup>1</sup>H-NMR <sup>c</sup>: from differential scanning calorimetry (DSC) <sup>d</sup>: from thermogravimetric analysis (TGA).

Polymer	$M_n$ [g/mol] <sup>a</sup>	PDI <sup>a</sup>	wt.-% PPerAc <sup>b</sup>	$T_{m1}$ [°C] <sup>c</sup>	$T_{m2}$ [°C] <sup>c</sup>	$T_{on}$ [°C] <sup>d</sup>
P3HT <b>3</b>	8900	1.12	0	208	--	308
P3HT-b-PPerAc <b>6</b>	16100	1.25	53.2	190	211	327
P3HT-b-PPerAc <b>7</b>	16900	1.24	59.7	191	211	327
P3HT-b-PPerAc <b>8</b>	20600	1.31	73.7	202	--	341
P3HT-b-PPerAc <b>9</b>	24800	1.53	81.4	206	--	348

We investigate the thermal properties of the block copolymers using thermogravimetric analysis (TGA) and differential scanning calorimetry (DSC) (table 1). TGA is conducted between 30 °C and 650 °C and shows very high thermal stability of the block copolymers, with onset temperatures between 327 °C and 348 °C. The DSC trace of P3HT **3** shows a melting temperature  $T_m$  of 208 °C (figure 2b). When measuring the homopolymer PPerAc, melting occurs at 192 °C. These two transitions are also observed in block copolymer **6**

where two melting peaks  $T_{m1}$  and  $T_{m2}$  emerge at 190 °C and 211 °C, respectively. The first melting point at 190 °C arises from PPerAcr segments whereas the second  $T_m$  of 211 °C correlates to the melting point of P3HT **3**. Block copolymer **7** with a slightly higher PPerAcr weight fraction exhibits the same behaviour. The observation of two melting points in a block copolymer with melting temperatures close to those of the respective homopolymers strongly suggests that in **6** and **7** two different types of domains are present. This is indicative of microphase separation. By contrast, block copolymers **8** and **9** with perylene weight fractions of 73.7 and 81.4, respectively, exhibit only one melting point that lies between the transitions of the two homopolymers. The increased block length of PPerAcr in **8** and **9** might be responsible for this behaviour, causing an increased melting point of the second segment. As a result, the  $T_m$  of both blocks shift closer together and finally appear as one single melting point.

The optical properties of the block copolymers also confirm that perylene bisimide moieties are attached to the P3HT block. UV-vis and photoluminescence (PL) data from THF solution are presented in figure 3. The data of PPerAcr is included in order to identify the contribution of both segments to the spectra. The UV-vis spectrum of macroinitiator **3** exhibits one broad absorption band with  $\lambda_{max}$  at 445 nm, and PPerAcr shows three vibronic bands of the  $S_0$ - $S_1$  transition at 470, 490 and 525 nm (figure 3a).<sup>[4]</sup> Unlike P3HT absorption which is characteristic for diluted P3HT chains, the PPerAcr spectrum corresponds to highly aggregated perylene bisimide moieties. This is not surprising since a close distance between adjacent chromophores is already achieved in a single PPerAcr chain. The absorbance spectra of all block copolymers show a superposition of P3HT and PPerAcr absorption, with contributions of the two segments according to their respective weight fractions. Visually, the color of the solutions shifts from orange to red for increasing degrees of polymerization of PPerAcr. The PL behaviour under the same conditions (0.02 mg/ml in THF) is investigated upon excitation at 400 nm and at 530 nm, where the absorption of P3HT and PPerAcr, respectively, is very high, giving rise to a selective excitation of each block. Upon excitation at 400 nm, P3HT **3** shows a bright yellow fluorescence at 565 nm and PPerAcr homopolymer emits only weak red light at 620 nm (figure 3b). Accordingly, the PL of the block copolymers mainly consists of P3HT emission at 565 nm which decreases for lower P3HT contents. Excitation at 530 nm causes bright emission from PPerAcr, which is now more intense than

emission from P3HT (figure 3c). The PL intensity of the block copolymers therefore increases for increasing degrees of polymerization of PPerAcr. These results clearly show that both types of chromophores, P3HT and PPerAcr are incorporated into the block copolymers. The PL of the block copolymers in film, however, is completely quenched, indicating electron transfer from P3HT to PPerAcr (not shown here).

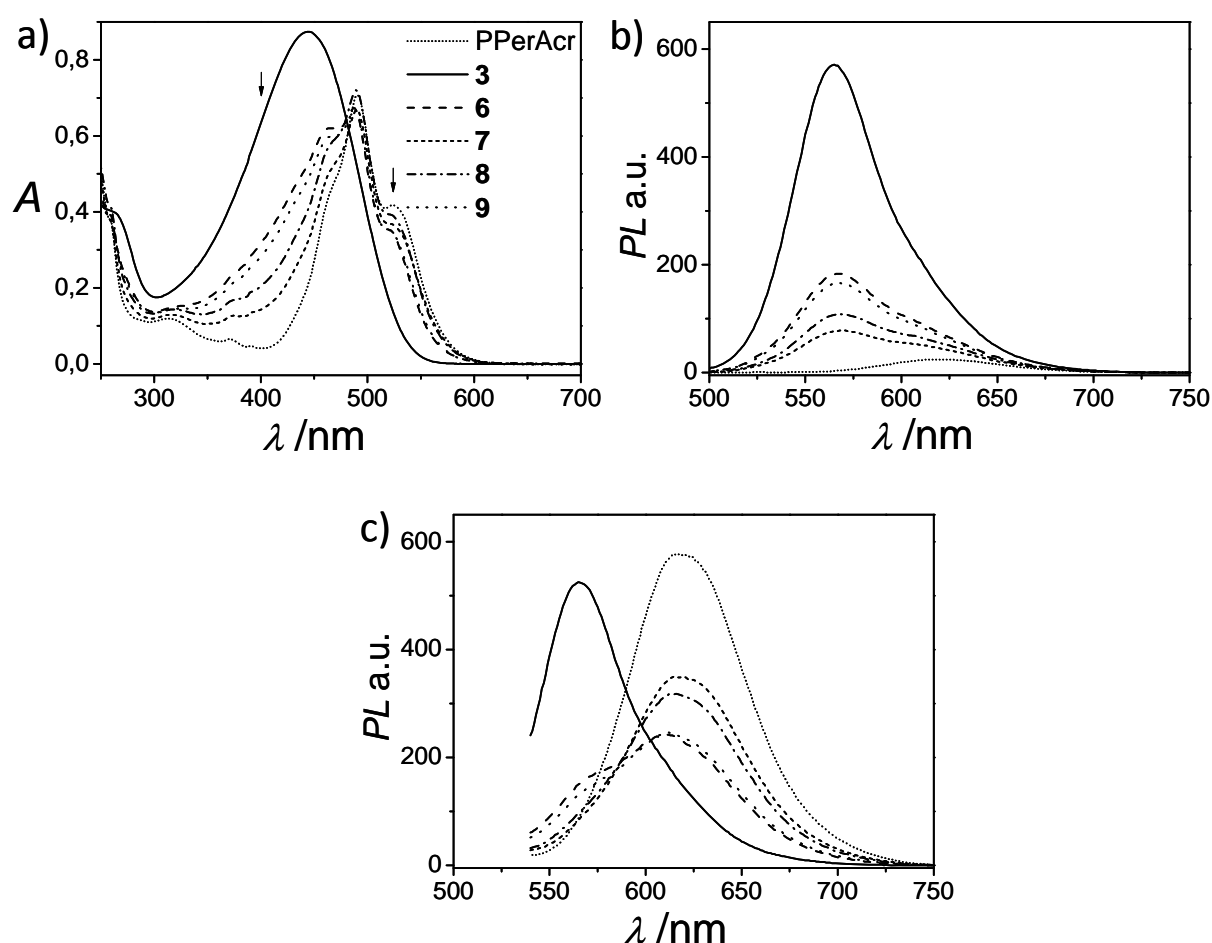


**Figure 3:** Absorption and emission spectra of macroinitiator P3HT-I 3 and block copolymers P3HT-block-PPerAcr 6-9 in solution (THF, 0.02 mg/ml). The code (dashes and dots) is equal for all. The data of a perylene bisimide homopolymer PPerAcr is also shown for clarity. a) absorbance spectra and b,c) photoluminescence spectra upon excitation at b) 400 nm and c) 530 nm. The arrows in a) indicate the wavelength of excitation.

In order to provide evidence for microphase separation, we perform scanning electron microscopy (SEM) on a bulk sample of **6** (figure 4). Microns long bright domains of PPerAcr are observed, which most probably are due to a fibrillar microstructure of PPerAcr in a P3HT matrix. The orientation of the fibrils is random, dot-like and elongated structures suggest

vertically and horizontally oriented domains. This is in contrast to fibrillar structures commonly observed in films of P3HT and P3HT block copolymers.<sup>[25]</sup> Here, the bright domains are due to aggregation of perylene bisimide. No structural changes were observed for longer annealing times suggesting the presence of an equilibrium morphology. Thus, we demonstrate for the first time that microphase separation is possible in a fully functionalized block copolymer consisting of two crystalline blocks. This finding unambiguously shows that defined charge transport pathways of both holes and electrons in separate domains can be provided in one single material.

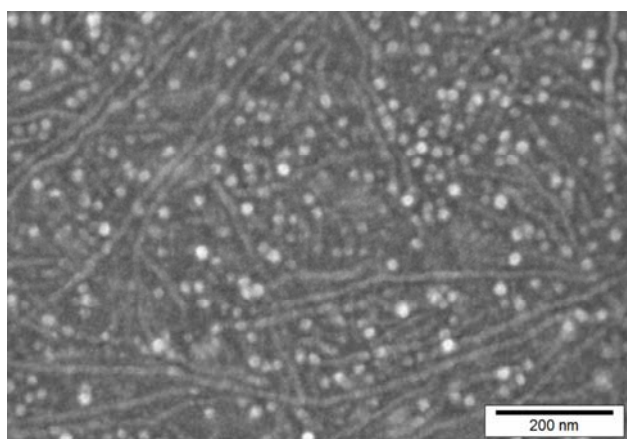


**Figure 4:** Scanning electron micrograph of the surface of a bulk sample of block copolymer 6 after annealing in chloroform vapor for four days. The pattern of dots and stripes indicates fibrillar PPerAcr structures in a P3HT matrix. Bright and dark regions correspond to PPerAcr and P3HT, respectively.

In conclusion, we present the first crystalline-crystalline donor-acceptor block copolymers with poly(3-hexylthiophene) as donor block and poly(perylen bisimide acrylate) as acceptor block. We show that the various complex issues in photovoltaic devices or ambipolar field effect transistors such as light absorption, the presence of a donor-acceptor heterojunction, photoluminescence quenching, crystallinity and microphase separation can thus be addressed by the tailor-made synthesis of a block copolymer. The observation of microphase separated domains in the bulk is extremely encouraging, especially when considering that both blocks are crystalline. This finding may also solve morphological problems encountered in organic solar cells from blends of P3HT and low molecular weight perylene bisimides, where external quantum efficiencies of 19 % were already demonstrated.<sup>[26,27]</sup> Therefore, we not only expect the novel block copolymers to outperform these simple blend devices but we also envision additional applications in ambipolar field effect transistors.

## Acknowledgements

Financial support of this work by the Deutsche Forschungsgemeinschaft (SFB 481) and the European Science Foundation (EUROCORES SOHYDs) is gratefully acknowledged.

## References

1. B. Thompson, J. M. J Fréchet, *Angew. Chem. Int. Ed.* **2008**, *47*, 58.
2. J. Zaumseil, H. Sirringhaus, *Chem. Rev.* **2007**, *107*, 1296.
3. F.S. Bates, G.H. Fredrickson, *Ann. Rev. Phys. Chem.* **1990**, *41*, 525.
4. S. M. Lindner, M. Thelakkat, *Macromolecules* **2004**, *37*, 8832.
5. S. M. Lindner, S. Hüttner, A. Chiche, M. Thelakkat, G. Krausch, *Angew. Chem. Int. Ed.* **2006**, *45*, 3364.
6. M. Sommer, S. M. Lindner, M. Thelakkat, *Adv. Funct. Mater.* **2007**, *17*, 1493.
7. S. M. Lindner, N. Kaufmann, M. Thelakkat, *Org. Electr.* **2007**, *8*, 69.
8. M. H. van der Veen, B. de Boer, U. Stalmach, K. I. van de Wetering, G. Hadziioannou, *Macromolecules* **2004**, *37*, 3673.
9. K. Sivula, Z. T. Ball, N. Watanabe, J. M. J. Frechet, *Adv. Mater.* **2006**, *18*, 206.
10. G. Tu, H. Li, M. Forster, R. Heiderhoff, L. J. Balk, U. Scherf, *Macromolecules* **2006**, *39*, 4327.
11. F. Richard, C. Brochon, N. Leclerc, D. Eckhardt, T. Heiser, G. Hadziioannou, *Macromol. Rapid Commun.* **2008**, *29*, 885.
12. R. S. Loewe, S. M. Khersonsky, R. D. McCullough, *Adv. Mater.* **1999**, *11*, 250.
13. R. Miyakoshi, A. Yokoyama, T. Yokozawa, *J. Am. Chem. Soc.* **2005**, *127*, 17542.
14. M. Jeffries-El, G. Sauve, R. D. McCullough, *Adv. Mater.* **2004**, *16*, 1017.
15. M. C. Iovu, M. Jeffries-El, E. E. Sheina, J. R. Cooper, R. D. McCullough, *Polymer* **2005**, *46*, 8582.
16. C. P. Radano, O. A. Scherman, N. Stingelin-Stutzmann, C. Müller, D. W. Breiby, P. Smith, R. A. J. Janssen, E. W. Meijer, *J. Am. Chem. Soc.* **2005**, *127*, 12502.
17. C.-A. Dai, W.-C. Yen, Y.-H. Lee, C.-C. Ho, W.-F. Su, *J. Am. Chem. Soc.* **2007**, *129*, 11036.
18. B. W. Boudouris, C. D. Frisbie, M. A. Hillmyer, *Macromolecules* **2008**, *41*, 67.

19. M. C. Iovu, C. R. Craley, M. Jeffries-El, A. B. Krankowski, R. Zhang, T. Kowalewski, R. D. McCullough, *Macromolecules* **2007**, *40*, 4733.
20. D. Benoit, V. Chaplinski, R. Braslau, C. J. Hawker, *J. Am. Chem. Soc.* **1999**, *121*, 3904.
21. R. Miyakoshi, A. Yokoyama, T. Yokozawa, *Macromol. Rapid Commun.* **2004**, *25*, 1663.
22. M. Sommer, M. Thelakkat, *Eur. Phys. J. Appl. Phys.* **2006**, *36*, 245.
23. B. Charleux, J. Nicolas, O. Guerret, *Macromolecules* **2005**, *38*, 5485.
24. S. Hüttner, M. Sommer, M. Thelakkat, *Appl. Phys. Lett.* **2008**, *92*, 093302.
25. J. Liu, E. Sheina, T. Kowalewski, R. D. McCullough, *Angew. Chem. Int. Ed.* **2002**, *41*, 329.
26. J. J. Dittmer, E. A. Marseglia, R. H. Friend, *Adv. Mater.* **2002**, *12*, 1270.
27. W. S. Shin, H.-H. Jeong, M.-K. Kim, S.-H. Jin, M.-R. Kim, J.-K. Lee, J. W. Lee, Y.-S. Gal, *J. Mater. Chem.* **2006**, *16*, 384.

## Supporting Information

**General information:** All glass apparatus were dried at 110 °C and cooled down under argon unless otherwise noted. Solvents used for precipitation and soxhlet extraction were distilled under normal atmosphere. Styrene was dried over CaH<sub>2</sub> and distilled prior to use. Dry 1,2-dichlorobenzene was purchased from Aldrich. THF was distilled over CaCl<sub>2</sub> and subsequently over potassium for at least three days each and stored under argon. Isopropylmagnesiumchlorid was purchased from Fluka. 2-bromo-3-hexyl-5-iodothiophene **1**<sup>[1]</sup> and Ni(dppp)Cl<sub>2</sub><sup>[2]</sup> were prepared according to literature procedures. 2,2,5-trimethyl-3-(1-(4'-chloromethyl)phenylethoxy)-4-phenyl-3-azahexane **2** and the corresponding free nitroxide **5** were synthesized according to Hawker et al.<sup>[3]</sup> Perylene bisimide acrylate PerAcr **4** was synthesized using a standard procedure.<sup>[4]</sup> For the synthesis of the block copolymers, the free nitroxide and styrene were added to the reaction mixture as stock solutions in 1,2-dichlorobenzene. <sup>1</sup>H NMR spectra were acquired on a Bruker AC 250 spectrometer (250 MHz). Molecular weights were determined by size exclusion chromatography (SEC) in THF containing 0.25 wt.-% tetrabutylammonium bromide with UV and RI detectors (Waters) using polystyrene standards for calibration. UV/vis spectra were recorded using a Hitachi U-

3000 spectrometer. Fluorescence spectra were recorded on a Shimadzu RF-5301 PC spectrofluorophotometer. The thermal degradation of polymers was studied using a Mettler Toledo TGA/SDTA 851 with a heating rate of 10 K/min under N<sub>2</sub> atmosphere. Differential scanning calorimetry was carried out with a Perkin Elmer Diamond DSC with a heating rate of 10 K/min under N<sub>2</sub> atmosphere. Scanning electron microscopy was done on a Zeiss Leo 1530 at a acceleration voltage of 1 kV. Samples for SEM were prepared on indium tin oxide. The polymer was placed on a substrate with a droplet of chlorobenzene, dried and put in a desiccator together with a beaker of chloroform. Before imaging, the sample was covered with 2 nm of platinum.

**Synthesis of macroinitiator P3HT 3.** A 250 ml schlenk flask equipped with a stirr bar and a septum was evacuated, flame dried, cooled down and the atmosphere was replaced with argon. 3.342 g (8.956 mmol) of **1** were added and the flask was evacuated again. 45 ml THF were added and the flask was cooled down to 0 °C. 5.43 ml (8.956 mmol) of <sup>i</sup>PrMgCl were added via syringe and the mixture was stirred for 90 min. A suspension of 139 mg Ni(dppp)Cl<sub>2</sub> (0.256 mmol) in 2 ml THF were rapidly introduced via syringe at 0 °C, upon which the color turned from yellowish to red and finally to dark brown. The mixture was allowed to warm to room temperature and then stirred for 1 h. In situ endcapping was done by adding the endcapper 2,2,5-trimethyl-3-(1-(4'-magnesiumchloromethyl)phenylethoxy)-4-phenyl-3-azahexane **2** (preparation of **2**: 150 mg (30 mmol) magnesium turnings and 1 ml THF were placed in a 5 ml schlenk tube and 2 g of 2,2,5-trimethyl-3-(1-(4'-chloromethyl)phenylethoxy)-4-phenyl-3-azahexane **2** (30 mmol) in 1 ml THF were added and the whole was stirred overnight). After 30 min, the reaction was stopped by pouring the mixture into 400 ml of methanol and the raw product was collected by filtration. After several washing cycles in methanol, the raw product was dissolved in toluene, precipitated into n-hexanes for the removal of oligomers, filtered and dried.  $M_{n,SEC} = 8900$  g/mol, PDI= 1.1, % RR= 93.8 (calculated from the methylene units at 2.8 and 2.6 ppm after subtraction of one endgroup).

<sup>1</sup>H-NMR (250 MHz, CDCl<sub>3</sub>);  $\delta$  (ppm)= 7.49-7.11 (m, 0.27 H, ar CH alkoxyamine), 6.98 (s, 1H), 4.88 (m, 0.03 H, CHON alkoxyamine), 4.08 (m, 0.06 H, benzylic CH<sub>2</sub> alkoxyamine), 3.40 and 3.27 (2d, 0.03 H, ONCH), 2.78 (t, 2H, CH<sub>2</sub>), 2.56 (m, 0.2 H, CH<sub>2</sub> TT-couplings and endproups),

1.70 (m, 2H, CH<sub>2</sub>), 1.36 (m, 6H, CH<sub>2</sub>), 0.91 (t, 3H, CH<sub>3</sub>), 0.53 and 0.21 (2d, 0.18 H, CH<sub>3</sub> alkoxyamine).

**General synthesis for P3HT-*b*-PPerAc 6-9.** In a 5 ml schlenk tube, 200 mg **3** (0.04 mmol), 1.7 mg (0.008 mmol) free nitroxide (TIPNO), styrene and perylene acrylate PerAc **4** were added together with *o*-dichlorobenzene (*o*-DCB). After degassing three times, the mixture was stirred at 125 °C. The polymerization was stopped by rapid cooling and the viscous product was dissolved in chlorobenzene. Precipitation into acetone and filtration yielded a dark raw product which was then further extracted in a soxhlet apparatus with ethyl methyl ketone until colorlessness of the extracted solution.

**Table 1.** Amount of monomers, solvent, reaction time and yield for the synthesis of block copolymers **6-9**.

polymer	styrene [mg]	PerAc [mg]	<i>o</i> -DCB [μl]	time [h]	yield [mg]
<b>6</b>	4.1 mg	600	400	9	363
<b>7</b>	6.2 mg	990	595	10	385
<b>8</b>	8.2 mg	1244	724	13	632
<b>9</b>	10.4 mg	1650	925	18	887

<sup>1</sup>H-NMR of **7** (shown for all) (250 MHz, CDCl<sub>3</sub>); δ (ppm)= 8.85-7.45 (br, 8H, ar CH perylene bisimide), 6.98 (s, 1.75 H, ar CH thiophene), 5.06 (br, 1H, CH perylene bisimide swallow tail), 4.04 (br, 4H, NCH<sub>2</sub> and OCH<sub>2</sub> perylene bisimide alkyl spacer), 2.75-2.48 (t+m, 3.54H, CH<sub>2</sub> thiophene), 2.17 (br, 3.24H, CH<sub>2</sub>), 1.93 (br, 2.85H, CH<sub>2</sub>), 1.8-1.0 (br, 59.2H, CH<sub>2</sub>), 1.0-0.7 (br, 12.9H, CH<sub>3</sub>).

1. R. Miyakoshi, A. Yokoyama, T. Yokozawa, *Macromol. Rapid Commun.* **2004**, *25*, 1663.
2. G. R. Van Hecke, W. D. Horrocks, *J. Inorg. Chem.* **1966**, *5*, 1968.
3. D. Benoit, V. Chaplinski, R. Braslau, C. J. Hawker, *J. Am. Chem. Soc.* **1999**, *121*, 3904.
4. S. M. Lindner, M. Thelakkat, *Macromolecules* **2004**, *37*, 8832.

## 5. Semiconductor Block Copolymers for Photovoltaic Applications

Michael Sommer,<sup>a</sup> Sven Hüttner,<sup>a,b</sup> and Mukundan Thelakkat<sup>a</sup>

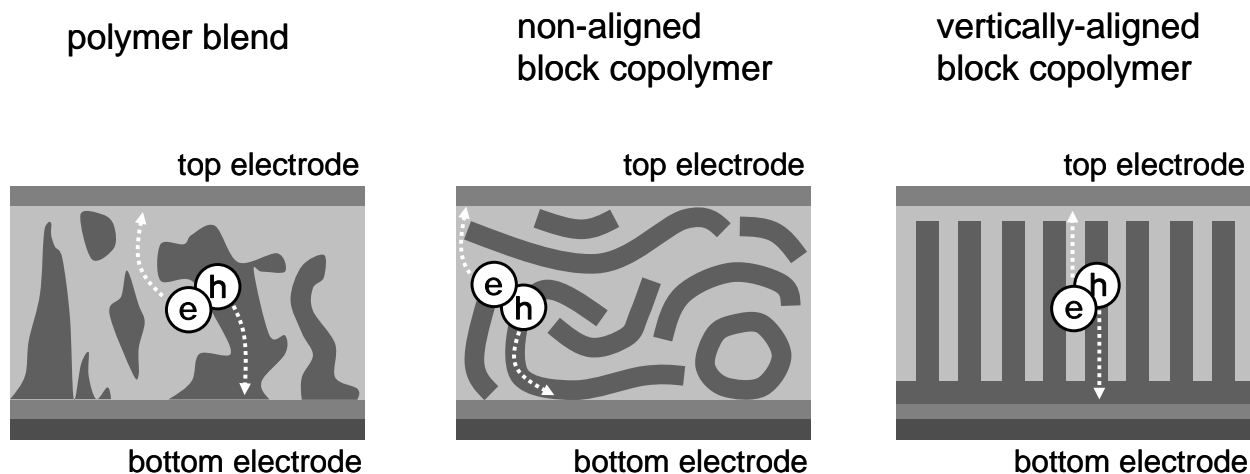
<sup>a</sup>Applied Functional Polymers and Macromolecular Chemistry I

Universität Bayreuth, Universitätsstr. 30, University of Bayreuth, 95444 Bayreuth, Germany

<sup>b</sup>Thin Films and Interfaces Group, Cavendish Laboratory, BSS Physics

11 JJ Thomson Avenue, Cambridge CB3 0HE, United Kingdom

[Michael.Sommer@uni-bayreuth.de](mailto:Michael.Sommer@uni-bayreuth.de), [Mukundan.Thelakkat@uni-bayreuth.de](mailto:Mukundan.Thelakkat@uni-bayreuth.de)



## Abstract

Tremendous research activities in synthesis and device engineering has been devoted to the development of donor-acceptor (D-A) bulk heterojunction solar cells in the last years. Several photophysical processes occur in such devices which have to be optimized for an efficient device operation. First, excitons that are created upon light absorption need to reach the D/A interface within their exciton diffusion length (10- 20 nm) where they dissociate into holes and electrons. Subsequent charge transport and finally charge collection at the electrodes can take place then, given that co-continuous pathways of donor and acceptor domains are provided. An active layer thickness larger than 200 nm is required for complete light absorption, and vertically aligned pathways with a high aspect ratio of either phase should protrude through the film, taking into account the small exciton diffusion lengths. The morphologies resulting from this ideal situation resemble those of vertically oriented, microphase separated block copolymer thin films, and hence suggest the importance of D-A block copolymers for organic photovoltaics. Furthermore, complex block copolymer architectures are not only desired in order to improve the morphological control but also to enhance the long term stability of the device. The potential of such block copolymers to microphase separate into well-defined structures that are several tens of nanometers in size thus addresses the morphological requirements mentioned above. This article gives an overview of the emerging field of donor acceptor block copolymers. General synthetic efforts that have been undertaken towards this direction are summarized. The donor-acceptor block copolymers prepared in our group are reviewed and complemented with recent work on crystalline-crystalline block copolymers, with a focus on polymerization methods to control block copolymer architecture, morphology and finally the device performance.

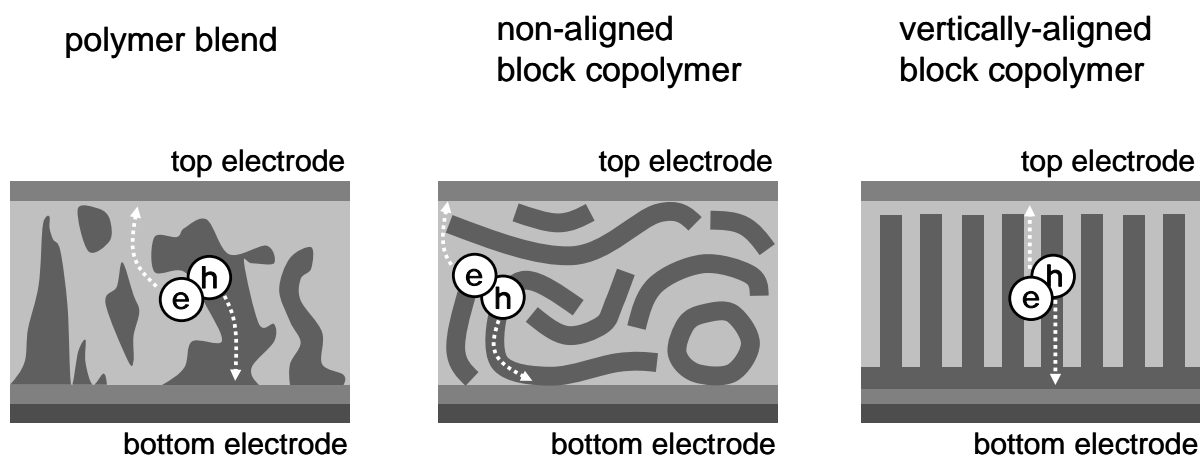
## 1. Introduction: History and donor acceptor block copolymer architectures

Since the first report of an efficient organic photovoltaic (OPV) device made by C. Tang *et al.* in 1986<sup>1</sup>, power conversion efficiencies (PCEs) are evolving together with an increased understanding of the underlying fundamental processes occurring in active layers of an electron donor (D) and an electron acceptor (A).<sup>2</sup> The continuous enhancement in device performance can partially be attributed to the development of novel materials with favourable electronic properties.<sup>3-5</sup> More importantly, intense efforts concerning the optimization of the active layer blend morphology have substantially contributed to the development of PCEs that now range between 4-6%.<sup>6-10</sup> Since charge generation and charge recombination in organic bulk heterojunction solar cells occur at the D/A interface, precise control of the size and the shape of this interface is crucial in order to achieve further improvements. From a materials chemists' point of view, it is therefore essential to develop new materials as well as new concepts that allow to improve morphology control.

A higher level of morphological control can be achieved by exploiting various interactions between either same molecules of donor or acceptor, or between the donor and the acceptor molecule. Furthermore, asymmetric surface fields of the device can induce a vertically segregated morphology suitable for bulk heterojunction solar cells.<sup>11</sup> For example, by processing a P3HT/PCBM blend together with a small amount of a fullerene derivative with fluorinated solubilizing groups, these fluorinated side chains segregated at the air-blend interface to form a pure acceptor monolayer onto which the aluminium electrode was deposited.<sup>12</sup> With the goal of creating supramolecular pathways of donor and acceptor groups,  $\pi$ - $\pi$  interactions<sup>13</sup> and hydrogen bonds were exploited.<sup>14</sup> In another study, hydrogen bonds between only the acceptor moiety perylene bisimide were introduced as a structure-directing tool.<sup>15</sup> As a result, thin films comprised of a three dimensional mesoscopic acceptor network could be fabricated. Most strikingly, this acceptor network architecture was maintained even when processing the material together with an amorphous donor polymer, giving a D-A heterojunction with defined morphology, charge transport pathways and domain sizes in the range of the exciton diffusion length.<sup>16</sup> This result is encouraging since perylene bisimides tend to form very large one-dimensional stacks or crystals<sup>17,18</sup>, which has restricted the use of this type of acceptor in organic solar cells up to now.<sup>19-21</sup> Even stronger interactions for interface tuning can be provided by a covalent bond between the donor and

the acceptor moiety. Manifold architectures have been designed, e.g D-A dyads<sup>22</sup> or double-cable polymers<sup>23,24</sup>, only to name a few. The motivation for the often challenging synthesis was clearly driven by the advantage of a highly intermixed D-A morphology capable of efficient charge separation. Once the charges are separated, they have to percolate towards the respective electrodes. This process occurs most efficiently when the transport pathways between the two electrodes are straight and do not exhibit dead ends.

Indeed, the phase separation of active layers of donor acceptor bulk heterojunction solar cells is an intricate issue. A phase separation in the nanoscale range is needed for efficient charge transport, yet macrophase separated polymer blends do not exhibit sufficient interfacial area for charge generation and recombination of the excitons will occur prior to charge separation.<sup>25-29</sup> In this respect the molecular junction - as realized in molecular assemblies of D-A dyads, or in the double cable polymers - enables perfect and stable mixing of donor and acceptor groups whereas a polymer blend tends to minimize its interfacial area. Consequently something in between - a stable morphology with co-continuous domains of D and A tens of nanometers thin - is sought to be obtained. Although this has been achieved quite successfully by accelerating and subsequently freezing in the demixing process of bulk heterojunction solar cells, the resulting morphologies are not stable and the domains are ill-defined. By contrast, the equilibrium microstructures of block copolymers are well-defined and can be tuned in size and shape when the molecular weight and the length of the individual blocks are varied.<sup>30</sup> Therefore, block copolymers that carry electronic functions hold great promise for the application in OPV's. Co-continuous morphologies suitable for photovoltaic active layers include cylindrical, lamellar or gyroidal phases. The construction of such microstructures from D-A block copolymers via self-assembly thus might solve the dilemma between the need of having ordered transport pathways and sufficient optical absorption on a length scale that is commensurate to the exciton diffusion length.<sup>31</sup> Furthermore, techniques for preparing ordered microstructures - meaning macroscopically aligned domains that are oriented perpendicular to the electrodes - are developed well and have been successfully demonstrated using conventional block copolymers without electronic functions.<sup>32-34</sup> A graphical illustration of various morphological scenarios from active layers from blends and block copolymers is depicted in scheme 1.



**Scheme 1.** Different donor acceptor active layer morphologies between the devices' electrodes. The left drawing depicts a polymer blend morphology with large, undefined and inhomogeneous domains. In the middle and at the right, schematic active layer morphologies of disordered and vertically aligned microphase separated block copolymer thin films are shown. Dark and light gray domains correspond to the donor and the acceptor phase, respectively.

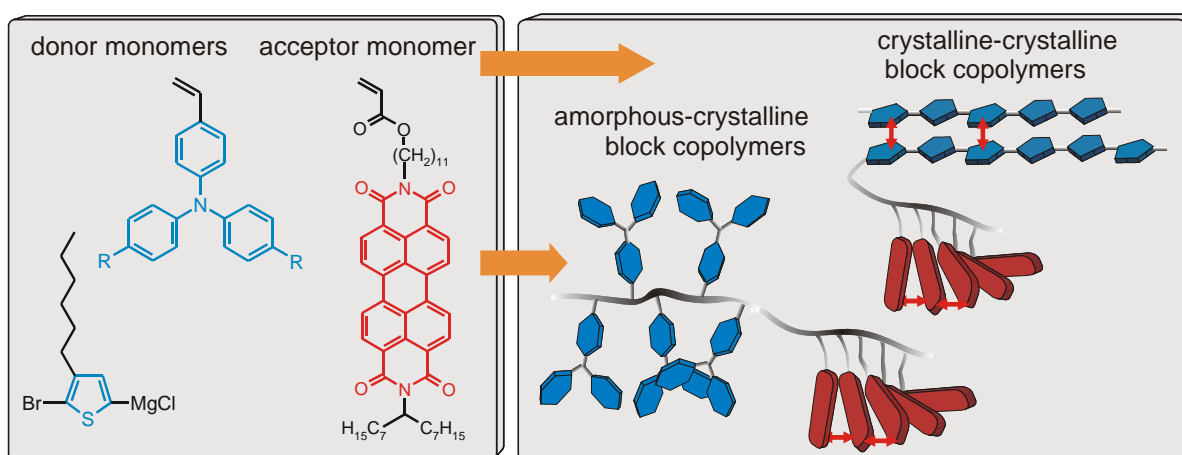
Whereas vertical alignment of cylindrical and lamellar block copolymers might be advantageous for improving the device performance, gyroidal films do not require alignment. Recently, an elegant example for this has been given by Snaith *et al.*, who used a double sacrificial block copolymer to incorporate a gyroidal TiO<sub>2</sub> replicate into liquid electrolyte dye-sensitized solar cells.<sup>35</sup> However, the direct formation of the gyroid mesophase from a fully functionalized donor acceptor block copolymer has not been realized up to now. The covalent connectivity of the donor and the acceptor blocks results in another positive advantage of these highly sophisticated polymer architectures: the equilibrium structure exhibits smaller domain sizes than polymer blends. If formed, further crystallization of the two phases, concomitant with an increase in domain size and a decrease in interfacial area, can thus be excluded. This is an important issue concerning the morphological long-term stability of OPV's.

In contrast to conventional and commercially available block copolymers, block copolymers that carry one or more electronically active blocks are rare and the synthesis is challenging. Very often, multi-step organic synthetic procedures have to be combined with one or more polymerization techniques. Further difficulties arise from the limited solubilities and the limited amount of material available from one batch, making the preparation of such materials tedious and time-consuming. Accordingly, only a few examples are known in the literature.

The first D-A block copolymers with suitable electronic properties for charge separation were synthesized in the group of Hadziioannou *et al.*, using a conjugated poly(phenylene vinylene) (PPV) block as macroinitiator for the nitroxide mediated radical polymerization (NMRP) of a second styrenic coil block. This second segment was converted to the acceptor block by attaching C<sub>60</sub> molecules.<sup>36</sup> As pointed out by the authors, very strong interactions between the fullerenes, either by partial cross-linking<sup>37</sup> or by the strong crystallization<sup>38</sup> possibly accounted for the lack of microdomains after C<sub>60</sub> functionalization. In another study, Scherf *et al.* prepared D-A triblock copolymers from monobromo-terminated P3HT and dibromo-cyano substituted CN-PPVs via Yamamoto coupling.<sup>39</sup> Freché *et al.* made use of ring opening metathesis polymerization (ROMP) to subsequently polymerize two macromonomers containing P3HT and fullerene. The products found application as compatibilizers in bulk heterojunction solar cells.<sup>40</sup> However, microphase separation was not demonstrated in these systems and only in two cases, a photovoltaic effect with solely the block copolymer as the active layer was reported.<sup>38,41</sup>

The D and A moieties used in the majority of the above mentioned synthetic approaches towards donor-acceptor block copolymers are conjugated polymers and fullerene derivatives. This makes the preparation very challenging and special attention has to be given to the introduction of appropriate solubilizing groups. A low weight fraction of e.g alkyl chains should render the polymer insoluble whereas a solubilizing group fraction that is too high will result in poor performance of the device since the amount of active material decreases. This is a general issue in such systems, and becomes clearly visible in the case of polymers containing fullerene.<sup>42</sup> Perylene bisimide (PBI) as an alternative electron acceptor has been overlooked for years since the power conversion efficiencies of solution-processed devices did not reach those of comparable polymer-fullerene cells.<sup>43</sup> The main reason was seen in the uncontrolled crystallization of PBI, resulting in large crystals concomitant with poor morphological control.<sup>19</sup> Yet, suitable electronic properties and absorption in the visible range make this acceptor compound interesting for light harvesting applications and apparently, PBI is regaining interest for photovoltaic applications.<sup>20,21,44</sup> Also, the chemical derivatization of the PBI core is feasible since the two distinct imide positions can be substituted independently without altering the electronic properties. Making use of these facts, Thelakkat *et al.* designed a highly soluble and polymerizable perylene bisimide

derivative bearing a branched alkyl substituent at one imide position and a linear, acrylate-functionalized alkyl spacer at the other imide position. The incorporation of this monomer into block copolymers with poly(triphenylamine) as the donor yielded highly soluble donor acceptor block copolymer exhibiting all important requirements for photovoltaic applications.<sup>45</sup> The valuable design and synthesis of this polymerizable electron conducting monomer marked the beginning of a variety of block copolymers with side-chain crystalline perylene bisimide blocks and donor blocks, either being amorphous or crystalline (scheme 2).



**Scheme 2.** Various donor and acceptor monomers can be combined to obtain block copolymers with either amorphous or crystalline segments. In the left box, the polymerizable monomers are shown. The right box depicts the schematic architectures of the resulting two main classes of D-A block copolymers: amorphous-crystalline and crystalline-crystalline block copolymers.

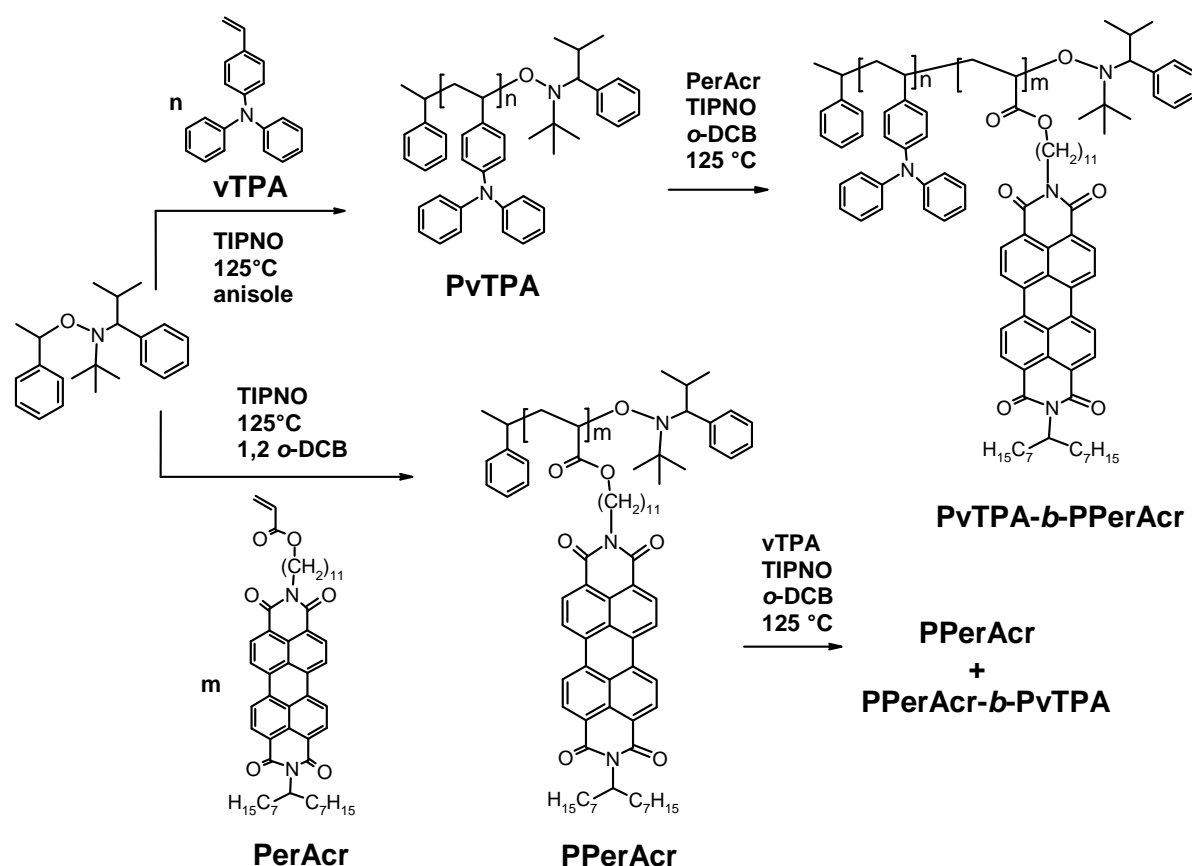
The following sections summarize the work of our group concerning the synthesis, the morphology and the application of such D-A block copolymers in photovoltaic devices. The paper is divided into two main sections: The first section covers amorphous-crystalline block copolymers, in which the donor function is taken care of amorphous side-chain poly(triarylamine)s. The architecture of such block copolymers is schematically shown in the right box of scheme 2. In the second section, very recent work on crystalline-crystalline block copolymers incorporating P3HT as donor block is presented. We try to comprehensively picture this interdisciplinary field by giving special emphasis to achievements as well as drawbacks in chemical synthesis. Furthermore, a broad and detailed characterization of the novel materials is given. Finally, the chapters are finished with unique results concerning the

morphology of these complex materials, and first promising results concerning the application in photovoltaic devices are presented.

## **2. Amorphous-crystalline donor acceptor block copolymers**

### **2.1. Synthesis and characterization**

With the advent of the polymerizable acceptor monomer perylene bisimide acrylate (PerAcr), an electronically eligible donor monomer and a suitable polymerization method had to be picked from the toolbox of organic and polymer chemistry. We chose vinyltriphenylamine (vTPA) as a starting point since the synthesis can be carried out in only one step and its energy levels form sufficient HOMO offset with perylene bisimide. This assures a sufficient driving force for efficient electron transfer from D to A. In general, living or “quasi-living” polymerization methods are necessary to create the required block copolymer architectures. Additional criteria such as tolerance to functional groups and impurities as well as a metal-free nature are to be preferred. Therefore, controlled radical polymerizations were selected and among the methods available, nitroxide mediated radical polymerization (NMRP) conformed to these preconditions.<sup>46</sup> Based on these building blocks, sequential NMRP of vTPA and PerAcr was performed using a common unimolecular alkoxyamine developed by Hawker *et al.*<sup>47</sup> The resulting synthesis of the fully functionalized block copolymers PvTPA-*b*-PPerAcr is shown in scheme 3.<sup>45</sup>

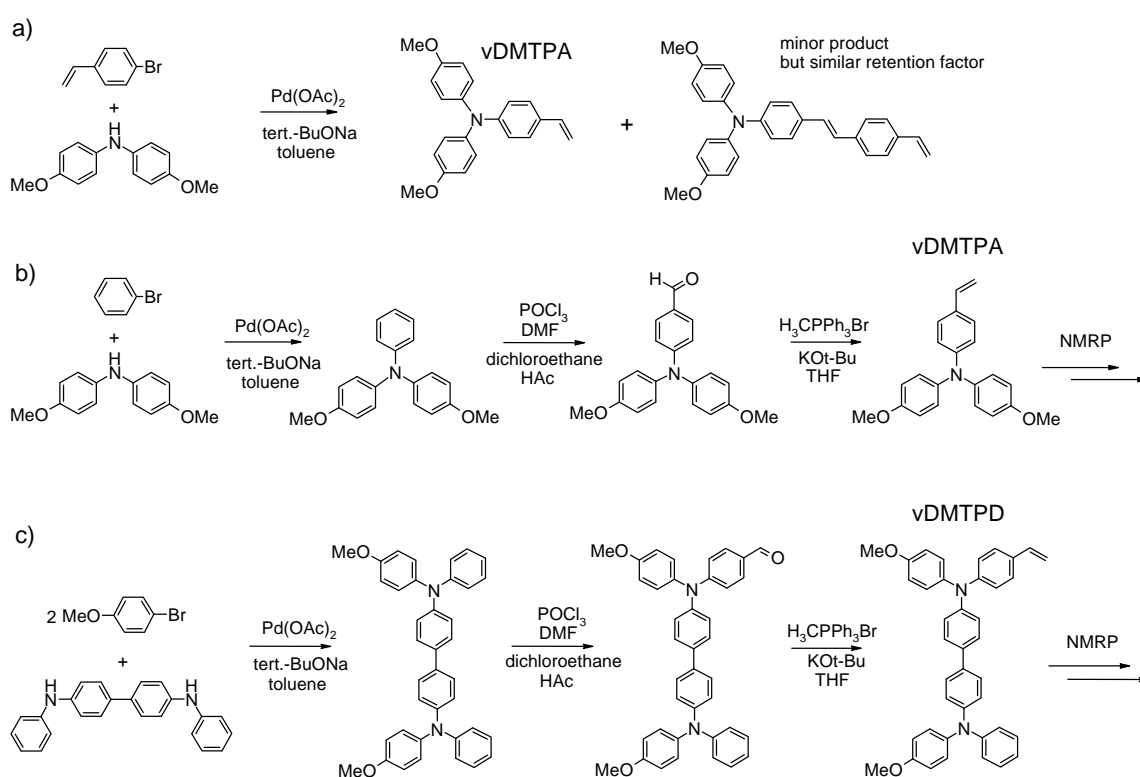


**Scheme 3.** Synthetic scheme of the two possible pathways towards PvTPA-b-PPerAc block copolymers via NMRP. Using PvTPA as a macroinitiator for the NMRP of PerAc gave monomodal block copolymers whereas starting from PPerAc as macroinitiator, a mixture of PPerAc and the corresponding PPerAc-b-PvTPA block copolymer was obtained. o-DCB: ortho-dichlorobenzene, TIPNO: 2,2,5-trimethyl-4-phenyl-3-azahexane-3-oxyl.

Interestingly, polymerizing the acrylate monomer PerAc starting from the styrenic PvTPA macroinitiator led to better-defined block copolymers than starting from the acrylate-based macroinitiator PPerAc. This is invers to the proposed order in the literature.<sup>46</sup> A reason for that can arise from chain transfer during the polymerization of PerAc producing dead chain ends that do not carry the mediating nitroxide.<sup>48</sup> When PerAc was polymerized as the second monomer the block length could be adjusted via the monomer to macroinitiator ratio and different block copolymers with varying acceptor content were obtained.

In order to vary the HOMO offset at the D-A heterojunction and the hole mobility of the donor block, we also prepared substituted triphenylamine and tetraphenylbenzidine monomers with two methoxy substituents.<sup>49</sup> Scheme 4 shows the synthesis of bis(4-methoxyphenyl)-4'-vinylphenylamine (vDMTPA) and N,N'-bis(4-methoxyphenyl)-N-phenyl-

*N*'-4-vinylphenyl-(1,1'-biphenyl)-4,4'-diamine (vDMTPD). The first monomer, vDMTPA, can be prepared from 4-bromostyrene and 4,4'-dimethoxydiphenylamine via Buchwald-Hartwig amination<sup>50</sup> in one step. However, the formation of a side product with a very similar retention factor made the purification of large monomer batches difficult (scheme 4a). To circumvent this, a three-step synthetic procedure was chosen instead as outlined in scheme 4b. Interestingly, vTPA gives a white powder after concentrating from solution whereas vDMTPA is viscous and difficult to handle, and therefore, crystals of vDMTPA were grown from *n*-hexanes. The latter step was vital for an increase in the control of the polymerization and the common features of a living character were observed. The NMRP in anisole for a monomer-initiator-free nitroxide ratio of 200:1:0.1 resulted in low polydispersities between 1.1 and 1.2. The desired molecular weights of PvDMTPA were obtained by either varying the polymerization time or the initiator to monomer ratio. Figure 1a shows the linear increase of the experimental molecular weight with conversion and figure 1b size exclusion chromatography curves of different macroinitiators with molecular weights between 5 and 30 kg/mol.



**Scheme 4.** a) One-step synthesis of bis(4-methoxyphenyl)-4'-vinylphenylamine (vDMTPA) and formation of the side product bis(4-methoxyphenyl)-4'-vinyl-4''-styrylamine. b) Three-step procedure of vDMTPA. c) Synthesis of *N,N'*-bis(4-methoxyphenyl)-*N*-phenyl-*N'*-4-vinylphenyl-(1,1'-biphenyl)-4,4'-diamine (vDMTPD). Synthesis of macroinitiator and the preparation of block copolymers via NMRP were carried out analogously to scheme 3.

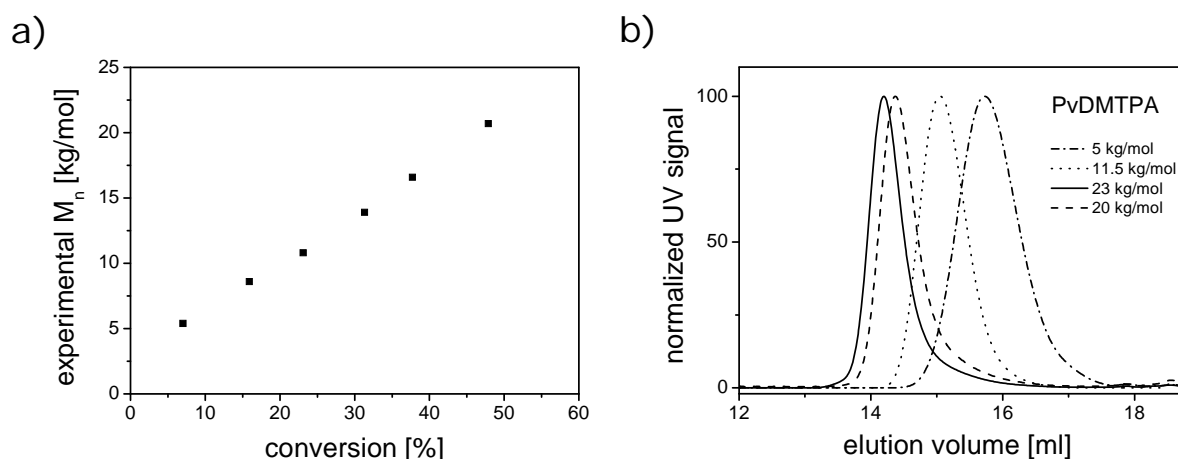


**Figure 1.** a) Linear increase of the experimental molecular weight of PvDMTPA vs conversion (determined by  $^1\text{H-NMR}$ ) for the NMRP of vDMTPA using a monomer-alkoxyamine-TIPNO ratio of 200:1:0.1. The extrapolated experimental molecular weight of 3.2 kg/mol at conversion= 0 % arises from calibration with polystyrene standards. b) SEC curves of the elution volume of different well-defined PvDMTPA macroinitiators.

The block copolymer synthesis of PvDMTPA-*b*-PPerAcr was conducted analogously to the reactions with PvTPA as a macroinitiator. Note that block copolymer synthesis with PerAcr became more difficult with increasing molecular weight of the macroinitiator. Longer reaction times were necessary and the block copolymers generally exhibited broader molecular weight distributions. This might be due to the increased sterical hindrance of the active chain end with increasing molecular weight of the macroinitiator, retarding the polymerization of PerAcr and increasing the probability of side reactions such as chain end decomposition.<sup>51</sup> An illustration for this is given in figure 2a and 2b, where two PvDMTPA macroinitiators with different molecular weights are shown together with their resulting block copolymers. Obviously, the SEC curve of the block copolymer in 2a ( $M_n$  PvDMTPA= 9 kg/mol) is symmetric and no macroinitiator signal is found, whereas the curve of block copolymer in 2b is asymmetric due to remaining PvDMTPA ( $M_n$  PvDMTPA= 18 kg/mol). This has to be kept in mind since block copolymers with larger blocks generally give a better device performance, as will be shown later.

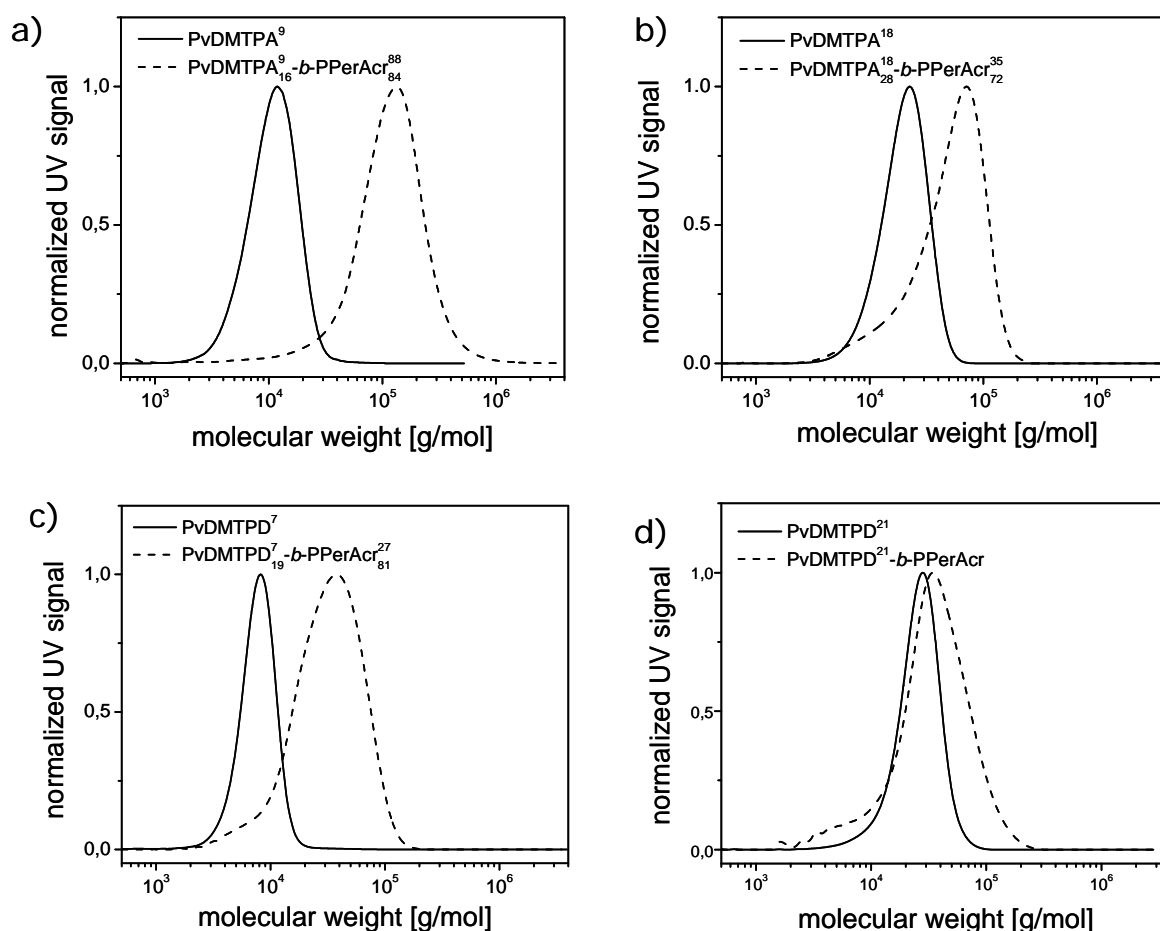
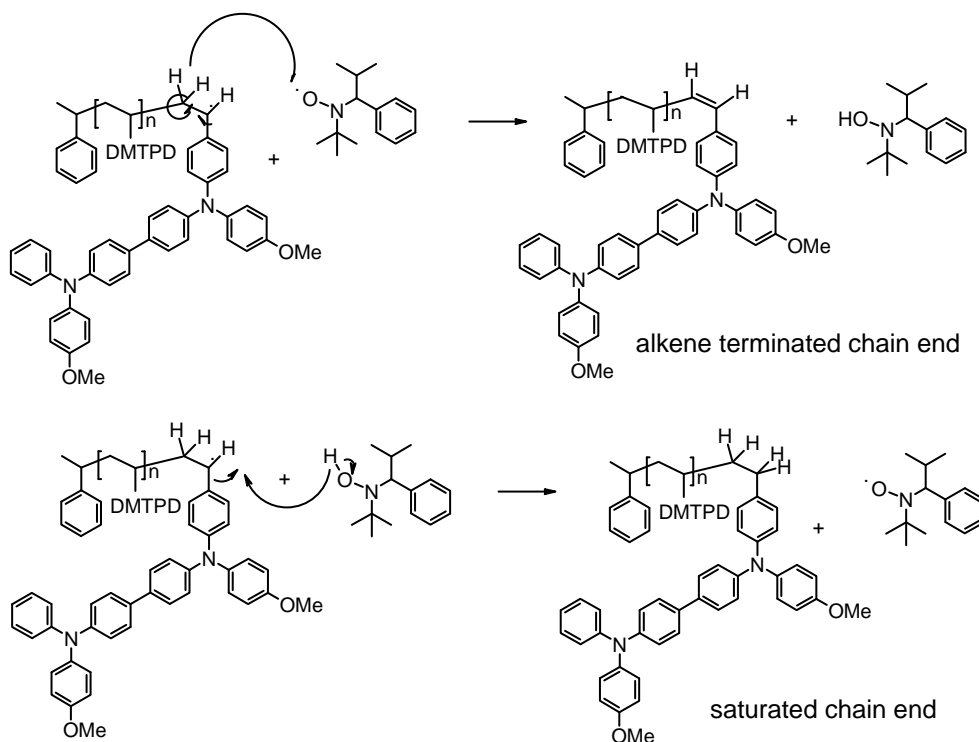


**Figure 2.** SEC curves of PvDMTPA and PvDMTPD macroinitiators together with their resulting block copolymers PvDMTPA-*b*-PPerAc and PvDMTPD-*b*-PPerAc. PvDMTPA blocks with an  $M_n$  of 9 kg/mol and 18 kg/mol were used in a) and b) and PvDMTPD blocks with an  $M_n$  of 7 kg/mol and 21 kg/mol in c) and d), respectively. Subscripts denote the weight fractions. The first superscript denotes the molecular weight of the macroinitiator and the second one the molecular weight of the block copolymer in kg/mol.

Finally, the concept of the amorphous side chain poly(triarylamines) was further extended to segments carrying tetraphenylbenzidines (TPDs). The reason for that is the enhanced charge carrier mobility of TPDs compared to TPAs.<sup>52,53</sup> Methoxygroups were introduced to the TPD unit in 4-position for the sake of solubility. Such electron-rich groups also give rise to tuning of the HOMO level<sup>54</sup>, providing an important tool not only for controlling solubility but also the electronic properties. The monomer synthesis of N,N'-bis(4-methoxyphenyl)-N-phenyl-N'-4-vinylphenyl-(1,1'-biphenyl)-4,4'-diamine (vDMTPD) and the subsequent polymerization via NMRP is depicted in scheme 3. Similar polymerization conditions that were already applied to the polymerizations of vDMTPA resulted in narrow-distributed and well defined

macroinitiators PvDMTPD with polydispersities around 1.2. However, polymerizations of vDMTPD had to be quenched at lower conversions, typically at ~30 %, since the viscosity of the reaction mixture increased faster compared to PvDMTPA. By using larger amounts of the solvent, only slightly higher conversions were achieved and the polydispersity increased to moderate values around 1.5. Thus, the monomer vDMTPD itself together with a small amount of solvent had to be used as reaction media and the polymer yields were accordingly lower. The synthesis of the second block was conducted analogously to vTPA and vDMTPA. However, when using PvDMTPD as a macroinitiator for the polymerization of PerAcr, the success of the block copolymer synthesis generally was strongly influenced by the molecular weight of PvDMTPD. When macroinitiators with chain lengths up to 10 kg/mol were used, a clear shift towards smaller elution volumes was observed in SEC after the polymerization of PerAcr, even though a shoulder remained at the elution volumes of the macroinitiator (figure 2c). This indicates the presence of non-functionalized PvDMTPD chains (arising from termination reactions during vDMTPD polymerization) or chain termination at early stages during the initiation step of the synthesis of the second block. PvDMTPD macroinitiators with higher molecular weights between 15 kg/mol and 20 kg/mol could not successfully start the controlled polymerization of PerAcr. In such cases, the SEC traces of the products did not shift to smaller elution volumes, and instead peak broadening occurred (figure 2d). Apparently, the increasingly challenging synthesis of the second block with higher molecular weights of the macroinitiator already observed in the case of PvDMTPA pursued for PvDMTPD. The sterical hindrance and the electron richness of the PvDMTPD radical might be responsible for this trend. An illustration for this is given in scheme 5 in which the general chain end composition mechanism of NMRP is depicted for PvDMTPD.



**Scheme 5.** Possible chain end degradation mechanisms during the NMRP of vDMTPD. Termination can occur during the polymerization of vDMTPD or when using PvDMTPD as a macroinitiator for the polymerization of the electron conducting monomer PerAc.

Indeed, the  $^1\text{H-NMR}$  spectrum of the ethyl methyl ketone fraction of the product after PerAc polymerization confirmed this assumption by featuring two dupletts at 5.57 ppm and 5.82 ppm, indicating the formation of the alkene-terminated PvDMTPD chain ends. The issue of chain end degradation also becomes visible when PvDMTPD is used as a macroinitiator for the NMRP of commercially available monomers such as 4-vinylpyridine (4vP). However, due to the fast polymerization of 4vP, chain end degradation in the beginning of the polymerization is likely to be suppressed to a certain degree and high molecular weight PvDMTPD macroinitiators were successfully incorporated into block copolymers PvDMTPD-*b*-P4vP.<sup>55</sup> Mixtures of PvDMTPD-*b*-P4vP and inorganic CdSe:Te nanocrystals formed highly ordered lamellar block copolymer morphologies with the inorganic n-type particles located exclusively in the P4vP domains. Such inorganic nanocrystal:block copolymer hybrid materials are very interesting for photovoltaic applications, since they combine the different and various advantages of the single systems, namely high electron mobility, morphological control on a nanoscopic level and processability.

## 2.2 Thermal properties

The thermal properties of the homopolymers and block copolymers were investigated by thermogravimetric analysis (TGA) and differential scanning calorimetry (DSC). These measurements determine thermal stabilities and phase transitions of the materials; informations that are necessary for later device annealing procedures. In the case of block copolymers with crystalline segments, additional insight can be gained concerning crystal size, degree of crystallinity and mechanism of crystallization. Figure 3a shows the TGA curves of the two homopolymers PvDMTPA and PPerAcr and the block copolymer PvDMTPA<sub>16</sub><sup>9</sup>-*b*-PPerAcr<sub>84</sub><sup>88</sup>. Subscripts denote the weight fractions. The first superscript denotes the molecular weight of the macroinitiator and the second one the molecular weight of the block copolymer in kg/mol.

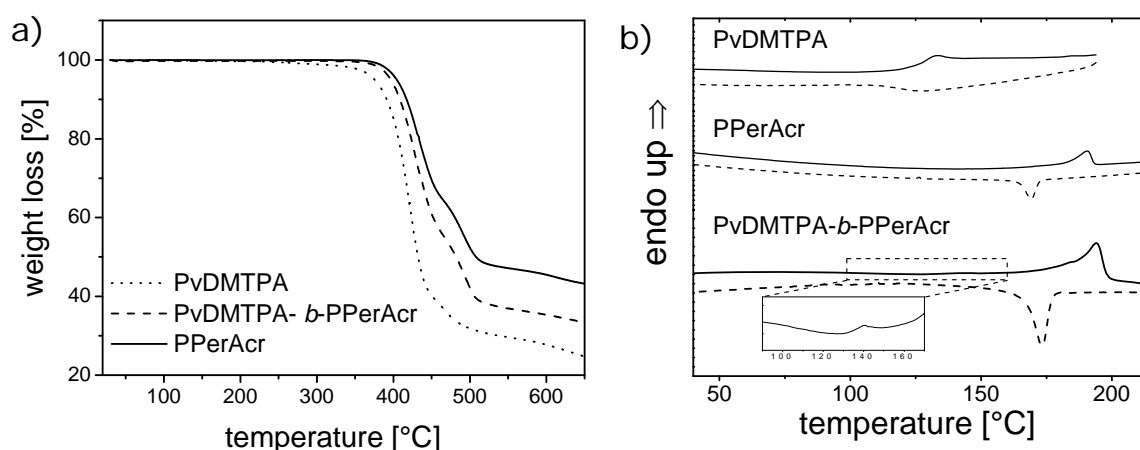


**Figure 3.** a) TGA curves of PvDMTPA, PPerAcr and PvDMTPA<sub>16</sub><sup>9</sup>-*b*-PPerAcr<sub>84</sub><sup>88</sup>. Curves were measured at 10 K/min under nitrogen. b) DSC curves of the same polymers measured at 10 K/min in the case of PPerAcr and at 20 K/min in the case of PvDMTPA and PvDMTPA<sub>16</sub><sup>9</sup>-*b*-PPerAcr<sub>84</sub><sup>88</sup>. The second heating (solid line) and the second cooling (dashed line) cycle is shown, curves are offset for clarity.

All the three compounds are thermally stable and exhibit onset temperatures of 221 °C, 323 °C and 306 °C, respectively. Also, the thermal stability is sufficiently high, and decomposition occurs only above the temperature range of the phase transitions. Figure 3b shows the DSC traces of these compounds. A glass transition temperature  $T_g$  of 129 °C is observed for the amorphous PvDMTPA and, compared to PvTPA ( $T_g$ = 150 °C), is reduced by 21 °C due to the methoxy substituents in para position. The PPerAcr block features a melting temperature  $T_m$  of 190 °C due to the side-chain crystallization. This side-chain crystallinity is caused by the

strong  $\pi$ - $\pi$  interactions of neighboring perylene bisimide units. Both transitions are present in the block copolymer - even though the  $T_g$  is weak due to the small weight fraction of the amorphous block of only 16 % (see inset of figure 3b) - and the temperatures of the transitions only deviate marginally compared to the homopolymers. The latter fact supports a microphase separation, that leads to a crystalline PPerAcr phase in an amorphous donor matrix. The melting enthalpies of PPerAcr and PvDMTPA<sub>16</sub><sup>9</sup>-*b*-PPerAcr<sub>84</sub><sup>88</sup> are 9.8 and 7.9 J/g, respectively. In general, compared to the homopolymer, a decrease of the melting enthalpies of the PPerAcr block with decreasing block length was observed.

### 2.3 Electronic and optical properties

In this section the materials are investigated in terms of their energy levels, their absorption profiles in film and their charge carrier mobilities. The HOMO and LUMO levels are estimated from cyclic voltammetry in solution in combination with UV-vis spectroscopy and the charge carrier mobilities are extracted from measurements on organic field effect transistors (OFETs). As will be shown, the methoxy groups of PvDMTPA influence both, the position of the HOMO energy level as well as the charge carrier mobility of the donor block. Cyclic voltammetry (CV) measurements of PvTPA in solution feature an irreversible oxidation peak at 0.4 V vs ferrocene (Fc), giving a HOMO energy level of 5.2 eV (figure 4a,b).<sup>56</sup> Irreversible oxidations are commonly observed for unsubstituted TPAs and the evolving new bands arise from dimerization products that are oxidized at lower potentials.<sup>57</sup> PvDMTPA is oxidized at 0.2 V vs Fc, corresponding to a HOMO level of 5.0 eV. The oxidation peak remains constant after several cycles, demonstrating the reversibility of oxidation. Surprisingly, the first oxidation of PvDMTPD also occurs at 0.2 V vs Fc, resulting in the same HOMO level as PvDMTPA. The cyclic voltammogram of PPerAcr did not exhibit a clear oxidation peak, and therefore the monomer PerAcr was used for HOMO level determination. This compound showed an oxidation at 1.2 V vs Fc, corresponding to a HOMO level of 6.0 eV. The first reductions of PerAcr and PPerAcr both occurred at -1.2 eV. Thus, the position of the LUMO level is 3.6 eV, and, as expected, is found to be independent of the molecular weight of PPerAcr. Generally, all events of oxidation and reduction were found to be independent of the molecular weight and the presence of the second block. The LUMO energy levels of the

amorphous donor blocks were estimated from the CV results and the UV-vis absorbance in film. Figure 4c shows the absorption of the three block copolymers. The donor blocks exhibit the typical triarylamine absorption up to 400 nm and PPerAcr features three characteristic bands between 400 nm and 600 nm, corresponding to a highly aggregated state of the PBI moieties.<sup>58</sup> Since the absorption profile is sensitive to changes in the relative orientation of the PBI chromophores<sup>59</sup>, we tentatively propose that stacking of backbone-neighbored PBI moieties occurs along columns with a rotational offset, in a similar fashion to what has been shown for low molecular weight PBIs.<sup>17</sup> Figure 4d depicts the resulting energy levels of the three donor polymers with PPerAcr as the acceptor. As can be clearly seen, the resulting energy level offsets are sufficiently large for efficient charge separation in all the block copolymers, being 0.8- 1.0 eV for  $\Delta$ HOMO and  $\sim$  1.5 eV for  $\Delta$ LUMO.<sup>60</sup>

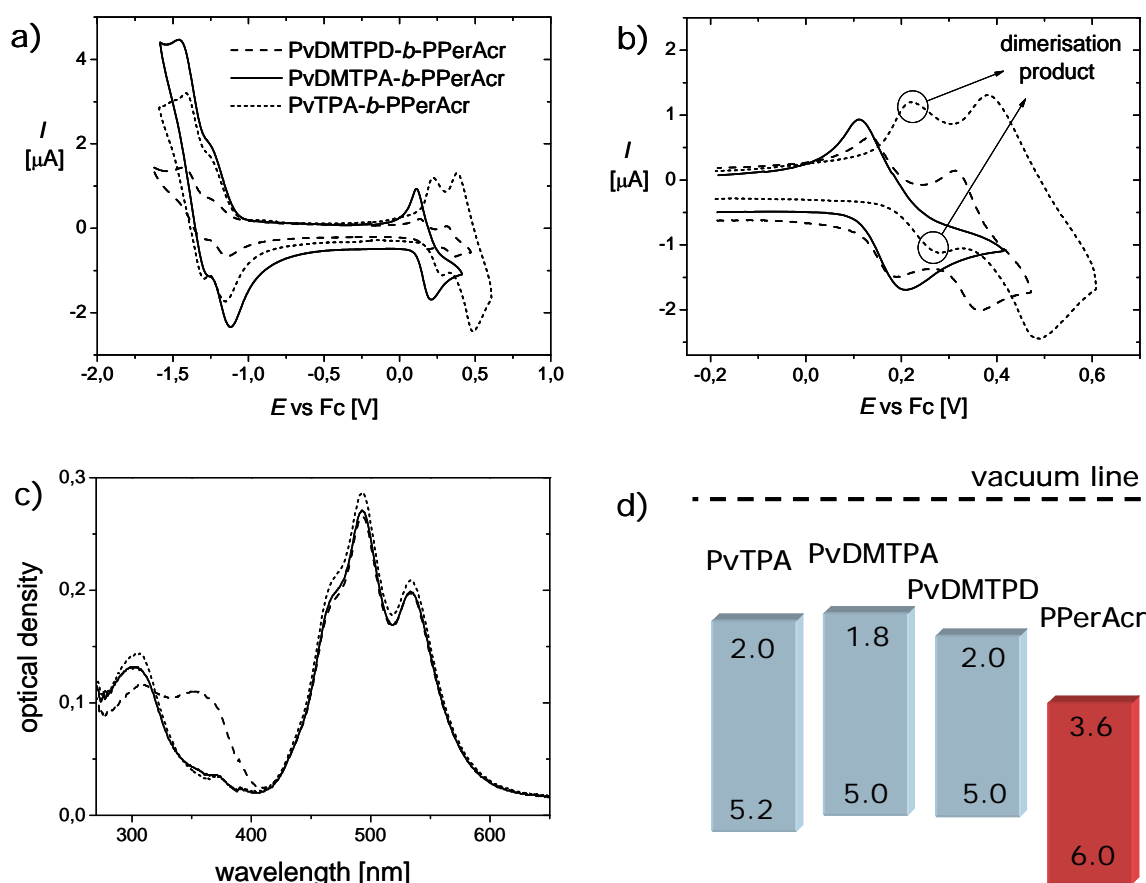


**Figure 4.** a) Cyclic voltammograms of PvTPA-*b*-PPerAcr (dotted line), PvDMTPA-*b*-PPerAcr (solid line) and PvDMTPD-*b*-PPerAcr (dashed line). b) Enlarged region of poly(triarylamine) oxidation. All curves were measured in *o*-dichlorobenzene containing tetrabutyl ammonium hexafluorophosphate at 50 mV/s vs Fc (Fc: ferrocene). c) Optical densities of films (70 nm) of PvTPA-*b*-PPerAcr (dotted line), PvDMTPA-*b*-PPerAcr (solid line) and PvDMTPD-*b*-PPerAcr (dashed line). Due to the similar content of PPerAcr in all block copolymers, the optical density between 400 and 600 nm is almost equal. d) Schematic drawing of the estimated energy levels in eV.

Organic field effect transistor measurements on the homopolymers were carried out for the determination of the charge carrier mobilities.<sup>61,62</sup> Generally, TPDs are better hole conductors than TPAs and therefore, a higher charge carrier mobility can be expected for polymer PvDMTPD. The simplest polymer PvTPA showed a very weak performance, with high threshold voltages, small on-off ratios and small charge carrier mobilities  $\mu$ . Annealing the sample at approximately 15 °C above its  $T_g$  caused a significant increase in the performance leading to over ten times higher drain currents and a charge carrier mobility of around  $3 \cdot 10^{-5}$  cm<sup>2</sup>/Vs. The threshold voltage remained still quite high at -37 V. In contrast, the two polymers PvDMTPA and PvDMTPD showed a different behaviour. Right after spin casting, both the PvDMTPA and the PvDMTPD performed significantly better, but no significant improvement was seen after thermal annealing. Both materials show low threshold voltages between -4 to -5 V. The PvDMTPD is superior in terms of its charge carrier mobility and its on-off ratio. The PvDMTPA has a mobility  $\mu_{\text{sat}} = 5 \cdot 10^{-5}$  cm<sup>2</sup>/Vs and an on-off ratio of  $10^2$ , whereby PvDMTPD has a mobility of  $\mu_{\text{sat}} = 1.2 \cdot 10^{-4}$  cm<sup>2</sup>/Vs and an on-off ratio of  $10^3$ . The transfer characteristics of the donor polymers after annealing are shown in figure 5a. In contrast, the electron mobility of PPerAcr depends strongly on the thermal history of the transistor device. Spin casting PPerAcr from chloroform yielded devices with weak performances and high threshold voltages around 20 V. This changes dramatically after annealing the samples at 210 °C for 60 min, which is above the melting temperature of PPerAcr of 190 °C. The threshold voltage drops significantly to 6.8 V, while the current and charge carrier mobility both increase by two orders of magnitude. Thus electron transport abilities of up to  $1.2 \cdot 10^{-3}$  cm<sup>2</sup>/Vs were achieved. Figure 5b shows the transfer plot of PPerAcr before and after annealing.

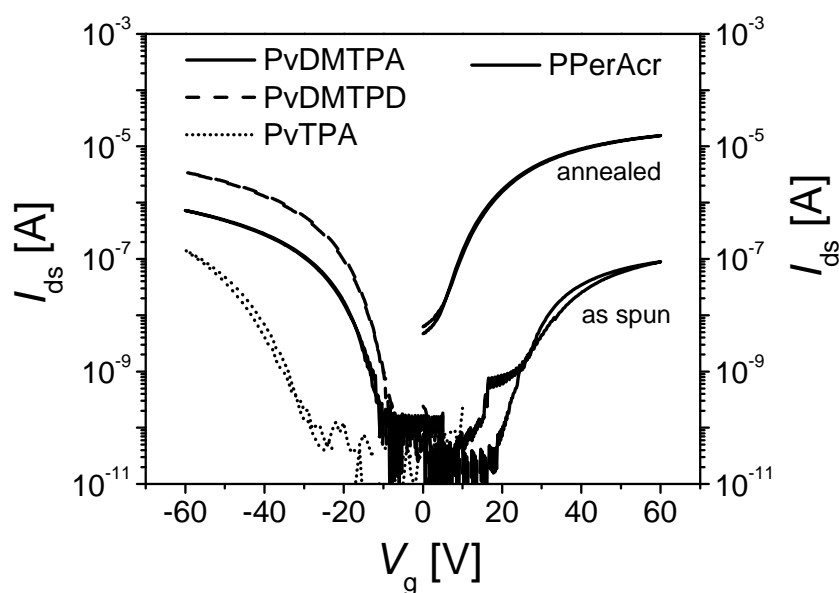


**Figure 5.** a) Transfer plots of the homopolymers PvTPA, PvDMTPA and PvDMTPD after thermal annealing above the  $T_g$  for a drain voltage of 60 V (negative gate voltage) and transfer characteristics of the PPerAcr homopolymer before and after annealing above the  $T_m$  (drain voltage 20 V, positive gate voltage).

Based on these results, we can derive several essential differences between PvTPA and PvDMTPA: Firstly, the HOMO level shifts from 5.2 eV to 5.0 eV. Secondly, PvDMTPA is electrochemically stable because the two para positions are blocked and can not give rise to dimerization reactions. Lastly, the charge carrier mobility of PvDMTPA is increased compared to PvTPA, due to the electron-rich methoxy substituents. The HOMO level position of PvDMTPA is maintained in PvDMTPD, which carries tetraphenylbenzidine moieties, and the charge carrier mobility of PvDMTPD is highest among the three donor polymers. Thus, if incorporated into block copolymers with the acceptor polymer PPerAcr, this set of amorphous donor blocks is ideal for correlating the solar cell performance with important parameters such as energy levels, charge carrier mobility and morphology. By opposing these results with morphological informations from electron microscopy, this structure-property relationship is evaluated in the following chapter

## 2.4 Morphology and device performance

In general, blends of amorphous donor polymers and PBI acceptors, being either small molecules or polymers, are not capable of a controlled phase separation. The crystallization of low molecular weight PBIs normally results in large and inhomogeneous crystals, and regarding the poly(perylene bisimide acrylate), macrophase separation with a concomitant crystallization leads to micron-sized domains. Block copolymers with one amorphous block

and one side-chain crystalline PPerAcr block can solve this problem quite elegantly by confining perylene bisimide crystallization in nanometer-sized, either cylindrical or lamellar domains.<sup>63</sup> This block copolymer approach is thus unique in controlling the size and the shape of the PPerAcr acceptor microdomains, and can now be used to tune down the structural features to the range of the exciton diffusion length. Indeed, block copolymers with all the functionalities required for photovoltaic applications can outperform their analogous polymer blends, as was demonstrated recently for the case of PvTPA-*b*-PPerAcr (figure 6).<sup>64</sup>

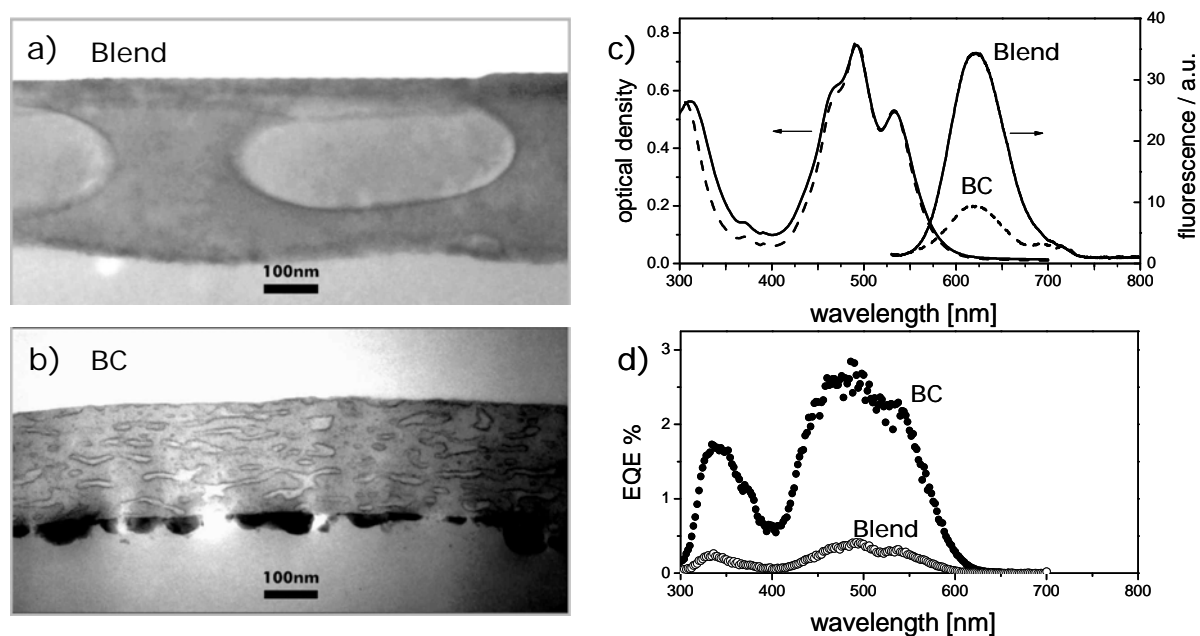


**Figure 6.** a) Cross sectional TEM of active layers of a PvTPA:PPerAcr blend and b) of a PvTPA-*b*-PPerAcr block copolymer (BC). c) Optical density and photoluminescence quenching. d) External quantum efficiency (EQE) of these same films. The films are stained with RuO<sub>4</sub>, bright regions in a) and b) are due to PPerAcr domains.

The two TEM pictures of figure 6 unambiguously point out the advantage of the block copolymer in terms of creating a larger interfacial area between the donor and the acceptor phase (figure 6b). Macrophase separation, as it occurs in the blend film (figure 6a), is impeded in the block copolymer due to the covalent connectivity of the two blocks. The larger interface of D and A in the block copolymer film also gives rise to a higher degree of photoluminescence quenching (figure 6c) and finally leads to a six-fold external quantum efficiency (EQE) and to a ten-fold improvement in the power conversion efficiency. In the

block copolymer film, more excitons can reach the D-A interface where they are separated into holes and electrons (figure 6d). Evidently, the structural features in figure 6b represent a non-equilibrium state due after spin casting the block copolymer from chloroform solutions. If at all, the domains seem to be oriented rather parallel than perpendicular to the substrate. It has to be elucidated how such a block copolymer thin film morphology can be aligned vertically. Yet, the large improvement of the block copolymer device demonstrates the huge potential this approach offers and further enhancement is expected by optimizing processing and post-production treatments. However, the improvement of device efficiency by the chemical tuning of the material properties is also of utmost importance. Therefore, the complex interplay between the HOMO level offset, the hole carrier mobility, the morphology and the device performance will be comprehensively outlined in the following. The morphologies of the block copolymers with different hole conductors were first investigated by transmission electron microscopy of bulk samples. For this purpose, the polymers were thermally annealed above their melting temperatures, embedded into epoxy resin and microtomed ( $\sim 50$  nm). Subsequent staining was done with  $\text{RuO}_4$ , which preferentially reacts with PPerAcr. The staining time turned out to be an important parameter. Short treatment with  $\text{RuO}_4$  vapor was necessary to generate a sharp contrast between the two phases whereas staining times exceeding 30 min resulted in broader structures. The observed effect of initial boundary staining might be due to preferential staining of  $\text{RuO}_4$  with the amorphous PPerAcr that surrounds the crystalline PPerAcr phase. Such a phenomenon has been reported for semi-crystalline block copolymers poly(ethylene)-*b*-poly(vinylcyclohexane).<sup>65</sup> Figure 7 shows the TEMs of PvTPA-*b*-PPerAcr, PvDMTPA-*b*-PPerAcr and PvDMTPD-*b*-PPerAcr.

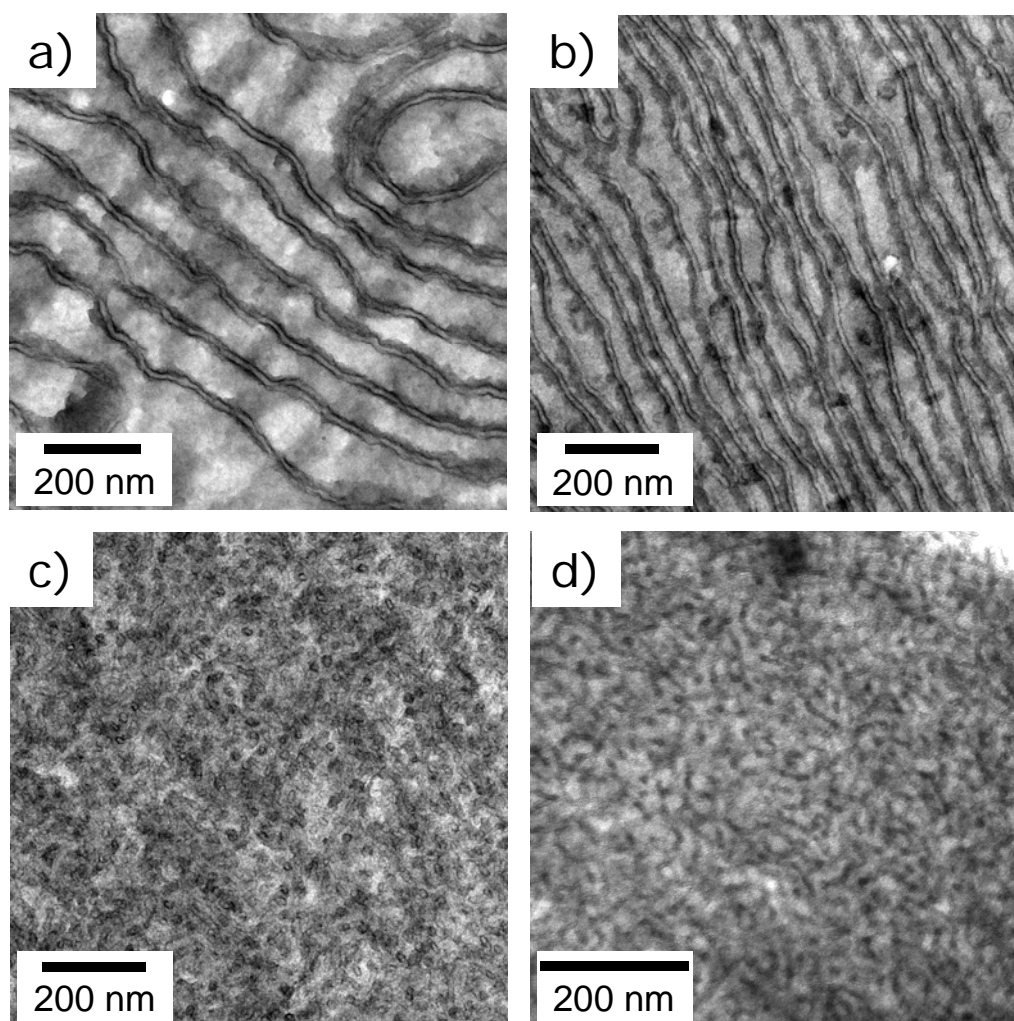


**Figure 7.** TEM pictures of thermally annealed bulk samples of a)  $\text{PvTPA}_{14}^{16}\text{-}b\text{-PPerAcr}_{86}^{26}$ , b)  $\text{PvDMTPA}_{28}^{18}\text{-}b\text{-PPerAcr}_{72}^{35}$ , c)  $\text{PvDMTPA}_{16}^9\text{-}b\text{-PPerAcr}_{84}^{88}$  and d)  $\text{PvDMTPD}_{19}^7\text{-}b\text{-PPerAcr}_{81}^{26}$ . Dark domains represent PPerAcr and the brighter ones the amorphous donor blocks. The samples were annealed above their melting temperatures, embedded into epoxy resin, microtomed and stained with  $\text{RuO}_4$ .

Figure 7a shows block copolymer  $\text{PvTPA}_{14}^{16}\text{-}b\text{-PPerAcr}_{86}^{26}$  with a donor block of  $\sim 16$  kg/mol, a PPerAcr weight fraction of 86 % and an overall molecular weight of  $\sim 26$  kg/mol. The microphase separated material exhibits crystalline PPerAcr lamellae (dark) in an amorphous PvTPA matrix (brighter). A similar morphology is observed from  $\text{PvDMTPA}_{28}^{18}\text{-}b\text{-PPerAcr}_{72}^{35}$  in figure 7b. Note that the term ‘wire-like’ used earlier in some of our publications maybe misleading, and will not be referred to as here.<sup>49,60</sup> The structures in figure 7c and 7d are substantially different compared to figures 7a and 7b. Worms or fibrils of PPerAcr appear in the micrographs of both polymers,  $\text{PvDMTPA}_{16}^9\text{-}b\text{-PPerAcr}_{84}^{88}$  (figure 7c) and  $\text{PvDMTPD}_{19}^7\text{-}b\text{-PPerAcr}_{81}^{26}$  (figure 7d). The morphologies in 7a and 7b are of particular interest for

photovoltaic applications since the both domains, donor as well as acceptor, percolate through the whole bulk sample. Since the molecular weight of the donor block is 16-18 kg/mol in 7a and 7b and 7-9 kg/mol in 7c and 7d, the length of the amorphous segment seems to decide on the formation of a lamellar morphology, if the PPerAcr weight fraction lies between 72 and 86 %. In order to correlate these structures with the PV device performance, solar cells were constructed from the same polymers. Note that the HOMO level offset is 1.0 eV in figure 7a and 0.8 eV in all the other polymers and that the hole carrier mobility increases from PvTPA (figure 7a) to PvDMTPA (figure 7b and 7c) to PvDMTPD (figure 7d). Indium tin-oxide (ITO) substrates covered with PEDOT:PSS were used for the preparation of photovoltaic devices. The active layer was spin cast from chloroform solutions (0.5 wt.-%) and the devices were completed with aluminum as top electrode. The current density-voltage ( $J$ - $V$ ) characteristics of these four polymers are shown in figure 8a.

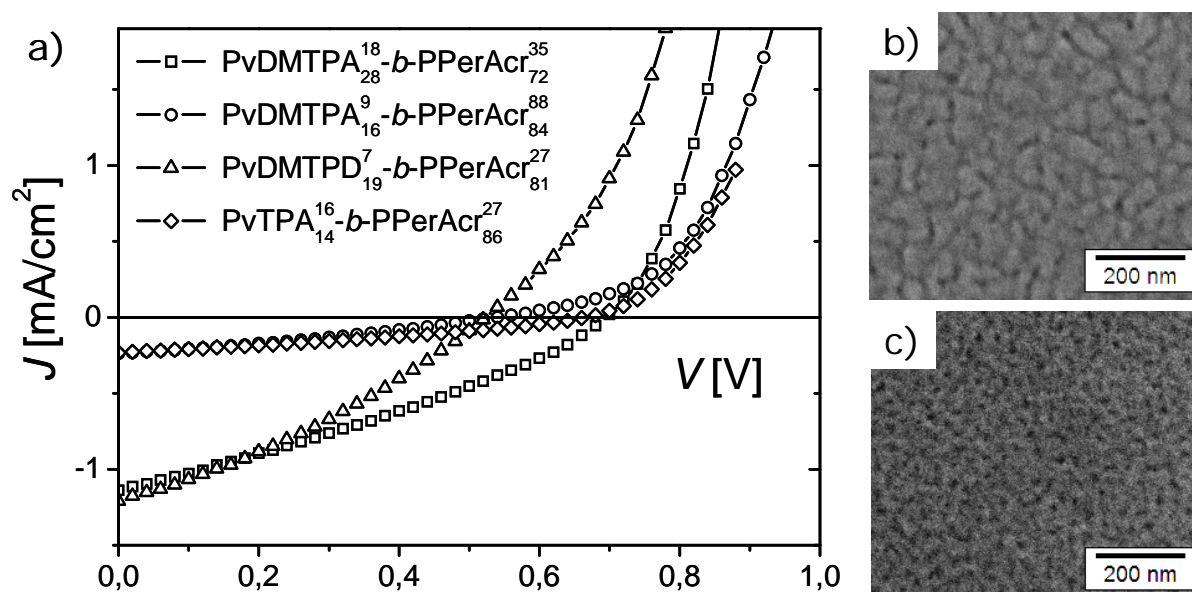


**Figure 8.** a)  $J$ - $V$ -characteristics of block copolymers with different donors and different molecular weights. b) SEM picture of the surface of the device made of PvDMTPA<sup>18</sup>-b-PPerAcr<sup>35</sup> solar cells. c) SEM picture of the surface of the device made of PvDMTPA<sup>9</sup>-b-PPerAcr<sup>88</sup>. Bright domains represent PPerAcr and the darker ones the amorphous donor blocks.

We first compare the  $J$ - $V$ -characteristics of the two block copolymers with PvTPA and PvDMTPA as donor and whose bulk morphologies are quite similar, as shown in figure 7a,b. The  $J_{SC}$  in the device made of PvDMTPA<sup>18</sup>-b-PPerAcr<sup>35</sup> amounts to 1.14 mA/cm<sup>2</sup> which is a

fivefold increase compared to  $0.23 \text{ mA/cm}^2$  in  $\text{PvTPA}_{14}^{16}\text{-}b\text{-PPerAcr}_{86}^{26}$ . This indicates that D-A charge transfer occurs more efficiently in the block copolymer with PvDMTPA than PvTPA as hole conductor, which is caused by the higher D/A HOMO offset (Fig. 4d). From the higher slope of the  $J$ - $V$ -curve of  $\text{PvDMTPA}_{28}^{18}\text{-}b\text{-PPerAcr}_{72}^{35}$  at open circuit conditions, it can be concluded that charges are injected more easily from PvDMTPA (HOMO= 5.0 eV) than from PvTPA (HOMO= 5.2 eV) into ITO. The maximum photovoltage that can be achieved at the D-A interface is given by  $\text{HOMO}_D\text{-LUMO}_A$ , implying a loss of photovoltage if  $\text{HOMO}_D$  is shifted to higher values. But this negative effect is compensated in  $\text{PvDMTPA}_{28}^{18}\text{-}b\text{-PPerAcr}_{72}^{35}$  due to an improvement in the hole transfer efficiency and, as a result, the  $V_{OC}$  of both devices are nearly the same (670 and 690 mV). Additionally, the different charge carrier mobilities of PvTPA and PvDMTPA contribute to the huge improvement of the device made of  $\text{PvDMTPA}_{28}^{18}\text{-}b\text{-PPerAcr}_{72}^{35}$ . Especially OFET devices as-spun from PvTPA and PvDMTPA exhibit a large difference in the hole carrier mobility, with  $\mu_{\text{hole}}$  being measured as  $1 \cdot 10^{-7}$  and  $3 \cdot 10^{-5} \text{ cm}^2/\text{Vs}$ , respectively. This difference decreases after thermal annealing, and values of  $3 \cdot 10^{-5} \text{ cm}^2/\text{Vs}$  and  $5 \cdot 10^{-5} \text{ cm}^2/\text{Vs}$ , respectively, are measured (see figure 5a).<sup>61</sup> Since the active layer of the block copolymer solar cells is spin cast from chloroform solution and the  $J$ - $V$ -characteristics are measured without annealing the devices, the large differences in the OFET hole mobilities as spun partially cause the five-fold increase in the short circuit current and in the power conversion efficiency of  $\text{PvDMTPA}_{28}^{18}\text{-}b\text{-PPerAcr}_{72}^{35}$ . The attachment of the methoxygroups thus influences the electronic properties of the amorphous donor polymers to a large extent, which again affects the device performance.

In the following, the impact of morphology on the  $J$ - $V$ -characteristics of  $\text{PvDMTPA}\text{-}b\text{-PPerAcr}$  block copolymers is elucidated. Block copolymer  $\text{PvDMTPA}_{28}^{18}\text{-}b\text{-PPerAcr}_{72}^{35}$  self-assembles into a lamellar morphology and  $\text{PvDMTPA}_{16}^9\text{-}b\text{-PPerAcr}_{84}^{88}$  exhibits shorter PPerAcr structures (see figure 7b,c). The power conversion efficiency of the device with the lamellar block copolymer is improved fivefold compared to  $\text{PvDMTPA}_{16}^9\text{-}b\text{-PPerAcr}_{84}^{88}$ . Both parameters, the  $J_{SC}$  and the  $V_{OC}$ , raise from  $0.24 \text{ mA/cm}^2$  to  $1.14 \text{ mA/cm}^2$  and from 530 mV to 690 mV, respectively. Since the HOMO level is 5.0 eV in both block copolymers and the charge carrier mobility is not altered, the difference in morphology must be responsible for the change in device performance. Also, the same amount of light is absorbed by the two block copolymers, as indicated by the same optical density of the active layers between 400

and 600 nm.  $\text{PvDMTPA}_{28}^{18}\text{-}b\text{-PPerAcr}_{72}^{35}$  and  $\text{PvDMTPA}_{16}^9\text{-}b\text{-PPerAcr}_{84}^{88}$  vary mainly in their hole conductor block length, resulting in different volume nanostructures.  $\text{PvDMTPA}_{28}^{18}\text{-}b\text{-PPerAcr}_{72}^{35}$  shows a lamellar morphology and  $\text{PvDMTPA}_{16}^9\text{-}b\text{-PPerAcr}_{84}^{88}$  exhibits shorter structures. As a consequence, charge percolation should be more favorable in the former case. This indicates that not only an adaptation of the energetic levels, but also the generation of longer and defined charge percolation pathways are required for improving the efficiency of a bulk heterojunction solar cell. Albeit the correlation of thermally annealed bulk structures with the device performance of active layers spun from chloroform can rationalize these findings, such a comparison is critical in general. In order to provide informations regarding the real device morphologies, scanning electron microscopy (SEM) was done on both  $\text{PvDMTPA}\text{-}b\text{-PPerAcr}$  devices after spin casting (figure 8b and 8c). In SEM, the contrast is inverted compared to TEM images. Now, the bright domains represent PPerAcr and the dark regions can be assigned to PvDMTPA. The surface of  $\text{PvDMTPA}_{28}^{18}\text{-}b\text{-PPerAcr}_{72}^{35}$  exhibits quite large and flaky domains of PPerAcr whereas the structural features of  $\text{PvDMTPA}_{16}^9\text{-}b\text{-PPerAcr}_{84}^{88}$  are smaller in terms of both, the donor as well as the acceptor domain size. On the one hand, this corroborates the picture of a better charge percolation in the device made of  $\text{PvDMTPA}_{28}^{18}\text{-}b\text{-PPerAcr}_{72}^{35}$  and, on the other hand, indicates that a domain size that is too small leads to inefficient charge transport and increased recombination rates.

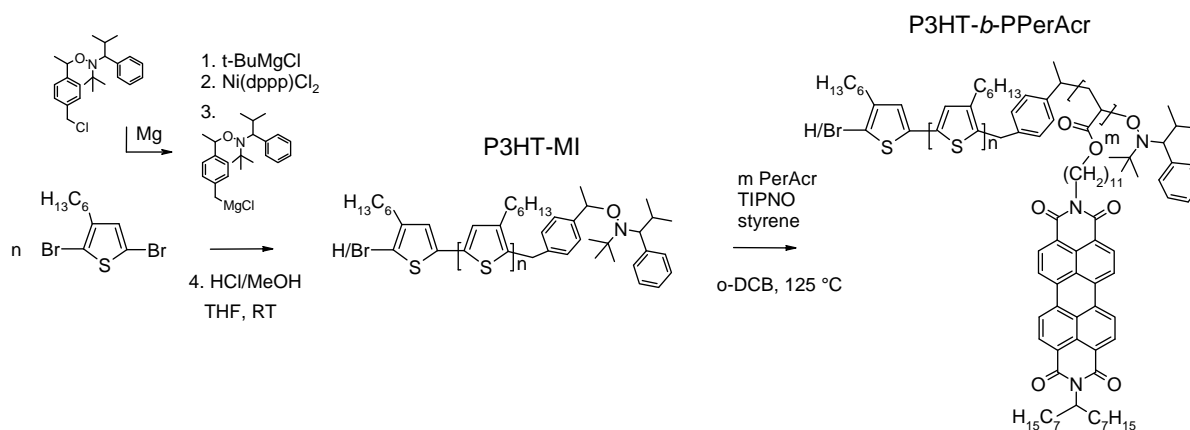
Finally, the effect of a PvDMTPD segment carrying efficient tetraphenylbenzidine hole transport units is considered and compared to the device performance with the block copolymers made from PvDMTPA macroinitiators. PvDMTPA already shows an improved charge transport compared to PvTPA, but PvDMTPD exhibits even higher hole mobilities (for mobilities and OFET transfer plots see figure 5). The HOMO energy levels in PvDMTPD and PvDMTPA both are 5.0 eV so that any differences in device performance can be ascribed to changes in morphology or charge carrier mobility. Choosing  $\text{PvDMTPA}_{16}^9\text{-}b\text{-PPerAcr}_{84}^{88}$  and  $\text{PvDMTPD}_{19}^7\text{-}b\text{-PPerAcr}_{81}^{26}$  for this comparison allows to exclude large effects of morphology, since their block lengths and compositions are similar (see figure 7c and 7d). In the device made of the PvDMTPD block copolymer, the improvement in the  $J_{\text{SC}}$  (1.21  $\text{mA}/\text{cm}^2$ ) is five-fold, whereas the open circuit voltage is 0.53 V in both cases. This result is encouraging since the short circuit current is highest among the four block copolymer

devices, although the TEM nanomorphology suggests the presence of a non-optimal worm-like morphology. Therefore the improved current can be attributed to the higher charge carrier mobility of tetraphenylbenzidines. Interestingly, devices made of block copolymers that exhibit lamellar nanostructures in the bulk (figure 7a and 7b) give higher open circuit voltages (0.67 and 0.69 V, respectively) than the ones with active layers of PvDMTPA<sub>16</sub><sup>9</sup>-*b*-PPerAcr<sub>84</sub><sup>88</sup> and PvDMTPD<sub>19</sub><sup>7</sup>-*b*-PPerAcr<sub>81</sub><sup>26</sup> (figure 7c and 7d). We therefore believe that a block copolymer such as PvDMTPD-*b*-PPerAcr can be designed to obtain lamellar domains, in which the synergetic effects of an improved hole transfer efficiency, an acceptable charge carrier mobility and a desired morphology can lead to very high power conversion efficiencies. Even higher charge carrier mobilities of the donor segments can be realized by employing conjugated, semi-crystalline polymers. A further advantage of this class of materials over the amorphous poly(triaryl amines) is the extended absorption in the visible range. These issues are addressed in the next chapter which is concerned with crystalline-crystalline block copolymers composed of poly(3-hexylthiophene) and PPerAcr.

### 3. Crystalline-crystalline donor acceptor block copolymers

#### 3.1 Synthesis and characterization

The objective of synthesizing block copolymers with poly(3-hexylthiophene) (P3HT) and PPerAcr involves combination of the two polymerization methods, Grignard Metathesis Polymerization (GRIM) and NMRP, in a straightforward fashion. Poly(3-alkylthiophenes) prepared via the GRIM method were first incorporated into block copolymers by McCullough et al, using polymeranalogous reactions to generate P3HT macroinitiators for the atom transfer radical polymerization (ATRP) of a second coil block.<sup>66,67</sup> Later on, this concept was extended to P3HT macroinitiators for NMRP and reversible addition fragmentation termination polymerization (RAFT).<sup>68</sup> The preparation of these macroinitiators included four steps and therefore, we aimed at an one-pot procedure. Protocols for the in-situ introduction of different endgroups were readily available from McCullough et al.<sup>69</sup>, giving an obvious pathway for a straightforward synthetic methodology towards P3HT block copolymers in two steps, as shown in scheme 6.<sup>70</sup>



**Scheme 6.** One-pot synthesis of P3HT-MI macroinitiators for NMRP followed by in-situ encapping with the Grignard derivative of a common alkoxyamine initiator. Starting from P3HT-MI, the acceptor monomer PerAc is polymerized to yield fully functionalized, double-crystalline block copolymers P3HT-*b*-PPerAc.

The in-situ introduction of the alkoxyamine at the end of the P3HT chain (capping efficiencies between 40 % and 85 %) was verified by  $^1\text{H-NMR}$ . The success of this reaction sensitively depended on the fairly complex polymerization conditions. McCullough et al found mixtures of mono- and dicapped P3HT species, depending on the type of Grignard used<sup>69</sup>, whereas we could only detect small amounts of dicapped P3HT macroinitiators. A mixture of mono- and dicapped macroinitiators leads to a mixture of diblock and triblock copolymers, which cannot be separated afterwards by simple extraction methods. This complicates characterization and can be disadvantageous regarding the self-assembly of the material. To gain additional insight into the various termination reactions of the GRIM during the in-situ endcapping with the alkoxyamine, the endgroups were analyzed using matrix-assisted laser desorption ionization time-of-flight (MALDI-TOF) as a function of endcapping time. For this purpose, aliquots were withdrawn after adding an eight-fold excess of the alkoxyamine endcapper, quenched with hydrochloric acid, and analyzed by MALDI-TOF.<sup>71</sup> The results are summarized in figure 10 and show the endgroups of a P3HT-alkoxyamine macroinitiator after 10 min, 1 h and 6 h of encapping time.

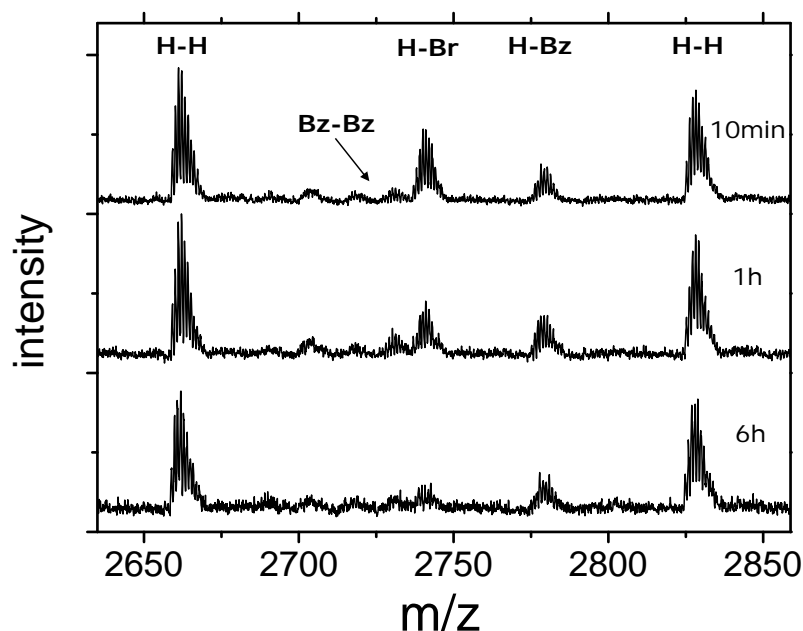


**Figure 10.** Evolution of P3HT endgroups during the encapping reaction with the Grignard-functionalized alkoxyamine as revealed by MALDI-TOF. The 16-mer is shown. Bz: benzylic fragment of the alkoxyamine.

Obviously, the alkoxyamine does not survive the MALDI ionization procedure and only P3HT chains with the benzylic fragment (Bz) are observed (similar to mass spectrometry of the low molecular weight alkoxyamine). A quantitative evaluation of the MALDI-TOF peak heights is critical since the peak intensities do not represent proportionally the amount of the respective species. Qualitatively, P3HTs with hydrogen-hydrogen (H-H), hydrogen-bromine (H-Br), hydrogen-alkoxyamine (H-Bz), and alkoxyamine-alkoxyamine (Bz-Bz) endgroups are found. On comparing the different spectra, most of the alkoxyamine endcapping occurs during the first minutes after adding the endcapper and increases only slightly afterwards. The overall degree of alkoxyamine endcapping is small in this case ( $\sim 40\%$  by  $^1\text{H-NMR}$ ), and despite the presence of further H-Br chain ends, these are not coupled to the initiator. Rather, the H-Br ends degrade, concomitant with an increase of the H-H ends. This indicates that despite the presence of Grignard-functionalized alkoxyamine, H-Br-terminated chains undergo a side-reaction which converts them into H-H-terminated chains. A general strategy for obtaining higher yields of alkoxyamine-terminated P3HT is therefore to use a larger

excess of endcapper. When an excess of alkoxyamine around 15 eq (with respect to the catalyst) was added, the degree of endcapping increased from 40 % to up to 80 %. However, a complete endcapping of all P3HT chains with alkoxyamine seems unlikely as long as degradation of bromine-terminated chains occurs during the GRIM. We believe that the simple and straightforward one-pot procedure compensates for incomplete encapping, and depending on the second segment, the non-functionalized P3HT can be removed afterwards via Soxhlet extraction. More critical is the presence of dicapped macroinitiators leading to triblock copolymers, since the separation of triblock and diblock copolymers is not possible by extraction methods. Using the in-situ endcapping method presented here, the fraction of P3HT with two alkoxyamine groups is small and as will be shown later, the polydispersities of the resulting block copolymers are sufficiently low (1.2-1.5).

In the second step, the P3HT-MI was used to polymerize PerAcr (scheme 5). The segment length of the PPerAcr can be well-adjusted by the reaction time as well as the ratio [P3HT-MI] to [PerAcr]. Similar reaction conditions applied earlier for block copolymer synthesis with PerAcr were successfully used here. The yield of the polymerization is limited by the viscosity of the reaction mixture; the reaction is typically stopped after 30 to 40 % conversion. Purification of the products can simply be achieved by soxhlet extraction, thereby removing non-functionalized P3HT and monomer PerAcr. P3HT-MI macroinitiators with different molecular weights were synthesized and incorporated into block copolymers with PPerAcr, as the P3HT molecular weight determines the performance of solar cells to a large extent.<sup>72</sup> The size exclusion chromatograms (SEC) of the block copolymers P3HT-*b*-PPerAcr, hereafter referred to as BC 16, 17, 21, 25, and 30, and their corresponding macroinitiators P3HT-MI 9 and P3HT-MI 17 are shown in figure 11 and demonstrate the successful block copolymer synthesis.

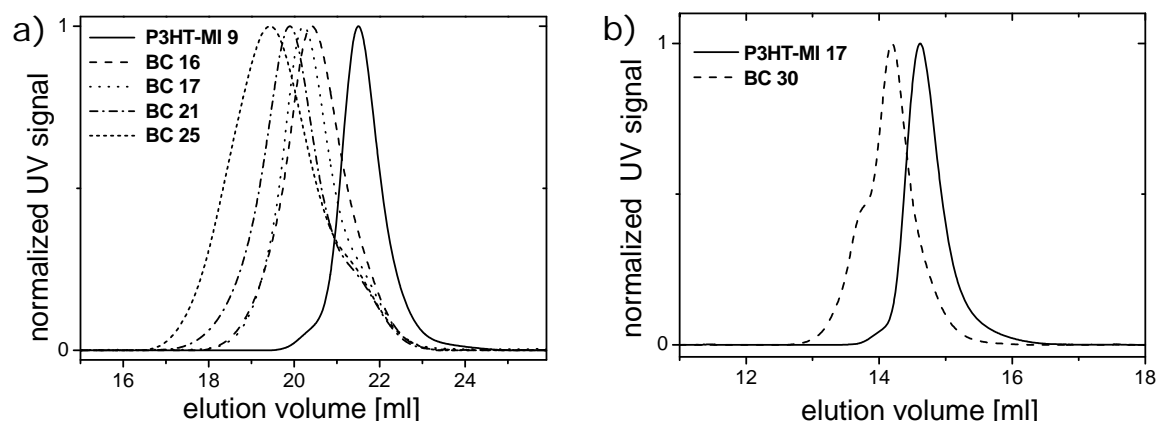


**Figure 11.** a) Size exclusion chromatography (SEC) of the macroinitiator P3HT-MI 9 ( $M_n = 8.9$  kg/mol) and the four block copolymers P3HT-*b*-PPerAcr BC 16, 17, 21 and 25 ( $M_n = 16.1$ , 16.9, 20.6 and 24.8 kg/mol, respectively). b) SEC curves of macroinitiator P3HT-MI 17 with a high molecular weight of 17.0 kg/mol and a resulting block copolymer P3HT-*b*-PPerAcr BC 30 ( $M_n = 29.5$  kg/mol). The curves were measured in THF containing 0.25 wt.-% tetrabutylammonium bromide in a) and pure THF was used as the eluent in b).

The molecular weights of BC 16, 17, 21, 25 and 30 are 16.1 kg/mol, 16.9 kg/mol, 20.6 kg/mol, 24.8 kg/mol, and 29.5 kg/mol, respectively, and the polydispersity indices are fairly low, between 1.15 and 1.31. Only for PPerAcr weight fractions as high as 80 % in BC 25, the PDI increases to 1.53. For the preparation of active layers in bulk heterojunction solar cells, the donor acceptor blend composition commonly lies between 1:1 to 1:4, depending on the polymer used. The PPerAcr weight fractions in our set of block copolymers exactly matches with these values, spanning the range between ~50 wt.-% (BC 16) and ~80 % (BC 25). Similarly to our observations concerning the increased difficulties of PerAcr polymerization with increasing  $M_n$  of poly(triarylamine) (see figure 2), PPerAcr blocks were more difficult to synthesize starting from the higher molecular weight macroinitiator P3HT-MI 17. This was manifested by prolonged reaction times and higher monomer to macroinitiator ratios that were necessary to obtain the same compositions compared to P3HT-MI 9. All parameters regarding the molecular weight, PDI and composition are shown in table 1.

**Table 1.** Molecular weights, polydispersity indices, compositions and thermal properties of homo- and block copolymers. The molecular weights were determined via SEC using polystyrene calibrations, the compositions via  $^1\text{H-NMR}$  and the thermal properties were derived from DSC measurements. The melting enthalpies are normalized to their weight fractions. <sup>a</sup>: a single melting peak appears. <sup>b</sup>: recrystallization of BC 30 shows a shoulder at 176 °C beside the main peak at 178 °C.

polymer	$M_{n,\text{P3HT}}$ [kg/mol]	$M_{n,\text{overall}}$ [kg/mol]	PDI	wt.-% PPerAcr	$T_{m1}$ [°C]	$T_{m2}$ [°C]	$T_{c1}$ [°C]	$T_{c2}$ [°C]	$\Delta H_{m,\text{P3HT}}$ [J/g]
PPerAcr	--	23	1.71	100	191	--	169	--	9.8
P3HT-MI 9	8.9	--	1.12	0	208	--	180	--	13.1
P3HT-MI 17	17.0	--	1.12	0	223	233	192	--	16.9
BC 16	8.9	16.1	1.25	55.7	190	211	148	162	10.3
BC 17	8.9	16.9	1.24	59.7	191	211	148	163	8.8
BC 21	8.9	20.6	1.31	73.7	202	--	172	--	-- <sup>a</sup>
BC 25	8.9	24.8	1.53	81.4	206	--	179	--	-- <sup>a</sup>
BC 30	17.0	29.5	1.15	54.9	204	244	178	-- <sup>b</sup>	15.4

### 3.2 Thermal properties

The behaviour of melting and crystallization of P3HT-*b*-PPerAcr is investigated by differential scanning calorimetry (DSC). Figure 12a shows the DSC curves of the homo- and block copolymers with P3HT-MI 9, and figure 12b displays the P3HT 17, BC 30 and PPerAcr. The temperatures of melting, crystallization and the melting enthalpies, together with the molecular weights and compositions, are summarized in table 1.

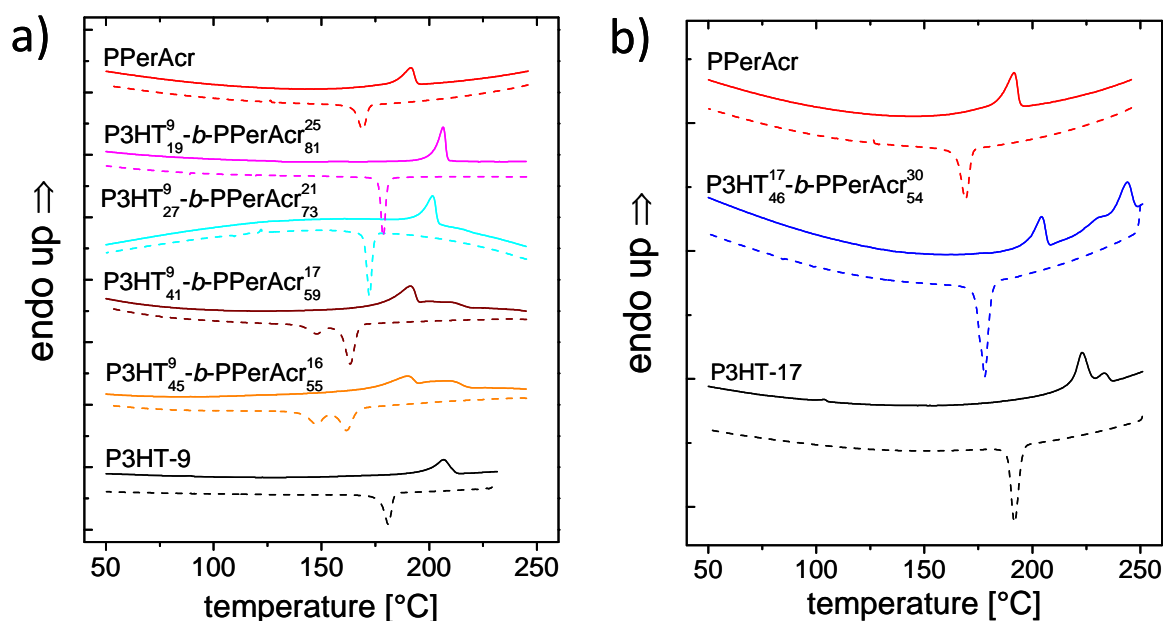


**Figure 12.** Differential scanning calorimetry of homo- and block copolymers. The second heating (solid line) and the second cooling curve (dashed line) is shown, curves were measured at 10 K/min under nitrogen, and are offset for clarity. a) Series of block copolymers starting from macroinitiator P3HT-MI 9 and the PPerAcr homopolymer. b) Macroinitiator P3HT-MI 17, block copolymer BC 30 and homopolymer PPerAcr. For molecular weights and composition see table 1.

The melting temperature  $T_m$  and the melting enthalpy  $\Delta H_m$  of P3HT strongly depend on the chain length for molecular weights up to 15 kg/mol, and then both saturate afterwards.<sup>73,74</sup> Macroinitiator P3HT-MI 9 exhibits a  $T_m$  of 211 °C and a  $\Delta H_m$  are 13.1 J/g (figure 12a). The homopolymer PPerAcr melts at 191 °C and has a melting enthalpy of 9.8 J/g. BC 16 shows two melting transitions at 190 °C and 211 °C, similar to the homopolymer temperatures. As observed for crystalline block copolymers, the crystalline domains exhibit melting enthalpies that are smaller than the values of the homopolymers<sup>75,76</sup> and this is observed for both domains, P3HT and PPerAcr in BC 16. BC 17 also shows two melting transitions, but compared to BC 16, the area of the first one becomes larger and the second one becomes smaller. Since the melting points of these block copolymers are comparable to the homopolymer transitions and since the melting enthalpy of the first  $T_m$  increases with increasing PPerAcr block length, we conclude that the first  $T_m$  of BC 16 and BC 17 is due to melting of PPerAcr segments and the second  $T_m$  is ascribed to P3HT melting. Upon cooling, BC 16 and BC 17 both show two recrystallizations at 162 °C and 148 °C. Surprisingly, the enthalpy of the first crystallization (at 162 °C) increases with increasing PPerAcr length,

suggesting that PPerAcr crystallizes first on cooling. Thus, in the series of BC 16-25, PPerAcr melts first *and* crystallizes first. It is known that crystalline-crystalline block copolymers with corresponding homopolymer melting temperatures that are far apart from each other, the block with the higher melting temperature recrystallizes first, followed by the block with the lower melting temperature.<sup>75,77,78</sup> This order might change if the difference between the individual  $T_m$ s is reduced. For example, Shiomi *et al.* reported that in poly(ethylene oxide)-*b*-poly( $\epsilon$ -caprolactone), PEO-*b*-PCL, PEO melts first and PCL recrystallizes first, although the  $T_m$ s for PEO and PCL are 65 and 55 °C, respectively.<sup>79</sup> However, in the case of BC 16 and BC 17, PPerAcr melts first *and* recrystallizes first. Note that the  $T_c$  of the P3HT block in BC 16 and BC 17 is 148 °C, whereas it is 180 °C in the corresponding macroinitiator P3HT 9. This large difference of 32 K probably results from confined P3HT crystallization between the spaces of the already crystallized PPerAcr domains. BC 21 and BC 25 have the same P3HT block as BC 16 and BC 17, but the PPerAcr fraction is higher, 73.7 and 81.4 %, respectively. Now, melting and crystallization of the two blocks appears as one transition.

The P3HT macroinitiator with 17 kg/mol shows two melting points at 223 °C and 233 °C (figure 12b). The observation of a second melting peak is explained by a smectic liquid crystalline behaviour.<sup>73</sup> The corresponding block copolymer BC 30 melts at 204 °C and at 244 °C. Whereas the first  $T_m$  is close to the  $T_m$  of pristine PPerAcr, the second one is higher than one would expect according to the  $T_m$  of P3HT-MI 17. The reason for this probably is due to soxhlet extraction of the block copolymer with methylene chloride, which removes the smaller block copolymer and homopolymer chains quite efficiently. Concerning the melting enthalpies of P3HT, values of 16.9 J/g (P3HT-MI 17) and 15.4 J/g (BC 30) are found. Thus, not only we find the same trend<sup>73,74</sup> of an increased  $\Delta H_m$  with increasing  $M_n(\text{P3HT})$  in the macroinitiators, but also in the two block copolymers BC 16 and BC 30 with very similar weight fractions (see table 1). The cooling curve of BC 30 shows one exotherm at 178 °C, with a slight shoulder at 176 °C. Probably this shoulder can be assigned to PPerAcr crystallization. We can also understand the coincidence of the two crystallization temperatures: The  $T_c$  of P3HT also depends strongly on its molecular weight. Therefore, crystallization of P3HT in BC 30 occurs at higher temperatures than in BC 16.

### 3.3 X-ray diffraction

X-ray diffraction (XRD) measurements give additional insight into the crystallinity of the double-crystalline donor acceptor block copolymers P3HT-*b*-PPerAcr. The powder X-ray diffraction patterns of the homo- and block copolymers are shown in figure 13. The thermally annealed macroinitiators P3HT 9 and P3HT 17 both show the well-known (100) reflection at  $2\theta = 5.36^\circ$  and  $5.25^\circ$ , respectively, due to the lamellar packing of the P3HT chains, and the slight shift of the peak with increasing molecular weight is in accordance with the literature (figure 13a,b).<sup>74</sup> Furthermore, a peak at  $2\theta = 23.4^\circ$  is observed in both macroinitiator patterns. Both are broad and lie between the (020) and the (002) reflections of P3HT<sup>73</sup>, and therefore are assumed to be a superposition of the (020) and the (002) peak (figure 13c). Here, only the XRD pattern of P3HT 9 is shown for clarity.

PPerAcr, on the other hand, exhibits a different diffraction pattern. The observed reflections arise from stacks of perylene bisimide moieties which are separated by the alkyl side groups. Within one stack, perylene bisimide units are stacked with a  $\pi$ - $\pi$  distance of 0.35 nm, as indicated by the reflection at  $2\theta = 25.6^\circ$ .<sup>58</sup> We assume the amorphous halo at  $2\theta = 19.6^\circ$  to arise from the disordered alkyl substituents of PBI. A graphic illustration of the proposed supramolecular structure of PPerAcr and the lamellar packing of P3HT is depicted in figure 13d and 13e, respectively. Similarly, low molecular weight PBIs with branched alkyl side groups were reported to form such stacks or columns.<sup>80</sup> The XRD patterns of BC 16, BC 17 and BC 30 (the PPerAcr weight fraction is  $\sim 55$ -60 %) are a superposition of the individual homopolymer reflections, and the contributions from the two homopolymers change with composition and molecular weight. Figure 13b shows the most intense reflection of PPerAcr and the 100 reflection of P3HT, normalized to the former. Obviously, the  $100_{\text{P3HT}}$  reflection becomes less intensive with increasing PPerAcr fraction in the series from BC 16 to BC 25. The  $100_{\text{P3HT}}$  reflection cannot be seen anymore in BC 21 and BC 25, which resemble the PPerAcr homopolymer pattern to a large extent. This is in accordance with the results from DSC (figure 12a), where only one melting point is observed for BC 21 and BC 25, but two for BC 16, BC 17 and BC 30. Note that the broadening of the reflections around  $2\theta \sim 5^\circ$  of BC 16, BC 17, and BC 30 is due to underlying peaks of PPerAcr. Interestingly, the comparison of the curves of BC 16 and BC 30 reveals that the  $100_{\text{P3HT}}$  reflection is more intensive in BC 30, indicating a higher crystallinity of P3HT. This result is in agreement with the results from

calorimetry, where the higher degree of P3HT crystallinity was already observed. Figure 13c shows the  $2\theta$  region between 15 and 30° of all samples. Here, the  $002_{\text{P3HT}}$  reflection and the  $\pi$ - $\pi$  stacking of PPerAcr are seen. Again, the  $002_{\text{P3HT}}$  peak becomes less intensive with increasing PPerAcr fraction, and no distinct  $002_{\text{P3HT}}$  peaks are observed for block copolymers BC 21 and BC 25 with the higher PPerAcr weight fractions. Obviously, these patterns of BC 21 and 25 are dominated by the reflections of the PPerAcr homopolymer in this region. BC 30 exhibits a slightly more intensive  $002_{\text{P3HT}}$  peak than BC 16, again indicating the higher P3HT crystallinity of BC 30.

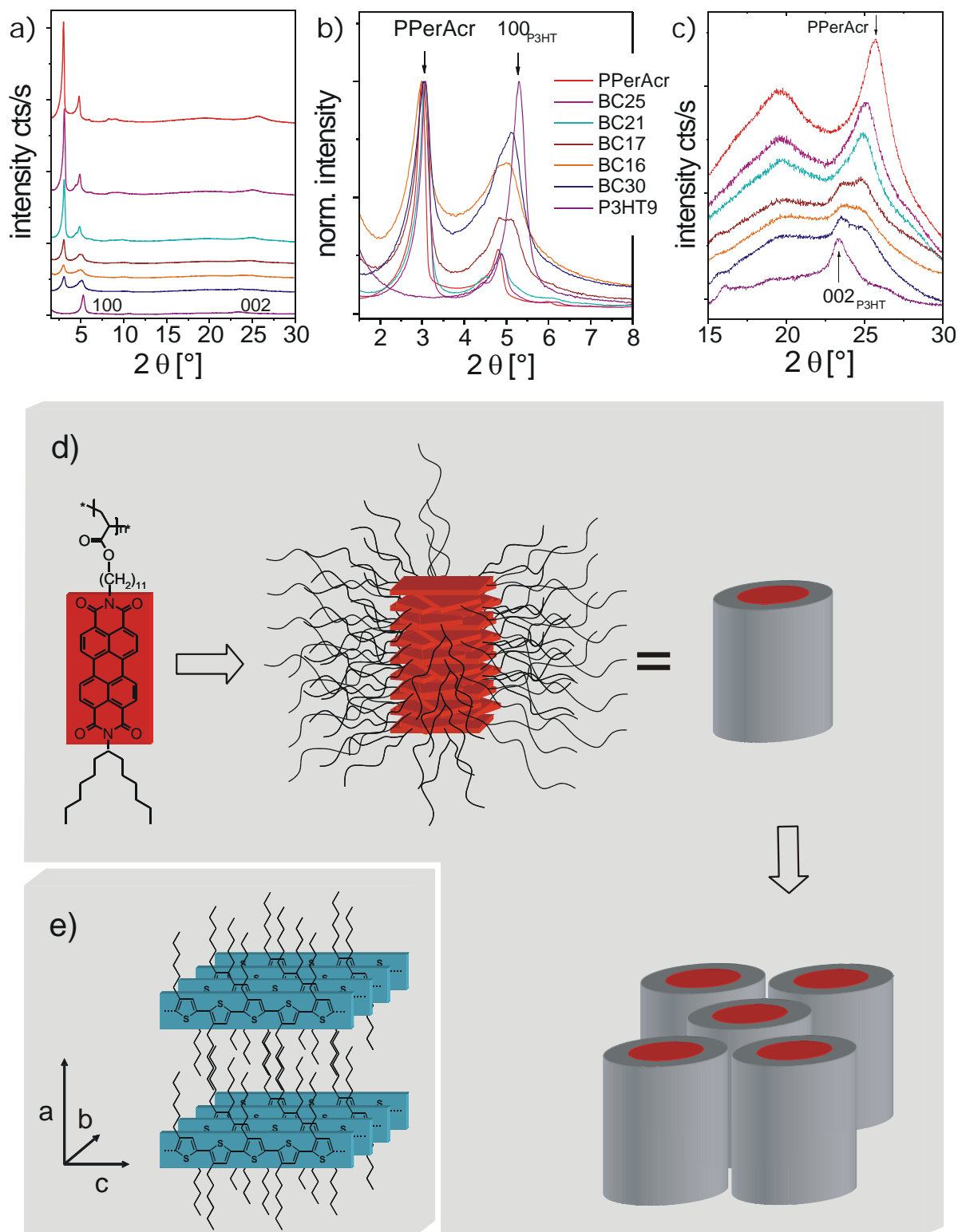


**Figure 13.** Supramolecular arrangement of double crystalline block copolymers P3HT-b-PPerAcr, as derived by powder X-ray diffraction measurements of thermally annealed homo- and block copolymer samples. The color code in b) is equal in all plots. a) shows the entire range measured and b) shows the normalized intensity between  $2\theta = 1-7^\circ$ , and c) the region between  $2\theta = 15-30^\circ$ . d) Schematic drawing of supramolecular arrangement of PPerAcr. Note that the unit cell is not determined and that the drawing might not reflect the exact geometry of the stacks. Rather, the separation of PBI units and alkyl groups is depicted. e) Lamellar packing of P3HT according to the literature.<sup>81</sup>

Furthermore, chloroform vapor annealed powder samples are measured. For this purpose, powders are exposed to chloroform vapor during several days, dried, milled, and measured. The resulting XRD patterns are shown in figure 14.

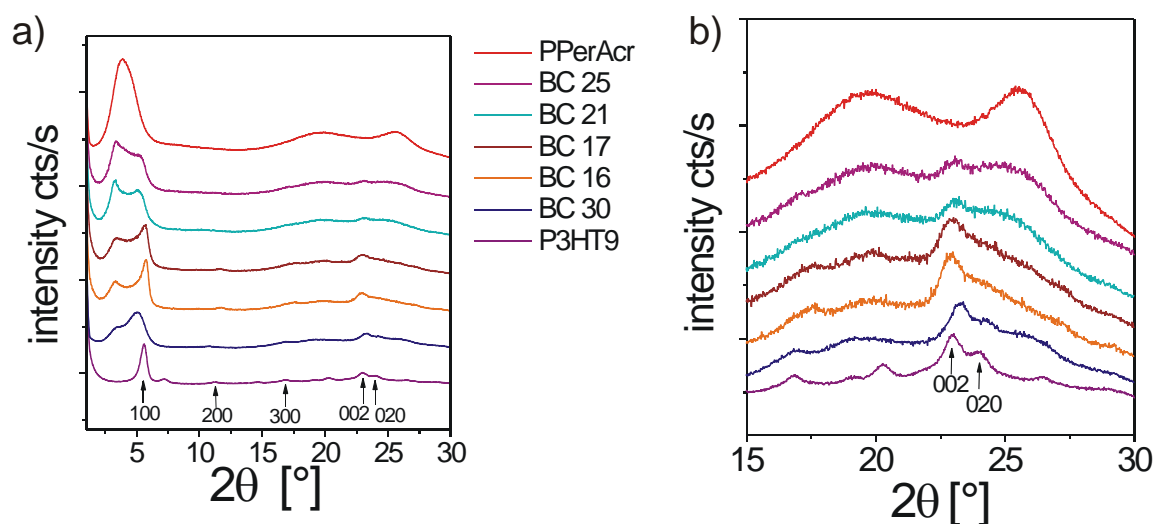


**Figure 14.** Powder X-ray diffraction measurements of chloroform vapor annealed homo- and block copolymer samples. a) full range between  $2\theta = 1 - 30^\circ$  is shown, b) enlarged region of  $2\theta = 15 - 30^\circ$ . Legend is valid for both plots.

Chloroform vapor annealing influences the XRD patterns of all samples to a large extent, and the signal intensity of all patterns is lower compared to the thermally annealed samples. Instead of the sharp reflections of PPerAcr in the thermally annealed sample, only one broad peak appears at  $2\theta = 3.87^\circ$ , corresponding to a  $d$  spacing of 2.3 nm (figure 14a). The reflection arising from  $\pi$ - $\pi$  stacking is broader as well, but the peak position remains at  $2\theta = 25.6^\circ$  (corresponding to 0.35 nm) compared to the thermally annealed sample. This suggests that the PPerAcr stacks are disordered after vapor annealing, with a mean distance of 2.3 nm. In contrast to this, the reflections of P3HT9 are resolved better compared to the thermally annealed sample, indicating a rearrangement and a higher order of the chains. Especially the 002 and 020 reflections are now clearly resolved. From these observations we conclude that chloroform vapor annealing breaks up the  $\pi$ - $\pi$  interactions of P3HT as well as PPerAcr. However, after drying of the samples, P3HT9 exhibits a higher degree of order, whereas the PPerAcr sample is less ordered. These two findings have a large effect on the

XRD patterns of the block copolymers: Here, chloroform vapor leads to a high chain mobility in PPerAcr, enabling rearrangement of P3HT chains. Therefore, the  $100_{\text{P3HT}}$  is more intense in BC 30, 16, and 17, compared to the reflection of PPerAcr at  $2\theta = 3.87^\circ$ , which was inverse in the thermally annealed samples. BC 21 and 25 now also show the  $100_{\text{P3HT}}$  reflection, whereas the corresponding thermally annealed samples almost revealed the PPerAcr homopolymer pattern. Qualitatively the same behaviour is observed in figure 14b. The  $002_{\text{P3HT}}$  reflection becomes visible in all block copolymer patterns, even in BC 21 and 25 with the small P3HT fractions, where only PPerAcr features were observed in the thermally annealed samples (see also figure 13c). The  $\pi$ - $\pi$  stacking peak of PPerAcr is only weak and very broad in the block copolymers.

We conclude that thermal annealing of PPerAcr leads to sharp reflections suggesting defined and ordered stacks. The  $\pi$ - $\pi$  distance of two PBI units inside one stack is 0.35 nm. In the thermally annealed block copolymer samples, these features dominate over the P3HT signals, as a consequence of order of crystallization (PPerAcr crystallizes first). When chloroform vapor annealing is applied, the  $\pi$ - $\pi$  interactions in PPerAcr break up which gives rise to rearrangement of P3HT chains, and therefore, the P3HT reflections dominate the XRD patterns.

### 3.4 Optical properties

The order of crystallization not only influences the thermal characteristics and the XRD patterns, but also the optical properties in the solid state. Even the solution spectra of PPerAcr exhibit features of aggregated perylene bisimides, since the PBI moieties are closely attached in side chains of a polyacrylate backbone. In THF solution, PPerAcr shows three main spectral features at 470, 490 and 525 nm resulting from the vibronic progressions of Frenkel excitons, but also from intermixed states with charge transfer excitons (figure 15a). These are a result from the strong operative interactions of the perylene bisimide moieties and their coupling of the respective dipole moments. The P3HT absorption profile in solution is highly dependent on the concentration, the temperature and the solvent used.<sup>82</sup> In dilute THF solutions, aggregation is not observed and P3HT-MI 9 features one broad absorption band peaking at 445 nm. The absorbance spectra of BC 16-25 show a superposition of P3HT

and PPerAcr absorption, with contributions of the two segments according to their respective weight fractions. Visually, the color of the solutions shifts from orange to red for increasing degrees of polymerization of PPerAcr (figure 16).

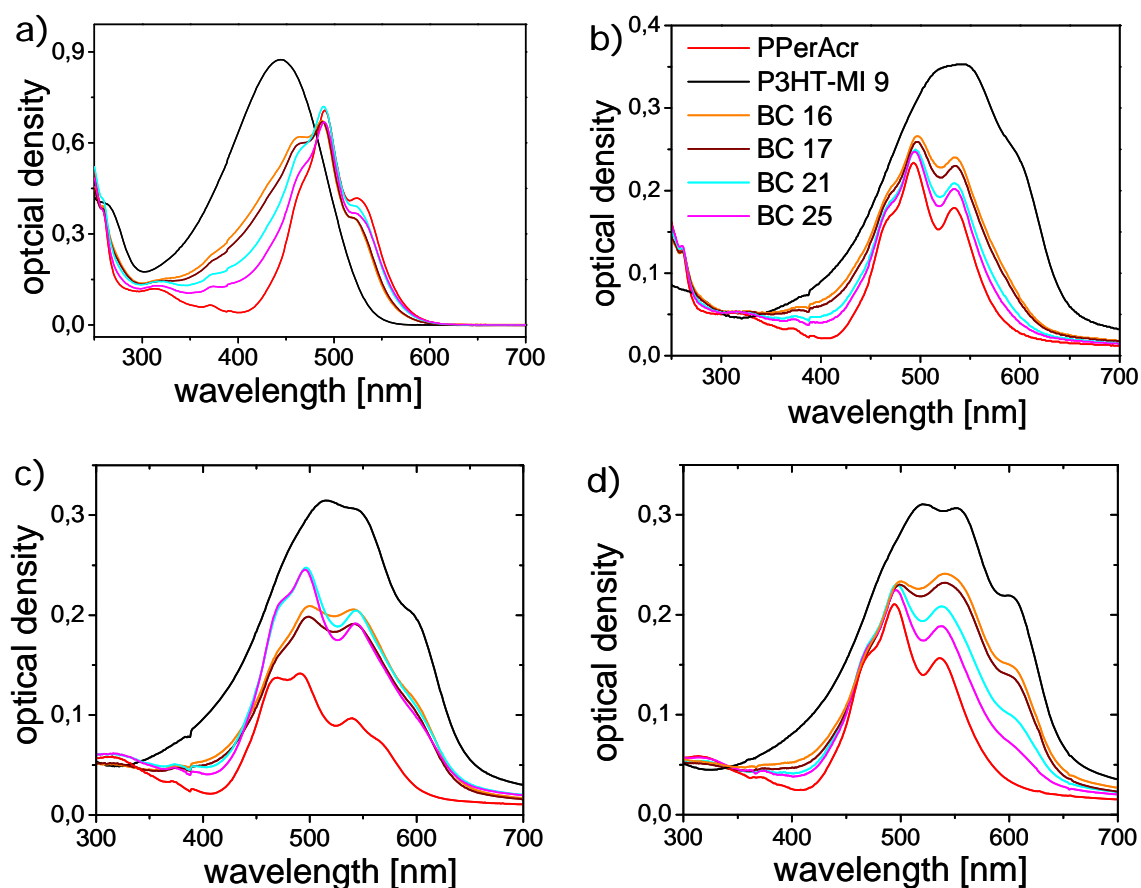


**Figure 15.** Optical densities (OD) of homopolymers P3HT-MI 9, PPerAcr, and block copolymers BC 16-25. a) THF solution (0.02 mg/ml). b) Films spun from chloroform solutions ( $\sim 70$  nm). c) Films spun from chloroform solutions followed by thermal treatment (30 min, 220 °C). d) Films spun from chloroform solutions followed by chloroform vapor annealing. Legend in a) is same for all.

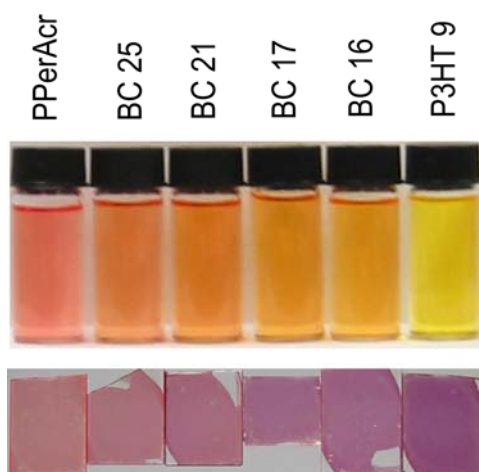


**Figure 16.** Color of homo- and block copolymers. Upper row: Solutions in THF at a concentration of 0.02 mg/ml, the corresponding UV-vis spectra are shown in figure 14a. Lower row: Thin films spun from chloroform and subsequently subjected to chloroform vapor annealing, the corresponding UV-vis spectra are shown in figure 14d.

The solid-state absorption of thin films cast from chloroform solutions is displayed in figure 15b. The onset of absorption of P3HT-MI 9 red-shifts by 100 nm to 650 nm. Compared to pristine PPerAcr, the block copolymer absorption is also extended into the red with increasing P3HT content, but lower than for the pristine P3HT-MI 9. The P3HT shoulder at around 610 nm, which is assigned to interchain exciton delocalization<sup>82,83</sup> is developed weakly in the block copolymer films, indicating a low degree of order. The reason for this is that during spin coating the block copolymers from chloroform solution, the P3HT blocks are not given sufficient time to rearrange as the films dry too fast.

Thermal annealing of the films above the second melting temperature results in a small improvement concerning vibronic resolution at 610 nm but these changes are much weaker than those after solvent vapor annealing (figure 15c). As reported recently, the intensity of the peak at 610 nm of thin films containing P3HT can be correlated to the degree of crystallinity.<sup>84</sup> The lower degree of P3HT crystallinity in the thermally treated block copolymer films is a logic consequence of the fact that PPerAcr crystallizes first upon cooling. Thus, P3HT has to solify within the geometric confinement of the already crystallized PPerAcr domains, which typically yields a lower degree of crystallinity compared to the pristine P3HT-MI 9 (cf to figure 12a and 13b).

The situation changes substantially upon exposing the films to chloroform vapor. This type of treatment has demonstrated to break up the  $\pi$ - $\pi$  interactions in PPerAcr efficiently.<sup>85</sup> Accordingly, the absorption profile of PPerAcr also changes dramatically, when compared to the PPerAcr spectrum after thermal annealing. In P3HT-MI 9, the shoulder at 610 nm is resolved well (figure 15d) due to rearrangement of P3HT chains during the solvent annealing. Rearrangement of P3HT also occurs in all block copolymers, where the absorption profiles now exhibit a clear peak at 610 nm. Even though the peak heights at 610 nm can not be correlated to the P3HT weight fractions measured by <sup>1</sup>H-NMR (due to the stronger absorption of P3HT compared to PPerAcr), the tendency of a higher absorption at 610 nm with increasing P3HT weight fraction is evident from figure 15a and from figure 16.

In order to further investigate the changes in the UV-vis spectra after solvent annealing, the absorption of a film of pristine P3HT-MI 9 was tracked *during* the vapor annealing process as a function of chloroform vapor saturation (figure 17a). Starting from a chloroform spin-casted film (thick solid line in figure 17a) we obtain a similar absorption profile compared to

figure 15b. With increasing solvent saturation, the optical density of the film decreases between 475- 650 nm, and increases between 300- 475 nm. The absorption in the high energy region is due to the presence of amorphous or single chains whereas absorption in the low energy region arises from aggregate formation. Therefore, with increasing chloroform vapor saturation, order and crystallinity decrease in the film for the benefit of the amorphous regions.<sup>82</sup> Quenching the annealing process with nitrogen dries the film, and an enhanced vibronic resolution is observed compared to the film as spun (dashed line in figure 17a).

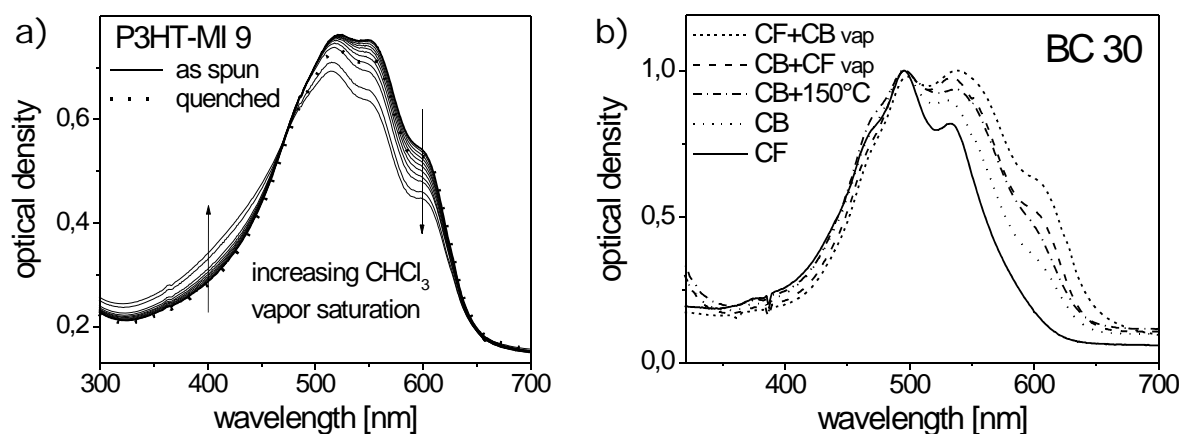


**Figure 17.** a) Evolution of the absorption profile of P3HT-MI 9 during the chloroform vapor annealing, as a function of vapor saturation. First, P3HT-MI 9 is spun from chloroform (thick solid line). The film is then placed into a chamber and UV-vis is measured for various chloroform vapor saturations between 10 % to 100 %. The chamber is then purged with nitrogen (thick dashed line). b) Normalized optical densities of BC 30. The plot shows the effect of the solvent used for spin coating ( $\text{CHCl}_3$ : chloroform, CB: chlorobenzene) and different post-annealing treatments on the degree of P3HT crystallinity, as evident from the optical density at 610 nm (150 °C: thermal annealing,  $\text{CHCl}_3$  vap: chloroform vapor annealing, CB vap: chlorobenzene vapor annealing).

Finally, the influence of the solvent used for spin coating and different post-annealing treatments on the absorption profile of BC 30 is investigated (figure 17b). This block copolymer exhibits the same composition as BC 16, but the overall molecular weight is twice as high (see table 1). After spin casting BC 30 from chloroform, the P3HT crystallinity is strongly disrupted (solid line). The use of chlorobenzene (CB) for spin coating promotes P3HT crystallinity (dotted line), which further increases after thermal annealing the film *below* the lower melting point (150 °C, 30 min, dashed-dotted line). Spin coating from chlorobenzene followed by chloroform vapor annealing again slightly enhances the optical density at 610

nm (dashed line). However, treating chloroform cast films with chlorobenzene vapor yields the highest P3HT crystallinities in BC among the annealing protocols tested (short dashes). The photoluminescence of these novel materials in solution has been investigated in detail elsewhere.<sup>70</sup> Both, P3HT and PPerAcr, can be excited almost independently at 400 and 530 nm, respectively. Excitation of the block copolymers at 400 nm gives rise to a yellow P3HT fluorescence peaking at 565 nm and excitation at 530 nm, where P3HT absorbs much weaker than PPerAcr (see figure 15a), a red fluorescence of PPerAcr is observed at 622 nm. The fluorescence of PPerAcr in film occurs at 622 nm and is thus not shifted towards larger wavelengths, as it is observed for low molecular weight PBIs.<sup>17</sup> The block copolymer films show almost complete PL quenching, indicative of electron transfer from P3HT to PPerAcr. This is supported by time-resolved absorption studies on these systems, which are currently underway.

### 3.5 Morphology of P3HT-*b*-PPerAcr

The complexity of the self-assembly in P3HT-*b*-PPerAcr results from the competition of several processes: P3HT crystallizes into a lamellar structure whereas PPerAcr forms columns. Additionally, microphase segregation might occur. The enthalpies of crystallization are 13.1 and 9.8 J/g for P3HT 9 and PPerAcr, respectively, which is about one order of magnitude higher than the typical enthalpic gain of a microphase segregation.<sup>86</sup> The morphologies of P3HT-*b*-PPerAcr are therefore expected to be dictated by the crystallization of the two blocks. Especially the order of crystallization is important since the block with the lower crystallization temperature has to crystallize within the confinement of the already solidified domains with the higher crystallization temperature. As revealed by DSC and XRD, PPerAcr crystallizes first in BC 16-25 and thus influences the crystallization of P3HT. For a rearrangement of the chains to be induced, the  $\pi$ - $\pi$  interactions of both, P3HT as well as PPerAcr need to break up. This can be efficiently done by using chloroform vapor annealing, as deduced from the UV-vis spectra. For these reasons, the samples for morphological investigations were subjected to solvent annealing. Bulk and thin film samples were prepared and imaged using scanning electron microscopy (SEM). We found excellent contrast between the two blocks (figure 18). For the assignment of bright and dark areas,

two P3HT:PPerAc blend films with extreme compositions were investigated. Films with P3HT as the minority component show darker droplets in a bright matrix and vice versa (not shown here). We therefore assign bright regions to PPerAc and darker domains to P3HT. The same contrast is observed in films of amorphous-crystalline block copolymers (see figure 8) and for block copolymers comprising polystyrene and PPerAc.<sup>63</sup> To emphasize the morphology control which can be achieved by P3HT-*b*-PPerAc, two images of blend films of P3HT and PBI, being the polymer PPerAc and a low molecular weight PBI compound, are shown in figure 18 k,l).

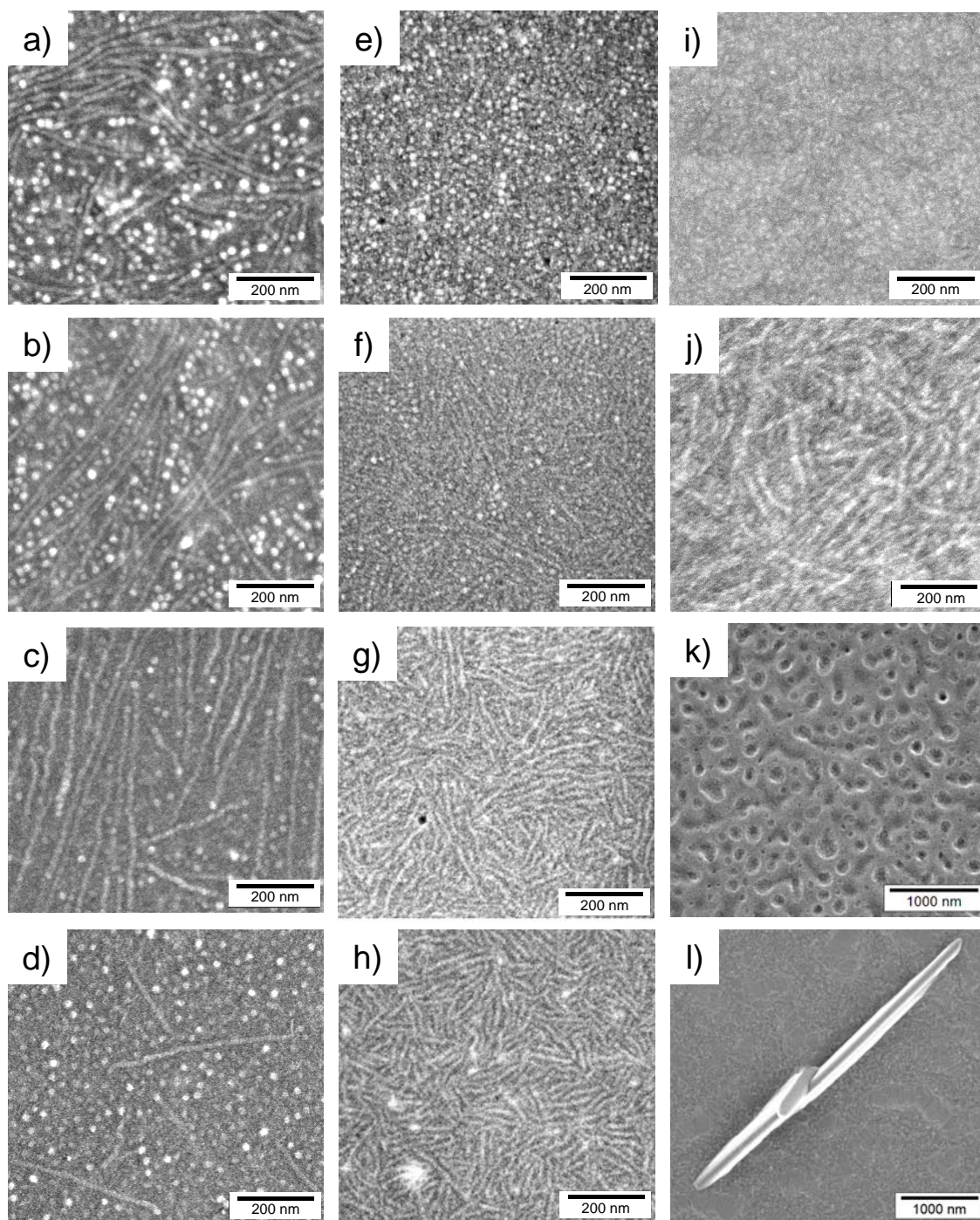


**Figure 18.** Morphology of different P3HT-PBI systems in bulk (drop casting from chlorobenzene) and in film (spin coating from chloroform) by scanning electron microscopy. Solvent annealing was applied to all samples. a-d) Bulk samples of BC 16-25, respectively (several microns thick, four days of chloroform vapor annealing). e-h) Thin films of BC 16-25, respectively ( $\sim 70$  nm, chloroform vapor annealing for 90 min). i) Thin film of BC 30 ( $\sim 150$  nm, chloroform vapor annealing for two days). j) Bulk sample of BC 30 (several microns thick, four days of chloroform vapor annealing). k) Thin film of a blend P3HT:PPerAc 40:60 ( $\sim 150$  nm, chloroform vapor annealing for 30 min). l) Thin film of a blend of P3HT and a low molecular weight perylene bisimide (*N,N*-Di(1-heptyloctyl)perylene-3,4:13,14-tetracarboxdiimide) 50:50 ( $\sim 150$  nm, chloroform vapor annealing for 30 min). Scale bars are 200 nm in a)-j) and 1  $\mu$ m in k)- l), bright and dark areas are assigned to perylene bisimide and P3HT, respectively. 2 nm of platinum were sputtered onto the samples prior to SEM imaging. Indium tin oxide substrates were used in all cases.

Since the morphologies of thin films and volume samples can differ from each other, they are discussed separately in the following. The volume samples (exposed to saturated chloroform vapor during four days) of BC 16 and BC 17 with PPerAcr weight fractions of 56 and 60 wt.-%, respectively (figure 18a,b) show similar micrographs with mixed patterns of bright dots and stripes, reflecting domains of PPerAcr. Most probably, these patterns are due to cylindrical or fiber-like PPerAcr domains in a P3HT matrix, with  $\sim 15$  nm in diameter and a domain spacing of  $\sim 21$  nm. The micrographs of BC 21 and BC 25 with the higher PPerAcr weight fractions of 74 and 81 wt.-%, respectively, also exhibit bright dots and strips in a darker matrix (figure 18c,d). Again, the bright regions are ascribed to PPerAcr rich domains. Interestingly, the diameter of the bright, PPerAcr-rich structures remains almost constant compared to figure 18a,b. It is therefore assumed that the dark regions in figure 18c and 18d are comprised of a mixed phase of P3HT and PPerAcr, in accordance with the results of DSC. BC 30 ( $M_n$  P3HT= 17 kg/mol, 55 wt.- PPerAcr) shows bright fibrils in a darker matrix (figure 18j). The distance between the fibrils of BC 30 is increased to  $\sim 31$  nm, reflecting the higher molecular weight of BC 30 compared to figure BC 16.

Several annealing procedures were applied to the preparation of the thin film samples. Whereas thermal annealing above the higher  $T_m$  of the block copolymers did not produce distinct structural features at the surface, films subjected to chloroform vapor (90 min, 90 % saturation) showed a good contrast. Longer annealing times led to substantial dewetting of the films. The micrographs of figures 18e-h represent the films of BC 16-25, respectively. In figure 18e (BC 16), an unique pattern of bright dots in a darker matrix appears, and to figure 18f (BC 17) dots and elongated structures are observed. This trend continues in figures 18g and 18h: The BC 21 and BC 25 only show elongated, fiber-like structures. While there is ambiguity over the extension of these structures into the bulk of the film, we observe a clear correlation between the increasing PPerAcr weight fraction and the decreasing number of dots from figure 18e to 18h. The surface of BC 30 does not show a distinct structure at the surface even after prolonged solvent annealing times using chloroform or chlorobenzene vapor.

These results emphasize the advantage of the covalent connectivity of P3HT and PPerAcr in terms of a controlled phase separation since the observed structures are commensurate with the exciton diffusion length. To further illustrate this two polymer blend films

comprising P3HT and PBI were prepared. In figure 18k a blend consisting of P3HT:PPerAcr 40:60 is seen. After solvent annealing for 30 min, dark P3HT-rich islands with domain sizes exceeding 100 nm result from demixing of the blend film. Figure 18l shows a blend film comprising 50 % P3HT and 50 % of a low molecular weight perylene bisimide (N,N'-Di(1-heptyloctyl)perylene-3,4:13,14-tetracarboxdiimide).<sup>80</sup> Here, diffusion and crystallization of the low molecular weight PBI leads to the formation of huge, micrometer long PBI crystals. Both film morphologies, the P3HT:PPerAcr blend as well as the P3HT:low molecular weight PBI blend, are not suitable for photovoltaic applications.

### 3.6 Device performance of P3HT-*b*-PPerAcr

One major drawback that causes active layer morphologies of blends of donor polymers and PBIs to be ill-defined is the uncontrolled crystallization of PBI and phase separation, as shown in figures 18 k,l). Such unfavorable morphologies do not provide sufficient interfacial area of the donor and the acceptor phase and can give rise to charge trapping, as was proposed for blends of conjugated polymers and PBI.<sup>19,43</sup> Consequently, the external quantum efficiencies and device performances are rather low. However, it is not only the uncontrolled crystallization of PBI that leads to poor morphological control and thus limits the device performance. The orientation of the crystals in the film and the relative orientation of PBI moieties towards each other is also very important in order to extract charges efficiently. For example, it has been shown that the angle of the rotational offset of stacked PBIs influences the charge transport properties along the columns.<sup>87</sup> A block copolymer such as P3HT-*b*-PPerAcr addresses all these issues since crystallization of PBI can be confined in microdomains. The alignment of the domains might also give rise to alignment of the crystals as well, and the relative orientation of neighbored chromophores may be tuned by changing the two substituents at the imide positions. The enhanced morphology control on the one hand, and the advantages of extended absorption and improved hole carrier mobility of P3HT (compared to the amorphous poly(triarylamine)s) on the other hand, render P3HT-*b*-PPerAcr truly promising for the application in photovoltaic devices.

BC 16- 25 were tested in photovoltaic devices using the device architecture indium tin-oxide (ITO)/PEDOT:PSS/block copolymer/aluminum. The block copolymers were spin cast from chloroform solutions (0.6 wt.-%). The photovoltaic response was first investigated by monitoring the external quantum efficiencies (EQE). Due to the XRD patterns (figure 14), the P3HT shoulder at 610 nm (figure 15d) and the evolution of structural features after solvent annealing (figure 18a-h), the devices were subjected to the same solvent annealing procedure. The best performance was obtained from BC 16 and BC 17, and furthermore was found to decrease with increasing PPerAcr block length. Therefore, a variety of post-annealing procedures was applied to devices after spin coating these block copolymers from chloroform. As an example, the results of BC 17 are presented in figure 19. The effect of thermal treatments on the EQE is presented in figure 19a, and 19b shows the effect of chloroform vapor annealing with or without additional thermal annealing. The devices were thermally annealed below the lower melting temperature (160 °C, 30 min) and above the higher melting temperature (225 °C, 30 min) (see thermal properties in figure 12a). At 160 °C, the alkyl side chains are in a molten state so that the P3HT backbones can rearrange within the morphology formed after spin coating. At 225 °C, an amorphous melt is present, from which PPerAcr crystallizes first upon cooling.

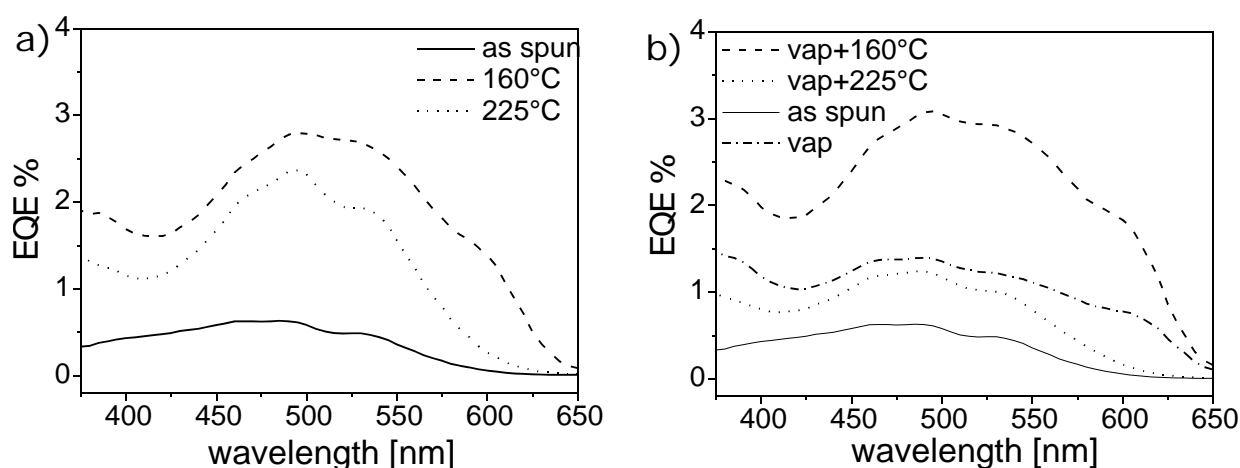


**Figure 19.** External quantum efficiencies of solar cells prepared from BC 17 after different annealing conditions. a) device performance as spun and after thermal annealing. b) performance as spun and after chloroform vapor annealing (vap) in combination with thermal annealing. Device architecture: ITO/PEDOT:PSS/active layer/aluminium.

The maximum EQE value of the device with the active layer spun from chloroform is below 1%. Thermal annealing of this device at 225 °C leads to a maximum EQE value of 2.5 %. But annealing at a lower temperature of 160 °C increases this value to 3 % (figure 19a). Interestingly, the improvement after annealing at 160 °C not only leads to higher EQE values, but also extends the spectral response of the block copolymer towards 650 nm. The shape of the EQE spectrum after annealing at 225 °C resembles the PPerAcr absorption profile whereas after annealing at 160 °C the P3HT shoulder at 610 nm can be observed clearly. We therefore anticipate that the contribution from P3HT to the photocurrent is low after annealing the device at 225 °C, but much higher after 160 °C. This is consistent with the results obtained from DSC, XRD, and UV-vis: When the material solidifies from its amorphous melt, PPerAcr crystallizes first and suppresses crystallization of P3HT, leading to a lower contribution of P3HT to the photocurrent. On the other hand, a post-production treatment below the melting point of PPerAcr at 160 °C leads to partial rearrangement of the P3HT chains within the morphology formed after spin coating, giving rise to a higher P3HT crystallinity and thus a higher contribution of P3HT to the photocurrent.

Combining thermal annealing with solvent annealing can further improve the EQE of BC 17 (figure 19b). The direct treatment of the device with chloroform vapor after spin casting only leads to a doubling of the maximum EQE value. Simultaneously, the spectral response is extended to the red, showing increased P3HT contribution to the photocurrent. This is expected since the absorption profile of BC 17 becomes well-resolved at 610 nm after this type of treatment, and since the reflections of P3HT dominate over the PPerAcr reflections in XRD (see figure 14 and 15d). Therefore, the enhanced absorption of P3HT increases the photocurrent towards 650 nm. Subsequent thermal annealing at 160 °C leads to a further doubling of the maximum EQE value to 3 % while maintaining the onset of spectral response, whereas subsequent thermal annealing at 225 °C decreases the device performance in terms of the maximum EQE value as well as the onset of the EQE curve. Again this can be rationalized by the findings from DSC that show that crystallization of PPerAcr suppresses P3HT crystallinity.

Note that this argumentation can only qualitatively explain the spectral response from different regions. In general, charge generation and recombination dynamics determine ultimately the device performance, and this is not only a function of crystallinity but also of

the domain size. The domain size is correlated to the segment lengths of the block copolymer and therefore, the higher molecular weight of BC 30 should result in larger domains. Figure 20 compares the device performance of BC 16 and BC 30. The composition is equal in these two polymers and their molecular weights are 16.1 kg/mol and 29.5 kg/mol, respectively (see table 1). The spectral response of BC 16 is similar compared to BC 17. Using chlorobenzene solutions for processing leads to a similar effect compared to the solvent vapor annealing procedure, including a doubling of the maximum EQE value and extension of the onset to 650 nm. Thus, by using higher boiling point solvents post-production treatments might be redundant. Spin coating BC 30 from chlorobenzene leads to very high EQEs approaching 30 % (figure 20a).<sup>88</sup> These EQE values are the highest reported for block copolymer solar cells and also exceed considerably those reported for blends of P3HT and low molecular weight perylene bisimides.<sup>19,20</sup> The drastic enhancement is explained by a higher degree of P3HT crystallinity and larger P3HT crystals in BC 30, which is reflected by the higher melting enthalpy and higher melting temperature of P3HT (see figure 12 and table 1). This should influence the hole mobility of P3HT.<sup>89</sup> In order to verify this, organic field effect transistors (OFETs) were fabricated to extract the charge carrier mobilities. The transfer plots of BC 16 and BC 30 are displayed in figure 20b. Both block copolymers exhibit p-channel behaviour after spin coating from chloroform solutions and the hole carrier mobilities of BC 16 and BC 30 were determined to be  $10^{-5}$  cm<sup>2</sup>/Vs and  $10^{-3}$  cm<sup>2</sup>/Vs, respectively. Thus, the increase of two orders of magnitude in the hole mobility is responsible for the huge increase in the EQE of BC 30.

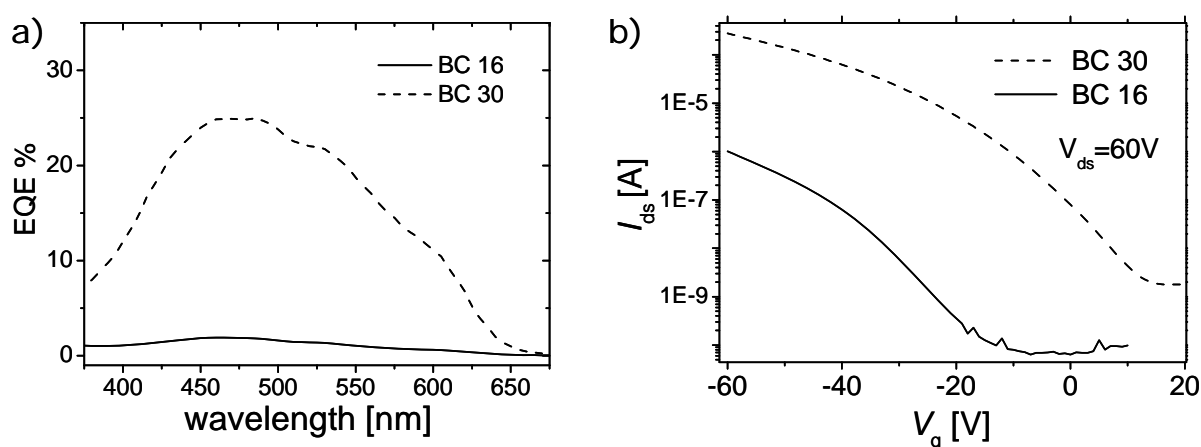


**Figure 20.** a) External quantum efficiency of BC 16 (solid) and BC 30 (dashed) after spin coating from chlorobenzene. b) Transfer plots of OFETs BC 16 (solid) and BC 30 (dashed) showing the huge increase in hole carrier mobility of two orders of magnitude. OFETs were prepared according to published procedures.<sup>62</sup>

Further fine-tuning of the molecular weight, composition, and device preparation conditions is necessary to ultimately improve the device performance, which currently is on the order of 0.2 %. These efficiencies are lower than one could expect from the high EQE values. Generally, we observed low fill factors (0.2- 0.3) in the devices, which points out the importance of further optimization of morphology. Note that thin films of BC 30 do not display a distinct structure in SEM, in contrast to the well-structured, but low-performing block copolymers BC 16-25 (see figure 18). While some ambiguity remains at this point, the results from DSC point out a larger domain size and a higher degree of crystallinity of BC 30 compared to BC 16. This rationalizes the outstanding performance of BC 30 in terms of its superior hole carrier mobility and high external quantum efficiency.<sup>88</sup> Further investigation and optimization of the morphology of BC 30 by different methods is therefore under study.

#### 4. Experimental

*Synthesis.* The synthesis of all block copolymers is described elsewhere.<sup>49,60,70</sup>

*Matrix-assisted laser desorption ionization time-of-flight spectrometry.* MALDI-TOF was performed according to ref.<sup>71</sup>

*Differential scanning calorimetry.* DSC experiments were carried out on a Perkin Elmer Diamond DSC with a heating rate of 10 K/min under N<sub>2</sub> atmosphere. Three cycles were measured, values were taken from the second cycle. Integration range of BC 16: PPerAcr: 150.0 °C- 192.2 °C, P3HT: 192.2 °C- 216.0 °C.

*Thermal gravimetry analysis.* TGA was studied using a Mettler Toledo TGA/SDTA 851 with a heating rate of 10 K/min under N<sub>2</sub> atmosphere.

*X-ray diffraction.* XRD patterns were acquired on a Guinier diffractometer (Huber) between  $\theta = 0.3^\circ$  and  $15^\circ$  in transmission geometry using monochromatic CuK $\alpha$  radiation (0.154 nm). Samples were either thermally or chloroform vapor annealed, milled and filled into glass capillaries. Step width was  $0.01^\circ$  with a collecting time of 50 s.

*UV-vis spectroscopy.* UV/vis spectra were recorded using a Hitachi U-3000 spectrometer. The in-situ UV-vis experiment of P3HT-9 during solvent annealing (figure 16a) was measured with a Hewlett-Packard 8453 diode array spectrometer. Between each measurement step approximately 5 min were given time to adjust to the new value.

*Solvent annealing.* Solvent annealing of bulk samples for SEM was carried out in a simple desiccator. Solvent annealing of thin films was done according to a published procedure.<sup>85</sup> Briefly, the saturation of the solvent vapour was controlled by mixing of dry nitrogen gas with nitrogen that is 100% saturated since it went through a washbottle with the respective solvent. The ratio was controlled over the flow of the gases by two electronic mass flow controllers (MKS) and consequently allowed to adjust the solvent vapour saturation continuously from 0-100%. The temperatures of the solvent reservoir and that of the sample chamber were controlled and kept equal. Unless otherwise noted, the following standard conditions were applied to thin films: Temperature of solvent and sample was 21 °C, solvent saturation 90 %, and the annealing time was 90 min. Solvent annealing of powder samples for XRD was done by exposing the powders to a stream of nitrogen saturated with chloroform. The flow of the stream was adjusted so that the powders did not get wet with chloroform.

*Scanning electron microscopy.* Samples for SEM were prepared either on indium tin oxide substrates, or the solar cells themselves were used. An inlens detector was used at a working distance of 2 mm and the acceleration voltage was 1 kV. Sputtering of 2 nm of platinum was done to avoid substantial charging of the surface.

*Organic field effect transistor* measurements and solar cell preparation was done according to published procedures.<sup>61,62,88</sup> All annealing steps were performed before evaporating aluminium.

## 5. Conclusions

In conclusion, we have shown that nitroxide mediated radical polymerization (NMRP) and Grignard Metathese Polymerization (GRIM) can be used, combined and customized to synthesize well-defined, fully functionalized block copolymers carrying both donor (D) and acceptor (A) blocks. Two different D-A block copolymer architectures are presented: amorphous-crystalline block copolymers PvTAA-*b*-PPerAcr with amorphous poly(triarylamine) donor blocks and side-chain crystalline poly(perylene bisimide acrylate) as acceptor block. Here, NMRP is successfully used to sequentially polymerize the D and A monomers. The second D-A block copolymer architecture consists of two crystalline

segments: Main chain crystalline poly(3-hexylthiophene) P3HT as the donor and side-chain crystalline PPerAc as the acceptor. For such a complex molecule to be synthesized, GRIM and NMRP are combined in a straightforward fashion, enabling the facile preparation of the novel block copolymers P3HT-*b*-PPerAc in only two steps.

The application of PvTAA-*b*-PPerAc block copolymers in single layer photovoltaic devices is demonstrated, and the block copolymers outperform their analogous blend devices by far. The device performance is further increased by varying block copolymer architecture, morphology, donor HOMO level, and hole carrier mobility. These parameters are strongly depending on each other, showing that further optimization of the solar cell performance is feasible by considering all parameters simultaneously.

The second block copolymer system P3HT-*b*-PPerAc is composed of two crystalline blocks, the segment lengths of which can be well controlled by varying the monomer to initiator ratio. The investigation of the thermal properties shows that PPerAc crystallizes first upon cooling, thereby suppressing the crystallinity of P3HT, depending on the block length of PPerAc. Concerning the device performance, the P3HT molecular weight is crucial for obtaining high external quantum efficiencies (EQE). Block copolymers with P3HT blocks of 9 kg/mol and compositions around 1:1 give low EQEs around 3 %, whereas doubling of the P3HT as well as the overall block copolymer molecular weight leads to EQE values approaching 30 %. These outstanding results not only require the investigation of the underlying photophysical processes, but also further synthetic efforts concerning fine-tuning of molecular weight and composition, as well as a complete understanding of the kinetics of competing crystallization and microphase separation, all of which are currently under study.

## 6. Acknowledgements

We thank W. Milius, University of Bayreuth, and T. Thurn-Albrecht, University of Halle, for fruitful discussions. Financial support of this work by the Deutsche Forschungsgemeinschaft (SFB 481, SPP 1355), the European Science Foundation (EUROCORES SOHYDs) and the Polyfilm EU Research Training Network is gratefully acknowledged. S.H. acknowledges a scholarship of the Bayerische Graduiertenförderung.

## 7. References

1. C. W. Tang, *Appl. Phys. Lett.* **1986**, *48*, 18.
2. B. A. Gregg, *J. Phys. Chem. B* **2003**, *107*, 4688.
3. M. M. Wienk, M. Turbiez, J. Gilot, R. A. J. Janssen, *Adv. Mater.* **2008**, *20*, 2556.
4. M. Lenes, G.-J. A. H. Wetzelaer, F. B. Kooistra, S. C. Veenstra, J. C. Hummelen, P. W. M. Blom, *Adv. Mater.* **2008**, *20*, 2116.
5. A. M. Ballantyne, L. Chen, J. Nelson, D. D. C. Bradley, Y. Astuti, A. Maurano, C. G. Shuttle, J. R. Durrant, M. Heeney, W. Duffy, I. McCulloch, *Adv. Mater.* **2007**, *19*, 4544.
6. G. Yu, J. Gao, J. C. Hummelen, *Science* **1995**, *270*, 1789.
7. W. Ma, C. Yang, X. Gong, K. Lee, A. J. Heeger, *Adv. Funct. Mater.* **2005**, *15*, 1617.
8. J. Peet, J. Y. Kim, N. E. Coates, W. L. Ma, D. Moses, A. J. Heeger, G. C. Bazan, *Nat. Mater.* **2007**, *6*, 497.
9. G. Li, V. Shrotriya, J. Huang, Y. Yao, T. Moriarty, K. Emery, Y. Yang, *Nat. Mater.* **2005**, *4*, 864.
10. J.-Y. Kim, K. Lee, N. E. Coates, D. Moses, T.-Q. Nguyen, M. Dante, A. J. Heeger, *Science* **2007**, *317*, 222.
11. A. C. Arias, N. Corcoran, M. Banach, R. H. Friend, J. D. MacKenzie, W. T. S. Huck, *Appl. Phys. Lett.*, **2002**, *80*, 1695.
12. Q. Wei, T. Nishizawa, K. Tajima, K. Hashimoto, *Adv. Mater.* **2008**, *20*, 2211.
13. S. S. Gayathri, M. Wielopolski, E. M. Pérez, G. Fernández, L. Sánchez, R. Viruela, E. Ortí, D. M. Guldi, N. Martín, *Angew. Chem.* **2009**, *48*, 815.
14. A. P. H. J. Schenning, J. v. Herrikhuyzen, P. Jonkheijm, Z. Chen, F. Würthner, E. W. Meijer, *J. Am. Chem. Soc.* **2002**, *124*, 10252.
15. F. Würthner, C. Bauer, V. Stepanenko, S. Yagai, *Adv. Mater.* **2008**, *20*, 1695.
16. A. Wicklein, S. Gosh, M. Sommer, F. Würthner, M. Thelakkat, *ACS Nano*, **2009**, *3*, 1107.
17. F. Würthner, Z. Chen, V. Dehm, V. Stepanenko, *Chem. Commun.*, **2006**, 1188.
18. K. Balakrishnan, A. Datar, R. Oitker, H. Chen, J. Zuo, L. Zang, *J. Am. Chem. Soc.*, **2005**, *127*, 10496.
19. J. J. Dittmer, E. A. Marseglia, R. H. Friend, *Adv. Mater.* **2002**, *12*, 1270.

20. W. S. Shin, H.-H. Jeong, M.-K. Kim, S.-H. Jin, M.-R. Kim, J.-K. Lee, J. W. Lee, Y.-S. Gal, *J. Mater. Chem.* **2006**, *16*, 384.
21. P. E. Keivanidis, I. A. Howard, R. H. Friend, *Adv. Funct. Mater.* **2008**, *18*, 3189.
22. T. Nishizawa, K. Tajima, K. Hashimoto, *J. Mater. Chem.* **2007**, *17*, 2440.
23. J. Roncali, *Chem. Soc. Rev.*, **2005**, *34*, 483.
24. Z. Tan, J. Hou, Y. He, E. Zhou, C. Yang, Y. Li, *Macromolecules* **2007**, *40*, 1868.
25. H. Hoppe, N. S. Sariciftci, *J. Mater. Chem.* **2006**, *16*, 45.
26. A. R. Campbell, J. M. Hodgkiss, S. Westenhoff, I. A. Howard, R. A. Marsh, C. R. McNeill, R. H. Friend, N. C. Greenham, *Nano Lett.*, **2008**, *8*, 3942.
27. J. van Duren, X. Yang, J. Loos, C. Bulle-Lieuwma, A. Sieval, J. Hummelen, R. Janssen, *Adv. Funct. Mater.* **2004**, *14*, 425.
28. P. Peumans, S. Uchida, S. R. Forrest, *Nature* **2003**, *425*, 158.
29. S. King, M. Sommer, S. Hüttner, M. Thelakkat, S. A. Haque, *J. Mater. Chem.* **2009**, *19*, 5436.
30. F. S. Bates, G. H. Fredrickson, *Ann. Rev. Phys. Chem.* **1990**, *41*, 525.
31. G. Buxton, N. Clarke, *Phys. Rev. B* **2006**, *74*, 085207.
32. S. H. Kim, M. J. Misner, T. P. Russell, *Adv. Mater.* **2004**, *16*, 2119.
33. T. Thurn-Albrecht, J. DeRouchey, T. P. Russell, H. M. Jaeger, *Macromolecules* **2000**, *33*, 3250.
34. D. E. Angelescu, J. H. Waller, R. A. Register, P. M. Chaikin, *Adv. Mater.* **2005**, *17*, 1878.
35. E. J. W. Crossland, M. Nedelcu, C. Ducati, S. Ludwigs, M. A. Hillmyer, U. Steiner, H. J. Snaith, *Nano Lett.*, **2009**, *9*, 2813.
36. U. Stalmach, B. de Boer, C. Videlot, P. F. van Hutten, G. Hadziioannou, *J. Am. Chem. Soc.*, **2000**, *122*, 5464.
37. M. H. van der Veen, B. de Boer, U. Stalmach, K. I. van de Wetering, G. Hadziioannou, *Macromolecules* **2004**, *37*, 3673.
38. S. Barrau, T. Heiser, F. Richard, C. Brochon, C. Ngov, K. van de Wetering, G. Hadziioannou, D. V. Anokhin, D. A. Ivanov, *Macromolecules* **2008**, *41*, 2701.
39. G. Tu, H. Li, M. Forster, R. Heiderhoff, L. J. Balk, U. Scherf, *Macromolecules* **2006**, *39*, 4327.
40. K. Sivula, Z. T. Ball, N. Watanabe, J. M. J. Frechet, *Adv. Mater.* **2006**, *18*, 206.

41. S.-S. Sun, C. Zhang, A. Ledbetter, S. Choi, K. Seo, C. E. Bonner, M. Drees, N. S. Sariciftci, *Appl. Phys. Lett.* **2007**, *90*, 043117.
42. M. Prato, *J. Mater. Chem.* **1997**, *7*, 1097.
43. J. J. Dittmer, R. Lazzaroni, P. Leclere, P. Moretti, M. Granstrom, K. Petritsch, E. A. Marseglia, R. H. Friend, J. L. Bredas, H. Rost, A. B. Holmes, *Sol. En. Mater. Sol. Cells* **2000**, *61*, 53.
44. S. Foster, C. E. Finlayson, P. E. Keivanidis, Y.-S. Huang, I. Hwang, R. H. Friend, M. B. J. Otten, L.-P. Lu, E. Schwartz, R. J. M. Nolte, A. E. Rowan, *Macromolecules*, **2009**, *42*, 2023.
45. S. M. Lindner, M. Thelakkat, *Macromolecules* **2004**, *37*, 8832.
46. C. Hawker, A. W. Bosman, E. Harth, *Chem. Rev.* **2001**, *101*, 3661.
47. D. Benoit, V. Chaplinski, R. Braslau, C. J. Hawker, *J. Am. Chem. Soc.*, **1999**, *121*, 3904.
48. A. Lang, M. Thelakkat, Diploma Thesis, University of Bayreuth 2007.
49. M. Sommer, M. Thelakkat, *Eur. Phys. J. Appl. Phys.*, **2006**, *36*, 245.
50. T. Yamamoto, M. Nishiyama, Y. Koie, *Tetrahedron Letters*, **1998**, *39*, 2367.
51. I. Li, B. A. Howell, K. Matyjaszewski, T. Shigemoto, P. B. Smith, D. B. Priddy, *Macromolecules* **1995**, *28*, 6692.
52. M. Stolka, D. M. Pai, D. S. Renfer, J. F. Yanus, *J. Pol. Sci., Pol. Chem. Ed.* **1983**, *21*, 969.
53. M. Abkowitz, D. M. Pai, *Philosophical Magazine B* **1986**, *53*, 193.
54. E. Bellmann, S. E. Shaheen, R. H. Grubbs, S. R. Marder, B. Kippelen, N. Peyghambarian, *Chem. Mater.* **1999**, *11*, 399.
55. S. Maria, A. S. Susha, M. Sommer, D. V. Talapin, A. L. Rogach, M. Thelakkat, *Macromolecules*, **2008**, *41*, 6081.
56. M. Thelakkat, H.-W. Schmidt, *Adv. Mater.*, **1998**, *10*, 219.
57. E. T. Seo, R. F. Nelson, J. M. Fritsch, L. S. Marcoux, D. W. Leedy, R. N. Adams, *J. Am. Chem. Soc.*, **1966**, *88*, 3498.
58. S. M. Lindner, N. Kaufmann, M. Thelakkat, *Org. Electr.* **2007**, *8*, 69.
59. J. Seibt, V. Dehm, F. Würthner, V. Engel, *J. Chem. Phys.* **2007**, *126*, 164308.
60. M. Sommer, S. M. Lindner, M. Thelakkat, *Adv. Funct. Mater.* **2007**, *17*, 1493.
61. S. Hüttner, M. Sommer, M. Thelakkat, *Appl. Phys. Lett.*, submitted.
62. S. Hüttner, M. Sommer, M. Thelakkat, *Appl. Phys. Lett.* **2008**, *92*, 093302.

63. M. Sommer, S. Hüttner, S. Wunder, *Adv. Mater.* **2008**, *20*, 2523.
64. S. M. Lindner, S. Hüttner, A. Chiche, M. Thelakkat, G. Krausch, *Angew. Chem. Int. Ed.* **2006**, *45*, 3364.
65. Y. L. Loo, R. A. Register, D. H. Adamson, *J. Polym. Sci. B: Polym. Phys.* **2000**, *38*, 2564.
66. J. Liu, E. Sheina, T. Kowalewski, R. D. McCullough, *Angew. Chem. Int. Ed.* **2002**, *41*, 329.
67. M. C. Iovu, M. Jeffries-EL, E. Sheina, J. R. Cooper, R. D. McCullough, *Polymer* **2005**, *46*, 8582.
68. M. C. Iovu, C. R. Craley, M. Jeffries-El, A. B. Krankowski, R. Zhang, T. Kowalewski, R. D. McCullough, *Macromolecules* **2007**, *40*, 4733.
69. M. Jeffries-El, G. Sauve, R. D. McCullough, *Adv. Mater.* **2004**, *16*, 1017.
70. M. Sommer, A. Lang, M. Thelakkat, *Angew. Chem. Int. Ed.* **2008**, *47*, 7901.
71. J. Liu, R. S. Loewe, R. D. McCullough, *Macromolecules* **1999**, *32*, 5777.
72. P. Schilinsky, U. Asawapirom, U. Scherf, M. Biele, C. J. Brabec, *Chem. Mater.* **2005**, *17*, 2175.
73. Z. Wu, A. Petzold, T. Henze, T. Thurn-Albrecht, R. Lohwasser, M. Sommer, M. Thelakkat, *Macromolecules*, submitted.
74. A. Zen, M. Saphiannikova, D. Neher, J. Grenzer, S. Grigorian, U. Pietsch, U. Asawapirom, S. Janietz, U. Scherf, I. Lieberwirth, G. Wegner, *Macromolecules* **2006**, *39*, 2162.
75. C. Müller, C. P. Radano, P. Smith, N. Stingelin-Stutzmann, *Polymer* **2008**, *49*, 3973.
76. B. W. Boudouris, C. D. Frisbie, M. A. Hillmyer, *Macromolecules* **2008**, *41*, 67.
77. I. W. Hamley, V. Castelletto, R. V. Castillo, A. J. Müller, C. M. Martin, E. Pollet, P. Dubois, *Macromolecules* **2005**, *38*, 463.
78. S. Nojima, Y. Akutsu, M. Akaba, S. Tanimoto, *Polymer* **2005**, *46*, 4060.
79. H. Takeshita, K. Fukumoto, T. Ohnishi, T. Ohkubo, M. Miya, K. Takenaka, T. Shiomi, *Polymer* **2006**, *47*, 8210.
80. F. Nolde, W. Pisula, S. Müller, C. Kohl, K. Müllen, *Chem. Mater.* **2006**, *18*, 3715.
81. T. J. Prosa, M. J. Winokur, J. Moulton, P. Smith, A. J. Heeger, *Macromolecules* **1992**, *25*, 4364.
82. J. Clark, C. Silva, R. H. Friend, F. C. Spano, *Phys. Rev. Lett.* **2007**, *98*, 206406.

83. R. Österbacka, C. P. An, X. M. Jiang, Z. V. Vardeny, *Science* **2000**, 287, 839.
84. U. Zhokhavets, T. Erb, G. Gobsch, M. Al-Ibrahim, O. Ambacher, *Chem. Phys. Lett.* **2006**, 418, 347.
85. S. Hüttner, M. Sommer, A. Chiche, G. Krausch, U. Steiner, M. Thelakkat, *Soft Matter*, **2009**, 5, 4206.
86. I. W. Hamley: *The physics of block copolymers*; Oxford University Press, Oxford 1998.
87. V. Marcon, J. Kirkpatrick, W. Pisula, D. Andrienko, *Phys. Stat. Sol. B* **2008**, 245, 820.
88. M. Sommer, S. Hüttner, U. Steiner, M. Thelakkat, *Appl. Phys. Lett.*, in print.
89. R. J. Kline, M. D. McGehee, E. N. Kadnikova, J. Liu, J. M. J. Fréchet, *Adv. Mater.* **2003**, 15, 1519.



## 6. Influence of the Molecular Weight of Double-Crystalline Donor-Acceptor Block Copolymers on the Performance of Polymer Solar Cells

Michael Sommer,<sup>a</sup> Sven Hüttner,<sup>a,b</sup> Ullrich Steiner,<sup>b</sup> and Mukundan Thelakkat<sup>a</sup>

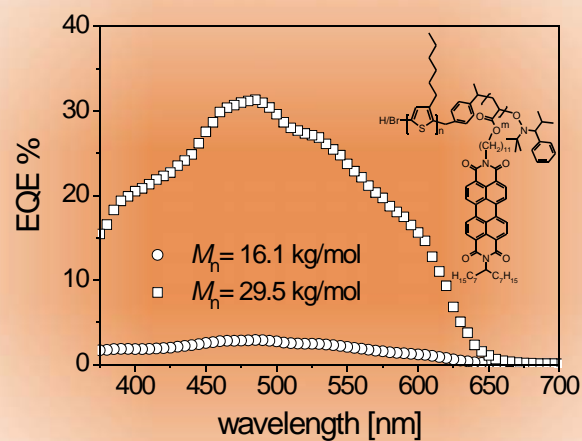
<sup>a</sup>Applied Functional Polymers and Macromolecular Chemistry I

Universität Bayreuth, Universitätsstr. 30, University of Bayreuth, 95444 Bayreuth, Germany

<sup>b</sup>Thin Films and Interfaces Group, Cavendish Laboratory, BSS Physics

11 JJ Thomson Avenue, Cambridge CB3 0HE, United Kingdom

[Michael.Sommer@uni-bayreuth.de](mailto:Michael.Sommer@uni-bayreuth.de), [Mukundan.Thelakkat@uni-bayreuth.de](mailto:Mukundan.Thelakkat@uni-bayreuth.de)



*Applied Physics Letters*, in print.

**Abstract**

We investigate the influence of the molecular weight of double-crystalline donor-acceptor block copolymers comprised of poly(3-hexylthiophene) P3HT as donor and poly(perylene bisimide acrylate) PPerAcr as acceptor segments on the device performance of polymer solar cells. Two block copolymers **1** and **2** exhibiting different molecular weights but the same composition are compared. Block copolymer **2** with the higher molecular weight shows an improvement in the hole carrier mobility  $\mu_{\text{OFET}}$  of more than two orders of magnitude, and an improvement in the external quantum efficiency EQE of one order of magnitude reaching 31%, which is the highest reported value for a block copolymer system.

Substantial research progress has been made in the field of solution-processed organic photovoltaic cells (OPVs) over the last decade.<sup>1,2</sup> In such devices, the active layer morphology has been shown to be crucial to the device performance.<sup>3-5</sup> State-of-the-art OPVs mostly employ blends of conjugated polymers as donor and fullerene derivatives as acceptor materials, which have already attained high power conversion efficiencies of ~4-6%.<sup>6-9</sup> Perylene bisimides (PBI) are promising acceptor materials due to their absorption in the visible region and their tendency to crystallize.<sup>10,11</sup> In general, a phase separation of the donor and acceptor material on a nanoscale is needed to separate charges efficiently, thereby addressing the conflict of the relatively large optical absorption length (~100 nm) and the short exciton diffusion length (~10 nm). Polymer blends comprised of low molecular weight PBIs and conjugated polymers such as poly(3-hexylthiophene) P3HT give rise to uncontrolled crystallization of PBI, and hence lead to a reduction in the interfacial area, hindered charge transport, and moderate device performance.<sup>12</sup> One possible approach to solve this is the use of polymers with PBI units in the main chain.<sup>13</sup> Yet, macrophase separation generally occurring in polymer-polymer blends is a drawback in terms of controlling the size and shape of the interfacial area. Block copolymers (BCPs) microphase separate into well-defined periodic nanostructures due to the interplay of covalent connectivity and demixing of the two polymer segments<sup>14</sup>, and therefore are expected to guarantee distinct charge transport pathways for both holes and electrons.<sup>15</sup> Indeed, the concept of fully functionalized BCPs comprised of amorphous donor blocks and side-chain crystalline perylene bisimide acceptor segments has demonstrated that co-continuous morphologies with domain sizes commensurate to the exciton diffusion length can be obtained while PBI crystallization is confined to microdomains.<sup>16-18</sup> This approach has recently been extended to double-crystalline BCPs comprised of P3HT and side chain crystalline PBI blocks by our group and others.<sup>19-21</sup>

Here, we report on the photovoltaic properties of these double-crystalline BCP systems. Two BCPs poly(3-hexylthiophene)-*b*-poly(perylen bisimide acrylate) P3HT-*b*-PPerAcr **1** and **2**, which possess the same composition but differ in molecular weight by a factor of 2, are compared in single component single layer solar cells (Fig. 1).

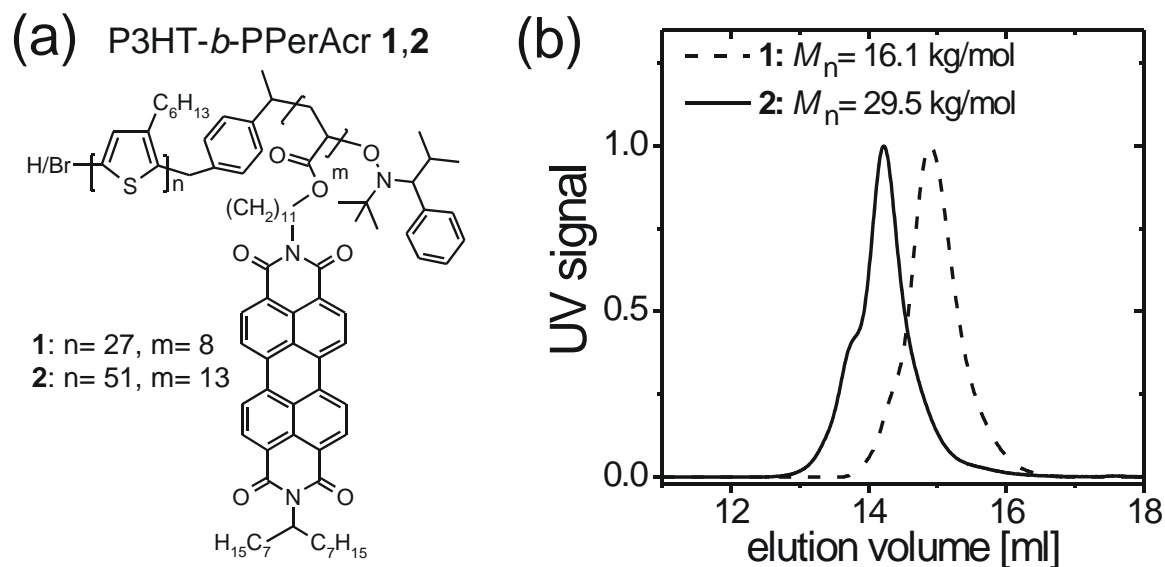


**Fig. 1** (a) Chemical structure of poly(3-hexylthiophene)-*b*-poly(perylene bisimide acrylate) P3HT-*b*-PPerAcr **1** and **2**. (b) SEC curves showing the difference in molecular weight. The composition is maintained at 55 wt.-%PPerAcr.

The synthesis of P3HT-*b*-PPerAcr **1** was reported recently.<sup>19</sup> A batch of the high molecular weight BCP **2** with exactly the same composition was synthesized analogously for this comparative study here. **1** and **2** exhibit molecular weights of 16.1 and 29.5 kg/mol (determined by SEC in THF using polystyrene standards), and very low polydispersities of 1.25 and 1.15, respectively. The molecular weights of the P3HT segments in **1** and **2** are 8.9 and 17.0 kg/mol, respectively. The content of PPerAcr (determined by <sup>1</sup>H-NMR) is maintained at 55 wt.-% in both BCPs. Since the charge carrier mobility of P3HT films depends on the molecular weight considerably, we assumed such a dependence to be of importance here as well.<sup>22,23</sup>

The absorption profiles of **1** and **2** in films spun from chlorobenzene are depicted in figure 2a.

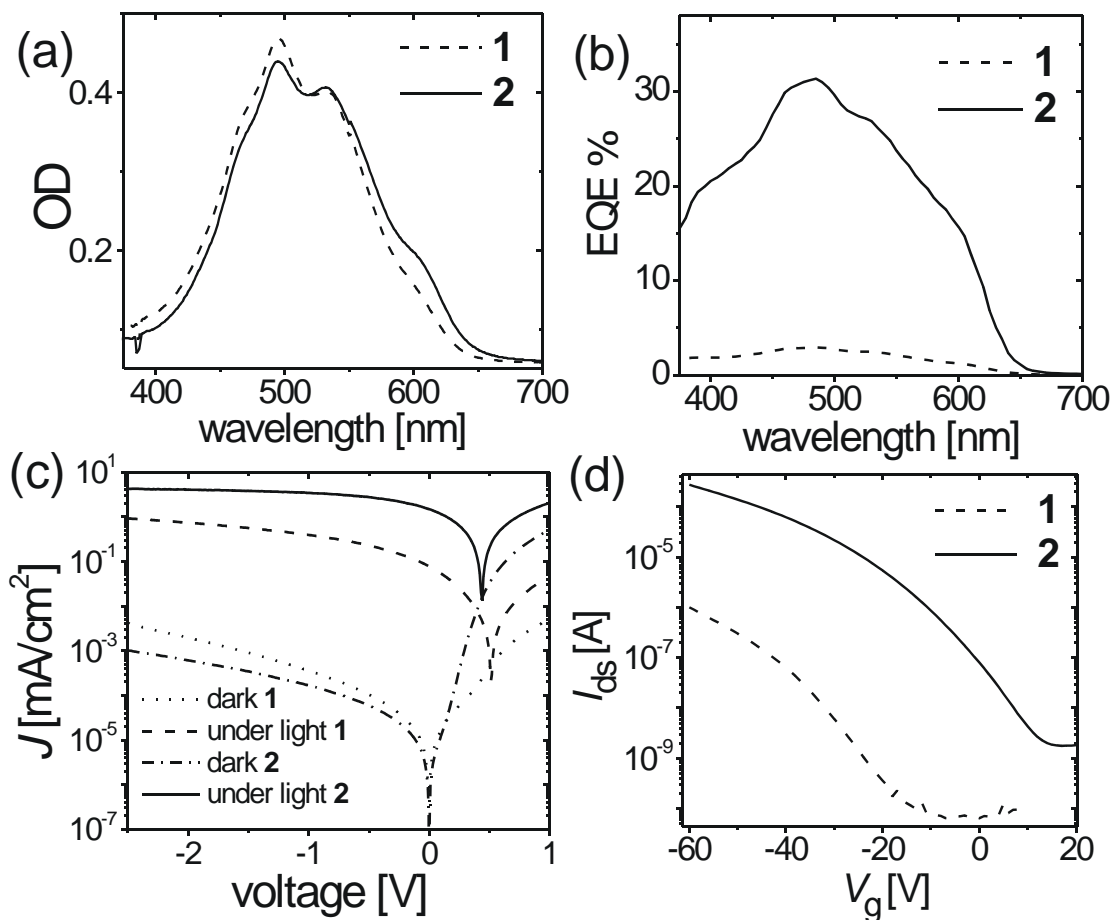


**Fig. 2** Optical and electrical properties of **1** and **2**. (a) Optical densities of thin films spin cast from chlorobenzene. (b) External quantum efficiency (EQE). (c) J-V-curves measured in the dark and under AM 1.5G conditions ( $100 \text{ mW/cm}^2$ ). (d) OFET transfer characteristics of **1** and **2** after spin coating from chloroform in bottom-gate bottom-contact devices with gold electrodes.

The common characteristic P3HT homopolymer absorption at 610 nm arising from interchain exciton delocalization<sup>24</sup> is visible in both block copolymers, however the intensity at 610 nm is higher for **2**, which indicates a higher degree of P3HT crystallinity.<sup>25</sup> Apart from this difference, the similar UV-vis profiles of both block copolymers guarantee that the same amount of light is absorbed in the devices. Solar cells were fabricated using the device structure ITO/PEDOT:PSS/active layer/Al. The best devices were obtained by spin coating solutions of 15 mg BCP in 1ml chlorobenzene at 700 r/min, giving a film thickness of  $\sim 60 \text{ nm}$ . Using these parameters, a maximum external quantum

efficiency (EQE) of 31 % at 495 nm was obtained for **2**. The average values measured from 16 solar cells resulted in an  $\text{EQE}_{\text{max}} = 25\%$ ,  $J_{\text{SC}} = 1.14 \text{ mA/cm}^2$ ,  $V_{\text{OC}} = 0.40 \text{ V}$ , fill factor = 27.6 % and  $\eta = 0.10\%$ . Additional post production treatments of devices made from **2** such as chloroform vapor annealing<sup>26</sup> or thermal annealing did not lead to further improvements in the external quantum efficiency. Devices with **1** as the active layer yielded EQE peak values of 3 % only (Fig. 2b). The corresponding  $J$ - $V$ -characteristics are shown in figure 2c. P3HT-*b*-PPerAcr **1** with a molecular weight of 16.1 kg/mol gave very low short circuit currents  $J_{\text{SC}}$  around  $0.08 \text{ mA/cm}^2$  and open circuit voltages  $V_{\text{OC}}$  of 0.51 V, resulting in poor power conversion efficiencies  $\eta$  of 0.007 %. Block copolymer **2** with a molecular weight of 29.5 kg/mol again shows a drastic improvement; a  $J_{\text{SC}}$  of  $1.5 \text{ mA/cm}^2$  and a power conversion efficiency  $\eta$  of 0.2 % are observed. The fill factor also increases from 0.17 to 0.25, and the open circuit voltage  $V_{\text{OC}}$  was 0.44 V. Organic field effect transistors (OFETs) with a bottom-gate bottom-contact configuration and gold electrodes using **1** and **2** as active layers both show p-channel behavior (Fig. 2d). The hole carrier mobility  $\mu_{\text{h}}$  of **2** after spin coating is  $5 \cdot 10^{-3} \text{ cm}^2/\text{Vs}$ , while the OFET device made of block copolymer **1** only shows a mobility of  $3 \cdot 10^{-5} \text{ cm}^2/\text{Vs}$ . Thus, BCP **2** with the higher molecular weight exhibits an improvement of the EQE by one order of magnitude in solar cells, and an improvement of the hole carrier mobility by more than two orders of magnitude compared to BCP **1**.

Differential scanning calorimetry (DSC) and X-ray scattering (XRD) experiments are used to investigate the phase behavior and to explain the huge difference in the device parameters of **1** and **2**. The DSC curve of **1** shows two endotherms at 190°C and 211°C that are ascribed to the melting of PPerAcr and P3HT, respectively (Fig. 3a).

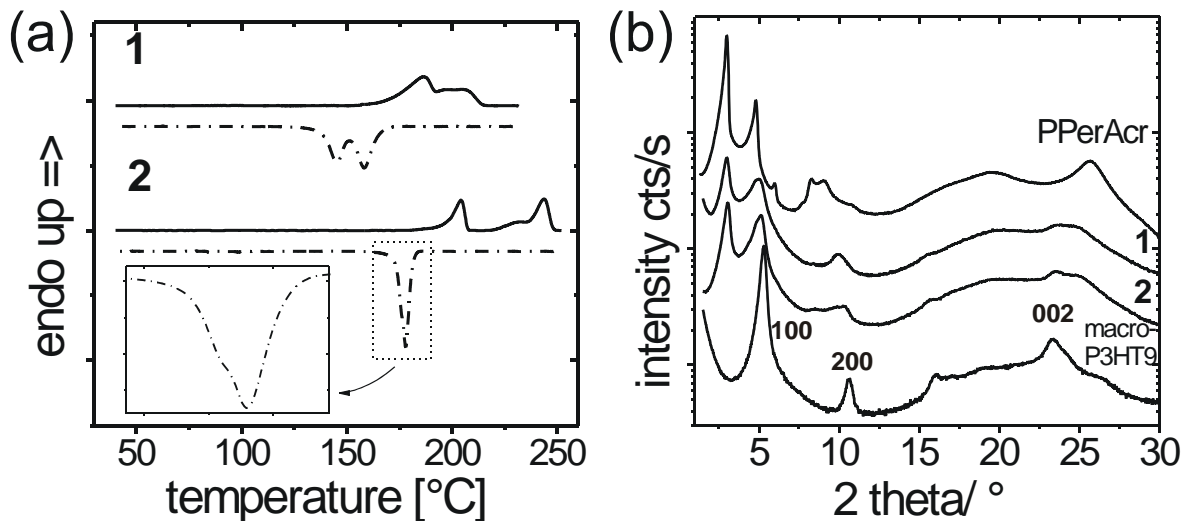


**Fig. 3** Crystallinity of P3HT-*b*-PPerAcryl **1** and **2**. (a) Differential scanning calorimetry at 10 K/min under nitrogen. The second heating (solid lines) and second cooling curves (dash-dots) are shown. The inset enlarges the recrystallization peak of **2**. (b) X-ray scattering of **1**, **2**, P3HT macroinitiator, and PPerAcryl homopolymer. Curves are offset in *y*-direction.

On cooling, PPerAcryl crystallizes first at 162°C followed by P3HT at 148°C. This is evidenced by the crystallization peak at 162°C, intensity increasing with increasing PPerAcryl weight fraction. In the heating curve of **2**, two endotherms are observed at 204°C and 244°C, corresponding to PPerAcryl and P3HT, respectively. Note that the difference in the melting temperatures of **2** is larger than of **1**. The single peak in the cooling curve of **2** at 178 °C entails the crystallization of both, P3HT and PPerAcryl. The magnification of this peak reveals a small shoulder at 176 °C (see inset of Fig. 3a), arising from PPerAcryl. Hence, crystallization of P3HT and PPerAcryl occurs almost simultaneously in BCP **2**. The larger distance between the two melting points and the coincidence of the two crystallizations in **2** are caused by the strong dependence of the melting and crystallization temperature of P3HT on its molecular weight.<sup>27</sup> Note that the thermal behavior of P3HT causes a fundamental difference in the thermal properties of **1** and **2**: On cooling from the melt, PPerAcryl crystallizes first in **1**, while simultaneous crystallization of the two blocks occurs in **2**. The different block lengths of P3HT in **1** and **2**, together with the varying behavior of crystallization, finally give rise to different degrees of P3HT crystallinity, as can be tracked by the melting enthalpies  $\Delta H_m$ .

$\Delta H_m(\text{P3HT})$  is 15.4 J/mol for **2**, but only 10.3 J/mol for **1**. Qualitatively, the lower degree of P3HT crystallinity in **1** is also visible from the different optical densities at 610 nm (Fig. 2a).<sup>25</sup> In addition, the higher melting point of 244°C of the P3HT segment in **2** depicts larger P3HT domains compared to those in **1**, which melt at 211°C. A larger domain size in turn should favor charge percolation and obviously is responsible for the improved hole transport in BCP **2**. Indeed, a similar dependence has been observed in amorphous-crystalline block copolymers, in which improvements of the OPV device performance with molecular weight were ascribed to better charge percolation due to microphase separation.<sup>28</sup>

Further investigation of the crystalline nature of P3HT-*b*-PPerAcr is accomplished using X-ray diffraction of thermally annealed powders (Fig. 3b). Both P3HT-macroinitiators exhibited very similar diffraction patterns. As a typical example, the XRD pattern of **1** is shown in figure 3b. The known (100), (200) and (002) reflections of lamellar stacks of P3HT are observed at  $2\theta$  values of 5.3°, 10.6°, 16.1°, and 23.4°, respectively, in agreement with reported values.<sup>29,30</sup> In the PPerAcr homopolymer two strong Bragg reflections appear at  $2\theta$  values of 3.0° and 4.8°, respectively. These result from a two-dimensional lattice formed by stacks of the PBI units of PPerAcr where the individual stacks are separated by the alkyl groups. An additional reflection at  $2\theta = 25.6^\circ$  indicates the  $\pi$ - $\pi$  distance of 0.35 nm between two PBI moieties within one stack. The two BCPs **1** and **2** feature the reflections of the individual homopolymers and hence, stacks of P3HT and PPerAcr coexist here. A comparison of the intensities  $100_{\text{P3HT}}/d(2\theta=3.0^\circ)_{\text{PPerAcr}}$  and  $002_{\text{P3HT}}/d(2\theta=25.6^\circ)_{\text{PPerAcr}}$  yields higher values for **2**, which is indicative of a higher degree of P3HT crystallinity. These results are in accordance with the higher degree of P3HT crystallinity of **2** observed in the absorption spectrum (Fig. 2a) and in the DSC curves (Fig. 3a).

In conclusion, we have shown that the molecular weight of double-crystalline donor acceptor block copolymers P3HT-*b*-PPerAcr is influencing their solar cell performance to a large extent. A higher molecular weight of P3HT-*b*-PPerAcr (and thus a larger block length of P3HT) leads to a larger degree of P3HT crystallinity and to larger P3HT crystals, which again favor charge percolation, increase the external quantum efficiency and finally the short circuit current. The reported EQE value of over 25% up to 31 % exceeds

those of blend cells comprised of P3HT and low molecular weight PBIs.<sup>11,21,31</sup> Current research is concerned with light intensity-dependent measurements and the improvement of the fill factor, which limit the overall device efficiency.

## Acknowledgements

Financial support by the Deutsche Forschungsgemeinschaft (SFB 481, SPP 1355), and the Polyfilm EU Research Training Network is gratefully acknowledged. S.H. acknowledges a scholarship of the Bayerische Graduiertenförderung. The authors are indebted to P. Kohn and T. Thurn-Albrecht, University of Halle, for fruitful discussions, and to R. H. Friend for the opportunity to use the solar cell preparation and characterization facilities.

## References

1. S. Günes, H. Neugebauer, N. S. Sariciftci, *Chem. Rev.* **2007**, *107*, 1324.
2. G. Dennler, M. C. Scharber, C. J. Brabec, *Adv. Mater.* **2009**, *21*, 1323.
3. H. Hoppe, N. S. Sariciftci, *J. Mater. Chem.* **2006**, *16*, 45.
4. M. C. Quiles, T. Ferenczi, T. Agostinelli, P. G. Etchegoin, Y. Kim, T. D. Anthopoulos, P. N. Stavrinou, D. D. C. Bradley, J. Nelson, *Nat. Mater.* **2008**, *7*, 158.
5. A. R. Campbell, J. M. Hodgkiss, S. Westenhoff, I. A. Howard, R. A. Marsh, C. R. McNeill, R. H. Friend, N. C. Greenham, *Nano Lett.* **2008**, *8*, 3942.
6. W. Ma, C. Yang, X. Gong, K. Lee, A. J. Heeger, *Adv. Funct. Mater.* **2005**, *15*, 1617.
7. G. Li, V. Shrotriya, J. Huang, Y. Yao, T. Moriarty, K. Emery, Y. Yang, *Nat. Mater.* **2005**, *4*, 864.
8. J. Peet, J. Y. Kim, N. E. Coates, W. L. Ma, D. Moses, A. J. Heeger, G. C. Bazan, *Nat. Mater.* **2007**, *6*, 497.
9. M. M. Wienk, M. Turbiez, J. Gilot, R. A. J. Janssen, *Adv. Mater.* **2008**, *20*, 2556.
10. L. Schmidt-Mende, A. Fechtenkötter, K. Müllen, E. Moons, R. H. Friend, J. D. MacKenzie, *Science* **2001**, *293*, 119.

11. P. E. Keivanidis, I. A. Howard, R. H. Friend, *Adv. Funct. Mater.* **2008**, *18*, 3189.
12. J. J. Dittmer, E. A. Marseglia, R. H. Friend, *Adv. Mater.* **2002**, *12*, 1270.
13. Z. Tan, E. Zhou, X. Zhan, X. Wang, Y. Li, S. Barlow, S. R. Marder, *Appl. Phys. Lett.* **2008**, *93*, 073309.
14. F. S. Bates, G. H. Fredrickson, *Ann. Rev. Phys. Chem.* **1990**, *41*, 525.
15. G. Buxton, N. Clarke, *Phys. Rev. B* **2006**, *74*, 085207.
16. S. M. Lindner, M. Thelakkat, *Macromolecules* **2004**, *37*, 8832.
17. S. M. Lindner, S. Hüttner, A. Chiche, M. Thelakkat, G. Krausch, *Angew. Chem. Int. Ed.* **2006**, *45*, 3364.
18. M. Sommer, S. M. Lindner, M. Thelakkat, *Adv. Funct. Mater.* **2007**, *17*, 1493.
19. M. Sommer, A. Lang, M. Thelakkat, *Angew. Chem. Int. Ed.* **2008**, *47*, 7901.
20. Q. Zhang, A. Cirpan, T. P. Russell, T. Emrick, *Macromolecules* **2009**, *42*, 1079.
21. S. Rajaram, P. B. Armstrong, B. J. Kim, J. M. J. Fréchet, *Chem. Mater.* **2009**, *21*, 1775.
22. R. J. Kline, M. D. McGehee, E. N. Kadnikova, J. Liu, J. M. J. Fréchet, M. F. Toney, *Macromolecules* **2005**, *38*, 3312.
23. J.-F. Chang, J. Clark, N. Zhao, H. Sirringhaus, D. W. Breiby, J. W. Andreasen, M. M. Nielsen, M. Giles, M. Heeney, I. McCulloch, *Phys. Rev. B* **2006**, *74*, 115318.
24. J. Clark, C. Silva, R. H. Friend, F. C. Spano, *Phys. Rev. Lett.* **2007**, *98*, 206406.
25. U. Zhokhavets, T. Erb, G. Gobsch, M. Al-Ibrahim, O. Ambacher, *Chem. Phys. Lett.* **2006**, *418*, 347.
26. S. Huettnner, M. Sommer, A. Chiche, G. Krausch, U. Steiner, M. Thelakkat, *Soft Matter* **2009**, *5*, 4206.
27. A. Zen, M. Saphiannikova, D. Neher, J. Grenzer, S. Grigorian, U. Pietsch, U. Asawapirom, S. Janietz, U. Scherf, I. Lieberwirth, G. Wegner, *Macromolecules*, **2006**, *39*, 2162.
28. S. King, M. Sommer, S. Huettnner, M. Thelakkat, S. A. Haque, *J. Mater. Chem.* **2009**, *19*, 5436.
29. T. J. Prosa, M. J. Winokur, J. Moulton, P. Smith, A. J. Heeger, *Macromolecules* **1992**, *25*, 4364.
30. S. Hugger, R. Thomann, T. Heinzel, T. Thurn-Albrecht, *Colloid Polym. Sci.* **2004**, *282*, 932.

31. W. S. Shin, H.-H. Jeong, M.-K. Kim, S.-H. Jin, M.-R. Kim, J.-K. Lee, J. W. Lee, Y.-S. Gal, *J. Mater. Chem.* **2006**, *16*, 384.



## 7. Novel Electron Conducting Block Copolymers: Morphological, Optical and Electrical Properties

<sup>a</sup>Michael Sommer, <sup>a,b</sup>Sven Hüttner, <sup>a</sup>Stefanie Wunder, and <sup>a</sup>Mukundan Thelakkat

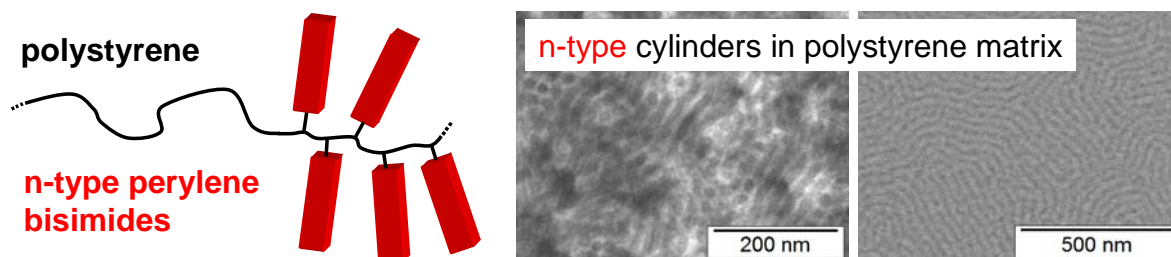
<sup>a</sup>Applied Functional Polymers and Macromolecular Chemistry I

Universität Bayreuth, Universitätsstr. 30, University of Bayreuth, 95444 Bayreuth, Germany

<sup>b</sup>Thin Films and Interfaces Group, Cavendish Laboratory, BSS Physics

11 JJ Thomson Avenue, Cambridge CB3 0HE, United Kingdom

[Michael.Sommer@uni-bayreuth.de](mailto:Michael.Sommer@uni-bayreuth.de), [Mukundan.Thelakkat@uni-bayreuth.de](mailto:Mukundan.Thelakkat@uni-bayreuth.de)



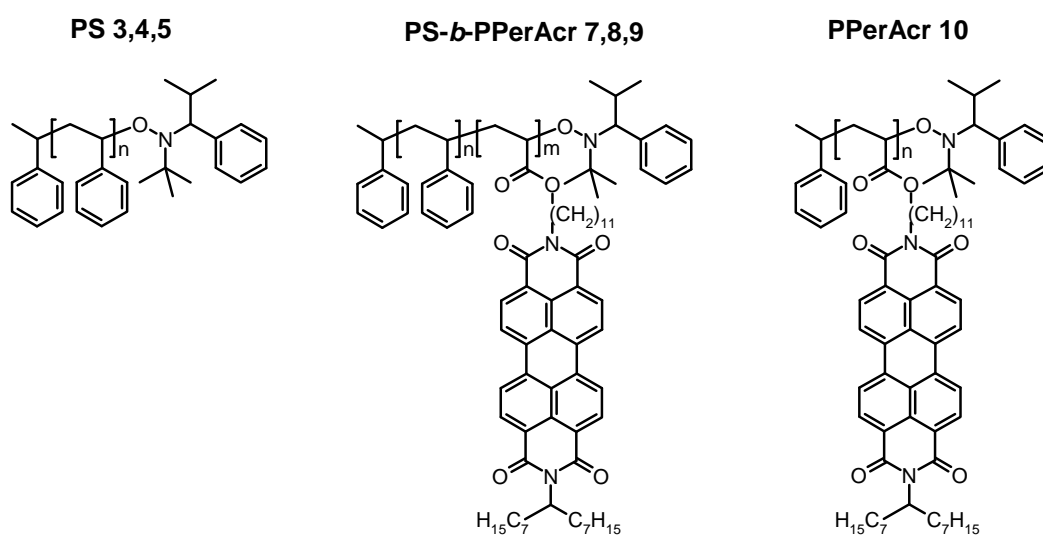
Understanding the fundamental processes in organic electronic devices such as organic solar cells (OSCs) or organic field effect transistors (OFETs) is essential for improving their performance. Regarding the active layer of the device, two issues have to be addressed. Firstly, the electronic properties of the materials should be selected carefully. Secondly, a defined and stable thin film morphology is mandatory for efficient operation and durability of devices. For instance, in OSCs, a vertically oriented morphology with microdomains of some tens of nanometers in size is needed to overcome the dilemma of absorption and short exciton diffusion length. At the same time, the separated charges have to be efficiently extracted at the electrodes.<sup>[1]</sup> Organic field effect transistors, on the other hand, require lateral charge transport in the plane of the substrate which results from the geometry of source and drain.<sup>[2]</sup> With all these devices, the fundamental question of the influence of ordered semiconducting pathways on the charge carrier mobility and finally on the device performance arises. This has been studied theoretically but an experimental demonstration has yet to follow.<sup>[3]</sup>

Block copolymers self-assemble into a variety of morphologies on a nanoscopic scale, making them extremely attractive for mesotechnology applications.<sup>[4,5]</sup> Electro-optically active block copolymers therefore offer the unique possibility of confining the active group in geometrically well-defined nanoscopic structures.<sup>[6]</sup> Further examples found in the literature include various hole conducting block copolymers in which main chain conjugated polymers are connected to flexible segments.<sup>[7]</sup> Electron conducting block copolymers, in contrast, have been rarely developed and the effect of morphology on the charge transport properties has not been reported.<sup>[8]</sup>

Recently, we reported the suitability and versatility of nitroxide mediated radical polymerization (NMRP) for the synthesis of donor-acceptor (DA) block copolymers.<sup>[9]</sup> This method is of additional interest for the development of semiconducting block copolymers due to its metal-free nature. A variation of the morphology and the electronic properties by altering the block lengths and the type of monomer was also feasible. Thus, using NMRP technique, complete control over chemical structure, morphology and function was accomplished.<sup>[10,11]</sup>

Here, we use this versatile synthetic method to combine both functional and commercially available monomers in order to prepare electron conducting nanostructures via block

copolymer self-assembly. Novel tailor-made electron conducting diblock copolymers polystyrene-*b*-poly(perylene bisimide acrylate) PS-*b*-PPerAc **7-9** (scheme 1) are synthesized and characterized by  $^1\text{H-NMR}$ , size exclusion chromatography (SEC) and differential scanning calorimetry (DSC). In addition, a perylene bisimide homopolymer poly(perylene bisimide acrylate) PPerAc **10** is synthesized for the sake of comparison of properties. We investigate both the bulk morphology and the thin film morphology of all block copolymers. As an example, the optical and electrical properties in thin films are studied in block copolymer **8**, which shows a cylindrical morphology. To understand the influence of the nanoscopic morphology on the  $\pi$ - $\pi$ -stacking of the pendant perylene bisimide moieties, a comparison with the analogous polymer blend PS:PPerAc **4:10** and the homopolymer PPerAc **10** (scheme 1) is made.



**Scheme 1.** Chemical structures of polystyrene 3-5, polystyrene-*b*-poly(perylene bisimide acrylate) 7-9 and poly(perylene bisimide acrylate) 10.

Three polystyrene macroinitiators PS **3**, **4**, **5** with molecular weights of 13.6, 21.8 and 35.1 kg/mol, respectively, and low polydispersity indices of 1.1 are synthesized by NMRP and used for the subsequent preparation of a series of block copolymers PS-*b*-PPerAc **7**, **8**, **9** with molecular weights of 22.3, 37.9 and 43.1 kg/mol, respectively.<sup>[12]</sup> The perylene bisimide homopolymer **10** has a comparable molecular weight of 30.9 kg/mol. SEC data, composition (from  $^1\text{H-NMR}$ ) and thermal properties are listed in table 1. DSC measurements of the block copolymers yield both glass transition temperatures ( $T_g$ ) around 100 °C due to PS segments

and melting peaks ( $T_m$ ) between 180 and 190 °C due to PPerAcr segments. This, in combination with the fact that these transitions correlate well with the  $T_g$  of the amorphous PS macroinitiator and the  $T_m$  of the crystalline PPerAcr homopolymer (table 1), is indicative for microphase separation. The melting enthalpies  $\Delta H$  of PPerAcr are 6.2, 10.0, and 9.9 J/g for **7**, **8**, and **9**, respectively. The PPerAcr homopolymer **10** exhibits a melting enthalpy of 9.8 J/g. The low melting enthalpy in block copolymer **7** of 6.2 J/g probably is due to the small block length of PPerAcr.

**Table 1.** Molecular weights and polydispersity indices (SEC), composition ( $^1\text{H-NMR}$ ) and thermal properties (DSC) of homopolymers **3**, **4**, **5**, **10** and block copolymers **7**, **8**, **9**. The melting enthalpies  $\Delta H$  of PPerAcr are normalized to their weight fractions.

polymer	$M_w$ [kg/mol]	PDI	wt.-% PerAcr	$T_g$ [°C]	$T_m$ [°C]	$\Delta H$ [J/g]
PS <b>3</b>	13.6	1.12	0	102	--	0
PS <b>4</b>	21.8	1.11	0	104	--	0
PS <b>5</b>	35.1	1.14	0	107	--	0
PS- <i>b</i> -PPerAcr <b>7</b>	22.3	1.38	68	96	179	6.2
PS- <i>b</i> -PPerAcr <b>8</b>	37.9	1.52	70	100	189	10.0
PS- <i>b</i> -PPerAcr <b>9</b>	43.1	1.78	65	105	192	9.9
PPerAcr <b>10</b>	30.9	1.86	100	--	193	9.8

We investigate the morphology of the block copolymers in bulk using transmission electron microscopy (TEM) and small angle X-ray scattering (SAXS), and the surface morphology of thin films using scanning electron microscopy (SEM). To guarantee comparability of the surface morphologies and the bulk structures, the same annealing conditions are applied to both types of samples. Figure 1a-c presents the TEM and figure 1d-f the SEM pictures. Due to preferential staining with ruthenium tetroxide, PPerAcr rich domains appear dark in TEM whereas they are bright in SEM (no staining). The contrast in SEM was determined from PS:PPerAcr blend films with extreme ratios. All block copolymers exhibit nanostructures with domain sizes ranging from 8 to 15 nm. Block copolymer **7** shows a lamellar structure (figure 1a), whereas in block copolymer **8** a cylindrical morphology with dark PPerAcr cylinders, that

are cut both horizontally and vertically, is observed (figure 1b). The cylinders are 15 nm in diameter and exhibit a spacing of 25 nm. The bulk structure of **9** (figure 1c) is more complex, fiber-like PPerAcr domains among lamellar regions of PPerAcr can be seen. The observation of coexisting might be a result of the bimodal character of the SEC curve, possibly due to the formation of PPerAcr homopolymer during the synthesis of the block copolymers. A detailed investigation of the phase behaviour of these semi-crystalline block copolymers hence is a matter of current experiments.

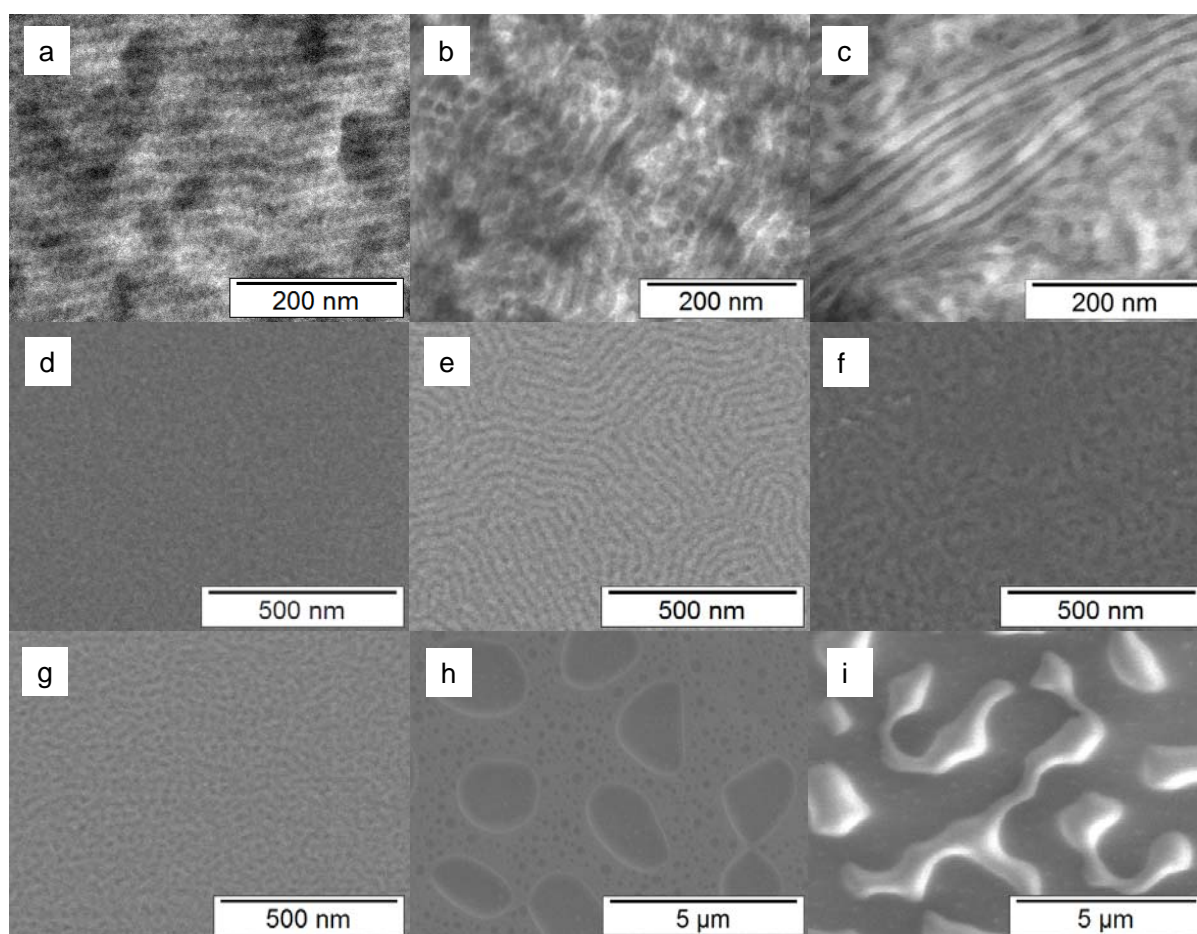


**Figure 1.** Upper row: TEM micrographs of a) block copolymer **7**, b) **8** and c) **9**. The samples are annealed at 210 °C for 1 h, embedded into epoxy resin, cut and stained with RuO<sub>4</sub>. Middle row: Top view SEM micrographs of films of d) block copolymer **7**, e) **8** and f) **9**. The samples are annealed at 210 °C for 1 h. Film thickness is about 150 nm. Lower row: Top view SEM micrographs of films of g) block copolymer **8** as spun h) polymer blend 4:10 as spun i) polymer blend 4:10 after annealing at 210 °C for 1h.

Obviously, all structures of the TEM micrographs are confirmed by SEM measurements. In thin films, the lamellar structures of **7** and the cylinders of **8** lie in plane of the substrate

(figures 1d, 1e). Accordingly, the surface morphology of **9** (figure 1f) exhibits structured and flat regions. Taking into consideration that the PPerAcr domains are oriented parallel to the substrate under these annealing conditions, the structured areas arise from lying PPerAcr worms whereas the flat regions represent lamellar regions. We point out that the TEM bulk structures can be reproduced in thin film under identical annealing conditions. Since microscopic methods only image a small part of the sample we performed additional SAXS experiments to corroborate these results. Figure 2 shows the SAXS curves of block copolymers **7-9**.

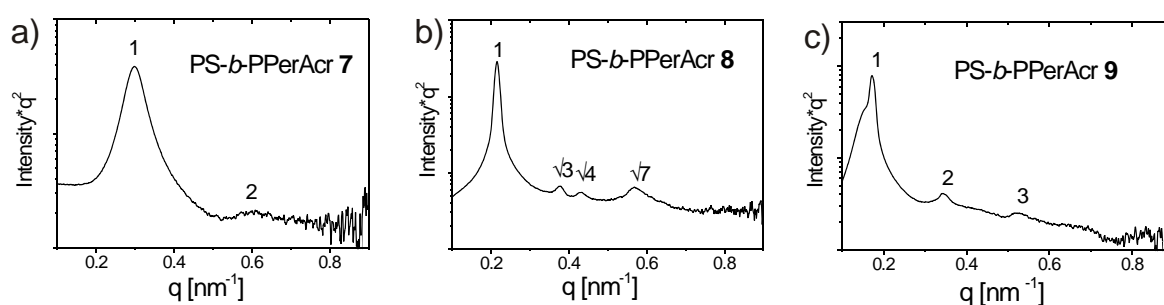


**Figure 2.** Small angle X-ray scattering curves of thermally annealed volume samples PS-*b*-PPerAcr. a) Block copolymer **7**, b) **8**, and c) **9**. Higher order reflections affirm lamellar and cylindrical morphologies from TEM.

In these SAXS curves, the first reflection is observed at  $q=0.298$ ,  $0.215$ ,  $0.172$  for **7**, **8**, and **9**, respectively, corresponding to  $d$  spacings of  $21.1$ ,  $29.2$ , and  $36.6$  nm, respectively. Furthermore, the higher order reflections unambiguously affirm the morphologies observed in TEM. Hereby, reflections of integer multiples are observed for the two lamellar block copolymers **7** and **9** (figure 2a,c), and multiples of  $\sqrt{3}$ ,  $\sqrt{4}$ , and  $\sqrt{7}$  are observed for the cylindrical block copolymer **8**. The first reflection in figure 2c exhibits a shoulder at smaller  $q$  values, which might be caused by the coexistence of additional structural features. This matches perfectly with the results from TEM: The bulk structure of **9** (figure 1c) shows a mixed morphology. Lamellar domains among a fiber-like structures are observed, and furthermore the domain spacing of the fiberlike-structure is larger than the lamellar spacing. Since the fiber-like structure is disordered, higher order reflections do not appear from this morphology, and consequently, the higher order reflections in figure 2c seem to be solely caused by the lamellar domains.

In order to elucidate whether the geometric confinement in block copolymer domains affects the  $\pi$ - $\pi$ -stacking of the perylene bisimide moieties, we investigate the optical properties of thin films of block copolymer **8**. The absorption and emission properties of perylene bisimides depend considerably on their molecular packing, which makes these techniques suitable to study aggregation phenomena.<sup>[13]</sup> Also, for comparison, thin films of homopolymer PPerAcr **10** and of a polymer blend of PS **4** and PPerAcr **10** (scheme 1) containing the same weight fractions as block copolymer **8**, are prepared. In order to understand and correlate the optical properties with morphology, we carry out SEM on these three samples. Figure 1g and 1e show the top view morphologies of block copolymer **8** before and after annealing at 210 °C, respectively. In figure 1h and 1i the blend films before and after thermal annealing are shown. The surface morphologies of homopolymer **10** before and after annealing are completely featureless and therefore omitted here.

In figure 1g, developed microdomains are observed, which, on annealing, transform into well-defined cylindrical domains, lying in the plane of the substrate (figure 1e). The surface of the polymer blend exhibits dark PS droplets dispersed in PPerAcr (figure 1h) before annealing. Thermal treatment of the blend leads to macrophase separated micron-sized PPerAcr rich domains, which can be seen as bright regions in figure 1i.

Figure 3a depicts the absorption spectra of the block copolymer, the homopolymer and the blend in films as spun. In all samples, the amount of perylene bisimide is kept constant. Accordingly, the third and second vibronic transitions at 470 nm and 492 nm are of very similar intensity. But, a slight difference in the peak intensities at 530 nm can be observed. The degree of aggregation of perylene bisimide can be described by comparing the peak heights or valley depths of the different vibronic bands.<sup>[13]</sup> Here, the quotient  $A_{492/530}$  of the peaks at 492 and 530 nm ( $\text{Intensity}_{492\text{nm}}/\text{Intensity}_{530\text{nm}}$ ) is used for a relative estimation of  $\pi$ - $\pi$ -stacking.<sup>[14]</sup> The higher the quotient, the stronger is the aggregation. The block copolymer, the homopolymer and the polymer blend exhibit  $A_{492/530}$  values of 1.49, 1.38 and 1.33, respectively. Apparently, the perylene bisimides moieties in the block copolymer as spun are more aggregated than in the other two samples due to confinement in microdomains. This explanation is also consistent with the morphologies observed via SEM (figure 1g) where the formation of microdomains can be seen. In the blend, on the other hand, the dilution of the

chromophores with polystyrene hinders aggregation and explains the lowest quotient of 1.33.

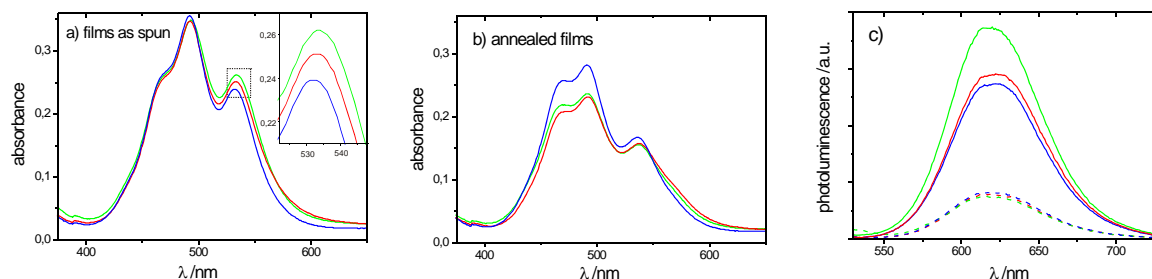


**Figure 3.** a) UV-Vis spectra of the films as spun. The inset shows the enlarged region of the first vibronic transition at 532 nm. b) UV-Vis spectra of the films annealed. c) Photoluminescence spectra of the films as spun (solid lines) and the films annealed (dashed lines). For all: red: homopolymer, green: polymer blend, blue: block copolymer.

Upon thermal annealing, a decrease in optical density of all films is observed (figure 3b). Additionally, a small red-shift of the peak at 532 nm occurs in all annealed films, whereas the wavelength of the second and third vibronic transitions do not change. As expected, the quotient  $A_{492/530}$  also increases in all films, with values of 1.69, 1.49 and 1.46 for the block copolymer, homopolymer and the polymer blend, respectively. Most interestingly, the cylindrical confinement in the block copolymer leads to the highest degree of aggregation of the perylene bisimide moieties among the three films. The blend and the homopolymer exhibit similar quotients, indicating similar degrees of aggregation which can be rationalized by the presence of macrodomains of PPerAcr in the blend.

By monitoring photoluminescence (PL) more insight into  $\pi$ - $\pi$ -stacked systems can be gained. For example, when amorphous films of perylene bis(phenethylimide) were exposed to methylene chloride vapor, the PL intensity initially decreased followed by an increase thereafter with progressive annealing time.<sup>[13]</sup> Würthner et al. reported the PL of tridodecylphenyl-substituted perylene bisimide stacks in solution to increase with increasing concentration.<sup>[15]</sup> However, in the case of PPerAcr, we found that a higher degree of aggregation led to a decrease in PL emission. In the non-annealed block copolymer film we observe the lowest PL intensity, indicating again a higher degree of aggregation (solid lines in figure 3c). This is also in accordance with the observations of UV-Vis spectroscopy. Upon annealing, the PL of all films is quenched drastically (dashed lines in figure 3c) which we

attribute to a higher degree of aggregation after annealing. Due to the weak PL intensities, differences regarding the degree of aggregation after annealing cannot be observed here. Quantitative studies correlating the aggregated state of the perylene bisimide moieties and morphology by methods such as X-ray scattering are currently underway.

The unique situation in which perylene bisimide moieties are closely packed within block copolymer domains can provide additional advantages for electronic transport. Low molecular weight perylene bisimides have been widely investigated in OFETs.<sup>[16]</sup> The confinement of functional units in microdomains can result in electronic transport properties which resemble or even exceed that of the respective homopolymer. In order to examine this, we prepare organic thin film transistors (OFET) with the block copolymers, a polymer blend and the PPerAcr homopolymer, and apply the same annealing procedures as for optical measurements. In table 2 the charge carrier mobilities are summarized.

**Table 2.** OFET mobilities [ $\text{cm}^2 \cdot \text{V}^{-1} \cdot \text{s}^{-1}$ ] of homopolymers, block copolymers, and blends, measured in bottom gate bottom contact device architectures.

	PS- <i>b</i> -PPerAcr <b>7</b>	PS- <i>b</i> -PPerAcr <b>8</b>	PS- <i>b</i> -PPerAcr <b>9</b>	PS:PPerAcr <b>4:10</b>	PPerAcr <b>10</b>
as spun	--	$3.5 \cdot 10^{-6}$	--	$4.3 \cdot 10^{-6}$	$9.6 \cdot 10^{-6}$
annealed	$9.1 \cdot 10^{-5}$	$1.2 \cdot 10^{-3}$	$2.4 \cdot 10^{-4}$	$7.9 \cdot 10^{-4}$	$1.2 \cdot 10^{-3}$

Only block copolymer **8** yields a weak, but measurable performance when processed from chloroform, whereas **7** and **9** did not show n-channel transport. After annealing the devices above the  $T_m$  of PPerAcr, electron mobilities of  $9.1 \cdot 10^{-5}$ ,  $1.2 \cdot 10^{-3}$ , and  $2.4 \cdot 10^{-4}$  were measured for **7**, **8**, and **9**, respectively. We assume that the OFET performance is dependent on the following two factors: the degree of PPerAcr crystallinity and the uniformness of morphology. The morphology of **7** seems to be uniform lamellae, but the melting enthalpy of PPerAcr is low compared to PPerAcr homopolymer **10** (see table 1). Block copolymer **9**, exhibits a melting enthalpy very similar to **10**, but the morphology is not homogeneous. Block copolymer **9** fulfills both these requirements: PPerAcr cylinders are found and the melting enthalpy is same as on PPerAcr **10**.

Furthermore, the device made of **9** is compared to the PS:PPerAcr blend and the PPerAcr homopolymer transistor. In the films as spun, low mobilities of  $3.5 \cdot 10^{-6}$ ,  $4.3 \cdot 10^{-6}$  and  $9.6 \cdot 10^{-6}$   $\text{cm}^2 \cdot \text{V}^{-1} \cdot \text{s}^{-1}$  for the block copolymer, the polymer blend and the homopolymer, respectively, are obtained. The block copolymer and the blend device exhibit slightly lower mobilities than the homopolymer due to dilution effects and lack of pronounced perylene domains. Thermal treatment improves the performance of all devices dramatically. In PPerAcr, the mobility has increased by about two orders of magnitude to  $1.2 \cdot 10^{-3}$   $\text{cm}^2 \cdot \text{V}^{-1} \cdot \text{s}^{-1}$ . A similar improvement is observed in the polymer blend device. In the block copolymer device, however, the best improvement of nearly three orders of magnitude is found, leading to a high mobility of  $1.2 \cdot 10^{-3}$   $\text{cm}^2 \cdot \text{V}^{-1} \cdot \text{s}^{-1}$ . Thus, the same electron transport mobility of PPerAcr homopolymer is achieved in a block copolymer which is diluted with a weight fraction of 30 % polystyrene. The real OFET surface morphologies characterized by SEM show the same features as in figure 1. This is the first report of a electron conducting block copolymer in which the charge transport properties do not suffer from dilution with non-electroactive segments. Detailed analysis of the OFET output and transfer characteristics will be reported elsewhere.<sup>[17]</sup>

To conclude, tailor-made electron conducting block copolymers PS-*b*-PPerAcr with pendant perylene bisimide moieties are synthesized. The variation of molecular weight and composition leads to different electron conducting morphologies such as lamella or cylinder with 8 to 15 nm in size. The comparison of the morphological, optical and electrical properties of the cylindrical block copolymer, the respective polymer blend and the perylene bisimide homopolymer indicates positive consequences of geometric confinement on perylene bisimide  $\pi$ - $\pi$ -interactions. The most remarkable result within this correlation is a higher degree of order in the block copolymer microdomains compared to the homopolymer. This influences the charge carrier mobility considerably. Therefore, in an OFET device, the block copolymer with a cylindrical morphology exhibits the same electron carrier mobility as the corresponding homopolymer, even though in the block copolymer the perylene bisimides are diluted with polystyrene. Thus, dilution with amorphous segments does not affect the charge transport mobility here. This is in contrast with recent studies on poly(3-hexylthiophene) block polymers in which the charge carrier mobility decreases when non-active amorphous segments are attached to the conjugated backbone.<sup>[18]</sup> A next step is the achievement of different equilibrium morphologies and their correlation to charge

transport properties. These findings will have substantial impact on the development of novel semiconducting block copolymers as well as self-assembled organic electronic devices in the future.

## Experimental

*Synthesis.* The preparation of PerAcr and PPerAcr is reported elsewhere [9].

*General procedure for polystyrene macroinitiators 3-5:* 2,89 g (27,78 mmol) styrene, 1,22 mg (0,005 mmol) free nitroxide [11], and 18,06 mg (0,056mmol) alkoxyamine [11] are placed in a 25 ml Schlenktube. After three freeze-thaw cycles, the mixture is stirred at 125 °C for 2-4 h, respectively. Cooling, dilution with THF and precipitation into methanol (2X), filtration, and drying over night yields white powders of PS macroinitiators. Yields: 568, 940, and 1516 mg of **3-5**, respectively.

$^1\text{H-NMR}$  (250 MHz,  $\text{CDCl}_3$ ):  $\delta$  (ppm)= 7.04 (br); 6.57 (br); 6.47 (br); 1.83 (br); 1.42 (br); 0.85 (br); 0.50 (br).

IR (in film);  $\nu$  [ $\text{cm}^{-1}$ ]= 3063 (w); 3017 (w); 2932 (w); 2847 (w); 1943 (m); 1867 (w); 1801 (w); 1742 (w); 1601 (m); 1495 (m); 1456 (m); 1067 (m); 1027 (m); 908 (m); 755 (s); 702 (s); 536 (s).  
SEC (THF, polystyrene standards): **3**:  $M_n$ : 12.1 kg/mol, PDI: 1.12. **4**:  $M_n$ : 19.6 kg/mol, PDI: 1.11. **5**:  $M_n$ : 30.8 kg/mol, PDI: 1.14.

*Synthesis of block copolymer 7:* In a 5 ml schlenktube, 100 mg (0.00822 mmol) PS **3**, 4.28 mg styrene (0.0411 mmol), and 679 mg (0.8223mmol) PerAcr are mixed with 391  $\mu\text{l}$  *o*-dichlorobenzene. After three freeze-thaw cycles, the flask is placed in an oil bath at 125 °C for 12 h. Cooling, dilution with THF, and precipitation into acetone yields a dark-red solid that is further purified by Soxhlet extraction with acetone over night. Yield: 68 mg, wt.-% PPerAcr: 68.4.

$^1\text{H-NMR}$  (250 MHz,  $\text{CDCl}_3$ ):  $\delta$  (ppm)= 8.1 (br); 7.0 (br); 6.6 (br); 6.5 (br); 5.0 (br); 4.0 (br); 2.2 (br); 1.9 (br); 1.8 (br); 1.3 (br); 1.2 (br); 0.8 (br).

IR (im Film);  $\nu$  [ $\text{cm}^{-1}$ ]= 3024 (m); 2919 (w); 2847 (w); 1734 (w); 1653 (m); 1593 (m); 1577 (w); 1492 (m); 1404 (m); 1346 (m); 1067 (m); 851(m); 809 (s); 746 (s); 689 (s); 620 (s); 543 (m).

SEC (THF, polystyrene standards):  $M_n$ : 16.1 kg/mol, PDI: 1.38.

*Synthesis of block copolymer 8:* In a 5 ml schlenktube, 100 mg (0.00492 mmol) PS **4**, 4.28 mg styrene (0.0411 mmol), and 679 mg (0.8223mmol) PerAcr are mixed with 391  $\mu\text{l}$  *o*-dichlorobenzene. After three freeze-thaw cycles, the flask is placed in an oil bath at 125 °C for 12 h. Cooling, dilution with THF, and precipitation into acetone yields a dark-red solid that is further purified by Soxhlet extraction with acetone over night. Yield: 174 mg, wt.-% PPerAcr: 70.1.

$^1\text{H-NMR}$  (250 MHz,  $\text{CDCl}_3$ ):  $\delta$  (ppm)= 8.1 (br); 7.0 (br); 6.6 (br); 6.5 (br); 5.0 (br); 4.0 (br); 2.2 (br); 1.9 (br); 1.8 (br); 1.3 (br); 1.2 (br); 0.8 (br).

IR (im Film);  $\nu$  [ $\text{cm}^{-1}$ ]= 3024 (m); 2919 (w); 2847 (w); 1734 (w); 1653 (m); 1593 (m); 1577 (w); 1492 (m); 1404 (m); 1346 (m); 1067 (m); 851(m); 809 (s); 746 (s); 689 (s); 620 (s); 543 (m).

SEC (THF, polystyrene standards):  $M_n$ : 24.9 kg/mol, PDI: 1.52.

*Synthesis of block copolymer 9:* In a 5 ml schlenktube, 81 mg (0.00246 mmol) PS **5**, 3.47 mg styrene (0.033 mmol), and 550 mg (0.667 mmol) PerAcr are mixed with 391  $\mu\text{l}$  *o*-dichlorobenzene. After three freeze-thaw cycles, the flask is placed in an oil bath at 125 °C for 12 h. Cooling, dilution with THF, and precipitation into acetone yields a dark-red solid that is further purified by Soxhlet extraction with acetone over night. Yield: 87 mg, wt.-% PPerAcr: 65.3.

$^1\text{H-NMR}$  (250 MHz,  $\text{CDCl}_3$ ):  $\delta$  (ppm)= 8.1 (br); 7.0 (br); 6.6 (br); 6.5 (br); 5.0 (br); 4.0 (br); 2.2 (br); 1.9 (br); 1.8 (br); 1.3 (br); 1.2 (br); 0.8 (br).

IR (im Film);  $\nu$  [ $\text{cm}^{-1}$ ]= 3024 (m); 2919 (w); 2847 (w); 1734 (w); 1653 (m); 1593 (m); 1577 (w); 1492 (m); 1404 (m); 1346 (m); 1067 (m); 851(m); 809 (s); 746 (s); 689 (s); 620 (s); 543 (m).

SEC (THF, polystyrene standards):  $M_n$ : 24.2 kg/mol, PDI: 1.78.

*Thin film preparation and annealing.* 1 wt.-% chloroform solutions of the polymer blend and the block copolymer are used. The PPerAcr content is maintained at 0.7 wt.-% to ensure the same amount of chromophores in all films. The solutions are filtered and finally spin-coated at 2000 r/min. For UV-Vis/photoluminescence spectra and scanning electron microscopy, quartz slides and indium tin oxide substrates, respectively, are used. Thermal annealing is done by placing the substrates on a hot plate and heating them at 210 °C for 1 h under nitrogen.

*UV-Vis and photoluminescence spectra.* UV-Vis spectra are recorded on a Hitachi 3000 spectrophotometer. Photoluminescence spectra are recorded on a Shimadzu RF 5301 PC spectrofluorophotometer with the film positioned at an angle of 45° to the incident beam. Excitation wavelength is 490 nm.

*Transmission electron microscopy.* Samples for TEM are annealed for 1 h on a hot plate under nitrogen, embedded into epoxy resin, microtomed and stained with ruthenium tetroxide for 10 min. Micrographs are taken on a Zeiss 902 at 80 kV.

*Scanning electron microscopy.* SE micrographs are recorded using a Zeiss Leo 1530 at an acceleration voltage of 0.75 kV. For detection an Inlens detector is used.

*Small angle X-ray scattering.* Synchrotron SAXS measurements were carried out at the ID2 beamline

at the ESRF, Grenoble. The diameter of the X-ray beam was 100 μm. The photon energy was set to 12.5 keV. SAXS patterns were recorded with a two-dimensional camera located at a distance of 10m from the sample within an evacuated flight tube. Before data analysis, background scattering was subtracted from the data and corrections were made for spatial distortions and for the detector efficiency. The 2-D SAXS patterns were finally integrated and Lorentz-corrected.

*Organic field effect transistor measurements.* Heavily doped n<sup>++</sup> silicon wafers are used as a gate contact with an insulating gate of 200 nm thermally grown silicon oxide. The source

drain electrodes are interdigitating gold contacts providing different transistor dimensions from 1  $\mu\text{m}$  to 20  $\mu\text{m}$  in channel length and 10 mm to 20 mm in channel width. The substrates are exposed to hexamethyldisilazane (HDMS) vapor for 3 h before rinsed with isopropanol. The polymers are spincoated from a 1.5 wt.-% chloroform solution at 2000 r/min in a glovebox like all following device annealing and characterization procedures. A HP 4155A or a HP 4155B semiconductor parameter analyzer is used to record the transfer and output characteristics. The mobility is determined from the transfer characteristics using  $\partial I_{ds}/\partial V_g = \mu C_i W/L$ , where  $C_i$  is the capacitance,  $W$  the channel width and  $L$  the channel length of the transistor.

### Acknowledgements

Financial support of this work by the Deutsche Forschungsgemeinschaft (SFB 481) and the European Science Foundation (EUROCORES SOHYDs) is gratefully acknowledged.

### References

1. P. Peumans, S. Uchida, S. R. Forrest, *Nature* **2003**, *425*, 158.
2. H. Sirringhaus, P. J. Brown, R. H. Friend, M. M. Nielsen, K. Bechgaard, B. M. W. Langeveld-Voss, A. J. H. Spiering, R. A. J. Janssen, E. W. Meijer, P. Herwig, D. M. de Leeuw, *Nature* **1999**, *401*, 685.
3. G. Buxton, N. Clarke, *Phys. Rev. B* **2006**, *74*, 085207.
4. F.S. Bates, G.H. Fredrickson, *Ann. Rev. Phys. Chem.* **1990**, *41*, 525.
5. M. J. Fasolka, A. M. Mayes, *Annu. Rev. Mater. Res.* **2001**, *31*, 323.
6. S. A. Jenekhe, X. L. Chen, *Science* **1998**, *279*, 1903.
7. a) K. Van De Wetering, C. Brochon, C. Ngov, G. Hadziioannou, *Macromolecules* **2006**, *39*, 4289. b) M. C. Iovu, C. R. Craley, M. Jeffries-El, A. B. Krankowski, R. Zhang, T. Kowalewski, R. D. McCullough, *Macromolecules* **2007**, *40*, 4377. c) P. Leclere, M. Surin, P. Jonkheijm, O. Henze, A. P. H. J. Schenning, F. Biscarini, A. C. Grimsdale, W. J.

- Feast, E. W. Meijer, K. Müllen, J. L. Bredas, R. Lazzaroni, *Eur. Poly. J.* **2004**, *40*, 885. d) C. P. Radano, O. A. Scherman, N. Stingelin-Stutzmann, C. Müller, D. W. Breiby, P. Smith, R. A. J. Janssen, E. W. Meijer, *J. Am. Chem. Soc.* **2005**, *127*, 12502. e) C.-A. Dai; W.-C. Yen, Y.-H. Lee, C.-C. Ho, W.-F. Su, *J. Am. Chem. Soc.* **2007**, *129*, 11036.
8. X. L. Chen, S. A. Jenekhe, *Macromolecules* **2000**, *33*, 4610.
  9. a) S. M. Lindner, M. Thelakkat, *Macromolecules* **2004**, *37*, 8832. b) M. Sommer, M. Thelakkat, *Eur. Phys. J. Appl. Phys.*, **2006**, *36*, 245.
  10. S. M. Lindner, S. Hüttner, A. Chiche, M. Thelakkat, G. Krausch, *Angew. Chem. Int. Ed.* **2006**, *45*, 3364.
  11. M. Sommer, S. M. Lindner, M. Thelakkat, *Adv. Funct. Mater.* **2007**, *17*, 1493.
  12. C. Hawker, A. W. Bosman, E. Harth, *Chem. Rev.* **2001**, *101*, 3661.
  13. a) B. A. Gregg, *J. Phys. Chem.* **1996**, *100*, 852. b) F. Würthner, *Chem. Comm.* **2004**, 1564.
  14. a) S. M. Lindner, N. Kaufmann, M. Thelakkat, *Org. Electr.* **2007**, *8*, 69. b) S. M. Lindner, M. Thelakkat, *Macr. Chem. Phys.* **2006**, *207*, 2084.
  15. F. Würthner, Z. Chen, V. Dehm, V. Stepanenko, *Chem. Comm.* **2006**, 1188.
  16. a) S. Tatemichi, M. Ichikawa, T. Koyama, Y. Taniguchi, *Appl. Phys. Lett.* **2006**, *89*, 112108. b) M.-M. Ling, P. Erk, M. Gomez, M. Koenemann, J. Locklin, Z. Bao, *Adv. Mater.* **2007**, *19*, 1123.
  17. S. Hüttner, M. Sommer, M. Thelakkat, *Appl. Phys. Lett.* **2008**, *92*, 093302.
  18. G. Sauve, R. D. McCullough, *Adv. Mater.* **2007**, *19*, 1822.
  19. B. Charleux, J. Nicolas, O. Guerret, *Macromolecules* **2005**, *38*, 5485.



## 8. n-Type Organic Field Effect Transistors from Perylene Bisimide Block Copolymers and Homopolymers

Sven Hüttner,<sup>a,b</sup> Michael Sommer,<sup>a</sup> and Mukundan Thelakkat<sup>a</sup>

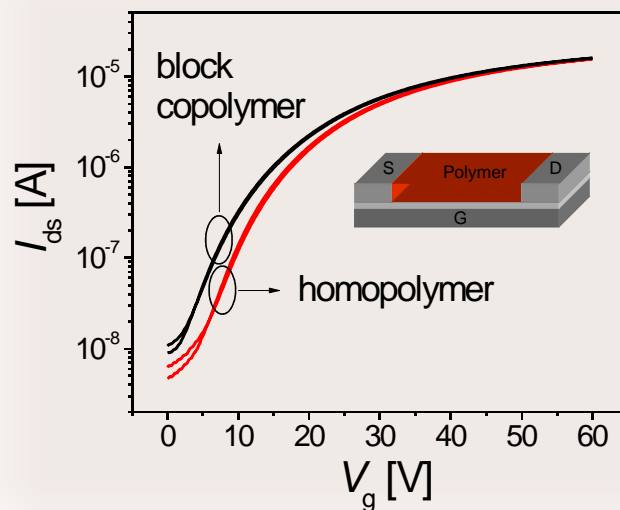
<sup>a</sup>Applied Functional Polymers and Macromolecular Chemistry I

Universität Bayreuth, Universitätsstr. 30, University of Bayreuth, 95444 Bayreuth, Germany

<sup>b</sup>Thin Films and Interfaces Group, Cavendish Laboratory, BSS Physics

11 JJ Thomson Avenue, Cambridge CB3 0HE, United Kingdom

[Sven.Huettner@uni-bayreuth.de](mailto:Sven.Huettner@uni-bayreuth.de), [Mukundan.Thelakkat@uni-bayreuth.de](mailto:Mukundan.Thelakkat@uni-bayreuth.de)



Published in *Applied Physics Letters*, **2008**, 92, 093302.

**Abstract**

We present organic field effect transistors (OFETs) based on solution-processable *n*-type polymers containing perylene bisimide as pendant groups. The OFET characteristics of a diblock copolymer consisting of polystyrene (PS) and poly(peryene bisimide acrylate) (PPerAcr) are compared. Thermal annealing improves the OFET performance by 2-3 orders of magnitude, which can be attributed to the improved order and interface properties in the transport layer, arising from the better alignment of the perylene bisimide moieties. Both polymers show excellent *n*-type performances with electron carrier mobilities of  $1.2 \cdot 10^{-3}$  cm<sup>2</sup>/Vs and low threshold voltages of 4-7 V.

Air-stable n-type materials are one of the critical material requirements in the field of organic electronics. In contrast to hole conducting materials (p-type), very few n-type materials are known which offer good electron transport properties in combination with high work function electrodes such as gold. Additionally, highly soluble, solution-processable materials are prerequisites for plastic electronics.

Low molecular weight perylene bisimide derivatives, also referred to as perylene diimide (PDI) or perylene tetracarboxylic diimide (PTCDI) derivatives are known to be good electron transporting materials<sup>[1,2]</sup> with electron mobilities of up to  $2.1 \text{ cm}^2/\text{Vs}$ .<sup>[3,4]</sup> For polymers containing perylene bisimide moieties values around  $10^{-2} \text{ cm}^2/\text{Vs}$  have been reported<sup>[5]</sup>, together with a good air stability.<sup>[6]</sup> Additionally, they show a high absorbance in the visible light and possess long exciton diffusion lengths.<sup>[7]</sup> The strong  $\pi$ - $\pi$  interactions are a key feature of this material, and depending on the chemical structure, lead to crystallinity or higher hierarchical orders such as the formation of discotic liquid crystals.<sup>[8]</sup> Therefore, they are suitable for n-type organic field effect transistors<sup>[9]</sup> as well as for organic heterojunction solar cells.<sup>[10]</sup> However, the morphology in thin layers plays a key role in device performance. Bulk heterojunction solar cells rely on the distinct structure, where donor and acceptor materials are perpendicular to the electrodes. A large interpenetrating interface between a hole and an electron transporting material is desired, as well as sufficient percolation paths to the electrodes. Organic field effect transistors, on the other hand, use a lateral device geometry, where the charge transport between the source and drain electrode is determined only by a thin layer on top of the gate oxide.<sup>[11]</sup> Here the alignment of molecules to the substrate and the formation of continuous domains or microcrystals between source and drain can have decisive effects on the device characteristics. Therefore OFET devices give direct information on the influence of morphology on transport properties of a material. Diblock copolymers are widely known for their ability to form self-assembled nanostructures. Here, two different polymer chains are covalently linked to each other. The demixing of the two polymer segments on the one hand, and the molecular connectivity on the other, lead to a nanostructured phase separation, the so-called microphase separation of the block copolymers.<sup>[12,13]</sup>

Depending on the respective volume ratio, interaction parameters of the respective blocks and molecular weight, lamellar, gyroidal, cylindrical or spherical morphologies can be found. Furthermore it has been shown that directional alignment of these nanostructures can be achieved for example by external fields<sup>[14]</sup>, shear forces<sup>[15]</sup>, solvent vapor atmospheres<sup>[16]</sup> or specific surface interactions. Thus, a morphology which resembles upstanding cylinders or lamellae of a n-type material in the matrix of a p-type material or vice versa may be the perfect structure for bulk heterojunction solar cells.<sup>[17]</sup> Initial investigations have already been undertaken to use the concept of block copolymer self assembly for organic electronics – both for bulk heterojunction solar cells<sup>[10,18]</sup> and for OFETs.<sup>[19]</sup>

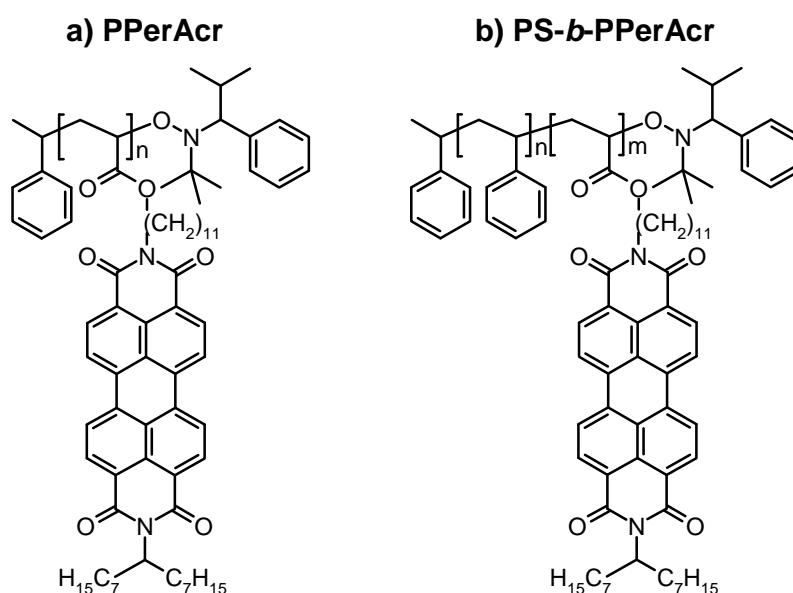


**Figure 1.** Chemical structures of the polymers: a) Homopolymer poly (perylene bisimide acrylate) (PPerAcr) and b) diblock copolymer polystyrene-*b*-poly(perylene bisimide acrylate).

Moving away from typical amorphous block copolymer systems with no electronic functions - on which it has been extensively reported over the last decades - to block copolymers which carry electronic functionalities, certain obstacles had to be overcome in their synthesis to avoid high polydispersity and to achieve good control over the molecular weight. Furthermore additional effects such as the formation of  $\pi$ - $\pi$  stacks and crystallites, as well as a difference in behavior due to the functionalized side groups are only beginning to be investigated.

In this paper we investigate the transport characteristics of a novel side chain perylene bisimide homopolymer poly(peryene bisimide acrylate) (PPerAc) and a novel perylene bisimide block copolymer, polystyrene-*b*-poly(peryene bisimide acrylate) PS-*b*-PPerAc in OFET devices. Figure 1a shows the molecular structure of PPerAc. The synthesis is described elsewhere<sup>[20]</sup> and the LUMO level of PPerAc is reported as 3.6 eV.<sup>[10]</sup> The perylene bisimide groups are linked to a polyacrylate backbone via a C11 spacer. The other end of the perylene bisimide core carries a branched C15 substituent. PPerAc has a melting point at around 190 °C. The crystallinity is caused by the strong  $\pi$ - $\pi$  interactions, also referred to as  $\pi$ - $\pi$  stacking, of the perylene bisimide groups, leading to a crystallinity of the sidechains.<sup>[21]</sup> The weight-average molecular weight of PPerAc is 30.9 kg/mol with a polydispersity of 1.86. The block copolymer PS-*b*-PPerAc (Fig. 1b) consists of PPerAc (70 wt %) and of polystyrene (30 wt %) blocks. Its overall molecular weight is 37.9 kg/mol with a polydispersity of 1.52. The block copolymer exhibits features from both components – the glass transition of PS which is around 100 °C and the melting point of PPerAc at 189 °C indicating the presence of phase separated domains in bulk.<sup>[22]</sup>

For the transistor substrates we used heavily n-doped silicon wafers with a common gate contact carrying a 200 nm thermally grown gate oxide layer. The source and drain contacts were lithographically patterned Au interdigitating electrodes. The substrates were cleaned and then exposed to hexamethyldisilazane (HMDS) vapour for approximately 3 h in order to silanize the substrates, rendering the dielectric surface hydrophobic. After the HMDS exposure the substrates were rinsed again with isopropanol. The polymers were spin-cast from a 1.5 wt% chloroform solution. This procedure and all subsequent device annealing and device characterization steps were carried out in a glove box in inert gas. The transistors were characterized using a HP4155A semiconductor parameter analyser. Table I summarizes the respective mobilities, threshold voltages and on/off ratios. All processed devices show only a very weak performance with threshold voltages around 20 V directly after spin casting. Figures 2b and 2d show the output and transfer characteristics of an as spun PPerAc thin film transistor. That changes dramatically after annealing the samples at 210 °C for 60 min, which is above the melting temperature of PPerAc (190 °C). Figures 2c and 2d show the corresponding output and transfer plots. The threshold voltage drops significantly to 6.8 V, while the current and charge carrier mobility both increase by two orders of

magnitude. Thus electron transport mobilities of up to  $1.2 \cdot 10^{-3} \text{ cm}^2/\text{Vs}$  were achieved for a device made of PPerAcr with a channel length of  $10 \mu\text{m}$  and a width of  $10 \text{ mm}$ .

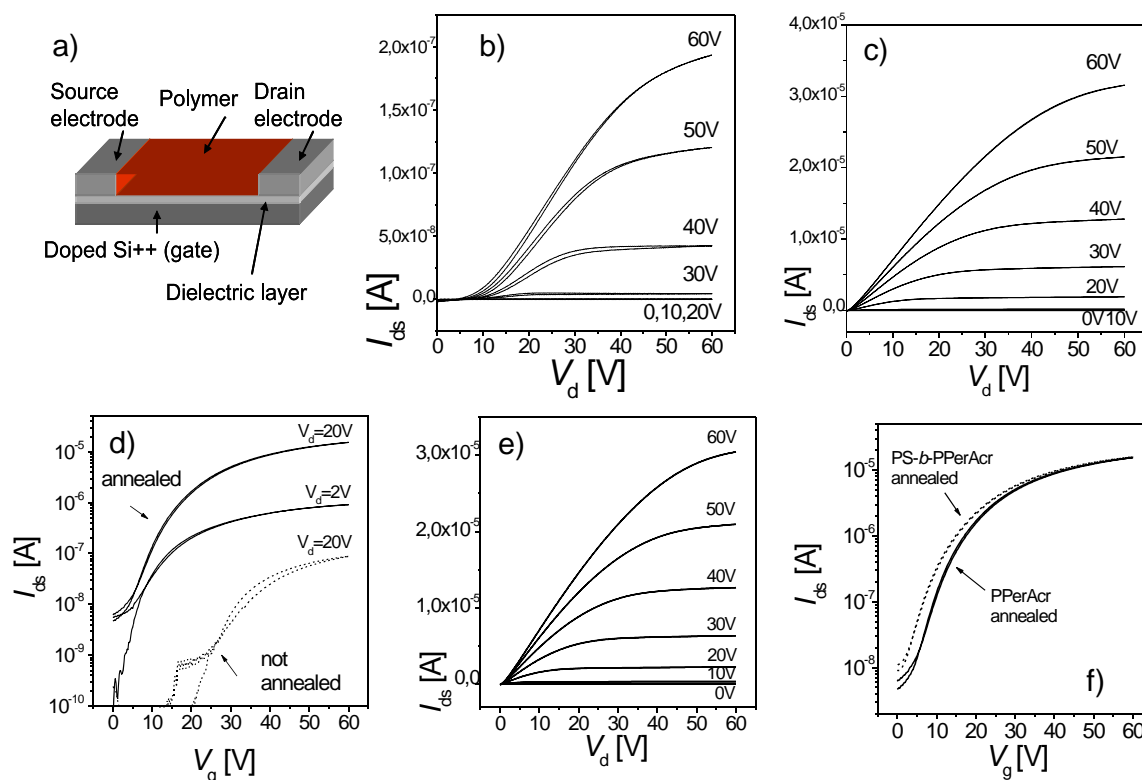


**Figure 2.** a) Schematic of a bottom gate OFET, b) output characteristics measured forwards and backwards of the homopolymer PPerAcr as spun, c) output characteristics of the annealed homopolymer PPerAcr showing no hysteresis, d) comparison of the transfer characteristics between unannealed (dashed line) and annealed homopolymer PPerAcr, e) output characteristics of the annealed block copolymer PS-*b*-PPerAcr, f) transfer characteristics of the block copolymer (dashed line) and the homopolymer (solid line) showing almost identical results.

**Table 1.** OFET characteristics of homopolymer and block copolymer devices.

Polymer	$\mu$ [ $\text{cm}^2/\text{Vs}$ ] <sup>a</sup>	$V_{th}$ <sup>b</sup>	On/Off	<sup>a</sup> The mobility $\mu$ has been calculated using the gradual channel approximation $\partial I_d/\partial V_g = \mu C_i W/L$ , where $C_i$ is the capacitance, $W$ the gate width and $L$ the gate length of the transistor.
PPerAcr (as spun)	$9.6 \cdot 10^{-6}$	21.8 V	$3.7 \cdot 10^2$	
PPerAcr (annealed)	$1.2 \cdot 10^{-3}$	6.8 V	$3.3 \cdot 10^4$	
PS- <i>b</i> -PPerAcr (as spun)	$3.5 \cdot 10^{-6}$	24.9 V	$1.0 \cdot 10^2$	<sup>b</sup> The threshold voltage $V_{th}$ has been determined through the intercept of a line fit through the linear part in the $I_{ds}^{1/2}$ vs. $V_g$ plot with the $V_g$ axis.
PS- <i>b</i> -PPerAcr (annealed)	$1.2 \cdot 10^{-3}$	4.1 V	$1.8 \cdot 10^3$	

In the same way we characterized the devices based on the block copolymer PS-*b*-PPerAcr containing 30 wt % PS. Surprisingly both materials, the pristine homopolymer and the block copolymer, show almost identical performances. The diblock copolymer also shows the same weak performance just after spin casting (not shown here), but after thermal annealing the output (Fig. 2e) and transfer characteristics (Fig. 2f) are almost identical to those of the homopolymer PPerAcr. The block copolymer shows an even lower threshold voltage of 4.1 V. After the annealing step both polymers show a fast onset of the linear regime in their output characteristics with increasing source drain voltage indicating a low contact resistance to the gold electrodes. The annealing step also increases the on/off-ratio by almost two orders of magnitude and the initial hysteresis, which was seen with respect to the forward and backward scans, has vanished.

These results suggest that the perylene bisimides moieties possess a favourable interaction with the substrate after annealing, since the charge transport in OFETs takes place only in a thin layer channel of some nanometers above the gate oxide. In the case of the block copolymer this means that the microdomains of the perylene bisimide containing block go down to the substrate during the annealing process. This phenomenon is widely known and originates from the strong surface interaction with one of the blocks.<sup>[23]</sup> The morphology in the OFET films of the block copolymer was studied using scanning electron microscopy (SEM). The top view SEM image clearly shows lying cylinders with diameters of around 15 nm and domain spacings of 20-25 nm. The film thickness is around 150 nm, which means that the visualized morphology appears at the polymer-air interface, a couple of domain spacings above the substrate interface. The preferred interaction of PPerAcr with the substrate is not visible from the top, however all electrical characterizations are indicative of this behavior. Furthermore the annealing process seems to lead to an optimized alignment of the perylene bisimides units within the microdomain itself resulting in a high electron transport mobility. This finding is even more impressive considering that PS (30 wt % in block copolymer) does not contribute to the charge transport at all. Generally in blends, copolymers and block copolymers, the charge carrier mobility decreases with dilution of the active components by an amorphous component.<sup>[19,24]</sup>

Only in semicrystalline multicomponent systems a device performance improvement has been reported in diluted systems.<sup>[25]</sup> In the case of PS-*b*-PerAcr, the electron carrier mobility remains the same as that in the homopolymer, due to possible morphological advantages resulting from the stacking of the bisimide units in a confined geometry. Annealing causes significant changes both in the electrical properties as well as in the morphology of these thin films, as demonstrated in SEM images of the block copolymer before and after annealing steps. Only after thermal treatment does the block copolymer show a distinct phase separation. The reason for this is that during film preparation from chloroform, which is a fast evaporating low boiling point solvent, the polymer chains are not given sufficient time to rearrange and therefore high order in the film is not achieved. This affects both, the phase separation itself, and the intermolecular interaction of the perylene bisimide moieties leading to high order.

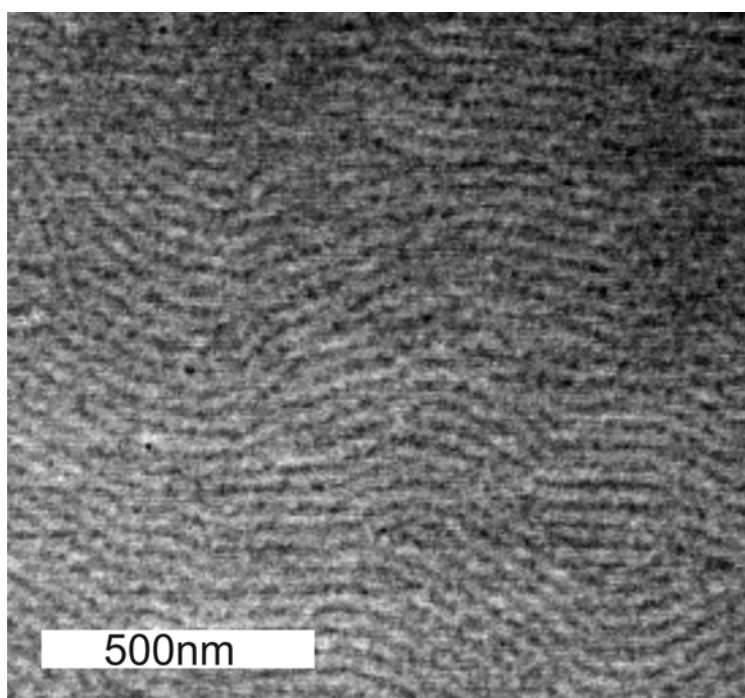


**Figure 3.** SEM top view image of an annealed PS-*b*-PPerAcr transistor. The block copolymer forms lying cylinders of PPerAcr (bright) in a matrix of polystyrene (dark) on the surface.

We conclude that new side chain perylene bisimide polymers - a homopolymer and a diblock copolymer- show an outstanding n-type performance with high electron transport mobilities, low threshold voltages and good electron injection from gold electrodes. A

thermal annealing step improves drastically the device performance. The charge transport properties are maintained in a block copolymer exhibiting cylindrical microdomains, where one block consists of insulating polystyrene with a content of 30 wt.-%. These results are promising not only for the further application of polymerized perylene bisimides as an electron transport material, but also to develop novel multifunctional materials, the charge transport properties of which can be well optimized in the respective microdomains of an ordered block copolymer. Thus the capability of block copolymers with distinct control of the morphology on a nanometer scale and extended charge transport pathways throughout the bulk, which lead to excitonic solar cells with a nanostructured bulk heterojunction<sup>[10,26]</sup> can also open the door to ambipolar transistors<sup>[27]</sup>, which is the current scope of our research.

## Acknowledgements

We acknowledge the financial support from projects SFB 481 (DFG) and EUROCORES ORGANISOLAR (ESF). SH thanks Universität Bayern e.V. for the financial support in the form of a scholarship of the Bayerische Graduiertenförderung.

## References

1. B. A. Jones, A. Facchetti, M. R. Wasielewski, T. J. Marks, *J. Am. Chem. Soc.* **2007**, *129*, 15259.
2. J. H. Oh, S. Liu, Z. Bao, R. Schmidt, F. Würthner, *Appl. Phys. Lett.* **2007**, *91*, 212107.
3. R. J. Chesterfield, J. C. McKeen, C. R. Newman, P. C. Ewbank, D. A. da Silva Filho, J.-L. Brédas, L. L. Miller, K. R. Mann, C. D. Frisbie, *J. Phys. Chem. B* **2004**, *108*, 19281.
4. S. Tatemichi, M. Ichikawa, T. Koyama, Y. Taniguchi, *Appl. Phys. Lett.* **2006**, *89*, 112108.
5. X. Zhan, Z. Tan, B. Domercq, Z. An, X. Zhang, S. Barlow, Y. Li, D. Zhu, B. Kippelen, S. R. Marder, *J. Am. Chem. Soc.* **2007**, *129*, 7246.
6. M.-M. Ling, P. Erk, M. Gomez, M. Koenemann, J. Locklin, Z. Bao, *Adv. Mater.* **2007**, *19*, 1123.
7. B. Gregg, *J. Phys. Chem. B* **2003**, *107*, 4688.
8. C. W. Struijk, A. B. Sieval, J. E. J. Dakhorst, M. van Dijk, P. Kimkes, R. B. M. Koehorst, H. Donker, T. J. Schaafsma, S. J. Picken, A. M. van de Craats, J. M. Warman, H. Zuilhof, E. J. R. Sudhölter, *J. Am. Chem. Soc.* **2000**, *122*, 11057.
9. P. R. L. Malenfant, C. D. Dimitrakopoulos, J. D. Gelorme, L. L. Kosbar, T. O. Graham, *Appl. Phys. Lett.* **2002**, *80*, 2517.
10. S. M. Lindner, S. Hüttner, A. Chiche, M. Thelakkat, G. Krausch, *Angew. Chem. Int. Ed.* **2006**, *45*, 3364.
11. H. Sirringhaus, *Adv. Mater.* **2005**, *17*, 2411.
12. F. S. Bates, *Annu. Rev. Mater. Sci.* **1990**, *26*, 501.
13. C. Park, J. Yoon, E. Thomas, *Polymer* **2003**, *44*, 6725.
14. T. Thurn-Albrecht, R. Steiner, J. DeRouchey, C. Stafford, E. Huang, M. Bal, M. Tuominen, C. Hawker, T. P. Russell, *Adv. Mater.* **2000**, *12*, 787.
15. D. E. Angelescu, J. H. Waller, R. A. Register, P. M. Chaikin, *Adv. Mater.* **2005**, *17*, 1878.

16. K. Fukunaga, T. Hashimoto, H. Elbs, G. Krausch, *Macromolecules* **2002**, *35*, 4406.
17. G. Buxton, N. Clarke, *Phys. Rev. B* **2006**, *74*, 085207.
18. G. Hadziannou, *MRS Bulletin* **2002**, *27*, 456.
19. G. Sauve, R. D. McCullough, *Adv. Mater.* **2007**, *19*, 1822.
20. S. M. Lindner, M. Thelakkat, *Macromolecules* **2004**, *37*, 8832.
21. S. M. Lindner, N. Kaufmann, M. Thelakkat, *Org. Electr.* **2007**, *8*, 69.
22. M. Sommer, S. Hüttner, S. Wunder, M. Thelakkat, *Adv. Mater.* **2008**, *20*, 2523.
23. C. Harrison, P. M. Chaikin, D. A. Huse, R. A. Register, D. H. Adamson, A. Daniel, E. Huang, P. Mansky, T. P. Russel, , C. J. Hawker, D. A. Egolf, I. V. Melinkov, E. Bodenschatz, *Macromolecules* **2000**, *33*, 857.
24. A. Babel, A. Jenekhe, *Macromolecules* **2004**, *37*, 9835.
25. S. Goffri, C. Müller, N. Stingelin-Stutzmann, D. W. Breiby, C. P. Radano, J. W. Andreasen, R. Thompson, R. A. J. Janssen, M. M. Nielsen, P. Smith, H. Sirringhaus, *Nature Mater.* **2006**, *5*, 950.
26. M. Sommer, S. M. Lindner, M. Thelakkat, *Adv. Funct. Mater.* **2007**, *17*, 1493.
27. C. Rost, D. J. Gundlach, S. Karg, W. Rieß, *J. Appl. Phys.* **2004**, *95*, 5782.



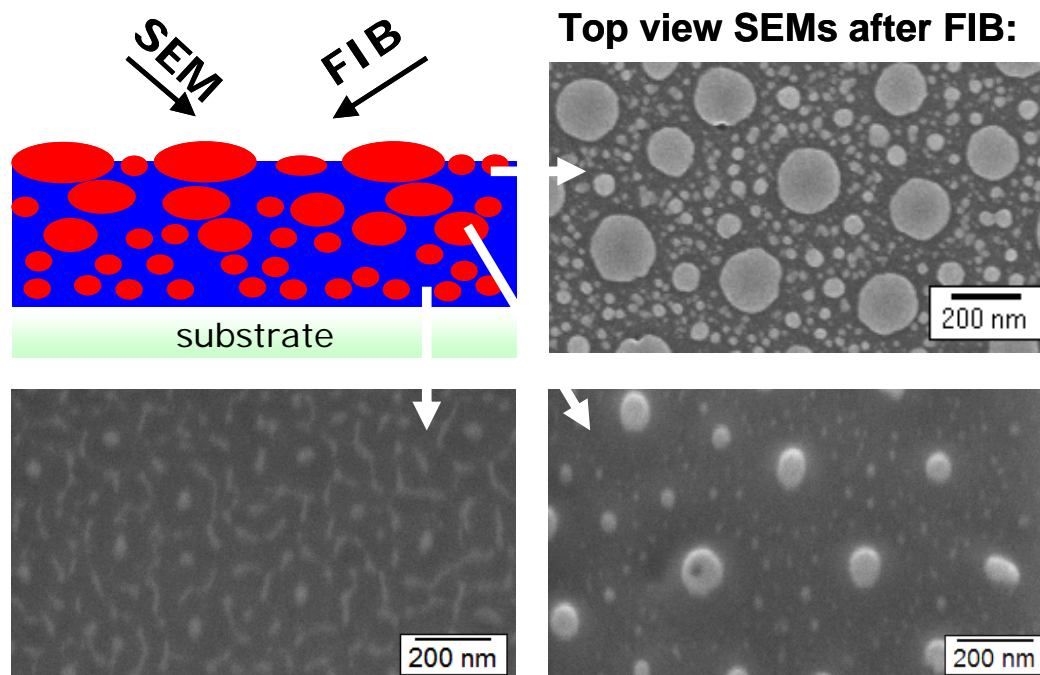
## 9. In Situ Imaging of Evolution of Morphology of Semiconductor Polymer Blends and Block Copolymers Using Focused Ion Beam and Scanning Electron Microscopy: Scope and Limitations

Michael Sommer and Mukundan Thelakkat

Applied Functional Polymers and Macromolecular Chemistry I

Universität Bayreuth, Universitätsstr. 30, University of Bayreuth, 95444 Bayreuth, Germany

[Michael.Sommer@uni-bayreuth.de](mailto:Michael.Sommer@uni-bayreuth.de), [Mukundan.Thelakkat@uni-bayreuth.de](mailto:Mukundan.Thelakkat@uni-bayreuth.de)



Provisionally accepted in *Applied Materials and Interfaces*

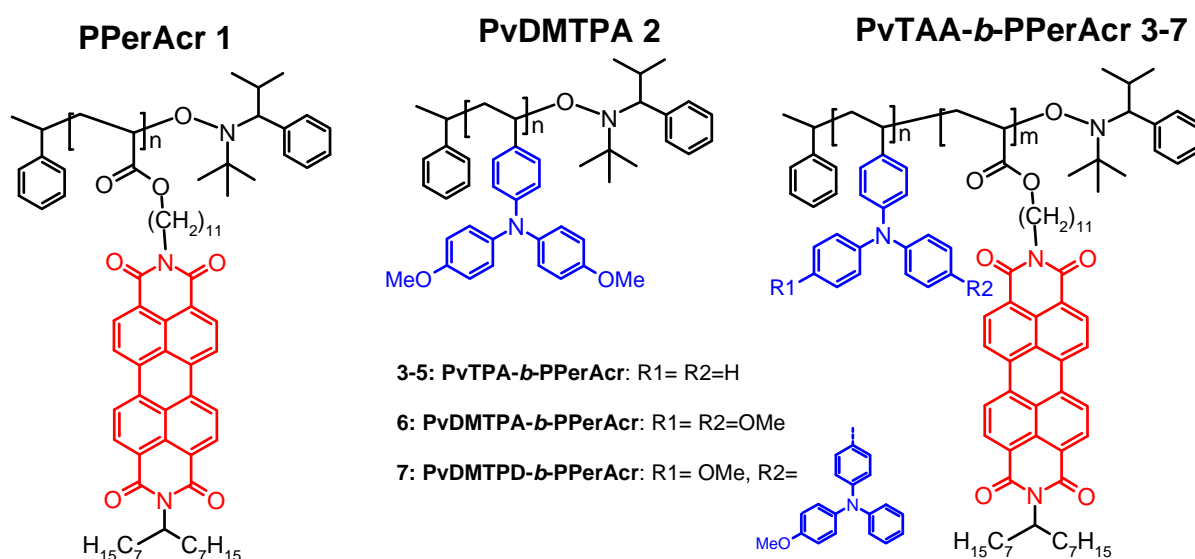
**Abstract**

The morphologies of amorphous-crystalline donor-acceptor polymer blend and block copolymer samples are monitored by the in-situ combination of focused ion beam (FIB) and scanning electron microscopy (SEM). We distinguish several different cases in order to elucidate the scope as well as the limitations of this combination of techniques: FIB etching of a block copolymer bulk sample uncovers a morphology that is equal to its TEM morphology, when the side walls of the etched hole are imaged via SEM (imaged area parallel to the incident FIB beam). In principle, this technique allows for in-situ thin film cross sectioning, however the evaporation of a protective metal cap and extensive optimization of the experimental parameters are required. When block copolymer films are etched down from the top followed by imaging the bottom of the exposed area, major artefacts are observed with progressive etching depth as a result of melting and dewetting of the film (imaged area is perpendicular to the incident FIB beam).

Increased attention has been drawn to the phase separation of semiconductor blends as they are widely used in organic photovoltaics (OPVs)<sup>[1-3]</sup> and in organic thin film transistors (OFETs)<sup>[4-6]</sup>, in which the morphology of the film plays a fundamental role. In OPVs, several studies demonstrate that a lateral phase separation with domain sizes in the range of some tens of nanometers is needed for increasing the external quantum efficiency whereas a vertical phase separation leading to wetting layers of the two components at both interfaces is sought to be obtained in order to optimize the open circuit voltage of the device.<sup>[7-11]</sup> The latter implies a composition gradient vertical to the film plane, and that surface and bulk morphologies of the film might be substantially different. These issues make techniques capable of imaging the surface as well as the bulk morphology of a thin film at the same time highly desirable. Microscopic methods mostly used for correlating microstructure with device performance are scanning force microscopy (SFM) or scanning electron microscopy (SEM). These techniques are useful for the investigation of the morphology at the surface, however, in case of a vertical phase separation, a complete picture of the whole film cannot be provided. To address this issue, microscopic methods were combined with ex-situ etching treatments, by which the three dimensional film morphology can be reconstructed. In this respect, conventional block copolymers were studied using SFM and oxygen plasma etching<sup>[12]</sup> and polymer blends using SFM and selective solvents.<sup>[13]</sup> In the case of semiconductor blends, dynamic secondary ion mass spectrometry (SIMS)<sup>[14]</sup> and the combination of fluorescence microscopy with oxygen plasma etching was employed.<sup>[15]</sup> Alternatively, transmission electron microscopy (TEM) of microtomed thin films can be used but sample preparation is time-consuming and not always successful.<sup>[16]</sup> On the other hand, the ex-situ preparation of TEM thin film cross sections using focused ion beam (FIB) is feasible here and has been successfully demonstrated for conventional block copolymers<sup>[17]</sup> as well as for active layers of photovoltaic cells.<sup>[18]</sup> This FIB "lift-out" technique<sup>[19]</sup> has further been used to study cross sections of OPV cells via SFM.<sup>[20]</sup> However, for a fast and convenient morphological investigation of binary polymer thin films exhibiting a vertical phase separation to be accomplished, the combination of in-situ etching procedures with microscopic methods is desirable.<sup>[21]</sup>

Here, we investigate the scope and the limitations of the in-situ combination of FIB and SEM for the detection of structural changes in semiconducting polymer films with progressive etching depth. By using photovoltaic active polymer blend and block copolymer samples, we show that in-situ etching and subsequent imaging of the exposed area can uncover a morphology widely free of artefacts under some circumstances. On the contrary, extensive FIB etching can also result in local heating and dewetting of thin films. The in-situ combination of FIB/SEM then produces major artefacts making this technique unelgible for morphological investigations.

The block copolymer and blend systems used here phase separate on different length scales, and are used as model systems to probe the combination of FIB and SEM. The polymers used are poly(perylene bisimide acrylate) (PPerAc) **1**, poly[bis(4-methoxyphenyl)-4'-vinylphenylamine] (PvDMTPA) **2**, and several block copolymers poly(triarylamine)-block-poly(perylene bisimide acrylate), including poly(vinyltriphenylamine)-*b*-poly(perylene bisimide acrylate) (PvTPA-*b*-PPerAc) **3-5**, poly[bis(4-methoxyphenyl)-4'-vinylphenylamine]-*b*-poly(perylene bisimide acrylate) (PvDMTPA-*b*-PPerAc) **6**, and poly[N,N'-bis(4-methoxyphenyl)-N-phenyl-N'-4-vinylphenyl-(1,1'-biphenyl)-4,4'-diamine]-*b*-poly(perylene bisimide acrylate) (PvDMTPD-*b*-PPerAc) **7**. The chemical structures are given in scheme 1a.



**Scheme 1.** a) Chemical structures of the homopolymers PvDMTPA **1**, PPerAc **2** and block copolymers PvTAA-*b*-PPerAc **3-7**.

The synthesis is reported elsewhere<sup>[22,23]</sup> and the application in solar cells has been demonstrated.<sup>[16,23,24,25]</sup> The molecular weights, polydispersity indices, compositions and static water contact angles of some films are collected in table 1. In the block copolymers, the first donor segment is amorphous, while the second acceptor block exhibits a side-chain crystallinity. This crystallinity is caused by the strong  $\pi$ - $\pi$  interactions of the perylene bisimides and results in melting temperatures between 170 and 200 °C.<sup>[26,27]</sup> For a measure of the surface energies, static water contact angles were determined on homopolymer films, and the values are given in table 1.

**Table 1.** Molecular weights, polydispersities, compositions, and static water contact angles of homopolymers and block copolymers. n.m.: not measured

Polymer	$M_n$ [kg/mol]	PDI	wt.-PPerAcr [%]	contact angle [°]
PPerAcr <b>1</b>	23.0	1.71	100	93.1 ± 0.6
PvDMTPA <b>2</b>	22.1	1.12	0	75.8 ± 0.8
PvTPA- <i>b</i> -PPerAcr <b>3</b>	27.9	1.47	64	n.m.
PvTPA- <i>b</i> -PPerAcr <b>4</b>	37.7	1.97	79	91.9 ± 0.9
PvTPA- <i>b</i> -PPerAcr <b>5</b>	9.2	1.43	73	n.m.
PvDMTPA- <i>b</i> -PPerAcr <b>6</b>	88.1	1.68	86	n.m.
PvDMTPD- <i>b</i> -PPerAcr <b>7</b>	17.2	1.62	80	n.m.

We first determine the contrast of SEM images between donor-rich and acceptor-rich domains. For this purpose, blend films comprising PPerAcr **1** and PvDMTPA **2** were spin cast from 1% chloroform solutions onto indium tin oxide substrates (150 nm film thickness), and stained using RuO<sub>4</sub> vapor. Extreme compositions (90:10, 10:90, wt:wt) were used (figure 1a,b). In the blend film with 90 wt.- of PPerAcr the surface is covered with bright droplets of various sizes, with the biggest ones between 150 and 200 nm, in a dark matrix, and the film containing 10 wt.- PPerAcr reveals some few bright droplets in a darker matrix (figure 1b). However, these few droplets are not homogeneously in contrast, but exhibit some bright spots inside (figure 1c). Furthermore, the area surrounding these bright spots is even darker

than the majority phase. The observation of some bright regions in the blend film for low contents of PPerAcr and coverage of the whole surface with bright droplets for high PPerAcr contents indicates that bright regions are PPerAcr-rich, and that darker ones are PvDMTPA-rich. The inhomogeneity of the droplets in figure 1b,c is further ascribed to the staining of the perylene bisimide core alone, whereby the alkyl substituents (~53 wt.-% in PPerAcr **1**) are considered to remain unstained thus appearing dark. Staining is not compulsory for SEM imaging but enhances the contrast. Note that the SEM contrast for various PPerAcr-based block copolymers carrying either amorphous donor blocks, polystyrene or poly(3-hexylthiophene) is qualitatively the same in all cases.<sup>[27-29]</sup> This SEM contrast of PPerAcr and PvDMTPA is inverted compared to transmission electron microscopy, where PPerAcr domains appear dark after RuO<sub>4</sub> vapor staining.<sup>[22-26]</sup>

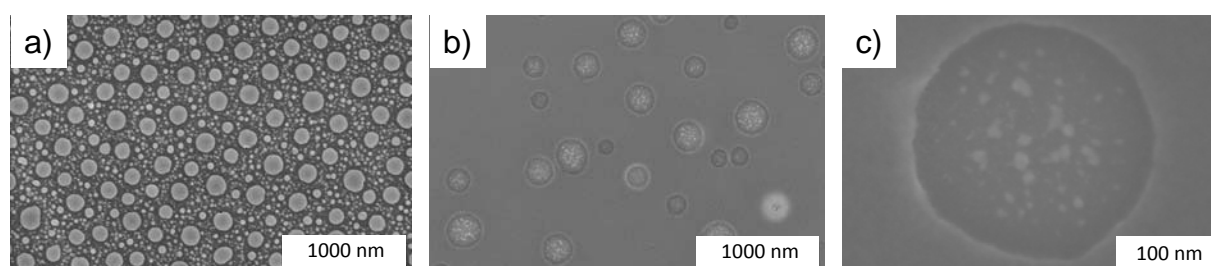


**Figure 1.** Determination of contrast (SEM) of stained blend films (~150 nm) comprised of PvDMTPA and PPerAcr. a) PvDMTPA:PPerAcr blend (10:90) after spin coating from chloroform and staining with RuO<sub>4</sub> for 10 min. b) PvDMTPA:PPerAcr blend (90:10) after spin coating from chloroform and staining with RuO<sub>4</sub> for 10 min. c) Enlarged PPerAcr droplet of figure 1b.

After having determined the contrast between PvDMTPA and PPerAcr in SEM, we now compare the morphologies of a PvDMTPA-*b*-PPerAcr bulk sample imaged via TEM and via FIB/SEM (figure 2). In PvDMTPA-*b*-PPerAcr **6** the same building blocks as present as in the blend samples. The TEM sample was prepared by microtoming a thermally annealed bulk sample (embedded in to epoxy resin), and the FIB/SEM sample by annealing a powder on indium tin oxide substrates. The annealing and staining procedures were kept equal for both samples. The two pictures are shown in figure 2. The TEM bulk cross section shows dark, worm-like structures that are 15 nm in diameter (figure 2a), whereas in the corresponding scanning electron micrograph the same morphology with inverted contrast is observed (figure 2b). Thus, the morphology observed by the standard method TEM can be successfully

reproduced with FIB/SEM, and the results are in accordance with the previously determined contrast. Note that in this case the imaged area is parallel to the incident FIB beam, and that a small milling current of 10 pA was used to polish the side walls of the etched hole (figure 2c). We can therefore exclude major damages during FIB etching here. We also note that image 2b was taken at a bulk sample depth of several micrometers (see figure 2c), showing that good phase contrast is observed even in larger depths. This indicates that staining for short times (10 min) is enough to stain the whole bulk sample.

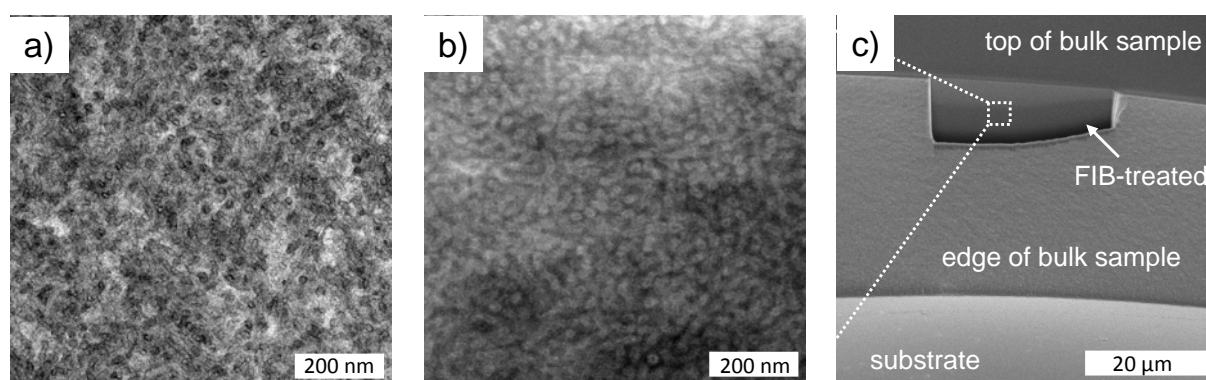


**Figure 2.** Bulk morphology of PvDMTPA-*b*-PPerAc **6** after staining with RuO<sub>4</sub>. a) TEM image, scale bar is 200 nm. b) SEM image, taken from a FIB etched area, scale bar is 200 nm. c) Overview of the bulk sample with FIB-etched area, scale bar is 20 μm.

Furthermore, the good resolution of the micrograph in figure 2b can partially be attributed to the flat and smooth surface of the etched area, which only appeared after polishing the side walls at very low milling currents (10 pA). Although the resolution of the SEM picture is lower compared to the TEM image, phase boundary staining (see hollow structures in figure 2b) can be observed, as is in figure 2a. This phenomenon has been ascribed to enhanced diffusivity of RuO<sub>4</sub> in the amorphous regions and preferential reaction with PPerAc.<sup>[24]</sup> Similar effects have been reported for crystalline block copolymers without electronic functions.<sup>[30,31]</sup>

Next, this procedure is applied by cross-sectioning a photovoltaic device made of PvTPA-*b*-PPerAc **3**. Preparation was done according to standard procedures.<sup>[24]</sup> The thin film (thickness ~70 nm) is etched at 100 pA from the top until the depth of the hole is larger than the active layer thickness (figure 3a). In order to prepare a fresh cross section with the smallest extend of artefacts possible, the milling current is then reduced to 10 pA and the

FIB beam is slowly moved to the borders in small increments (approx. 1 nm/ 1 sec). The resulting cross section (figure 3d) clearly shows the bright indium tin oxide substrate, the unstructured PEDOT:PSS polymer anode, and the nanostructured active layer. Again, bright regions are due to PPerAcr while the dark matrix is comprised of amorphous PvTPA. For comparison, the TEM bulk cross section of the same material is shown in figure 3c, showing dark PPerAcr lamellae in a bright PvTPA matrix. However, the film-air interface does not exhibit a sharp and defined edge rather than a radius, since the surface of the film was not protected during the etching procedure. Therefore, in the upper part of figure 3d the cross section merges into the film surface as can be rationalized from the film thickness of  $\sim 70$ nm. Thus, the in-situ preparation of a precise cross section with defined interfaces is hard to achieve.

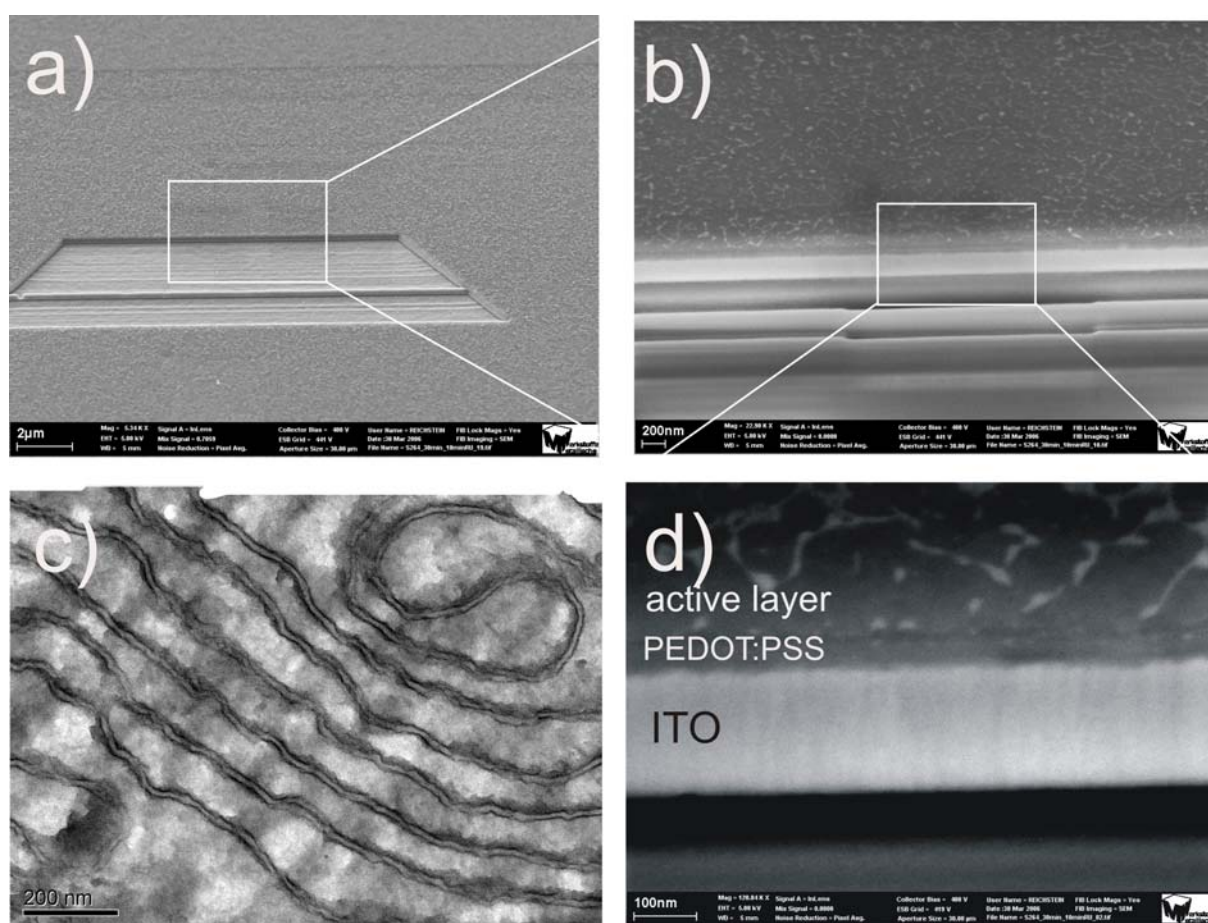


**Figure 3.** In situ thin film cross sectioning of a photovoltaic device made of PvTPA-*b*-PPerAcr **3** without metal cap (a,b,d). PPerAcr is bright in a,b,d, and dark in c). a) Overview of etched film, b) magnification of a), d) magnification of b). c) TEM cross section of a thermally annealed bulk sample showing lamellar PPerAcr domains in an amorphous PvTPA matrix.

We therefore test the use of a protective metal cap evaporated on top of the photovoltaic active layer. In the case of common photovoltaic devices, the aluminium top electrode can readily be used. For this purpose, a solar cell made from PvDMTPD-*b*-PPerAcr **7** is used. Preparation of the solar cell as well as the cross section was done according to the procedure above, and the film thickness was 70 nm. Figure 4 shows the resulting cross sections together with the TEM morphology for comparison.

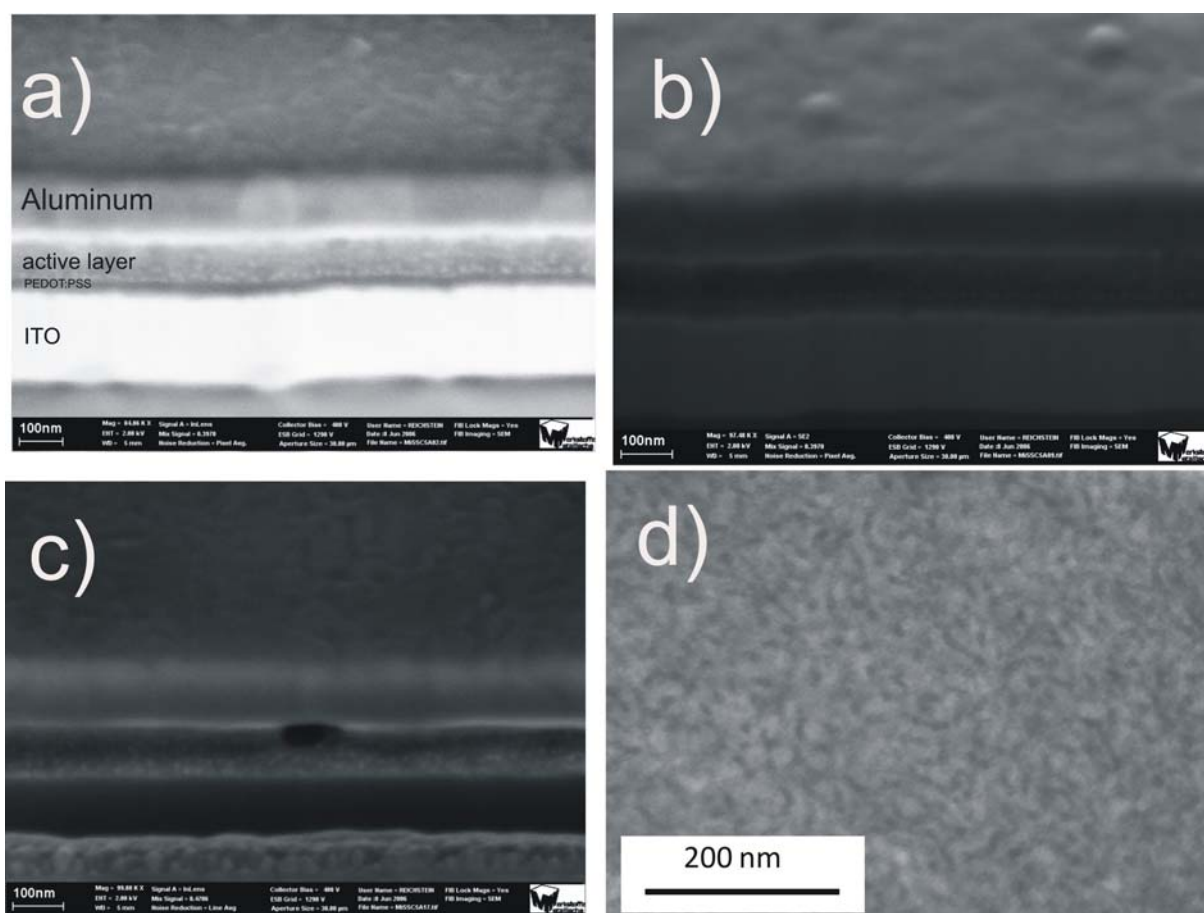


**Figure 4** In situ thin film cross sectioning of PvDMTPD-*b*-PPerAcr **7** with metal cap (aluminium, a,b,d) and bulk TEM cross section (d). a) inlense detector at high brightness, b) SE2 detector, c) inlense detector at low brightness, d) TEM bulk sample cross section of thermally annealed powder.

Figure 4a shows the cross section including the ITO substrate, the PEDOT:PSS layer, the active layer and the aluminium electrode. The active layer exhibits bright fine dots of PPerAcr (~10 nm) in the PvDMTPD matrix. This corresponds well to the TEM cross section of a thermally annealed bulk sample with short isolated PPerAcr worms 8-10 nm in size.<sup>24</sup>

However, the Al/active layer interface of figure 4a is not sharp but bright. Lowering the brightness solved this problem but also led to a loss in contrast within the active layer (figure 4c). In addition, the PEDOT:PSS layer was no longer observed. The use of a SE2 detector instead of the inlense detector gave relatively sharp interfaces, both at the PEDOT:PSS/active layer and at the active layer/aluminium (figure 4b). But, similar to figure 4c, the contrast between PPerAcr and PvDMTPD within the active layer suffered when using the SE2 detector.

The conclusions from figures 3 and 4 can be summarized as follows: In-situ preparation of thin film cross sections prepared via FIB is possible when small currents are used for polishing. The active layer has to be protected with a metal cap to prevent etching of the upper edge leading to radius formation. However, it is difficult to obtain good contrast within the active layer as well sharp interfaces between the individual layers at the same time. The moderate contrast within the active layer of figure 4 is also a result of the small domain size of block copolymer **7**, and the resolution of SEM, which is generally more limited compared to SFM or TEM. The latter preponderates in thin films, in which the area to be imaged is limited.

Based on these results, is it natural to think of etching down thin films layer by layer in order to reconstruct the 3d nanomorphology (nanotomography) rather than preparing one cross section. Using nanotomography<sup>[12]</sup> opposed to a thin film cross section, more data has to be acquired, but also more information can be extracted. We therefore applied the “deposition mode” of the FIB/SEM to a thin film of PvTPA-*b*-PPerAcr **4**. Thereby, an area of 10 x 15  $\mu\text{m}$  was exposed to the beam at a milling current of 100 pA. In this mode, the beam operates line by line in the defined area until it is manually blanked prior to SEM imaging. Larger currents etched the films too fast, and thus did not allow for observations of changes in morphology in convenient time scales. Note that using this approach the incident FIB beam is perpendicular to the imaged area, which is in contrast to figures 2-4. Block copolymer **4** did not show discernible structural features at the surface using SFM or SEM, and the surface of this film also stayed featureless after staining with RuO<sub>4</sub>. A drop-casted film of **4** was exposed to the FIB for times of up to 400 s at 100 pA, and SEM pictures were taken every 30 seconds while the FIB beam was blanked. Figure 5 shows the series of micrographs obtained. The defect in 5a-f demonstrates that FIB exposure and subsequent imaging always

occurred at the same position of the sample. The surface is completely unstructured before FIB treatment, indicative of the formation of a PPerAcr monolayer. PvTPA is less polar than the PvDMTPA block used in the blend film and in the block copolymer bulk samples. This is obvious from contact angles of  $85.8^\circ$  and  $75.8^\circ$ , respectively, and the small difference can be rationalized by the presence of the two methoxy groups in PvDMTPA. However, compared to PPerAcr with a contact angle of  $93.1^\circ$ , the same trend is preserved and both amorphous donor polymers should prefer interaction with the substrate rather than with air during film formation. Furthermore, the PvTPA-*b*-PPerAcr **4** films exhibited water contact angles of  $92.9^\circ$  (contact angle of homopolymer PPerAcr:  $93.1^\circ$ ), supporting the picture of a PPerAcr monolayer at the air-film interface. Since we have provided evidence that staining with  $\text{RuO}_4$  occurs throughout the sample, we can exclude the possibility of the surface being stained more intense than the bulk of the film.

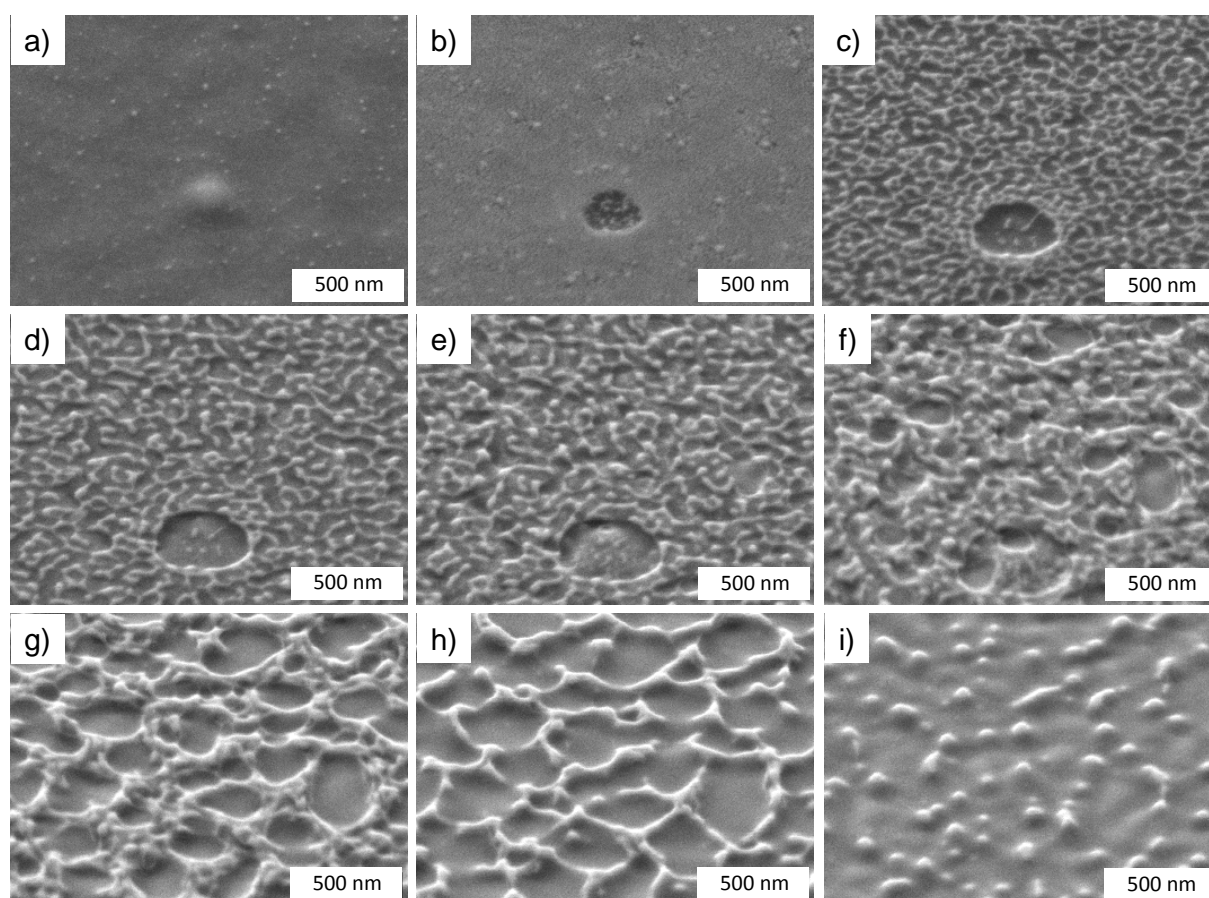


**Figure 5.** SEM top view micrographs of a film of PvTPA-*b*-PPerAcr **4** after staining with  $\text{RuO}_4$  for 10 min and after FIB etching for different times. An area containing a defect was chosen to show that etching always occurred at the same position. a) FIB exposure time 0 sec, b) 30 sec, c) 60 sec, d) 90 sec, e) 120 sec, f) 180 sec, g) 240 sec, h) 300 sec, and f) 360 sec. The scale bar in all pictures is 500 nm.

Upon etching, the PPerAcr monolayer vanishes and structural features appear. Non-defined and disordered regions of PPerAcr in a PvTPA matrix are observed. The bright regions of PPerAcr are ~20-25 nm in diameter and have a distance of approximately 55-65 nm (figure 5c). These spacings correlate with domain sizes obtained from TEM (see inset figure 5c). With increasing etching time, etching does not occur homogeneously anymore for both domains and protrusions of PPerAcr are created (Figure 5c). A reason for that can arise from the amorphous PvTPA regions being etched faster than the highly crystalline PPerAcr domains, which are additionally enriched with RuO<sub>4</sub>. In addition, we observe an increase in the domain size as well as the distance of the bright regions. The bright regions of PPerAcr are now ~40-50 nm in diameter and have a distance of several hundred nanometer (figure 5h). This phenomenon is accompanied with dewetting of the film, as can be derived from the formation of holes (figure 5d-h). The increase in PPerAcr domain size and distance, and the observation of dewetting can only be explained if chain damage, local heating above T<sub>m</sub> of PPerAcr and mass transport are assumed. We further assume that the extent of these conditions increases with prolonged etching time, and arises from the FIB beam perpendicular to the film plane. Thus, the imaged area absorbs the whole energy of the gallium ions leading to chain decomposition and melting of the film. The morphologies of figure 5 thus contain a considerable extent of artefacts and do not reflect the real morphologies of the film.

Further efforts were made in order to elucidate the extend of artefacts in thin films after FIB etching under the conditions of figure 5. We therefore investigated three different block copolymers PvTPA-*b*-PPerAcr **3-5** with different molecular weights and compositions (see table 1 for properties). Drop-casted films of the three block copolymers were etched for 480 sec each using the deposition mode, and the imaged area was compared to TEM bulk cross sections. Figure 6a-c shows the films before etching, and figures 6 d-f show the FIB exposed areas after etching for 480 sec. Figures 6g-i show the TEM cross sections of thermally annealed bulk samples.

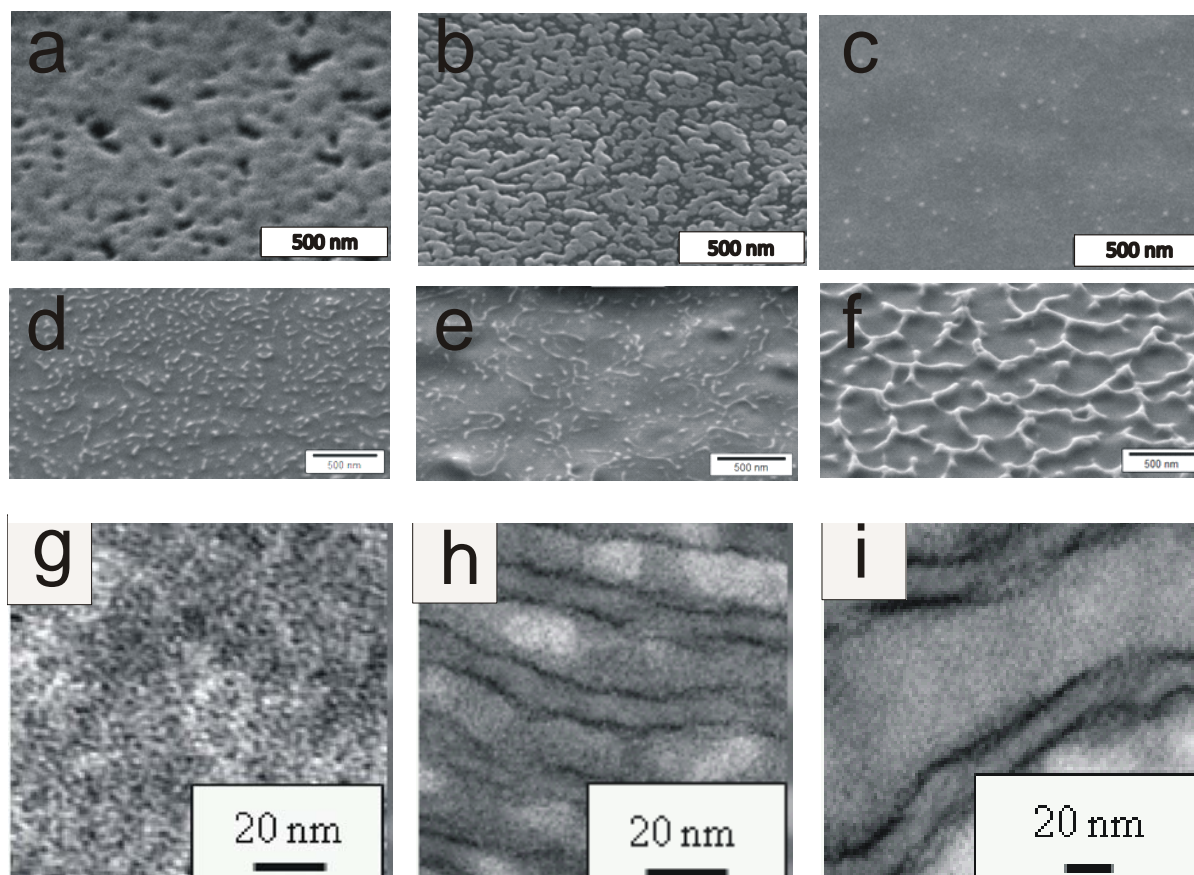


**Figure 6.** Comparison of different PvTPA-*b*-PPerAcr films before and after etching with TEM bulk samples. a-c) films before etching, d-f) films after etching at 100 pA for 480 sec, and g-i) TEM cross sections of thermally annealed bulk samples. a,d,g are obtained from PvTPA-*b*-PPerAcr **5**, b,e,h from PvTPA-*b*-PPerAcr **3**, and c,f,i from PvTPA-*b*-PPerAcr **4**. Scale bar is 500 nm in a)-f) and 20 nm in g)-i). Pictures g)-i) are taken from ref [25].

While the surface of PvTPA-*b*-PPerAcr **4** is featureless (compare figure 5a), PvTPA-*b*-PPerAcr **3** exhibits bright PPerAcr islands (same polymer as figure 3), and PvTPA-*b*-PPerAcr **5** shows a somewhat porous structure (figures 6a-c). However, the explanation of these structures is not our aim here. Rather, we seek to obtain information on the morphology of these films after prolonged etching times, and when major artefacts (as observed in figure 5) can be assumed to be present. Since fragmentation and melting of the block copolymer destroy the microphase separated morphology and potentially can result in blend-like structures, the question arises to what extent the observed morphologies reflect the original film structures, and to what extent completely new domains are formed. Such a comparison is critical in general, since the TEM images are obtained from thermally annealed bulk samples whereas the FIB/SEM images are obtained from drop casted films (chloroform). However, a

correlation is still feasible here when regarding the change of the domain size as a parameter of relevance, since this is determined by the block length (different in block copolymers **3-5**), and since this changes upon chain fragmentation during FIB exposure.

After etching the dropcasted films for 480 sec, the surface effects vanish and different structures appear in the three films of 3-5 (figures 6 d-f). Block copolymer *PvTPA-b-PPerAcr 5* with the smallest molecular weight of 9.2 kg/mol (7 PerAcr repeat units) shows bright PPerAcr dots with a maximum size of ~10 nm, although the corresponding TEM picture (figure 6g) does not indicate a microphase separated structure.<sup>[25]</sup> The latter fact would lead to the expectation that no structure is observable in SEM as well. Conversely the observation of contrast in SEM (figure 6d) indicates that a phase separation is induced during FIB etching. Block copolymer *PvTPA-b-PPerAcr 3* with a molecular weight of 27.5 kg/mol (20 PerAcr repeat units) exhibits elongated bright structures with a similar diameter (figure 6e). Here the TEM lamellar morphology shows crystalline PPerAcr lamellae (aprox. 10 nm thin) in the amorphous PvTPA matrix (figure 6h). Figures 6 f and I are from *PvTPA-b-PPerAcr 4* with a molecular weight of 37.7 kg/mol (27 PerAcr repeat units). The PPerAcr lamellae from TEM is thicker here (~20 nm), and also the morphology after FIB etching for 480 sec reveals thicker domains. Thus, the following conclusions can be made: The morphologies of thin films after layer by layer FIB etching leads to substantial artefacts due to chain fragmentation and local melting of the film. This leads to dewetting, to apparently larger domain sizes, and eventually induces a phase separation when the block copolymer itself does not phase separate. However, the comparison of the FIB/SEM morphologies of the two block copolymers *PvTPA-b-PPerAcr 3* and **4** with TEM data show that the FIB/SEM images are not completely dominated by the artefacts and therefore still preserve some information of the “real” morphology.

Finally, a polymer blend comprised of PvDMTPA and PPerAcr is used for layer-by layer etching via FIB. Here, the effect of chain fragmentation can be neglected since a blend is already present, and FIB etching with progressive etching depth should be observable with less artefacts. Therefore, the film with a high percentage of PPerAcr (90 wt.-%, see figure 1a) was used for FIB etching. In this blend film, rounded acceptor-rich domains 150- 200 nm in size prevail at the film-air interface (figure 7a).

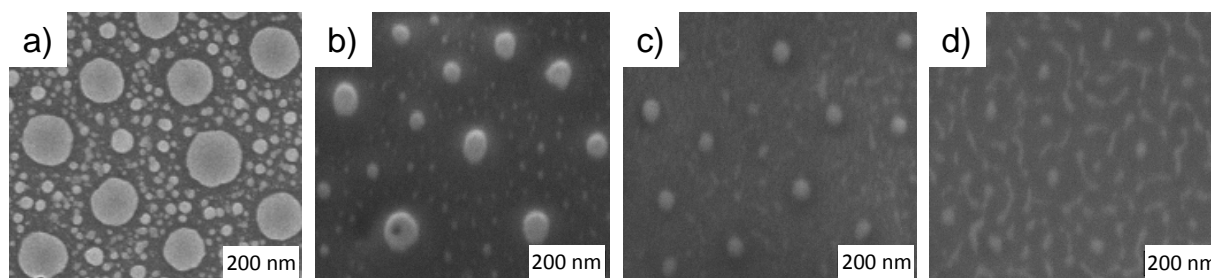


**Figure 7.** SEM images of a PvDMTPA:PPerAcr blend film (10:90) after different FIB exposure times. a) pristine blend surface b) after 30 s, c) after 60 s, and d) after 90 s of FIB exposure time.

Under the same etching conditions used before, the film was etched in-situ for 30, 60 and 90 s and the exposed regions were subsequently imaged by SEM. Clearly, the droplet size decreases from  $\sim 150$  nm to about  $\sim 60$ ,  $\sim 30$ , and  $\sim 20$  nm after 30, 60, and 90s of FIB exposure, respectively (figure 2). The observation of bigger domains at the surface and smaller ones in the bulk of the film can be explained by considering the surface energies and the solubilities of PvDMTPA and PPerAcr.<sup>[13]</sup> For a measure of the surface energies, water contact angles were determined on homopolymer films prepared under same conditions. Thereby, PvDMTPA and PPerAcr exhibit contact angles of  $75.8 \pm 0.8$  and  $93.1 \pm 0.6$ , respectively, suggesting that PPerAcr has a lower surface energy than PvDMTPA (table 1). Furthermore we assume the solubility in chloroform of PvDMTPA to be substantially higher than of PPerAcr, owing to the amorphous and crystalline nature of the two polymers, respectively, and their comparable molecular weights. Thus, PvDMTPA with the lower water contact angle is attracted to the polar ITO substrate during spin coating and the formation of rounded PPerAcr droplets can be explained by the lower solubility of PPerAcr in chloroform.<sup>[13]</sup> The difference in surface energies can be rationalized when considering the chemical structures of the two materials. PPeracr exhibits a large fraction of alkylgroups, whereas PvDMTPA mostly consists of phenyl rings and methoxy groups. The observation of larger structures at the surface and smaller ones in the interior of the film is also known from blends of insulating polymers.<sup>[32]</sup> Note that the structures observed here are non-equilibrium morphologies owing to the fast evaporation of chloroform during spin coating, and are expected to enlarge upon further annealing. However the domain sizes are large enough to be characterized well by SEM, and the observation of larger domains at the

surface and smaller ones in the interior of the film provides a suitable vertical gradient for the combination of FIB and SEM to be tested.

We emphasize that the difference in solubilities and surface energies in both films, the PvDMTPA:PPerAcr blend and in the PvTPA-*b*-PPerAcr block copolymer, are responsible for an enrichment of the acceptor material PPerAcr at the polymer-air interface. This should be beneficial for the open circuit voltage in OPVs if a device architecture such as ITO/PEDOT:PSS/active layer/aluminium is used in which the cathode is deposited on top of the film.<sup>[8]</sup> In organic photovoltaics in which morphological issues become extremely important, surface and interface effects have to be considered so that information from the correlation of surface morphology with device architecture and performance can be understood. Thus, for given asymmetric surface fields in common OPV device architectures the polymer architecture and the polarity of the solubilizing groups of the active material (in this case the alkyl substituents) can be chemically designed in a reasonable way. This concept of preferential wetting has already been applied successfully to ternary blends of poly(3-hexylthiophene), PCBM ([6,6]-phenyl-C<sub>61</sub>-butyric acid methyl ester), and a small amount of a PCBM derivative with fluorinated side chains. Here, the fluorocarbon side chains segregated at the air-film interface and led to an increase in the photovoltaic performance.<sup>[33]</sup>

In conclusion, we have investigated the applicability of the in-situ combination of focused ion beam and scanning electron microscopy for morphological investigations of photovoltaic active polymer blend and block copolymer samples. Using bulk samples, this method can uncover a morphology widely free of artefacts under some circumstances. These include small milling currents and that the area to be imaged is parallel to the incident FIB beam. This etching procedure can in principle be applied to thin films, however the evaporation of a metal cap and extensive optimization of the imaging parameters are required. On the contrary, extensive FIB etching can also result in chain fragmentation, local heating and dewetting of thin block copolymer films. The in-situ combination of FIB/SEM then produces major artefacts making this technique uneligible for morphological investigations. In blend films, these artefacts are observed to a lesser degree and a vertical composition gradient can

be observed. We therefore conclude that the FIB/SEM technique is limited but can be applied under the certain circumstances mentioned above. The destructive nature of the method presented is compensated for the investigation in real space.

### **Acknowledgements**

Financial support of this work by the Deutsche Forschungsgemeinschaft (SFB 481, SPP 1355), the European Science Foundation (EUROCORES SOHYDs) is gratefully acknowledged. The authors thank W. Reichstein and U. Glatzel for valuable help and beamtime at the Carl Zeiss 1540EsB Cross Beam, and R. Magerle (Technische Universität Chemnitz) for fruitful discussions.

### **Experimental**

*Bulk sample preparation:* TEM samples were prepared by annealing the block copolymer for one hour at 210 °C, embedding into epoxy resin, microtoming and staining with RuO<sub>4</sub> vapor for 10 min. TEM measurements were performed on a Zeiss 902 at 80 kV. SEM/FIB samples were prepared by melting down solid bulk material onto indium tin-oxide substrates followed by annealing at 210 °C for one hour.

*Film preparation:* Blend films were spin cast from chloroform solutions at 2000 r/min with a total concentration of 1 wt.-% onto glass substrates (contact angle measurements) or indium tin oxide substrates (FIB-SEM measurements), resulting in 150 nm thin films. Block copolymer films were prepared by drop casting 1 wt.-% chloroform solutions. Drop casted films were thicker, between 200 to 300 nm. Staining was carried out by exposing all films to RuO<sub>4</sub> vapor for 10 min.

*Static contact angle measurements:* The contact angles were determined using the sessile drop method with millipore water as liquid and a Dataphysics OCA Instrument was used to calculate the contact angle. Contact angles of at least five different positions on one film were measured and the given error is estimated from the standard deviation of these values.

*Focused ion beam and scanning electron microscopy:* Focused ion beam and scanning electron microscopy experiments were carried out on a 1540EsB Cross Beam from Carl Zeiss. Bulk samples were coarsly milled in the linear mode at 500 pA. Fine milling (polishing) was done at 10 pA while moving the beam slowly towards to the side walls. This polished side wall was then imaged by SEM (figure 3b,c). Large area milling of the films was done in the deposition mode at milling currents of 100 pA. For that purpose a rectangle 10  $\mu\text{m}$  x 15  $\mu\text{m}$  in size was defined and SEM pictures were taken every 30 seconds. The acceleration voltage was 5 kV and the working distance 5 mm. An inlense detector was used for detection.

## References

1. H. Hoppe, N. S. Sariciftci, *J. Mater. Chem.* **2006**, *16*, 45.
2. M. Campoy-Quiles, T. Ferenczi, T. Agostinelli, P. G. Etchegoin, Y. Kim, T. D. Anthopoulos, P. N. Stavrinou, D. D. C. Bradley, J. Nelson, *Nat. Mater.* **2008**, *7*, 158.
3. S. Günes, H. Neugebauer, N. S. Sariciftci, *Chem. Rev.* **2007**, *107*, 1324.
4. E. J. Meijer, D. M. de Leeuw, S. Setayesh, E. van Veenendaal, B. -H. Huisman, P. W. M. Blom, J. C. Hummelen, U. Scherf, T. M. Klapwijk, *Nat. Mater.* **2003**, *2*, 678.
5. S. Goffri, C. Müller, N. Stingelin-Stutzmann, D. W. Breiby, C. P. Radano, J. W. Andreasen, R. Thompson, R. A. J. Janssen, M. M. Nielsen, P. Smith, H. Sirringhaus, *Nat. Mater.* **2006**, *5*, 960.
6. L. Qiu, J. A. Lim, X. Wang, W. H. Lee, M. Hwang, K. Cho, *Adv. Mater.* **2008**, *20*, 1141.
7. A. C. Arias, J. D. MacKenzie, R. Stevenson, J. J. M. Halls, M. Inbasekaran, E. P. Woo, D. Richards, R. H. Friend, *Macromolecules* **2001**, *34*, 6005.
8. H. J. Snaith, N. C. Greenham, R. H. Friend, *Adv. Mater.* **2004**, *16*, 1640.
9. B. Sun, H. J. Snaith, A. S. Dhoot, S. Westenhoff, N. C. Greenham, *J. Appl. Phys.* **2005**, *97*, 014914.
10. A. C. Arias, N. Corcoran, M. Banach, R. H. Friend, J. D. McKenzie, *Appl. Phys. Lett.* **2002**, *80*, 1695.
11. T. Kietzke, H.-H. Hörhold, D. Neher, *Chem. Mater.* **2005**, *17*, 6532.
12. R. Magerle, *Phys. Rev. Lett.* **2000**, *85*, 2749.
13. S. Walheim, M. Boltau, J. Mlynek, G. Krausch, U. Steiner, *Macromolecules* **1997**, *30*, 4995.

14. C. M. Björström, S. Nilsson, A. Bernasik, A. Budkowski, M. Andersson, K. O. Magnusson, E. Moons, *Appl. Surf. Sci.* **2007**, *253*, 3906.
15. Y. Xia, R. H. Friend, *Adv. Mater.* **2006**, *18*, 1371.
16. a) S. M. Lindner, S. Hüttner, A. Chiche, M. Thelakkat, G. Krausch, *Angew. Chem. Int. Ed.* **2006**, *45*, 3364. b) S. Huettner, M. Sommer, A. Chiche, G. Krausch, U. Steiner, M. Thelakkat, *Soft Matter*, **2009**, *5*, 4206.
17. H. White, Y. Pu, M. Rafailovich, J. Sokolov, A.H. King, L.A. Giannuzzi, C. Urbanik-Shannon, B.W. Kempshall, A. Eisenberg, S.A. Schwarz, Y.M. Strzhemechny, *Polymer* **2001**, *42*, 1613.
18. J. Loos, J. K. J. van Duren, F. Morrissey, R. A. J. Janssen, *Polymer* **2002**, *43*, 7493.
19. M. Sugiyama, G. Sigesato, *J. Electron Microscopy* **2004**, *53*, 527.
20. D. W. Steuerman, A. Garcia, M. Dante, R. Yang, J. P. Löfvander, T.-Q. Nguyen, *Adv. Mater.* **2008**, *20*, 528.
21. M. Hund, H. Herold, *Rev. Sci. Instrum.* **2007**, *78*, 063703.
22. S. M. Lindner, M. Thelakkat, *Macromolecules* **2004**, *37*, 8832.
23. M. Sommer, M. Thelakkat, *Eur. Phys. J. Appl. Phys.* **2006**, *36*, 245.
24. M. Sommer, S. M. Lindner, M. Thelakkat, *Adv. Funct. Mater.* **2007**, *17*, 1493.
25. S. King, M. Sommer, S. Huettner, M. Thelakkat, S. A. Haque, *J. Mater. Chem.* **2009**, *19*, 5436.
26. S. M. Lindner, N. Kaufmann, M. Thelakkat, *Org. Electr.* **2007**, *8*, 69.
27. M. Sommer, S. Huettner, S. Wunder, M. Thelakkat, *Adv. Mater.* **2008**, *20*, 2523.
28. M. Sommer, A. Lang, M. Thelakkat, *Angew. Chem. Int. Ed.* **2008**, *47*, 7901.
29. M. Sommer, S. Huettner, M. Thelakkat, *Adv. Poly. Sci.*, in print.
30. A. K. Khandpur, C. W. Macosko, F. S. Bates, *J. Polym. Sci. Part B Polym. Phys.* **1995**, *33*, 247.
31. Y.-L. Loo, R. A. Register, D. H. Adamson, *J. Polym. Sci. Part B Polym. Phys.* **2000**, *38*, 2564.
32. P. Müller-Buschbaum, *Prog. Col. Polym. Sci.* 2006, *132*, 23.
33. Q. Wei, T. Nishizawa, K. Tajima, K. Hashimoto, *Adv. Mater.* **2008**, *20*, 2211.



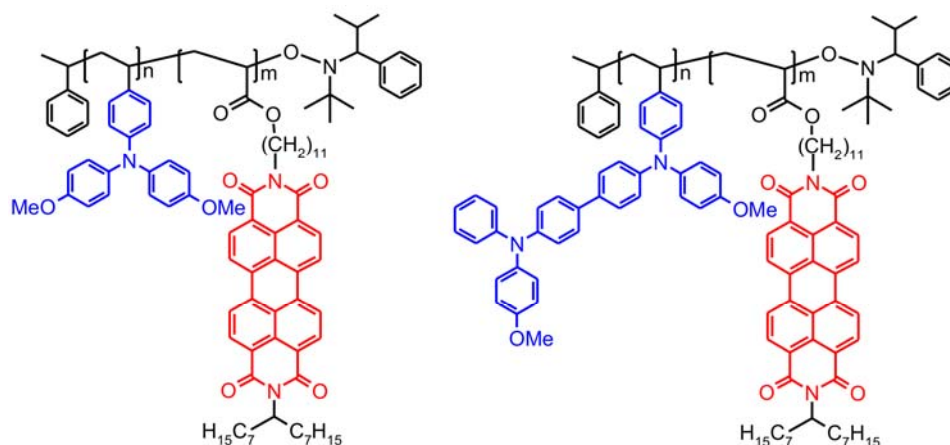
## 10. Synthesis, Characterization and Application of Donor-Acceptor Block Copolymers in Nanostructured Bulk Heterojunction Solar Cells

Michael Sommer and Mukundan Thelakkat

Applied Functional Polymers and Macromolecular Chemistry I

Universitätsstr. 30, University of Bayreuth, 95444 Bayreuth, Germany

[Michael.Sommer@uni-bayreuth.de](mailto:Michael.Sommer@uni-bayreuth.de), [Mukundan.Thelakkat@uni-bayreuth.de](mailto:Mukundan.Thelakkat@uni-bayreuth.de)



Published in *The European Physical Journal - Applied Physics*, **2006**, 36, 245.

## Abstract

The synthesis and properties of two semiconducting donor-acceptor (D-A) block copolymers and their application in nanostructured bulk heterojunction solar cells are reported. The donor segments were obtained via nitroxide mediated polymerization of either bis(4-methoxyphenyl)-4'-vinylphenylamine or N,N'-bis(4-methoxyphenyl)-N-phenyl-N'-4-vinylphenyl-[1,1'-biphenyl]-4,4'-diamine. Narrow-distributed macroinitiators, poly{bis(4-methoxyphenyl)-4'-vinylphenylamine} (PvDMTPA) and poly{N,N'-bis(4-methoxyphenyl)-N-phenyl-N'-4-vinylphenyl-[1,1'-biphenyl]-4,4'-diamine} (PvDMTPD) were used to polymerize the acceptor monomer perylene diimide acrylate (PerAcr) to yield block copolymers with well-defined molecular weights. Different diblock copolymers, PvDMTPA-*block*-PPerAcr and PvDMTPD-*block*-PPerAcr, with high perylene diimide weight fractions were prepared. The block copolymers exhibited efficient fluorescence quenching. Transmission electron microscopy revealed wire-like and worm-like nanostructures throughout bulk samples. Thin film photovoltaic devices showed short circuit currents  $J_{SC}$  of up to 1.21 mA/cm<sup>2</sup> and power conversion efficiencies  $\eta$  of 0.32 % under AM 1.5 illumination conditions.

## Introduction

Organic semiconductor devices are of growing interest because of low-cost and simple production and their suitability for flexible and large area applications. Among these devices, photovoltaic cells are gaining increased attention.<sup>[1]</sup> Different concepts and solar cell architectures have emerged in the last twenty years, including vapour-deposited devices<sup>[2,3]</sup>, solution-processed polymer/ polymer systems<sup>[4-6]</sup>, polymer/ small molecule systems<sup>[7-10]</sup> and block copolymers<sup>[11-14]</sup>. All systems employ D-A heterojunctions in order to efficiently separate charges from generated excitons. Bulk heterojunctions that consist of mixtures of the two components generally lack control of defined morphologies. In general, the variation of the morphology of a conjugated polymer/ PCBM heterojunction is feasible using different solvents for spin-coating, different PCBM weight fractions and thermal post-production treatments<sup>[15]</sup>, but the resulting thin film structures are not stable on longer time scales<sup>[16]</sup>. To increase the stability of the bicontinuous morphology compatibilizers<sup>[16]</sup> and crosslinkable PCBM derivatives<sup>[17]</sup> have been used. Therefore, stable nanostructured bulk heterojunctions with defined charge percolation pathways and domains in the range of the exciton diffusion length are desirable. Block copolymers that phase separate on the nanometer scale afford one possibility to generate stable nanostructures with defined and manageable shape. However, the incorporation of functionalities needed for solar cell applications into block copolymers remains a challenging task for synthetic chemists. The field of block copolymers carrying conjugated segments and fullerene derivatives has been investigated earlier.<sup>[12,16,18]</sup> Very recently, the synthesis of fully conjugated D-A block copolymers was demonstrated.<sup>[19]</sup> Based on side-chain block copolymers, we reported on the synthesis and application of D-A diblock copolymers carrying various triphenylamines and perylene diimide derivatives as donor and acceptor moieties, respectively.<sup>[13,14,20,21]</sup> This contribution describes the synthesis and properties of two novel diblock copolymers with substituted poly(triphenylamine)s as the donor block, PvDMTPA-*b*-PPerAcr and PvDMTPD-*b*-PPerAcr (Fig. 1).

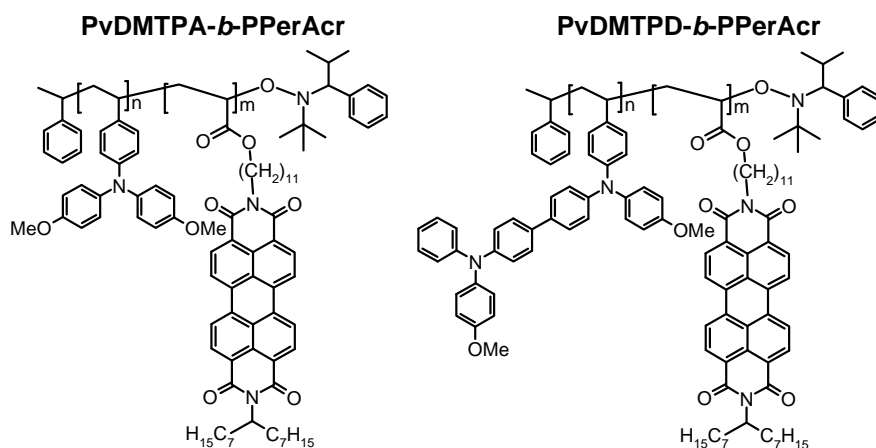


**Figure 1:** Chemical structures of fully functionalized block copolymers PvDMTPA-*b*-PPerAcr (4a, 4b) and PvDMTPD-*b*-PPerAcr (5).

UV-Vis spectroscopy and fluorescence (FL) quenching experiments demonstrated efficient FL quenching in block copolymer films. The hole conductor moieties bis(4-methoxyphenyl)phenylamine (DMTPA) and N,N'-bis(4-methoxyphenyl)-N,N'-diphenyl-[1,1'-biphenyl]-4,4'-diamine (DMTPD) were chosen as their HOMO values lie around 0.2 eV higher than that of triphenylamine (TPA).<sup>[14]</sup> The hole transfer rate and consequently the dye regeneration depends on the energetic driving force at the interface, which is defined as  $HOMO_D - HOMO_A$ . As previously shown, the D-A charge transfer rate can be maximized by increasing this donor-acceptor HOMO offset in a given system.<sup>[22,23]</sup> Additionally, PvDMTPD-*b*-PPerAcr gives information about the influence of the better hole conductor tetraphenylbenzidine<sup>[24,25]</sup> on the photovoltaic parameters. Finally, photovoltaic devices only made of the block copolymers were produced. To correlate and understand the photovoltaic performance we also report on the bulk nanostructures of these polymers as a result of microphase separation.

## Synthesis

Nitroxide mediated polymerization (NMP)<sup>[26]</sup> was chosen as it is metal-free and tolerant to impurities such as oxygen or water. Monomer vDMTPA was synthesized according to literature<sup>[27]</sup> and vDMTPD was obtained from DMTPD<sup>[28]</sup> via Vilsmeier and Wittig reactions. The polymerizations were successfully carried out starting from these monomers and a second generation initiator developed by Hawker *et al.*<sup>[29]</sup> Small amounts of the

corresponding free nitroxide were also added to control the reaction rates of the polymerizations.<sup>[20,29]</sup> The optimization of the polymerization reaction conditions resulted in macroinitiators (MI) PvDMTPA (**1a,b**) and PvDMTPD (**2**) with low polydispersities (PDI) of around 1.2. The linear dependence of  $M_n$  versus conversion was observed, which proved the controlled character of the polymerization. Thus, macroinitiators with desired number molecular weights  $M_n$  between 10 and 20 kg/mol were obtained. These low molecular weights guarantee sufficient solubility required for the facile polymerization of the second monomer PerAc **3** in a mixture of **1a, 1b** or **2, 3**, 5 mol-% styrene and o-dichlorobenzene (Fig. 2). The small amount of styrene added was helpful in maintaining sufficient control of the reactions.<sup>[30]</sup> Different block copolymers PvDMTPA<sub>16</sub>-*b*-PPerAc<sub>84</sub> (**4a**), PvDMTPA<sub>28</sub>-*b*-PPerAc<sub>72</sub> (**4b**) and PvDMTPD<sub>19</sub>-*b*-PPerAc<sub>81</sub> (**5**) with high perylene diimide weight fractions of 84, 72 and 81 wt.-%, respectively, were synthesized (table 1).

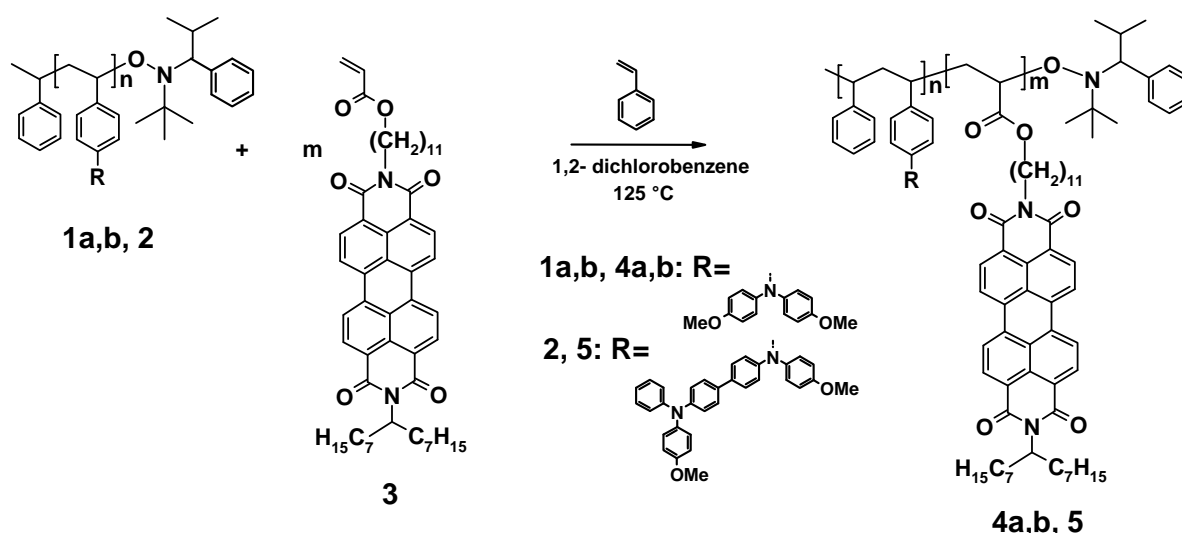


**Figure 2:** Reaction scheme for the synthesis of block copolymers PvDMTPA<sub>16</sub>-*b*-PPerAc<sub>84</sub> **4a**, PvDMTPA<sub>28</sub>-*b*-PPerAc<sub>72</sub> **4b** and PvDMTPD<sub>19</sub>-*b*-PPerAc<sub>81</sub> **5**.

**Table 1:** Molecular weights, polydispersities and PPerAc weight fractions of block copolymers **4a, 4b** and **5**. [M]:[MI]: Monomer **3** to macroinitiator ratio.

Macro- initiator (MI)	Block Copolymer (BC)	[M]:[MI]	$M_n$ MI (GPC) [kg/mol]	$M_n$ BC (GPC) [kg/mol]	PDI MI	PDI BC	wt.-% PerAc ( <sup>1</sup> H-NMR)
<b>1a</b>	<b>4a</b>	120:1	9.4	88.3	1.26	1.66	84
<b>1b</b>	<b>4b</b>	240:1	17.7	34.6	1.23	1.76	72
<b>2</b>	<b>5</b>	100:1	7.2	26.5	1.14	1.66	81

## Characterization

UV-Vis and FL spectroscopy in thin films ( $\sim 150$  nm) were carried out. The donor segments absorb between 270 and 400 nm, the acceptor segment absorbs between 400 and 600 nm. When excited at the absorption maximum of perylene diimide at 490 nm, the films showed a broad fluorescence peak at around 610 nm. All block copolymers exhibit efficient FL quenching. As an example, the optical density and FL intensity of a perylene homopolymer (PPerAcr), a polymer blend containing the two homopolymers PPerAcr and PvDMTPA with the same composition and polymer **4a** are given in figure 3. Particular care was taken to ensure an identical optical density of the three films between 400 and 600 nm, which is the precondition for comparing FL intensities. As a result, fluorescence intensity decreased drastically from PPerAcr to the polymer blend by 30 % and to block copolymer **4a** by 77 %. Since energy transfer from acceptor to donor is almost impossible, the FL quenching can be explained most probably as a result of electron transfer from D to A. The higher degree of quenching in the block copolymer film can be attributed to the larger interface between donor and acceptor which again is determined by the covalent connectivity of the two segments.<sup>[13]</sup> As polymer blends usually are not miscible, they tend to macrophase separate, whereas block copolymers rather show nanosized domains.

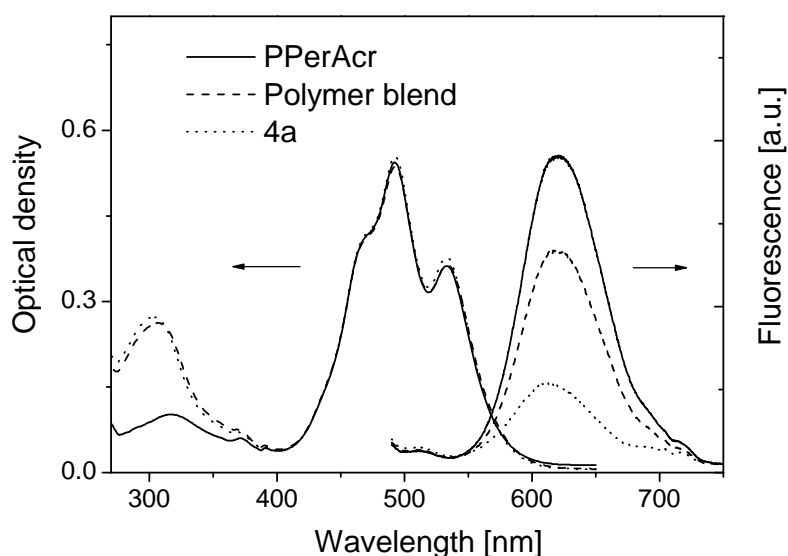


**Figure 3:** UV-Vis spectra (left) and fluorescence intensity (right) of 150 nm thin films of PPerAcr homopolymer (solid line), the block copolymer **4a** (dotted line) and a PPerAcr:PvDMTPA polymer blend having the same weight composition as the block copolymer (dashed line).

An investigation of the microphase separation was carried out employing transmission electron microscopy (TEM). Figure 4 displays cross sections of volume samples of the block copolymers. The darker regions represent perylene diimide domains. Polymer **4a** exhibited short structures, whereas **4b** showed lamellar structures, 13 nm in diameter. Polymer **5**, however, exhibited thinner and very short structures. Further detailed studies of these nanostructures are underway. The lamellar structures are very interesting for photovoltaic applications as they provide a large donor-acceptor interface for efficient charge separation and at the same time crystalline perylene diimide charge percolation pathways for highly anisotropic electron transport.

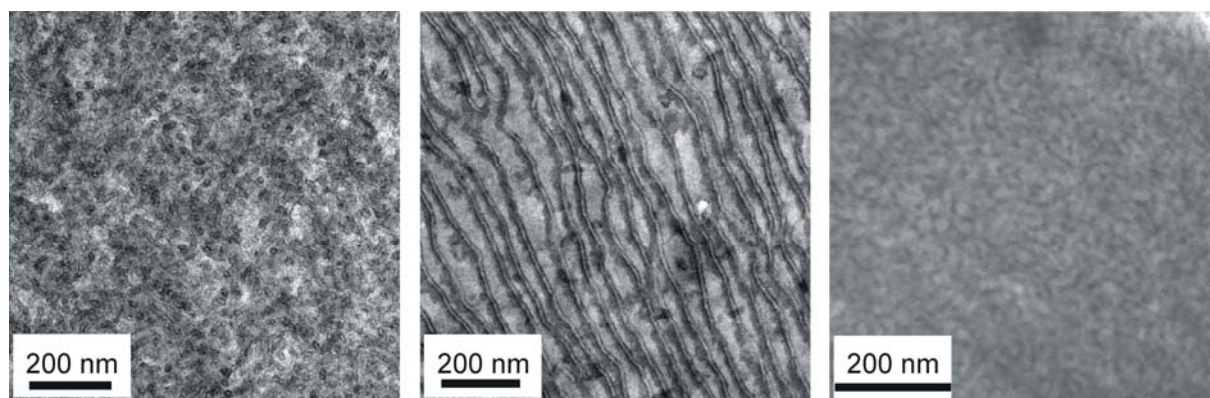


**Figure 4:** Cross sectional transmission electron micrographs of block copolymers **4a** (a), **4b** (b) and **5** (c). All volume samples were tempered at 210 °C, embedded in epoxy resin, cut and stained with  $\text{RuO}_4$ .

Figure 5 shows the  $J$ - $V$ -characteristics of the thin film devices made of **4a**, **4b** and **5**. **4b** delivered a short circuit current  $J_{\text{SC}} = 1.14 \text{ mA/cm}^2$ , an open circuit voltage  $V_{\text{OC}} = 690 \text{ mV}$  and a power conversion efficiency  $\eta = 0.32$ , whereas these parameters are only  $0.24 \text{ mA/cm}^2$ ,  $530 \text{ mV}$  and  $0.065$  for **4a**, respectively. We believe that the increase in  $J_{\text{SC}}$  and  $V_{\text{OC}}$  in **4b** is due to possible lamellar structures in the solar cells. Polymer **5** with shorter structures in the bulk gave  $J_{\text{SC}} = 1.21 \text{ mA/cm}^2$ ,  $V_{\text{OC}} = 530 \text{ mV}$  and  $\eta = 0.26 \%$ . The high current in **5** can be attributed to the higher charge carrier mobility of tetraphenylbenzidines. The influence of composition, block length and resulting morphology of  $\text{PvDMTPD-}b\text{-PPerAcr}$  on photovoltaic performance is currently investigated.

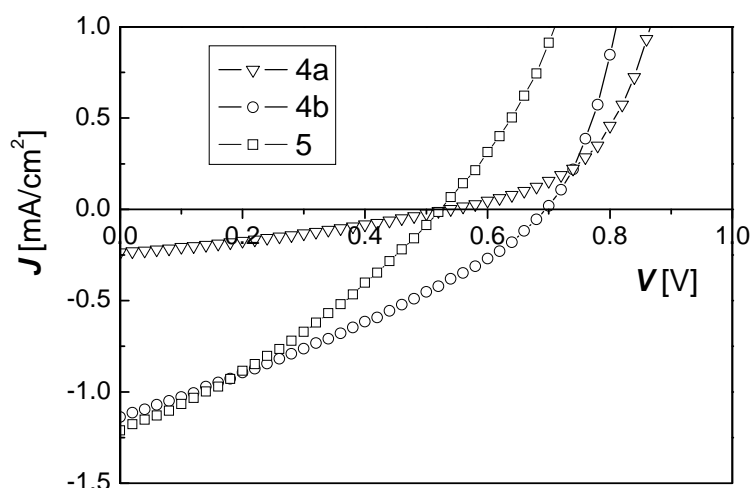


**Figure 5:** *J-V*-characteristics of *PvDMTPA*<sub>16</sub>-*b*-*PPerAcr*<sub>84</sub> **4a** (triangles), *PvDMTPA*<sub>28</sub>-*b*-*PPerAcr*<sub>72</sub> **4b** (circles) and *PvDMTPD*<sub>19</sub>-*b*-*PPerAcr*<sub>81</sub> **5** (squares).

**Table 2:** Photovoltaic parameters of solar cells with **4a**, **4b** and **5** as active materials.

Block Copolymer	$J_{sc}$ [mA/cm <sup>2</sup> ]	$V_{oc}$ [mV]	FF	$\eta$ [%]
<b>4a</b>	0.24	530	0.32	0.052
<b>4b</b>	1.14	690	0.32	0.323
<b>5</b>	1.21	530	0.31	0.262

## Conclusion

NMP was used to synthesize well-defined donor-acceptor block copolymers with triphenylamines or tetraphenylbenzidines and perylene diimide functionalities. The block copolymers showed strong fluorescence quenching in thin films which is ascribed to the large donor-acceptor interface in the block copolymers. TEM cross sections of block copolymer **4b** revealed spectacular long nanowire-like structures that stem from perylene diimide  $\pi$ - $\pi$ -stacking. This polymer also exhibited the best performance in the photovoltaic device. Polymer **5** with a less favorable worm-like nanostructure still performed well, probably due to the presence of a better hole conductor block. Therefore, it might be speculated that block copolymers such as **5** with a nanowire structure should even show

much better performance. Furthermore, the high potential of these outstanding block copolymers for photovoltaics is convincingly demonstrated.

## Experimental

The detailed synthetic procedures of initiator, monomers, macroinitiators and block copolymers as well as solar cell preparation are published elsewhere.<sup>[14]</sup> Active layer thickness was 70 nm and the active area of a single device 0.18 cm<sup>2</sup>. The *I-V*-characteristics were measured using a simulated AM 1.5 spectrum at 77 mW/cm<sup>2</sup> and under a nitrogen atmosphere.

## Acknowledgements

Financial support for this work by the Deutsche Forschungsgemeinschaft (DFG) under SFB 481 is gratefully acknowledged. The authors thank A. Göpfert and C. Kunert for TEM measurements and H. Wietasch for valuable help in synthesis.

## References

1. C. J. Brabec, J. A. Hauch, P. Schilinsky, C. Waldauf, *MRS Bull.* **2005**, *30*, 50.
2. C. W. Tang, *Appl. Phys. Lett.* **1986**, *48*, 183.
3. P. Peumans, A. Yakimov, S. R. Forrest, *J. Appl. Phys.* **2003**, *93*, 3693.
4. Granstrom, K. Petritsch, A. C. Arias, A. Lux, M. R. Andersson, and R. H. Friend, *Nature* **1998**, *395*, 257.
5. J. J. M. Halls, C. A. Walsh, N. C. Greenham, E.A. Marseglia, R. H. Friend, S. C. Moratti, A. B. Holmes, *Nature* **1995**, *376*, 498.
6. T. Kietzke, H.-H. Hoerhold, D. Neher, *Chem. Mater.* **2005**, *17*, 6532.
7. G. Yu, J. Gao, J. C. Hummelen, F. Wudl, A. J. Heeger, *Science* **1995**, *270*, 1789.
8. C. J. Brabec, N. S. Sariciftci, J. C. Hummelen, *Adv. Funct. Mater.* **2001**, *11*, 15.

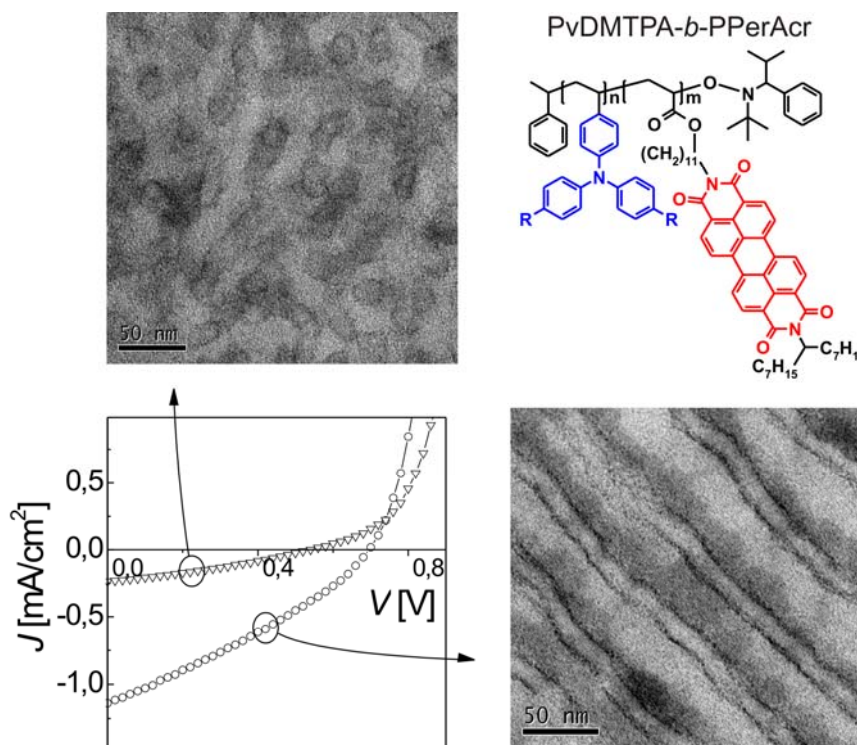
9. J.-I. Nakamura, C. Yokoe, K. Murata, *J. Appl. Phys.* **2004**, *11*, 6878.
10. W. Ma, C. Yang, X. Gong, K. Lee, A. J. Heeger, *Adv. Funct. Mater.* **2005**, *15*, 1617.
11. G. Hadziioannou, *MRS Bull.* **2002**, *27*, 456.
12. R. Segalman, C. Brochon, G. Hadziioannou, in "Organic Photovoltaics", edited by S. S. Sun and N. S. Sariciftci (CRC Press, Taylor and Francis Group, **2005**)
13. S. M. Lindner, S. Hüttner, A. Chiche, M. Thelakkat, G. Krausch, *Angew. Chemie Int. Ed.* **2006**, *45*, 3364.
14. M. Sommer, S. M. Lindner, M. Thelakkat, *Adv. Funct. Mater.* **2007**, *17*, 1493.
15. H. Hoppe, N. S. Sariciftci, *J. Mater. Chem.* **2006**, *16*, 45.
16. K. Sivula, Z. T. Ball, N. Watanabe, J. M. J. Frechet, *Adv. Mater.* **2006**, *18*, 206.
17. M. Drees, H. Hoppe, C. Winder, H. Neugebauer, N. S. Sariciftci, W. Schwinger, F. Schäßler, C. Topf, M. C. Scharber, Z. Zhu and R. Gaudiana, *J. Mater. Chem.* **2005**, *15*, 5158.
18. M. H. van der Veen, B. de Boer, U. Stalmach, K. I. van de Wetering, G. Hadziioannou, *Macromolecules* **2004**, *37*, 3673.
19. G. Tu, H. Li, M. Forster, R. Heiderhoff, L. J. Balk, U. Scherf, *Macromolecules* **2006**, *13*, 4327.
20. S. M. Lindner, M. Thelakkat, *Macromolecules* **2004**, *37*, 8832.
21. S. M. Lindner, N. Kaufmann, M. Thelakkat, *Organic Electronics*, **2007**, *8*, 69.
22. S. A. Haque, T. Park, A. B. Holmes, J. R. Durrant, *ChemPhysChem* **2003**, *1*, 89.
23. R. Bilke, A. Leicht, C. Jäger, M. Thelakkat, C. Schmitz, H. Karickal, D. Haarer, *Synth. Met.* **2001**, *124*, 91.
24. I. G. Hill, A. Kahn, Z. G. Soos, R. A. Pascal, *Chem. Phys. Lett.* **2000**, *327*, 181.
25. M. Stolka, D. M. Pai, D. S. Renfer, J. F. Yanus, *J. Pol. Sci., Pol. Chem. Ed.* **1983**, *21*, 969.
26. C. Hawker, A. W. Bosman, E. Harth, *Chem. Rev.* **2001**, *101*, 3661.
27. T. Yamamoto, M. Nishiyama, Y. Koie, *Tetrahedron Letters* **1998**, *39*, 2367.
28. C. Schmitz, M. Thelakkat, H. W. Schmidt, *Adv. Mater.* **1999**, *11*, 821.
29. D. Benoit, V. Chaplinski, R. Braslau, C. J. Hawker, *J. Am. Chem. Soc.* **1999**, *121*, 3904.
30. B. Charleux, J. Nicholas, O. Guerret, *Macromolecules* **2005**, *38*, 5485.

# 11. Microphase Separated Donor-Acceptor Diblock Copolymer Polymer Solar Cells: Influence of HOMO Energy Levels and Morphology

Michael Sommer, Stefan M. Lindner, and Mukundan Thelakkat

Applied Functional Polymers and and Macromolecular Chemistry I  
Universitätsstr. 30, University of Bayreuth, 95444 Bayreuth, Germany

[Michael.Sommer@uni-bayreuth.de](mailto:Michael.Sommer@uni-bayreuth.de), [Mukundan.Thelakkat@uni-bayreuth.de](mailto:Mukundan.Thelakkat@uni-bayreuth.de)



Published in *Advanced Functional Materials*, **2007**, *17*, 1493.

## Abstract

We report on the synthesis of novel semiconducting donor-acceptor (D-A) diblock copolymers containing functional moieties for hole transport, electron transport and light absorption by means of nitroxide mediated polymerization (NMP). The first block representing the donor is either made up of substituted triphenylamines (poly[bis(4-methoxyphenyl)-4'-vinylphenylamine], PvDMTPA) or substituted tetraphenylbenzidines (poly[N,N'-bis(4-methoxyphenyl)-N-phenyl-N'-4-vinylphenyl-(1,1'-biphenyl)-4,4'-diamine], PvDMTPD). The second block consists of perylene diimide side groups attached via a flexible spacer to a polyacrylate backbone (PPerAcr). This block is responsible for absorption in the visible range and for electron transport properties. The electrochemical properties of these fully functionalized diblock copolymers PvDMTPA-*b*-PPerAcr and PvDMTPD-*b*-PPerAcr are investigated by cyclic voltammetry (CV) and the morphology using transmission electron microscopy (TEM). All diblock copolymers exhibit microphase separated domains in the form of either lamellar or worm-like structures made of perylene diimide embedded in a hole conductor matrix. In single active layer organic solar cells, PvDMTPD-*b*-PPerAcr reveals a fourfold improvement in power conversion efficiency ( $\eta = 0.26\%$ ,  $J_{SC} = 1.21 \text{ mA/cm}^2$ ) and PvDMTPA-*b*-PPerAcr a fivefold increased efficiency ( $\eta = 0.32\%$ ,  $J_{SC} = 1.14 \text{ mA/cm}^2$ ) compared to its unsubstituted analogue PvTPA-*block*-PPerAcr ( $\eta = 0.065\%$ ,  $J_{SC} = 0.23 \text{ mA/cm}^2$ ).

## Introduction

In the field of photovoltaics, organic devices are gaining increased attention<sup>[1]</sup> compared to their inorganic counterparts made of silicon owing to the inherent advantages of low cost and large area fabrication. Different concepts and solar cell architectures have been developed, including small molecule/ small molecule multilayers<sup>[2,3]</sup> and blends<sup>[4,5]</sup>, polymer/ polymer bilayers<sup>[6]</sup> and blends<sup>[7,8]</sup>, polymer/ small molecules bilayers<sup>[9]</sup> and blends<sup>[10-13]</sup> and block copolymers.<sup>[14]</sup> All systems employ Donor-Acceptor (D-A) Heterojunctions in order to efficiently separate charges from generated excitons. Using P3HT/PCBM bulk heterojunctions, a striking power conversion efficiency of about 5 % has been realized.<sup>[13]</sup> Most of the bulk heterojunctions that consist of D-A mixtures, generally lack control of defined morphologies. Albeit the morphology of a conjugated polymer/PCBM heterojunction can be tuned to nanoscopic scale by the use of different solvents for spin-coating, different PCBM weight fractions and thermal post-production treatments<sup>[15]</sup>, the resulting thin film structures are not stable on longer time scales.<sup>[16]</sup> To increase the stability of the bicontinuous morphology, compatibilizers<sup>[16]</sup> and crosslinkable PCBM derivatives<sup>[17]</sup> have been tested. Moreover, thicker devices are needed to harvest the incident light completely. The efficiencies of thicker devices, however, decrease dramatically. Hence, stable nanostructured bulk heterojunctions with defined charge percolation pathways and domains in the range of the exciton diffusion length are desirable. This can be achieved using block copolymers that exhibit phase separation on the nanometer scale.<sup>[18]</sup> Some successful attempts to covalently link donor and acceptor functions in block copolymers have been carried out using two different conjugated polymers<sup>[19]</sup> and conjugated polymers with fullerene derivatives.<sup>[16,20]</sup> Earlier, we reported on the synthesis and application of a microphase separated D-A block copolymer, poly(bisphenyl-4-vinylphenylamine)-*b*-poly(perylene diimide acrylat) PvTPA-*b*-PPerAcr (Fig. 1).<sup>[14,21]</sup> In this block copolymer, the  $\pi$ - $\pi$  stacking of the perylene diimide side group highly favors the formation of thin perylene diimide wire-shaped structures with a constant thickness of 13 nm extended over several microns. The use of PvTPA-*b*-PPerAcr in a photovoltaic cell was compared to its analogous polymer blend system, where the block copolymer device surpassed the polymer blend device by one order of magnitude with respect to efficiency.<sup>[14]</sup> This tremendous

improvement could be attributed to the larger D-A interface in the block copolymer than in the polymer blend originating from microphase separated domains.

Here, the synthesis and characterization of two novel block copolymers, PvDMTPA-*b*-PPerAcr and PvDMTPD-*b*-PPerAcr, are reported. In these block copolymers, the hole conducting moieties are bis(4-methoxyphenyl)phenylamine (DMTPA) and N,N'-bis(4-methoxyphenyl)-N,N'-diphenyl-(1,1'-biphenyl)-4,4'-diamine (DMTPD), respectively (Fig. 1).

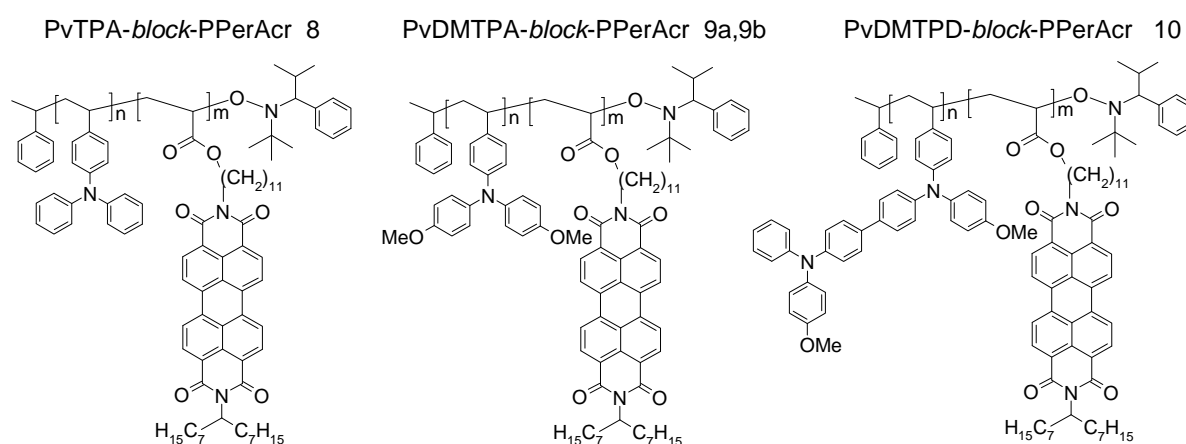


**Figure 1:** Chemical structures and compositions of the diblock copolymers compared here: PvTPA<sub>14</sub>-*b*-PPerAcr<sub>86</sub> (8), PvDMTPA<sub>28</sub>-*b*-PPerAcr<sub>72</sub> (9a), PvDMTPA<sub>16</sub>-*b*-PPerAcr<sub>84</sub> (9b), and PvDMTPD<sub>19</sub>-*b*-PPerAcr<sub>81</sub> (10). The subscripts correspond to the weight fractions of the respective blocks.

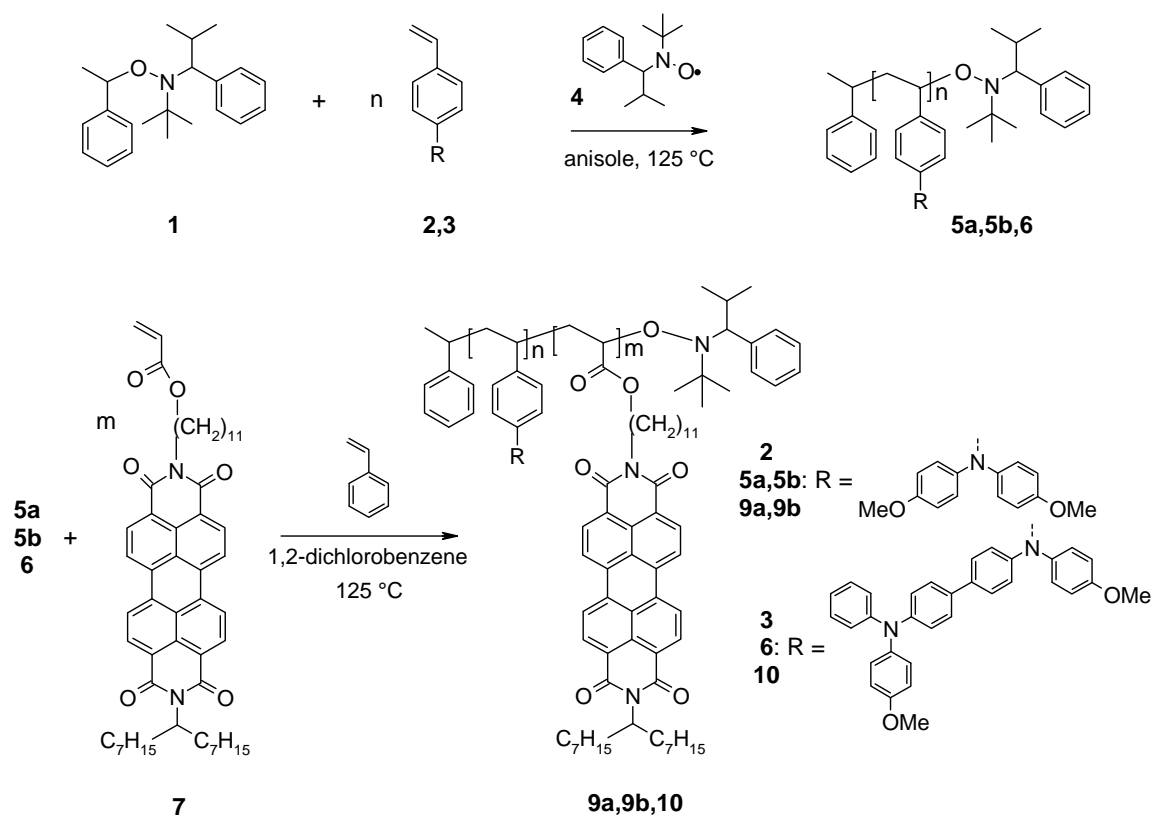
The new hole conductor moieties which are electron-richer than TPA were selected in order to vary HOMO values, to improve electrochemical stability and hole carrier mobility. The block copolymers were synthesized from their corresponding macroinitiators PvDMTPA and PvDMTPD using NMP. TEM cross sections of volume samples revealed different nanostructures in the form of lamellar or worm-like perylene diimide domains for high PerAcr weight fractions between 72 and 86 wt.-% due to perylene diimide  $\pi$ - $\pi$  stacking. The novel block copolymers were then tested in single active layer solar cells and the influence of the new hole transport blocks and morphologies were correlated with the solar cell performance.

## Results and discussion

### Synthesis of donor-acceptor diblock copolymers

Different diblock copolymers with varying perylene diimide content, macroinitiator block length and with varying hole conductor were synthesized employing nitroxide mediated polymerization (NMP)<sup>[21,22]</sup> (scheme 1). NMP could be successfully applied for the controlled polymerization of the novel monomers **2** and **3** for the first time. The detailed synthetic procedures of monomers **2** and **3** are given as supporting information. The polymerization reactions of **2** and **3** were optimized with respect to initiator to monomer ratio, amount of solvent and equivalents of free nitroxide **4** to obtain low polydispersities, controlled molecular weights and acceptable yields for macroinitiators poly[bis(4-methoxyphenyl)-4'-vinylphenylamine] (PvDMTPA) and (poly[N,N'-bis(4-methoxyphenyl)-N-phenyl-N'-4-vinylphenyl-(1,1'-biphenyl)-4,4'-diamine] (PvDMTPD). Thus, two PvDMTPA macroinitiators **5a** ( $M_n = 17.7$  kg/mol, PDI= 1.23) and **5b** ( $M_n = 9.4$  kg/mol, PDI= 1.26) as well as a PvDMTPD macroinitiator **6** ( $M_n = 7.2$  kg/mol, PDI= 1.14) were synthesized.

These macroinitiators were employed to sequentially polymerize perylene diimide acrylat monomer **7** (PerAc)<sup>[21]</sup> to obtain two series of block copolymers, PvDMTPA-*b*-PPerAc and PvDMTPD-*b*-PPerAc. The synthesis of the block copolymers was realized in the absence of the free nitroxide **4** using concentrated mixtures of macroinitiator and **7**. Additionally, 5 mol.-% of styrene were added to maintain sufficient control in the absence of **4**. Thereby, block copolymers carrying different hole conductor moieties and with different compositions were obtained. Within these synthesized block copolymers, we found interesting nanoscopic structures in the composition range between 72 to 86 wt.-% PPerAc. For the purpose of comparative studies here, the block copolymers PvDMTPA<sub>28</sub>-*b*-PPerAc<sub>72</sub> **9a** ( $M_n = 34.6$  kg/mol), PvDMTPA<sub>16</sub>-*b*-PPerAc<sub>84</sub> **9b** ( $M_n = 88.3$  kg/mol) and PvDMTPD<sub>19</sub>-*b*-PPerAc<sub>81</sub> **10** ( $M_n = 26.5$  kg/mol) having comparable weight fractions of PerAc were selected and compared with PvTPA<sub>14</sub>-*b*-PPerAc<sub>86</sub> **8** ( $M_n = 26.9$  kg/mol)<sup>[21]</sup> (Fig. 1). The subscripts indicate weight fractions of the respective blocks.



**Scheme 1:** Reaction scheme of macroinitiator and diblock copolymer synthesis. The monomer to initiator ratio was 200:1 (**5a** and **5b**), 80:1 (**6**), 240:1 (**9a**), 120:1 (**9b**) and 100:1 (**10**).

The polymers were characterized by size exclusion chromatography (SEC),  $^1\text{H-NMR}$  spectroscopy and differential scanning calorimetry (DSC), the data is summarized in table 1. GPC eluograms of all block copolymers exhibited the expected shift to lower elution volumes compared to their macroinitiators. Monomodal molecular weight distributions observed for the block copolymers indicate the absence of any remaining macroinitiator. The PerAcr weight fractions were determined by  $^1\text{H-NMR}$  spectroscopy. The block copolymers possess glass transition temperatures ( $T_g$ ) between 131 and 150 °C and melting temperatures ( $T_m$ ) between 183 and 198 °C. The  $T_g$  corresponds to the amorphous hole conductor block and the  $T_m$  to the semi-crystalline PerAcr block.  $T_g$  of the macroinitiator and  $T_m$  of the PPerAcr homopolymer correlate well with  $T_g$  and  $T_m$  observed in the corresponding block copolymers.

**Table 1:** Molecular weights, polydispersity indices, PerAcr weight fractions and thermal properties of block copolymers **8-10**. <sup>[a]</sup>: Data of PvTPA-*b*-PPerAcr **8** is given for means of comparison. The molecular weights and polydispersities were determined via GPC relative to polystyrene standards. Thermal properties were determined at 10 K/min, values were taken from second heating curve. BC: block copolymer, MI: macroinitiator.

BC	$M_n$ MI [kg/mol]	PDI MI	$M_n$ BC [kg/mol]	PDI BC	wt.-% PerAcr ( <sup>1</sup> H-NMR)	$T_g$ [°C]	$T_m$ [°C]
<b>8</b> <sup>[a]</sup>	15.8	1.20	26.9	1.50	86	150	198
<b>9a</b>	17.7	1.23	34.6	1.76	72	131	183
<b>9b</b>	9.4	1.26	88.3	1.66	84	134	194
<b>10</b>	7.2	1.14	26.5	1.67	81	148	191

### Microphase separation and morphology

The existence of both  $T_g$  due to the amorphous hole conductor segment and  $T_m$  due to crystalline perylene diimide side groups already indicated the presence of phase separated domains. For further investigations, TEM cross sections of thick volume samples were prepared. Figure 2 shows two pictures of each block copolymer with different magnifications, darker regions stem from  $\pi$ - $\pi$  stacked perylene diimide side groups. We observed lamellar and worm-like structures originating from PPerAcr segments. For short staining times with RuO<sub>4</sub>, these nanostructures are initially stained at the boundaries and for long staining times, the whole structures appear dark. The structures shown here are stained only for a short time. The effect of initial boundary staining can be due to favorable diffusion of RuO<sub>4</sub> through the amorphous phase and preferential reaction with perylene diimide. Block copolymers **8** and **9a** show lamellar structures whereas **9b** and **10** exhibit short worm-like structures, all the domain sizes being in the nanoscopic range. It should be noted that **8** and **9a** have relatively long amorphous blocks, whereas **9b** and **10** have shorter ones (see table 1). On comparing block copolymers **9a** and **9b** carrying the same hole conducting moieties, the amorphous block length seems to decide the capability of formation of the lamellar structure, if the PPerAcr content lies between 72 to 86 wt.-%. For example, **9a** obtained from a longer macroinitiator exhibits lamellar structures, whereas **9b**, which was obtained from a shorter macroinitiator shows worm-like structures. We assume that the

worm-like structures in pictures 2g and 2h from polymers **9b** and **10**, respectively, also arise from the short amorphous block length. Apparently, for the lamellar nanostructures to be formed, macroinitiator molecular weights higher than 10 to 12 kg/mol and PPerAcr contents between 72 and 86 wt.-% are necessary.

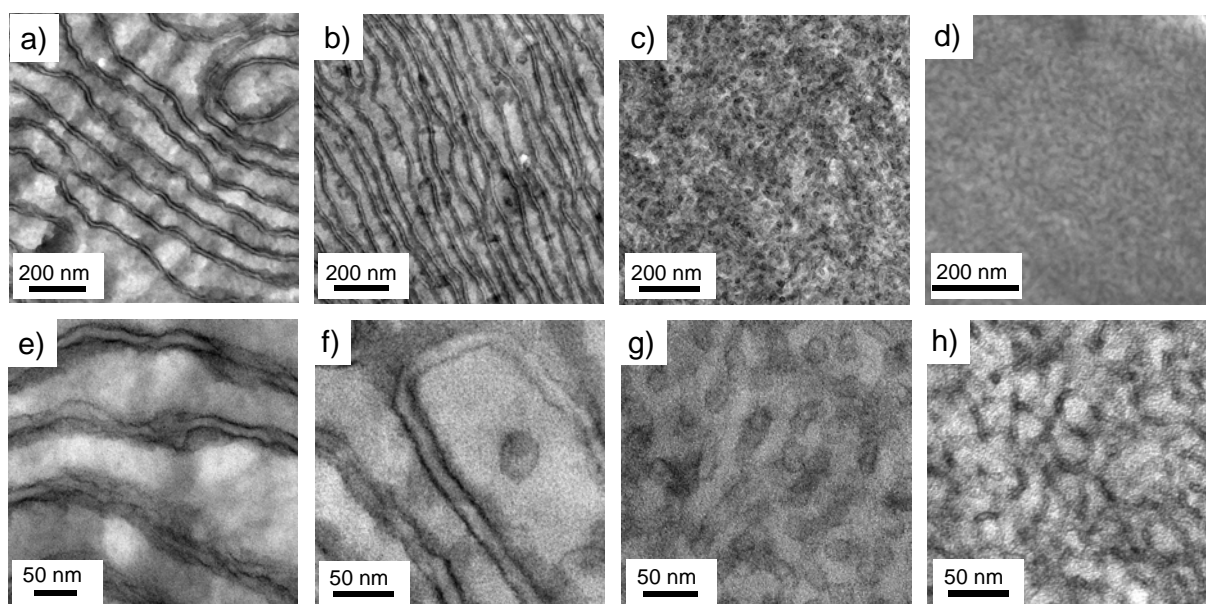


**Figure 2:** TEM cross sections of block copolymers **8** (a,e), **9a** (b,f), **9b** (c,g) and **10** (d,h). All volume samples were tempered at 210 °C, embedded in epoxy resin, cut and stained with RuO<sub>4</sub>.

Despite slightly different PPerAcr contents of **8** and **9a** (86 and 72 wt.-%, respectively), their nanostructures are very similar with respect to diameter and length. For both polymers, the diameter of nanostructure is about 15 nm. If aligned perpendicular to the electrodes, these interesting lamellar structures appear to be ideal for solar cell applications as they provide percolation pathways in which anisotropic charge transport will be facilitated. Furthermore, the structures observed here enable thicker devices with higher optical densities maintaining structural dimensions in the range of the exciton diffusion length.

### Cyclic voltammetry

The HOMO and LUMO levels of the synthesized block copolymers were determined using cyclic voltammetry (CV). The measurements were conducted in solution using a glassy

carbon working electrode in a three electrode assembly and potentiostat set up. Figure 3a presents the cyclic voltammograms of PvTPA-*b*-PPerAcr (**8**), PvDMTPA-*b*-PPerAcr (**9b**), PvDMTPD-*b*-PPerAcr (**10**), in figure 3b the range of oxidation of **8** and **9b** is magnified. As expected, polymer **9b** exhibits the same cyclic voltammogram as **9a** and is therefore omitted here.

It is well known that unsubstituted triphenylamines dimerize upon electrochemical oxidation to give TPD-derivatives.<sup>[23]</sup> Due to the lower HOMO value of the TPD-moiety, these dimers can act as traps<sup>[24,25]</sup> for holes that are transported within the hole conductor. This unfavorable reaction can be avoided by either protecting the para positions of the triphenylamine group or by stabilizing the radical cation with electron rich groups.<sup>[26]</sup> Both are realized in PvDMTPA-*b*-PPerAcr where the two para positions are blocked with the methoxy substituents which additionally increase the stability of the radical cation (Fig. 3). TPD derivatives do not show this behavior in general due to the formation of highly stabilized radical cations.

To determine the HOMO-LUMO energy values, each measurement was calibrated with ferrocene (Fc). Table 2 summarizes the measured potentials and the determined HOMO and LUMO levels. All the block copolymers exhibit the characteristic double reduction peak of perylene diimide unit, the first reduction occurring at -1.2 V vs Fc (Fig. 3a). This results in LUMO values of 3.6 eV for all the block copolymers, taking 4.8 eV as the ferrocene HOMO value. Polymer **8** with PvTPA as donor segment shows the first oxidation at 0.44 V vs Fc on the first cycle and a new oxidation peak at 0.25 V vs Fc appears in the second cycle due to the formation of TPD derivative by dimerization. As can be seen from the monomodal peak in figure 3b, PvDMTPA does not dimerize and its oxidation potential  $E_{Ox1}$  is 0.16 V vs Fc. Thus, the resulting HOMO level decreases from 5.24 eV in PvTPA to 4.96 eV in PvDMTPA. PvDMTPD shows the characteristic two-step reversible oxidation observed in tetraphenylbenzidines. The measured  $E_{Ox1}$  and the HOMO values of **10** are 0.16 V vs Fc and 4.96 eV, respectively, and are therefore equal to the values of PvDMTPA (Fig. 3a). The HOMO value of 6.0 eV for PPerAcr was taken from a cyclic voltammogram of its model compound.

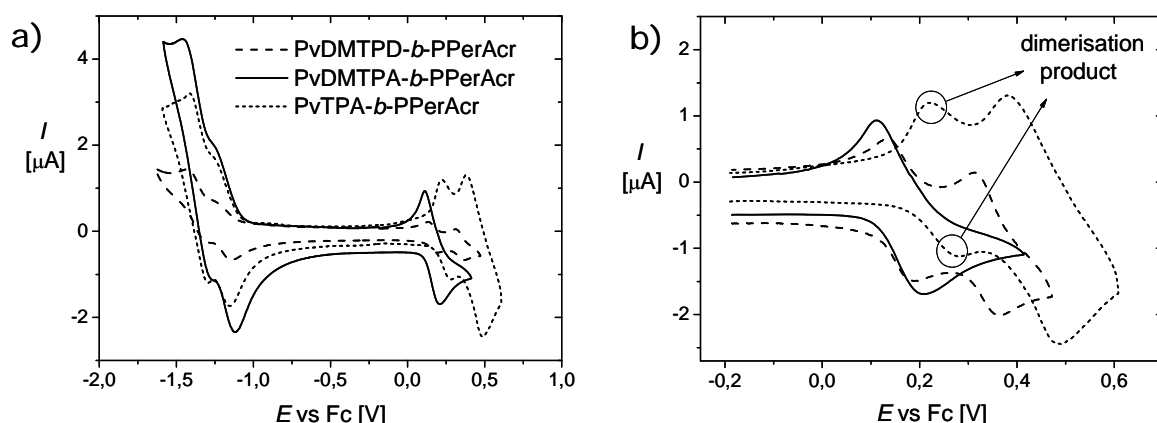


**Figure 3:** a) Cyclic voltammograms of **8** (dotted line), **9b** (solid line) and **10** (dashed line). The left part of the curves represents the first and second reduction of the perylene diimide segment and the right part the oxidations of the hole conductor units. b) Only the enlarged oxidation range of **8** and **9b** is shown. Curves were measured in *o*-dichlorobenzene with tetrabutylammonium hexafluorophosphate as conducting electrolyte and at 50 mV/s. Fc: Ferrocene.

**Table 2:** HOMO and LUMO levels of block copolymers PvTPA-*b*-PPerAcr (**8**), PvDMTPA-*b*-PPerAcr (**9b**) and PvDMTPD-*b*-PPerAcr (**10**) measured by CV. <sup>[a]</sup>: Oxidation peak of PvTPA from first cycle; in the second cycle a new oxidation peak due to the dimer appears at 0.25 V vs Fc.

BC	$E_{\text{OX}1}$ vs. Fc [V]	$E_{\text{RED}1}$ vs. Fc [V]	HOMO [eV]	LUMO [eV]
<b>8</b>	0.44 <sup>[a]</sup>	-1.21	5.2	3.6
<b>9b</b>	0.16	-1.19	5.0	3.6
<b>10</b>	0.16	-1.21	5.0	3.6

### Photovoltaic applications

All four block copolymers were tested in single layer devices in order to compare the influence of HOMO levels, morphology and a possible improvement in hole transport. Current-voltage characteristics were measured under AM 1.5 spectral conditions at 77 mW/cm<sup>2</sup>. The UV-Vis spectra of thin films (70 nm) made from the solutions used for device preparation are given in figure 4. The hole conductor moieties absorb up to 400 nm and the PPerAcr segments between 400 and 600 nm with characteristic vibronic bands for a highly aggregated state.<sup>[27]</sup> As can be clearly seen, the intensity of absorption in the visible range due to the perylene diimide moiety, which contributes mainly to light harvesting in solar

cells, is almost equal in all films. Thus, any difference in solar cell performance can be attributed to interface effects and difference in morphology.

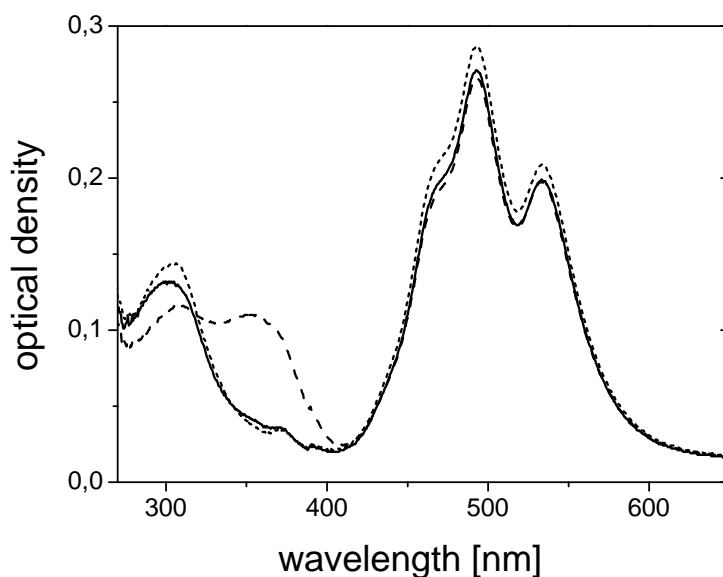


**Figure 4:** UV-Vis spectra of thin films (70 nm) of block copolymers **8** (dotted line), **9a** (dashed-dotted line), **9b** (solid line) and **10** (dashed line). The films have the same thickness as the active layers in the solar cells.

In general, the D-A charge transfer rate and consequently the dye regeneration depend on the energetic driving force at the interface, which is defined as  $\Delta G_{D-A} = \text{HOMO}_D - \text{HOMO}_A$ . As previously shown, the D-A charge transfer rate can be maximized by varying the HOMO of the donor in a given system.<sup>[28,29]</sup> Thus, a direct comparison of **8** (HOMO= 5.2 eV) and **9a** (HOMO= 5.0 eV) as active materials in the device helps us to understand the influence of HOMO donor level on the photovoltaic parameters. We also point out that **8** and **9a** exhibit very similar bulk nanostructures. This is important for the comparison of the two polymers in the device, as morphology is, in addition to the energetic levels, one of the crucial parameters influencing the performance.

Figure 5a presents the *J-V*-characteristics of solar cells prepared from block copolymers **8** (HOMO= 5.2 eV) and **9a** (5.0 eV) under the same conditions. In 5b, the energetic levels of the block copolymers, as determined from CV, are depicted. Table 3 summarizes the photovoltaic parameters such as short circuit current ( $J_{SC}$ ), open circuit voltage ( $V_{OC}$ ), fill factor (*FF*) and power conversion efficiency ( $\eta$ ).  $J_{SC}$  in the device made of **9a** amounts to 1.14 mA/cm<sup>2</sup> which represents a fivefold increase compared to 0.23 mA/cm<sup>2</sup> in **8**. This indicates

that D-A charge transfer occurs more efficiently in **9a** than in **8**, which is caused by the higher D-A HOMO offset in **9a** (Fig. 5b), and, which again seems to be more favorable to overcome the exciton binding energy of the perylene diimide group. A quantification of the hole transfer rate at the D-A interface in block copolymer **9a** can be elucidated by time-resolved absorption studies which is currently under investigation. From the higher slope of the  $J$ - $V$ -curve of **9a** at open circuit conditions, it can be concluded that charges are injected more easily from **9a** (HOMO= 5.0 eV) than from **8** (HOMO= 5.2 eV) into ITO. The maximum photovoltage that can be achieved at the D-A interface is given by  $\text{HOMO}_D\text{-LUMO}_A$ . This implies a loss of photovoltage if  $\text{HOMO}_D$  is shifted to higher values. This negative effect is compensated in **9a** due to an improvement in hole transfer efficiency. Thus,  $V_{\text{OC}}$  in both devices are nearly the same (670 to 690 mV). The shift of the HOMO in **9a** to higher values therefore improves the performance of the solar cell by a factor of 5 in power conversion efficiency.

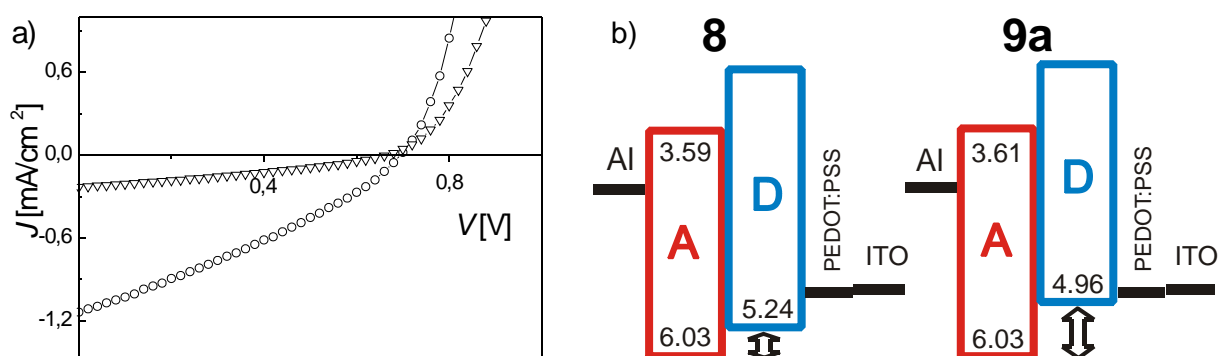


**Figure 5:** a)  $J$ - $V$ -characteristics of block copolymer **8** (triangles) and **9a** (circles). The measurements were carried out under white light illumination (AM 1.5 spectral conditions,  $77 \text{ mW/cm}^2$ ) in a  $\text{N}_2$  atmosphere. b) Energy level diagram for both devices. In **9a** the energetic driving force is higher due to a larger HOMO offset (represented as  $\hat{=}$ ) compared to **8**. The given acceptor HOMO level of 6.0 eV is determined from a low molecular weight perylene diimide model compound. All energetic values are obtained from CV in solution.

**Table 3:** Photovoltaic parameters of all solar cells made from block copolymers **8**, **9a**, **9b** and **10**.

BC	$J_{\text{sc}}$ [mA/cm <sup>2</sup> ]	$V_{\text{oc}}$ [mV]	FF	$\eta$ [%]
<b>8</b>	0.23	670	0.32	0.065
<b>9a</b>	1.14	690	0.32	0.323
<b>9b</b>	0.24	530	0.32	0.052
<b>10</b>	1.21	530	0.31	0.262

In the following, the  $J$ - $V$ -characteristics of block copolymers **9a** and **9b** are compared. In the device made of **9a**, the power conversion efficiency has improved fivefold compared to **9b** (Fig. 6a).  $J_{SC}$  and  $V_{OC}$  raise from  $0.24 \text{ mA/cm}^2$  to  $1.14 \text{ mA/cm}^2$  and from  $530 \text{ mV}$  to  $690 \text{ mV}$ , respectively. The HOMO levels are  $5.0 \text{ eV}$  in both block polymers. Block copolymers **9a** and **9b** vary mainly in their hole conductor block length, resulting in different volume nanostructures. **9a** shows a lamellar and **9b** short worm-like structures. As a consequence, the charge percolation in **9a** should be more favorable than in **9b**. This indicates that not only an adaptation of the energetic levels, but also the generation of defined charge percolation pathways is required for improving the efficiency of a bulk heterojunction solar cell.

Block copolymers **9a**, **9b** and **10** exhibit the same HOMO level, which should result in the same hole transfer efficiency at the D-A interface. However, charge carrier mobilities of TPA and TPD are expected to differ by about one order of magnitude.<sup>[30,31]</sup> Therefore, comparing PvDMTPA-*b*-PPerAcr and PvDMTPD-*b*-PPerAcr, we expect to gain information regarding improved hole transport mobility. For a comparison, **9b** was chosen instead of **9a** because of the similarity in morphology and PPerAcr content of **9b** and **10** (Fig. 6b). In the device made of **10**, a fourfold improvement in short circuit current ( $1.21 \text{ mA/cm}^2$ ) was measured. This can be attributed to the higher charge carrier mobility of TPDs.

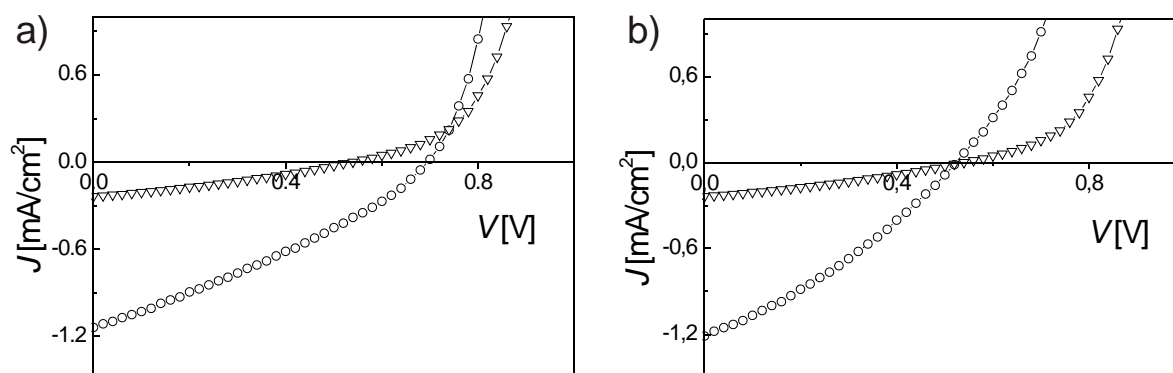


**Figure 6:** a: Comparison of  $J$ - $V$ -characteristics of block copolymers **9a** with lamellar structure (circles) and **9b** with worm-like structure (triangles). b:  $J$ - $V$ -characteristics of block copolymers **9b** with DMTPA as HTM (triangles) and **10** with DMTPD as HTM (circles) are compared. All measurements were carried out under white light illumination (AM 1.5 spectral conditions,  $77 \text{ mW/cm}^2$ ) in a  $N_2$  atmosphere.

It is also interesting to note that the devices made of block copolymers **8** and **9a** exhibit higher  $V_{OC}$  than the ones made of **9b** and **10**. Polymers **8** and **9a** show voltages of 670 and 690 mV, respectively, whereas **9b** and **10** deliver 530 mV. This again correlates well with morphology: The block copolymers that form lamellar structures (**8** and **9a**) yield higher open circuit voltages in the device. However, it must be mentioned that correlation of device morphology and solar cell performance should be carried out in order to quantify these first results. This is necessary as surface energies and geometric confinement play important roles in thin films. Thus, for further interpretation and correlation of solar cell performance, thin film morphology studies of the devices themselves have to be carried out which is under current investigation.

## Conclusion

We synthesized novel semiconducting fully functionalized diblock copolymers, in which the hole transport segment was varied in order to study the influence of HOMO level, morphology and charge carrier mobility in solar cells. All the polymers presented here exhibit nanostructured bulk heterojunctions required for photovoltaic applications. Block copolymers **8** and **9a** show ideal lamellar nanodomains 15 nm in diameter, which is in the same range as the exciton diffusion length for the absorbing species. The shift in HOMO value of **9a**, **9b** and **10** results in improved energetic driving force at the D-A interface, which in turn improves the short circuit current to 1.14 mA/cm<sup>2</sup> and the power conversion efficiency to 0.32 %. The lamellar morphology is essential to facilitate charge percolation. The positive influence of this type of morphology could be confirmed in polymer **9a**. Moreover, the current and efficiency can be improved by using PvDMTPD-*b*-PPerAcr **10** having efficient hole transport units. We therefore believe that a block copolymer such as PvDMTPD-*b*-PPerAcr can be designed to obtain lamellar domains, in which the synergetic effect of improved hole transfer efficiency, high charge carrier mobility and desired morphology can lead to very high power conversion efficiencies. All devices presented here exhibit high series resistance and therefore low fill factors. An improvement in the fill factor can be achieved by aligning the lamellar domains vertically to the contact electrodes. Here,

standard methods such as solvent annealing<sup>[32]</sup> or electric field induced alignment<sup>[33]</sup> of block copolymer domains can be employed. In conclusion, we have demonstrated several concepts for improving the solar cell performance using self assembling block copolymers. This evidently points out the huge potential of block copolymers as functional materials for nanostructured bulk heterojunction photovoltaic devices.

## Experimental

*Synthesis.* The initiator **1**, nitroxide **4** and monomer **7** were synthesized according to literature.<sup>[21,34]</sup> The monomer **2**, bis(4-methoxyphenyl)-4'-vinylphenylamine, was synthesized from 4-bromostyrene and bis(4,4'-dimethoxyphenyl)amine using a Buchwald-Hartwig amination.<sup>[35]</sup> Monomer **3**, N,N'-bis(4-methoxyphenyl)-N-phenyl-N'-4-vinylphenyl-[1,1'-biphenyl]-4,4'-diamine, was synthesized via Vilsmeier and Wittig reactions starting from N,N'-bis(4-methoxyphenyl)-N,N'-diphenyl-[1,1'-biphenyl]-4,4'-diamine.<sup>[36]</sup> Detailed synthetic procedures of monomers **2**, **3**, macroinitiators **5**, **6** and block copolymers **9a**, **9b**, **10** are given in supporting information.

*Instrumentation.* <sup>1</sup>H-NMR spectra were recorded on a Bruker AC 250 spectrometer (250 MHz) and calibrated to the signal of the respective solvent. FT-IR spectra were recorded on a BIO-RAD Digilab FTS 40. Mass spectra were measured on a Finnigan MAT 8500 at 70 eV. GPC measurements were carried out in THF containing 0.25 wt.-% tetrabutylammonium bromide using UV and RI detectors (Waters). For calibration, polystyrene standards and 1,2-dichlorobenzene as an internal standard were used. Differential scanning calorimetry was carried out at heating rates of 10 K/min between 30 °C and 210 °C under N<sub>2</sub> with a Perkin Elmer Diamond DSC. For TEM sample preparation, molten samples were embedded in epoxy resin, cut and stained with RuO<sub>4</sub>. Measurements were performed on a Zeiss 902 at 80 kV. Cyclic voltammograms were recorded using a Princeton Applied Research Potentiostat Galvanostat in combination with a three electrode assembly. A glassy carbon electrode was used as working electrode and Ag/AgNO<sub>3</sub> as reference electrode. All measurements were carried out under argon in dry o-dichlorobenzene with 0.1 M tetrabutylammonium hexafluorophosphate as conducting electrolyte. The scan speed was 50 mV/s, HOMO and LUMO values were determined relative to that of ferrocene.

*Solar cell preparation and characterization.* For the preparation of the solar cells, pre-etched and cleaned ITO substrates with a sheet resistance of  $10 \Omega/\square$  were used. A 30 nm thin layer of PEDOT:PSS (Aldrich, electronic grade) was deposited by spin-coating a 1:1 mixture of the filtered dispersion and deionized water at 2000 r/min. The active layer was obtained on top of this layer by spin-coating 0.5 wt.-% chloroform solutions of the block copolymers at 2000 r/min, resulting in 70 nm thin films. 130 nm thin Al electrodes were evaporated at  $10^{-6}$  mbar, the active area of a single device was  $0.18 \text{ cm}^2$ . *J-V*-characteristics were measured under a simulated AM 1.5 spectrum ( $77 \text{ mW/cm}^2$ , Oriel setup with 150 W xenon arc lamp and suitable filters) in a  $\text{N}_2$  atmosphere.

### **Acknowledgements**

Financial support of this work by the Deutsche Forschungsgemeinschaft (DFG) is gratefully acknowledged. The authors thank A. Göpfert and C. Kunert for TEM measurements and H. Wietasch for help in synthesis.

## References

1. C.J. Brabec, J.A. Hauch, P. Schilinsky, C. Waldauf, *MRS Bull.* **2005**, *30*, 50.
2. C. W. Tang, *Appl. Phys. Lett.* **1986**, *48*, 183.
3. C. W. Chu, Y. Shao, V. Shrotriya, Y. Yang, *Appl. Phys. Lett.* **2005**, *86*, 243506.
4. P. Peumans, S. Uchida, S. R. Forrest, *Nature* **2003**, *425*, 158.
5. S. Uchida, J. Xue, B. P. Rand; S. R. Forrest, *Appl. Phys. Lett.* **2004**, *84*, 4218.
6. M. Granstrom, K. Petritsch, A. C. Arias, A. Lux, M. R. Andersson, and R. H. Friend, *Nature* **1998**, *395*, 257.
7. J. J. M. Halls, C. A. Walsh, N. C. Greenham, E.A. Marseglia, R. H. Friend, S. C. Moratti, A. B. Holmes, *Nature* **1995**, *376*, 498.
8. T. Kietzke, H.-H. Hörhold, D. Neher, *Chem. Mater.* **2005**, *17*, 6532.
9. A. J. Breeze, A. Salomon, D. S. Ginley, B. A. Gregg, H. Tillmann, and H.-H. Hörhold, *Appl. Phys. Lett.* **2002**, *81*, 3085.
10. G. Yu, J. Gao, J. C. Hummelen, *Science* **1995**, *270*, 1789.
11. J.-I. Nakamura, C. Yokoe, K. Murata, *J. Appl. Phys.* **2004**, *11*, 6878.
12. C. J. Brabec, N. S. Sariciftci, J. C. Hummelen, *Adv. Funct. Mater.* **2001**, *11*, 15.
13. W. Ma, C. Yang, X. Gong, K. Lee, A. J. Heeger, *Adv. Funct. Mater.* **2005**, *15*, 1617.
14. S. M. Lindner, S. Hüttner, A. Chiche, M. Thelakkat, G. Krausch, *Angew. Chemie Int. Ed.* **2006**, *45*, 3364.
15. H. Hoppe, N. S. Sariciftci, *J. Mater. Chem.* **2006**, *16*, 45.
16. K. Sivula, Z. T. Ball, N. Watanabe, J. M. J. Frechet, *Adv. Mater.* **2006**, *18*, 206.
17. M. Drees, H. Hoppe, C. Winder, H. Neugebauer, N. S. Sariciftci, W. Schwinger, F. Schöffler, C. Topf, M. C. Scharber, Z. Zhu, R. Gaudiana, *J. Mater. Chem.* **2005**, *15*, 5158.
18. F.S. Bates, G.H. Fredrickson, *Ann. Rev. Phys. Chem.* **1990**, *41*, 525.
19. G. Tu, H. Li, M. Forster, R. Heiderhoff, L. J. Balk, U. Scherf, *Macromolecules* **2006**, *39*, 4327.
20. M. H. van der Veen, B. de Boer, U. Stalmach, K. I. van de Wetering, G. Hadziioannou, *Macromolecules* **2004**, *37*, 3673.
21. S. M. Lindner, M. Thelakkat, *Macromolecules* **2004**, *37*, 8832.
22. C. Hawker, A. W. Bosman, E. Harth, *Chem. Rev.* **2001**, *101*, 3661.

23. E. T. Seo, R. F. Nelson, J. M. Fritsch, L. S. Marcoux, D. W. Leedy, R. N. Adams, *J. Am. Chem. Soc.* **1966**, *88*, 3498.
24. H. Zhao, C. Tanjuncto, S. Thayumanavan, *Tetrahedron Letters* **2001**, *42*, 4421.
25. C. Jäger, D. Haarer, B. Peng, M. Thelakkat, *Appl. Phys. Lett.* **2004**, *85*, 6185.
26. L. Hagopian, G. Köhler, R. I. Walter, *J. Phys. Chem.* **1967**, *71*, 2290.
27. F. Würthner, Z. Chen, V. Dehm, V. Stepanenko, *ChemComm* **2006**, 1188.
28. S. A. Haque, T. Park, A. B. Holmes, J. R. Durrant, *ChemPhysChem* **2003**, *1*, 89.
29. R. Bilke, A. Leicht, C. Jäger, M. Thelakkat, C. Schmitz, H. Karickal, D. Haarer, *Synth. Met.* **2001**, *124*, 91.
30. M. Stolka, D. M. Pai, D. S. Renfer, J. F. Yanus, *J. Pol. Sci., Pol. Chem. Ed.* **1983**, *21*, 969.
31. M. Abkowitz, D. M. Pai, *Philosophical Magazine B* **1986**, *53*, 193.
32. S. H. Kim, M. J. Misner, T. P. Russell, *Adv. Mater.* **2004**, *16*, 2119.
33. T. Thurn-Albrecht, J. DeRouchey, T. P. Russell, *Macromolecules* **2000**, *33*, 3250.
34. D. Benoit, V. Chaplinski, R. Braslau, C. J. Hawker, *J. Am. Chem. Soc.* **1999**, *121*, 3904.
35. T. Yamamoto, M. Nishiyama, Y. Koie, *Tetrahedron Letters* **1998**, *39*, 2367.
36. C. Schmitz, M. Thelakkat, H. W. Schmidt, *Adv. Mater.* **1999**, *11*, 821.

## Supporting Information

**General information:** All glass apparatus were dried at 110 °C and cooled down under argon. Solvents used for column chromatography and precipitation were distilled under normal atmosphere. Styrene was distilled over CaH<sub>2</sub> in an argon atmosphere. Dry THF was distilled over KOH, K and K/benzophenone, respectively. POCl<sub>3</sub> was purchased from Aldrich and distilled under argon directly prior to use. DMF was obtained from Fluka and distilled over CaH<sub>2</sub>. Dichloroethane was purchased from Aldrich and dried over molecular sieve. Methyltriphenylphosphonium bromide was purchased from Fluka. Bis(4-methoxyphenyl)-4'-vinylphenylamine was purchased from Lancaster. Dry 1,2-dichlorobenzene, dry anisole, methyl ethyl ketone and 4-bromostyrene were purchased from Aldrich and used as received, t-butoxide was obtained from Merck.

**Synthesis of 2: Bis(4-methoxyphenyl)-4'-vinylphenylamine.** In a three necked flask, 9.28 g (40 mmol) bis(4,4'-dimethoxyphenyl)amine, 8.79 g (48 mmol) 4-bromostyrene, 5 g (52 mmol) Na-tert.-butoxide and 90 mg (0.4 mmol) Pd(OAc)<sub>2</sub> are dissolved in dry toluene under argon. To start the reaction, 0.324 g (1.6 mmol) (tert.-butyl)<sub>3</sub>P (solution in toluene) are added via syringe to the mixture. The mixture is stirred for 1 h at 100 °C, the progress of the reaction is followed by TLC. The dark mixture is then cooled to room temperature, filtered over basic alumina and the solvents are removed under reduced pressure. The raw product (black oil) is purified by column chromatography (cyclohexane: THF, 20:1), which gives a colorless, viscous product. It is dissolved in n-hexane under argon, sealed and kept in a cool place. After hours to days, white-yellow crystals of **2** emerged. TLC (cyclohexane: THF, 50:1, R<sub>f</sub>= 0.28).

IR (in film);  $\nu$  [cm<sup>-1</sup>]= 3038 (m), 2998 (m), 2950 (m), 2905 (m), 2833 (s), 2059 (w), 2020 (w), 1898 (w), 1811 (w), 1601 (s), 1504 (s), 1463 (s), 1441 (s), 1321 (s), 1234 (s), 1178 (s), 1106 (s), 1035 (s), 991 (s), 900 (s), 830 (s), 722 (m), 577 (s), 526 (s).

<sup>1</sup>H-NMR (250 MHz, CD<sub>2</sub>Cl<sub>2</sub>);  $\delta$  (ppm)= 7.19- 7.23 (m, 2H); 7.00- 7.04 (m, 4H); 6.80- 6.84 (m, 6H); 6.62 (dd, <sup>3</sup>J<sub>HHcis</sub>= 10.9 Hz, <sup>3</sup>J<sub>HHtrans</sub>= 17.53 Hz, 1H); 5.57 (d, <sup>3</sup>J<sub>HHtrans</sub>= 17.53 Hz, 1H); 5.07 (d, <sup>3</sup>J<sub>HHcis</sub>= 10.9 Hz, 1H); 3.77 (s, 6H, OCH<sub>3</sub>).

MS (EI, 70 eV);  $m/z$ = 331 (100) [M<sup>+</sup>]; 316 (78) [M<sup>+</sup>-Me]; 198 (6); 166 (6); 77 (9) [Ph<sup>+</sup>].

**Synthesis of 3: N,N'-bis(4-methoxyphenyl)-N-phenyl-N'-4-vinylphenyl-[1,1'-biphenyl]-4,4'-diamine** was synthesized in two steps via Vilsmeier and Wittig reactions.

**Step I: N,N'-bis(4-methoxyphenyl)-N-phenyl-N'-4-formylphenyl-[1,1'-biphenyl]-4,4'-diamine.** In a three necked flask, 6 ml DMF are cooled to 0 °C under argon and 0.91 ml (10 mmol) POCl<sub>3</sub> (freshly distilled) are added and stirred for 30 min. After ice bath removal the solution is stirred until the evolution of a red color. In a separate three necked flask, 5.48 g (10 mmol) N,N'-bis(4-methoxyphenyl)-N,N'-diphenyl-[1,1'-biphenyl]-4,4'-diamine<sup>[1]</sup> are stirred in 50 ml dichloroethane under argon at 0 °C and the POCl<sub>3</sub>/ DMF mixture is added via syringe. After stirring for 15 min, the temperature is raised to 80 °C for 3 h. The mixture is cooled to room temperature and is then added dropwise to 5 g sodium acetate in 50 ml ice/water under vigorous stirring where it is left overnight. After washing the aqueous layer several times with chloroform, the organic layers are combined and dried over sodium sulfate. The solvents are removed under reduced pressure and the crude product is purified by column chromatography (CH<sub>2</sub>Cl<sub>2</sub>). Yield 54 %. TCL (CH<sub>2</sub>Cl<sub>2</sub>, R<sub>f</sub>= 0.22).

IR (in film);  $\nu$  [cm<sup>-1</sup>]= 3034 (s), 3000 (m), 2907 (m), 2835 (s), 1693 (s), 1592 (s), 1500 (s), 1440 (m), 1244 (s), 1162 (s), 1108 (m), 1035 (s), 823 (s), 697 (m).

<sup>1</sup>H-NMR (250 MHz, CD<sub>2</sub>Cl<sub>2</sub>);  $\delta$  (ppm)= 9.77 (s, 1H, CHO); 7.64 (d, <sup>3</sup>J<sub>HH</sub>= 8.85 Hz, 2H); 7.53 (d, <sup>3</sup>J<sub>HH</sub>= 8.85 Hz, 2H); 7.44 (d, <sup>3</sup>J<sub>HH</sub>= 8.85 Hz, 2H); 7.28- 6.84 (m, 19H); 3.81 (s, 6H, OCH<sub>3</sub>).

MS (EI, 70 eV);  $m/z$ = 576 (100) [M<sup>+</sup>]; 561 (8) [M<sup>+</sup>-Me]; 288 (18); 273 (13).

**Step II: N,N'-bis(4-methoxyphenyl)-N-phenyl-N'-4-vinylphenyl-[1,1'-biphenyl]-4,4'-diamine.**

In a three necked flask, 3.64 g (6.31 mmol) N,N'-bis(4-methoxyphenyl)-N-phenyl-N'-4-formylphenyl-[1,1'-biphenyl]-4,4'-diamine and 9.02 g (25.24 mmol) methyltriphenylphosphonium bromide are dissolved in 100 ml dry THF under argon. 2.83 g (25.24 mmol) potassium t-butoxide are added and the mixture is stirred at 20 °C for around 1 h, the disappearance of the educt is verified by thin layer chromatography. After completion of the reaction, 50 ml 10 % acetic acid are added and it is stirred for 1 h at 5 °C. The aqueous layer is extracted twice with chloroform, the organic layers are combined and extracted two times with water, dried over sodium sulfate and the solvents are removed under reduced pressure. The residue is dissolved in a small amount of THF and precipitated

in ammoniacal methanol. After column chromatography (cyclohexane: ethyl acetate, 9:1) the product is freeze-dried. Yield 72 %. TCL (cyclohexane, ethyl acetate, 9:1,  $R_f = 0.44$ ).

IR (in film);  $\nu$  [ $\text{cm}^{-1}$ ] = 3035 (s), 3006 (s), 2950 (s), 2933 (m), 2844 (m), 1717 (w), 1600 (m), 1506 (s), 1320 (m), 1242 (m), 1180 (m), 1037 (s), 831 (s), 696 (m).

$^1\text{H-NMR}$  (250 MHz,  $\text{CDCl}_3$ );  $\delta$  (ppm) = 7.44- 7.34 (m, 4H); 7.29- 7.18 (m, 4H); 7.13- 6.90 (m, 13 H); 6.88- 6.80 (m, 4H), 6.64 (dd,  $^3J_{\text{HHtrans}} = 17.7$  Hz,  $^3J_{\text{HHcis}} = 10.9$  Hz, 1H); 5.60 (d,  $^3J_{\text{HHtrans}} = 17.7$  Hz, 1H); 5.12 (d,  $^3J_{\text{HHcis}} = 10.9$  Hz, 1H); 3.79 (s, 6H,  $\text{OCH}_3$ ). MS (EI, 70 eV);  $m/z = 574$  (100) [ $\text{M}^+$ ]; 559 (7) [ $\text{M}^+ - \text{Me}$ ]; 287 (16); 272 (11).

**Synthesis of 5a, 5b: PvDMTPA.** 2.17 g (6.548 mmol) **2** were filled into a 10 ml flask under argon. Solutions of **1** (10.66 mg, 0.0327 mmol in 500  $\mu\text{l}$  anisole) and **4** (0.72 mg, 0.0033 mmol in 43  $\mu\text{l}$  anisole) were added. After degassing, the mixture was stirred at 125  $^\circ\text{C}$  for 20 min (**5b**) and 38 min (**5a**) to get molecular weights of 9.4 and 17.7 kg/mol, respectively. The polymerization was quenched by rapid cooling. Dilution in THF and precipitation (3x) in methanol (**5b**) and isopropanol (**5a**) yielded 304 mg of **5b** and 543 mg of **5a** as white powders.

$^1\text{H-NMR}$  (250 MHz,  $\text{CDCl}_3$ );  $\delta$  (ppm) = 6.80 (br,  $\text{CH}^{\text{ar}}$ ), 6.58 (br,  $\text{CH}^{\text{ar}}$ ), 3.59 (br,  $\text{OCH}_3$ ), 1.83 (br, CH), 1.48 (br,  $\text{CH}_2$ ).

**Synthesis of 6: PvDMTPD.** 1.81 g (3.157 mmol) **3** were filled into a 10 ml flask under argon. Solutions of **1** (12.84 mg, 0.0395 mmol in 400  $\mu\text{l}$  anisole) and **4** (4.35 mg, 0.0197 mmol in 54  $\mu\text{l}$  anisole) were added. After degassing, the mixture was stirred at 125  $^\circ\text{C}$  for 210 min. The polymerization was quenched by rapid cooling. Dilution in THF and precipitation (3x) in acetone yielded **6** as a white powder (408 mg).

$^1\text{H-NMR}$  (250 MHz,  $\text{CD}_2\text{Cl}_2$ );  $\delta$  (ppm) = 7.10 (br,  $\text{CH}^{\text{ar}}$ ), 6.88 (br,  $\text{CH}^{\text{ar}}$ ), 6.80 (br,  $\text{CH}^{\text{ar}}$ ), 6.53 (br,  $\text{CH}^{\text{ar}}$ ), 3.76 (br,  $\text{OCH}_3$ ), 3.64 (br,  $\text{OCH}_3$ ), 1.97 (br, CH), 1.57 (br,  $\text{CH}_2$ ).

**Synthesis of 9a: PvDMTPA<sub>28</sub>-block-PPerAcr<sub>72</sub>.** 50 mg (0.0028 mmol) **5** and 520 mg (0.678 mmol) **7** were filled in a 5 ml flask. A solution of styrene (3.53 mg, 0.0339 mmol in 35  $\mu\text{l}$  1,2-dichlorobenzene) and 100  $\mu\text{l}$  1,2-dichlorobenzene were added. After degassing, the mixture

was stirred at 125 °C for 11 h. The polymerization was stopped by rapid cooling. Dilution in THF and precipitation in acetone (3x) yielded **9** as a brittle dark-red solid (85 mg).

<sup>1</sup>H-NMR (250 MHz, CDCl<sub>3</sub>); δ (ppm)= 8.06 (br, CH<sup>ar</sup> perylene), 7.90 (br, CH<sup>ar</sup> perylene), 7.65 (br, CH<sup>ar</sup> perylene), 6.97 (br, CH<sup>ar</sup> TPA), 6.57 (br, CH<sup>ar</sup> TPA), 5.04 (br, NCH), 3.80 (br, OCH<sub>2</sub>, NCH<sub>2</sub>), 3.58 (br, OCH<sub>3</sub>), 2.15 (br, CH<sup>al</sup>), 1.92 (br, CH<sup>al</sup>), 1.64 (br, CH<sup>al</sup>), 1.33 (br, CH<sup>al</sup>), 1.23 (br, CH<sup>al</sup>), 0.82 (br, CH<sub>3</sub>).

**Synthesis of 9b: PvDMTPA<sub>16</sub>-block-PPerAcr<sub>84</sub>.** 94 mg (0.01 mmol) **5** und 990 mg (1.2 mmol) **7** were filled in a 10 ml flask. A solution of styrene (6.25 mg, 0.06 mmol in 50 µl 1,2-dichlorobenzene) and 200 µl 1,2-dichlorobenzene were added. After degassing, the mixture was stirred at 125 °C for 24 h. The polymerization was stopped by rapid cooling. Dilution in THF and precipitation in acetone was followed by soxhlet extraction in n-hexane for 5 d. The polymer was then diluted in chlorobenzene and precipitated in methyl ethyl ketone (2x) to yield **10** as a brittle dark-red solid (200 mg).

<sup>1</sup>H-NMR (250 MHz, CDCl<sub>3</sub>); δ (ppm)= 8.02 (br, CH<sup>ar</sup> perylene), 7.86 (br, CH<sup>ar</sup> perylene), 7.61 (br, CH<sup>ar</sup> perylene), 6.79 (br, CH<sup>ar</sup> TPA), 6.57 (br, CH<sup>ar</sup> TPA), 5.00 (br, NCH), 4.01 (br, OCH<sub>2</sub>, NCH<sub>2</sub>), 3.58 (br, OCH<sub>3</sub>), 2.15 (br, CH<sup>al</sup>), 1.90 (br, CH<sup>al</sup>), 1.69 (br, CH<sup>al</sup>), 1.33 (br, CH<sup>al</sup>), 1.23 (br, CH<sup>al</sup>), 0.81 (br, CH<sub>3</sub>).

**Synthesis of 10: PvDMTPD<sub>19</sub>-block-PPerAcr<sub>81</sub>.** 30 mg (0.0042 mmol) **6** and 344 mg (0.42 mmol) **7** were filled in a 5 ml flask. A solution of styrene (2.38 mg, 0.021 mmol in 187 µl 1,2-dichlorobenzene) was added. After degassing, the mixture was stirred at 125 °C for 20 h. The polymerization was stopped by rapid cooling. Dilution in chlorobenzene and precipitation in methyl ethyl ketone (3x) yielded **10** as a brittle dark-red solid (62 mg).

<sup>1</sup>H-NMR (250 MHz, CDCl<sub>3</sub>); δ (ppm)= 8.00 (br, CH<sup>ar</sup> perylene), 7.95 (br, CH<sup>ar</sup> perylene), 7.61 (br, CH<sup>ar</sup> perylene), 7.08 (br, CH<sup>ar</sup> TPD), 6.90 (br, CH<sup>ar</sup> TPD), 6.81 (br, CH<sup>ar</sup> TPD), 6.49 (br, CH<sup>ar</sup> TPD), 5.01 (br, NCH), 4.01 (br, OCH<sub>2</sub>, NCH<sub>2</sub>), 3.66 (br, OCH<sub>3</sub>), 3.44 (br, OCH<sub>3</sub>), 2.15 (br, OCH<sub>2</sub>CH<sub>2</sub>), 1.90 (br, NCH<sub>2</sub>CH<sub>2</sub>), 1.69 (br, NCH(CH<sub>2</sub>)<sub>2</sub>), 1.33 (br, CH<sup>al</sup>), 1.23 (br, CH<sup>al</sup>), 0.82 (br, CH<sub>3</sub>).

1. C. Schmitz, M. Thelakkat, H. W. Schmidt, *Adv. Mater.* **1999**, *11*, 821.

## List of Publications

17. Z. Wu, A. Petzold, T. Henze, T. Thurn-Albrecht, R. Lohwasser, **M. Sommer**, M. Thelakkat:  
Hierarchical, temperature and molecular weight dependent equilibrium structures in semiconducting poly(3-hexylthiophene),  
*Macromolecules*, submitted
16. **M. Sommer**, S. Hüttner, M. Thelakkat:  
Conjugated block copolymers for photovoltaic applications,  
*Advances in Polymer Science*, in print.
15. S. Hüttner, **M. Sommer**, A. Chiche, G. Krausch, U. Steiner, M. Thelakkat:  
A solvent annealing method for polymer electronics,  
*Soft Matter*, **2009**, 5, 4206.
14. **M. Sommer**, S. Hüttner, M. Thelakkat:  
Crystalline-crystalline donor acceptor block copolymers for photovoltaic applications,  
Book chapter in: *Ideas in Chemistry*, Wiley-Ich, in print.
13. **M. Sommer**, S. Hüttner, U. Steiner, M. Thelakkat:  
Influence of the molecular weight of double-crystalline donor acceptor block copolymers on the performance of polymer solar cells,  
*Applied Physics Letters*, in print.
12. **M. Sommer**, M. Thelakkat:  
In situ imaging of evolution of morphology of semiconductor polymer blends and block copolymers using focused ion beam and scanning electron microscopy,  
*Applied Materials and Interfaces*, provisionally accepted.

11. **M. Sommer**, S. Hüttner, M. Thelakkat:  
Semiconductor block copolymers for photovoltaic applications,  
*Journal of Materials Chemistry*, submitted.
10. E. M. Barea, G. Garcia-Belmonte, **M. Sommer**, S. Hüttner, H. J. Bolink, M. Thelakkat:  
Determination of charge carrier mobility of hole transporting polytriarylamine-based diodes,  
*Thin Solid Films*, **2009**, DOI: 10.1016/j.tsf.2009.10.003.
9. S. King, **M. Sommer**, S. Hüttner, M. Thelakkat, S. A. Haque:  
Charge separation and recombination in self-organizing nanostructured donor-acceptor block copolymer films,  
*Journal of Materials Chemistry*, **2009**, *19*, 5436.
8. A. Wicklein, S. Gosh, **M. Sommer**, F. Würthner, M. Thelakkat:  
Self-assembly of semiconductor organogelator nanowires for photoinduced charge separation,  
*ACS Nano*, **2009**, *3*, 1107.
7. **M. Sommer**, A. Lang, M. Thelakkat:  
Crystalline-crystalline donor-acceptor block copolymers,  
*Angewandte Chemie International Edition*, **2008**, *47*, 7901.
6. S. Maria, A. S. Sussha, **M. Sommer**, D. V. Talapin, A. L. Rogach, M. Thelakkat:  
Morphology control in polymer nanocomposites using self-organizing semiconductor block copolymers,  
*Macromolecules*, **2008**, *41*, 6081.

5. **M. Sommer**, S. Hüttner, S. Wunder, M. Thelakkat:  
Novel electron conducting block copolymers: Morphological, optical and electronic properties,  
*Advanced Materials*, **2008**, *20*, 2523.
  
4. S. Hüttner, **M. Sommer**, M. Thelakkat:  
N-type organic field effect transistors from perylene bisimide block copolymers and homopolymers,  
*Applied Physics Letters*, **2008**, *92*, 093302.
  
3. **M. Sommer**, S. M. Lindner, M. Thelakkat:  
Influence of HOMO energy levels and morphology of microphase separated donor-acceptor diblock copolymers in polymer solar cells,  
*Advanced Functional Materials*, **2007**, *17*, 1493.
  
2. **M. Sommer**, M. Thelakkat:  
Synthesis, characterization and application of donor-acceptor block copolymers in nanostructured bulk heterojunction solar cells:  
*European Physical Journal Applied Physics*, **2006**, *36*, 245.
  
1. L. Ruiz-Perez, A. Pryke, **M. Sommer**, G. Battaglia, I. Soutar, L. Swanson, M. Geoghegan:  
Conformation of poly(methacrylic acid) chains in dilute aqueous solution,  
*Macromolecules*, **2008**, *41*, 2203.



## Danksagung

Direkt oder indirekt beigetragen zu dieser Arbeit haben viele Helfer, Partner und Freunde, welche hier kurz erwähnt werden sollen:

Zuerst möchte ich mich herzlichst bei meinem Betreuer dieser Arbeit, Prof. Dr. Mukundan Thelakkat, für die grosse Freiheit in der Forschung, die intensive Betreuung, sowie für die vielen Aufmunterungen nach synthetischen Fehlschlägen bedanken. Diese besondere Art der Betreuung hat massgeblich zu dem Erfolg dieser Arbeit beigetragen und ist keinesfalls selbstverständlich. Auch die Möglichkeit, an zahlreichen nationalen und internationalen Konferenzen teilzunehmen, hat meinen Horizont erweitert und letztendlich diese Arbeit geprägt. Vielen, herzlichen Dank!

Herrn Prof. Dr. Hans W. Schmidt möchte ich für die Bereitstellung eines gut ausgestatteten Laborplatzes danken.

Grosser Dank gebührt auch Sven Hüttner, der mit ungebremsten Interesse und Engagement vieles möglich gemacht hat und diese Arbeit um zahlreiche Erkenntnisse bereichert hat. Gerade zu Zeiten von geringerer Motivation war dies eine grosse Stütze. Unzählige Dinge, wären an dieser Stelle zu nennen, von denen die wichtigsten beinhalten: Messungen von organischen Feldeffekttransistoren, die kontrollierte Lösungsmitteldampfbehandlung und die zeitaufgelösten Spektroskopiemessungen. Danke!

Vielen Dank an unsere Gruppe *AFuPo*, die sich in den letzten zwei Jahren aufgrund intensiver Kochabende immer besser formiert hat. Ein besonderes Dankeschön an Helga Wietasch für die Unterstützung in der Synthese in Steinbock-Manier! Danke auch an Sebastián Maria, André Wicklein, Andreas Lang, Ruth Lohwasser, Katja Willinger und Peter Bauer, in deren Arbeiten die ein oder andere Verbindung von mir Verwendung finden konnte, und für die Unterstützung am TEM.

Danke auch an die vielen Praktikanten und HiWis für die Hilfe bei anstrengender Laborarbeit: Tobias Tokumaru, Nadine Kaufmann, Stefanie Wunder, Stefan Weiss, Ruth Lohwasser und Katharina Neumann.

Bei der gesamten Gruppe in der MCI möchte ich mich für die Unterstützung während der letzten vier Jahre bedanken. Danke vor allem an Robin Pettau für die kontinuierliche Versorgung mit trockenem THF, an Andre Wicklein für die Guinier-Messungen, Klaus Kreger für Einblicke in die Tiefen der GPC und stete Diskussionsbereitschaft, Christina Löffler für die Unterstützung im GPC-Team, Michi Rothmann für die Unterstützung in Computerfragen, und Benjamin Gössler für die Einweisung am REM.

Werner Reichstein und Holger Laukant möchte ich für die Unterstützung und Einweisung beim Carl Zeiss Cross Beam danken.

Wolfgang Milius gebührt grosser Dank für die Hilfe bei der Indizierung des Polymers PPerAcr.

Danke auch an Andreas Walther für sein Interesse an Blockcopolymeren mit funktionellen Blöcken, vor allem jedoch für die grosse Hilfe bei der anionischen Polymerisation, auch wenn letztendlich andere schneller waren...

...aber auch an die restlichen Mitglieder der MC II für Hilfe hier und da, Grillfeste, Milch, Kaffee, an Jiang Yuan, Sabine Wunder, und Felix Schacher.

Bei der PC II, vor allem bei Markus Hund und Alexandra Schweikart, möchte ich mich für die Nachhilfe am Rasterkraftmikroskop, und bei Carmen Kunert für die Hilfe am TEM bedanken. Danke auch an Alexander Böker und Kerstin Schindler für ihr Interesse and Polymeren für Solarzellen und die Kooperation.

Bei Florian Spreitler möchte ich mich für sein Interesse und die Einzelmolekülspektroskopiemessungen an PPerAcr bedanken.

Danke an unsere vielen Kooperationspartner ausserhalb der Universität Bayreuth, die uns in wichtigen Fragen weiterhelfen und unseren Horizont erweitern: Simon King und Saif Haque (Imperial College London), Andrei Sussha und Andrey Rogach (LMU Universität München), Zhiyong Wu und Thomas Thurn-Albrecht (Universität Halle), Ali Cirpan (University of Amherst, Massachussetts), Chetan Raj-Singh und Harald Hoppe (Universität Ilmenau), Gérama Garcia-Belmonte (Universitat Jaume), Martin Heeney (Queens University of London), und Kristin Schmidt (University of Santa Barbara).

Zuletzt danke ich herzlichst meiner lieben Familie für die Unterstützung während der gesamten Zeit. Vor allem jedoch auch meiner lieben Schwester Sabine und meiner lieben Freundin Christiane für die Unterstützung und das Korrekturlesen der Manuskripte! Vielen lieben Dank!

## **Erklärung**

Hiermit erkläre ich, dass ich die Arbeit selbstständig verfasst und keine anderen als die angegebenen Hilfsmittel verwendet habe.

Ferner erkläre ich, dass ich anderweitig mit oder ohne Erfolg nicht versucht habe, diese Dissertation einzureichen. Ich habe keine gleichartige Doktorarbeit an einer anderen Hochschule endgültig nicht bestanden.

Bayreuth, März 2009

(Michael Sommer)